Elucidating Mechanisms for Drug Combination Nanoparticles to Enhance and Prolong Lymphatic Exposure: Experimental and Modeling Approaches

John Cavin Kraft II

A dissertation

submitted in partial fulfillment of the

requirements for the degree of

Doctor of Philosophy

University of Washington

2018

Reading Committee:

Rodney J. Y. Ho, Chair

Kenneth E. Thummel

Shiu-Lok Hu

Program Authorized to Offer Degree:

Pharmaceutics

University of Washington

Abstract

Elucidating Mechanisms for Drug Combination Nanoparticles to Enhance and Prolong Lymphatic Exposure: Experimental and Modeling Approaches

John Cavin Kraft II

Chair of the Supervisory Committee:
Rodney J. Y. Ho
Department of Pharmaceutics

Human immunodeficiency virus (HIV) infection and metastatic cancers impact over 50 million people worldwide. Because HIV and metastatic cancers exploit the lymphatics to persist and spread, enhanced and prolonged lymphatic exposure to drug combinations is essential for treating these diseases. Unfortunately, many oral and intravenous small molecule drug therapies exhibit limited lymphatic exposure, which can lead to subtherapeutic drug levels and drug resistance. Moreover, most therapeutic strategies and decisions for these diseases are not made with lymphatic drug exposure in mind, largely because accounting for and understanding lymphatic drug levels is complex, and limited tools exist for this. Thus, there is a need for tools to better understand lymphatic drug exposure and for strategies to selectively deliver drug combinations to the lymphatics. We previously developed lymphatic-targeted drug combination nanoparticles (DcNPs), however, the mechanisms that enable DcNPs to target drug combinations to the lymphatics remained to be elucidated. Understanding these mechanisms could open up new therapeutic strategies for treating lymphatic diseases. Therefore, the goals of this thesis are 1) to develop novel tools to help understand lymphatic drug exposure and 2) to use these tools to elucidate how DcNPs enable enhanced and prolonged lymphatic exposure. First, this thesis describes for the first time that a single injection of DcNPs enabled enhanced and prolonged drug levels in HIV host cells (lymph node and blood lymphocytes) that were persistently higher than those in the plasma. Then, to assess lymphatic drug exposure and to elucidate the mechanisms of this sustained targeting of drug combinations to lymphocytes with DcNPs, novel tools were developed, namely near-infrared fluorescent DcNPs to track their *in vivo* distribution pathways in real-time, and mechanism-based pharmacokinetic (MBPK) models. Together these tools elucidated that DcNPs undergo lymphatic first-pass distribution and lymph node and lymphocyte retention, which leads to the enhanced and prolonged lymphatic exposure to drug combinations. This is the first time that the novel concept of lymph nodes and lymphocytes serving as body-wide drug depots to enable long-acting pharmacokinetics for drug combinations in both the lymphatics and the plasma has been described. These novel long-acting mechanisms and tools for assessing lymphatic exposure have significant potential to be used to develop new treatment strategies for lymphatic diseases.

Lay Abstract

Over 50 million individuals worldwide are impacted by human immunodeficiency virus (HIV) infection and metastatic cancer, which exploit the lymphatic system to persist and spread. However, the lymphatics are poorly understood and this has prevented the development of effective lymphatic therapies. To address these limitations, we previously pioneered a lymphatic drug delivery platform for drug combinations. This thesis has developed and employed a suite of quantitative tools to understand the mechanisms this drug combination platform uses for enhanced and prolonged lymphatic exposure. This new understanding coupled with these quantitative tools have significant potential to be used for the development of new therapeutic strategies for lymphatic diseases.

TABLE OF CONTENTS

LIST OF FIGURES

LIST OF TABLES

ACKNOWLEDGEMENTS

First, I want to thank my mentor, Rodney Ho, for being a truly exceptional PhD advisor, both on the personal side of things and on the science side of things. His caring heart and rigorous practice of science has helped me grow both as a person and pharmaceutical scientist. My PhD training experience has been extremely unique and challenging in terms of its scope and the science I was exposed to, and I thank him from the bottom of my heart for providing me this opportunity and for everything he has taught me and done for me. I also had the pleasure and good fortune to be mentored by Danny Shen, who I've learned valuable lessons and character traits from. He is an inspiration and role model to us all, and I thank him for taking me under his wing through our pharmacokinetic modeling work. I've learned a tremendous amount through observing him conduct himself as a colleague, an educator, a scientist, and as one of the kindest people I know.

Next, I want to thank all of my incredible lab members and those involved in the TLC-ART program who have been a pleasure to work with each and every day. It has been a privilege forming friendships with this group, and I'll value these friendships throughout my life.

I'd also like to thank my thesis reading committee, Drs. Ken Thummel, Shiu-Lok Hu, and Rodney Ho, for the time and effort they spent to read and provide feedback on my thesis. I've learned valuable lessons from Ken and Shiu-Lok as a graduate student that I will hold dear. Shiu-Lok has a wonderful way of teaching how to ask significant, testable questions and organizing one's line of investigation by following the most significant questions. He also teaches wonderful analogies such as research is like cultivating your own garden – you plant this seed here, fertilize

a little here, this is the best season to grow this, etc. And Ken has done so much for our Department, making it one of the premier places for pharmaceutical science training and research in the world. It has been simply amazing to observe him over the years masterfully interact with and lead the faculty, students, and staff.

I also want to thank the funding that has made this research and my training possible. Specifically, I thank the U.S. government and its commitment to biomedical research and training. NIH grants that funded my training and research are as follows: UM1 AI120176-03, T32-GM007750, TL1-1TR002318-01, 1S10OD010652-01, and AI27757.

Last but not least, I want to thank my amazing loved ones. I thank my incredible wife, my sisters Jenny and Ellie, and my parents for all of their tremendous love and support. This PhD journey would not have been possible without their love and inspiration, for which I'm truly blessed to have.

DEDICATION

To Oumou, the half of me who has made me whole ever since the moment we found each other.

Chapter 1. **Introduction**

1.1 Background and Significance

There has been a growing recognition that the lymphatics have key roles in diseases, including inflammation, infection, metastatic spread of cancer, lymphedema, obesity, diabetes, and cardiovascular disease (Mortimer and Rockson 2014). Taken together, hundreds of millions of individuals throughout the world are impacted by such diseases with etiologies that involve the lymphatics (Ruddle 2014). More specifically, human immunodeficiency virus (HIV) and metastatic cancers exploit lymphatic pathways to persist and spread throughout the body in over 50 million people worldwide (IARC 2018). However, most therapeutic strategies and decisions for these diseases are not made with lymphatic drug exposure in mind, largely because limited tools and practices exist to account for drug level time courses and exposures in the complex body-wide lymphatic network of vessels and nodes. As a result, these recent advances in understanding the roles of the lymphatics in pathological processes have sparked the recognition that lymphatic-targeted therapies have the potential to transform disease treatment. Moreover, there is currently a gap in knowledge for understanding lymphatic drug exposure due to limited tools being available to assess drug exposure in the complex and diffuse lymphatic tissues throughout the body. This thesis aims to help address this gap.

Currently, most therapeutic decisions are made based on target plasma drug concentrations which may not always predict the lymph, lymph node, and lymphatic tissue drug kinetics or overall exposure. For instance, in normal functioning lymphatics, many oral (PO) and intravenous (IV) small molecule drug therapies that are quickly eliminated from the blood may have limited *penetration* from the blood to lymphatics as well as limited *retention* in lymph nodes and lymphoid tissues as demonstrated with orally administered HIV drugs (Kinman, Brodie et al. 2003, Fletcher,

Staskus et al. 2014, Lorenzo-Redondo, Fryer et al. 2016, Estes, Kityo et al. 2017, Lee, Hatano et al. 2017). These lower lymphatic drug levels can lead to subtherapeutic concentrations that make these therapies ineffective or prone to induction of drug resistance. Therefore, lymphatic drug-targeting strategies that *enhance* and *prolong* lymphatic exposure are needed to address this lymphatic drug insufficiency.

Moreover, disease states and invasive therapies can significantly impact the ability of drug to reach lymphatic tissues. In disease states such as human immunodeficiency virus (HIV) infection and metastatic cancer, virus-infected cells and advancing metastatic cancer cells reside in and spread through the lymphatic system. This can significantly impact lymphatic function through abnormalities that alter lymph vessel density, dilation, contraction, flow, and lymph node function (Estes 2013, Trevaskis, Kaminskas et al. 2015). For instance, HIV patients exhibit a progressive pattern of lymph node destruction that culminates in end-stage acquired immunodeficiency syndrome (AIDS) (Biberfeld, Ost et al. 1987, Ioachim, Cronin et al. 1990). In metastatic cancer, lymphatic function is altered by peri-tumoral lymphangiogenesis, lymph vessel dilation, and increased lymph flow draining from the tumor (Swartz and Lund 2012). In addition, invasive surgical removal of metastatic lymph nodes (lymphadenectomy) and obliteration of lymph node metastases using radiation therapy can disrupt lymphatic flow, and lead to morbidities such as swelling and lymphedema (Ashikaga, Krag et al. 2010). As a result, these changes in lymphatic function due to disease states and invasive therapies can significantly impact the access of drug to lymphatic tissues. However, there currently exists a gap in knowledge on the impact of disease-mediated and treatment-mediated changes in lymphatic function on lymphatic access of drugs. With an ability (e.g., a tool or approach) to assess in detail lymphatic vessel pathways and

lymphoid tissues that could be exposed to drug, this could create a new paradigm for making treatment decisions for lymphatic diseases.

Unfortunately, preclinical and clinical assessment of lymphatic drug exposure is complex and detailed knowledge on time and extent of drug distribution and exposure is limited. Understanding of the kinetics of a dosage form and route of administration and their impact on how drugs are distributed between blood and lymph, and to which extent drug molecules reach peripheral and more central lymphatics and the extent of drug exposure, could begin to address how most effective therapeutic strategies could be implemented. Recently, minimally invasive catheterization of the thoracic lymph duct in humans was described (Nadolski and Itkin 2013), which will hopefully lead to greater understanding of lymphatic drug exposure. However, since this only samples thoracic lymph drug levels at a terminal point before lymph enters the blood, it cannot sufficiently assess specific changes in lymphatic function in localized regions of the body, and cannot discern drug access and time courses in the complex networks of lymph vessels and nodes. Clearly, the ability to assess details of lymphatic drug exposure is missing.

Clinically, lymphatic mapping involves using blue dye and/or radiocolloids. Blue dye small molecules can be seen only at the tissue surface with the naked eye and carry significant risks of anaphylaxis and skin necrosis; radiocolloids can be easily detected through tissue mass with a handheld device but have poor resolution and use harmful ionizing radiation (Verbeek, Troyan et al. 2014, Johnson, Chick et al. 2016). This makes these diagnostic approaches suboptimal for assessing lymphatic pathways available for drug access (to ensure lymphatic drug exposure) and using this information to guide therapeutic decisions. Therefore, a new tool is

needed that can sensitively detect alterations in lymphatic function due to disease or invasive treatments, and can also assess lymphatic drug distribution pathways to guide therapeutic decisions. A non-invasive imaging technology that can visualize in detail the lymph vessel and node networks throughout the body using safe (non-ionizing) near-infrared fluorescent (NIRF) lymphatic-targeted nanoparticles could serve as such a tool. In this way, lymphatic drug delivery strategies (using lymphotropic nanoparticles) could be used to image lymphatic function or involvement in disease, to assess lymphatic drug access. Through a better understanding of lymphatic drug distribution pathways and lymphatic exposure (i.e., the kinetics of lymphatic drug disposition), this could result in enhanced therapeutic outcomes and could open up entirely new therapeutic strategies.

Furthermore, with increased understanding of molecular mechanisms of diseases such as infection and cancer, these diseases are increasingly treated with *drug combinations* that act at multiple protein targets of a given pathogen (e.g., viral proteins or overexpressed cancer-associated drug targets) to enhance efficacy and suppress drug resistance. A classic example of this is the treatment of HIV infection with oral combination antiretroviral therapy (cART). However, having multiple orally administered drugs being handled independently by the body creates further complications for treating lymphatic diseases. With multiple drugs distributing independently, there are variable pharmacokinetics for each drug—different distribution profiles, and drug levels rise, peak, and fall at different rates and extents. Ideally, drug combinations should be presented at predetermined concentrations to target sites, and maintained at these concentrations over time. To accomplish this, a drug carrier platform that can *target*, *accumulate*, and *retain* a consistent molar ratio of a combination of two or more drugs in target cells within lymphoid tissues would

be highly valuable. This cannot be achieved with currently approved fixed-dose oral combination dosage forms or by simply combining drugs into parenteral formulations.

To address this, our laboratory has developed a drug combination injectable formulation platform for HIV therapy that is known as drug combination nanoparticles (DcNPs) (Freeling, Koehn et al. 2014, Freeling, Koehn et al. 2015). HIV infection is an appropriate model to study the ability of DcNPs to provide drug exposure in lymphatic tissues, which harbor residual HIV disease and are a barrier to achieving curative treatment, because the pathobiology of residual and active HIV replication is intimately linked to the entire lymphatic system. In other words, the target sites for HIV are in the lymphatic system. Specifically, lymphocytes (particularly $CD4^+$ T cells) in lymph nodes and lymphoid tissues throughout the body are the primary target and host for HIV replication, their decline in the body is linked to the development and progression of AIDS, and they are chronically infected despite undetectable plasma viral levels during oral cART (Embretson, Zupancic et al. 1993, Pantaleo, Graziosi et al. 1993, Estes 2013). In addition, lymphatic drug insufficiency has been documented in HIV patients and has been associated with residual viral levels in lymphoid tissues (Fletcher, Staskus et al. 2014, Lorenzo-Redondo, Fryer et al. 2016). Because low lymphatic drug levels may lead to ongoing viral replication and thus viral persistence, there is the potential that enhancing lymphatic exposure to antiretroviral combinations with DcNPs could improve therapeutic efficacy by overcoming this lymphatic drug insufficiency and enhancing the ability of drug combinations to prevent ongoing viral replication in lymphoid tissues.

However, currently, this hypothesis that subtherapeutic lymphatic drug levels lead to low levels of ongoing viral replication, and this ongoing replication largely prevents eradication of HIV from lymphoid tissue sanctuaries, is a point of vigorous debate in the HIV field. A common criticism of the studies by Fletcher *et al.* (Fletcher, Staskus et al. 2014) and Lorenzo-Redondo *et al.* (Lorenzo-Redondo, Fryer et al. 2016) is that analyzing patients during the first 6 months of antiretroviral therapy may be too short of a treatment duration and is insufficient to investigate the role of ongoing viral replication in persistent viral reservoirs (Kearney, Wiegand et al. 2017, Rosenbloom, Hill et al. 2017). Scientists against the lymphatic drug insufficiency hypothesis argue that any ongoing replication in lymphoid tissue viral reservoirs is at such low and undetectable levels that it is highly unlikely to be the mechanism that sustains the reservoir (Chakradhar 2018). Instead, this camp points to viral persistence under antiretroviral therapy being due to HIV exploiting complex immune mechanisms designed to sustain life-long persistence of cellular immune memory (Kuo and Lichterfeld 2018). In other words, HIV exploits key immunological memory mechanisms that have evolved in humans to not die out over a lifespan. Thus, antiretroviral therapy that merely halts HIV replication is not designed to be effective at clearing long-term memory immune cells with integrated viral DNA. However, perhaps maintaining consistent and effective antiretroviral drug levels in lymphoid tissues via DcNPs could allow any ongoing replication in lymphoid tissues to be totally eliminated, and thereby create more opportunity for the immune system and/or other therapeutic approaches targeted at the latent viral reservoir to be effective. To shed light on this debate and help advance HIV treatment efficacy, more sensitive and systematic time-course studies that provide data on viral and drug levels in lymphoid tissues, and the specific cell types that harbor integrated virus, are required to gain a deeper understanding. Recent reviews and perspectives discuss this debate and the current

understanding of HIV reservoirs and long-term viral persistence during antiretroviral therapy (Rodrigues, Ruffin et al. 2017, Chakradhar 2018, Kuo and Lichterfeld 2018, Sengupta and Siliciano 2018).

Preliminary studies of DcNPs for HIV treatment in non-human primates showed promise in their ability to (1) target drug combinations to lymphocytes in both lymph nodes and the blood, and (2) to sustain drug levels in the plasma and lymphocytes in the blood (Freeling, Koehn et al. 2014, Freeling, Koehn et al. 2015). However, the underlying mechanisms that contributed to the lymph node- and cell-targeting and long-acting pharmacokinetics—in other words, the processes involved in the subcutaneous absorption and distribution of DcNPs—remained to be elucidated. With such knowledge, a major step could be taken to further the development and translation of DcNPs for treatment of lymphatic diseases. In addition, understanding these mechanisms could open up new therapeutic strategies for treating lymphatic diseases.

Therefore, the goal of this thesis is to understand these mechanisms through investigating the differential lymphatic distribution pathways between free small molecule combinations and DcNP-bound small molecule combinations. We developed and employed novel tools and approaches (i.e., *in vivo* imaging of DcNP distribution pathways, and mathematical pharmacokinetic modeling) to enable mechanistic studies of an integrated model that encompasses the absorption from the administration site and disposition of DcNPs and their drug cargo. We validated the model with prospective experimental studies to validate and refine the mechanism-based pharmacokinetic models. Through understanding the specific mechanisms that lead to the key outcomes of lymphocyte-targeting and long-acting pharmacokinetics of DcNP-bound small

molecule drug combinations, we now can better optimize the safety and efficacy of DcNP chemotherapies, and advance the clinical translation of DcNPs for not only HIV treatment, but potentially for multiple lymphatic diseases. In addition, the NIRF lymphatic imaging/mapping tool developed in this thesis could be used to assess the impact of disease- and treatment-mediated changes in lymphatic function on lymphatic drug access; this could open up new treatment paradigms for lymphatic diseases.

The purpose of this introductory chapter is to examine (1) prevalent diseases that involve the lymphatics to appreciate the impact that lymphatic-targeted therapies could have, (2) the anatomical, physiological, and experimental factors relevant to targeting drugs to lymphatic cells and tissues, (3) experimental evidence of small molecule and macromolecule lymphatic drug delivery and the implications of these studies for DcNPs, and (4) long-acting drug regimens that came before DcNPs. Following these sections, the central hypothesis, sub-hypotheses, and aims of this thesis will be presented prior to an outline of the subsequent chapters that specifically address these hypotheses and aims.

1.2 Disease Etiologies that Involve the Lymphatic System

Unfortunately, there currently exists a lack of understanding of lymphatic disease among health professionals (Rockson 2017). This is thought to partly be due to the average American medical school graduate receiving an exposure to the lymphatic circulation for less than 30 minutes within a 4-year medical education (Rockson, Granger et al. 2004). Another reason is the difficulty of visualizing the transparent lymphatic vessels, which has led to the lymphatics historically being ignored in research. This sentiment is not new—Philip McMaster commented

in his Harvey Lecture in 1942, "The functions of the lymphatic system have remained largely unknown (since its discovery). Two influences have contributed to our state of ignorance, a lack of suitable methods of study…and a lack of interest" (McMaster 1942). Through the development of a near-infrared lymphatic imaging tool and elucidation of key pharmacokinetic mechanisms for a drug combination lymphatic delivery platform (DcNPs), this thesis has narrowed these knowledge gaps and has created potential to open up new therapeutic strategies for lymphatic disease. Below, some key disease etiologies that involve the lymphatic system are discussed. More extensive reviews have been recently published (Mortimer and Rockson 2014, Betterman and Harvey 2016, Padera, Meijer et al. 2016). Many of these lymphatic diseases have the potential to be diagnosed and/or treated with DcNPs.

HIV-1 infects and damages the entire lymphatic system by establishing productive infection that disseminates throughout presumably every lymphoid tissue in the body (Scharko, Perlman et al. 1996). This widespread infection of lymphoid tissue is unique among infectious pathogens (Estes 2013). It has a profound effect on organ systems integrally linked to secondary lymphoid tissues and immune function, such as the gastrointestinal tract, which during HIV infection undergoes epithelial barrier damage and associated microbial translocation that creates another persistent source of immune activation (Brenchley, Price et al. 2006, Brenchley and Douek 2008, Estes, Harris et al. 2010, Brenchley and Douek 2012). A scheme of four distinct histopathological lesion classifications are established for the prognosis of HIV disease progression based on the degree of damage to lymphoid tissue follicular structures: (i) follicular hyperplasia, (ii) follicular lysis, (iii) follicular atrophy with or without fibrosis, and (iv) follicular and lymphocytic depletion (Vago, Antonacci et al. 1989, Baroni and Uccini 1990). Early studies

of lymph nodes from HIV patients also demonstrated focal hemorrhages, extensive cellular destruction, accumulation of neutrophils, phagocytosis of nuclear debris, proliferation of blood vessels, immunoblasts, and peculiar aggregates of clear cells that were classified as acute lymphadenitis. These studies suggested that lymphadenitis in HIV infection was induced by a microorganism, likely a virus that resulted in lymphotropism that resulted in destruction of CD4+ T lymphocytes (Domingo and Chin 1983, Ioachim, Lerner et al. 1983, Ioachim, Lerner et al. 1983). Once HIV was identified as the causative virus for AIDS (Barre-Sinoussi, Chermann et al. 1983, Gallo, Sarin et al. 1983), HIV antigens and viral particles were found within lymph nodes from patients at all phases of disease, particularly within germinal centers associated with follicular dendritic cells (FDCs) (Ward, O'Leary et al. 1987, Baroni, Pezzella et al. 1988, Schuurman, Krone et al. 1988). These reports highlight the central role of secondary lymphoid tissues in HIV, and provide a key rationale for targeting drug to these tissues.

Lymphedema, a vascular disorder, is a cardinal manifestation of lymphatic malfunction. It is a chronic condition resulting from the body's inability to drain lymph fluid. It leads to interstitial edema of protein-rich interstitial fluid, presence of significant inflammatory cell infiltrate, and dysregulated regional immune responses (Paskett, Dean et al. 2012). Subsequently, it leads to adipose tissue deposition and fibrosis, and later stages may lead to debilitating architectural alteration of the skin and supporting tissues and tissue destruction (Paskett, Dean et al. 2012). There are two forms. Primary lymphedema occurs infrequently on a heritable basis (e.g., Milroy's disease due to a missense inactivating mutation of vascular endothelial growth factor 3 (*Vegfr3*)). Secondary lymphedema, or acquired lymphedema, is most common in the Western world, and arises as a treatment-related side effect of lymph node resection and

radiotherapy in cancer patients or after parasitic infection. Approximately 15-50% of cancer survivors suffer from lymphedema (about 10 million Americans) and over 90 million individuals globally have lymphedema due to lymphatic filariasis (Rockson 2012). It is not simply obstruction of lymph flow that leads to lymphedema that develops from cancer treatment. Paradoxically, patients with breast-cancer related lymphedema following removal of axillary lymph nodes have significantly higher, not lower, peripheral lymph flows following surgery (Stanton, Modi et al. 2009). This suggests lymphedema development is systemically driven, and it is hypothesized to result from an inflammatory abnormality. Current pharmacotherapeutic options for lymphedema are limited and largely ineffective. However, an ongoing clinical trial (NCT02700529) is testing bestatin, a clinically-approved inhibitor of leukotriene A_4 hydrolase (LTA_4H) within the eicosanoid pathway, as an oral drug therapy for lymphedema and has shown promising results in a murine model (Tian, Rockson et al. 2017, Jiang, Nicolls et al. 2018).

While primary tumors can be resected by surgery or treated with radiation and/or chemotherapy, there are often residual cancer cells remaining in the body that have metastasized from the primary tumor. It is metastases, not the primary tumor, that most often cause cancer-related death (Chaffer and Weinberg 2011). The preferential route for cancer cell spread from a primary tumor is through the lymphatics. This underpins the sentinel lymph node (that is, first draining) biopsy procedure in many cancers for cancer progression staging and for early detection of metastatic spread. Detailed histological analysis of several types of solid tumors have revealed that lymphatic vessels are collapsed and rarely functional inside tumors, but functional lymphatics do occupy peripheral zones around tumors (Mouta Carreira, Nasser et al. 2001, Weinberg 2014). Despite this, cancer cells do indeed succeed in entering the lymphatics to metastasize, especially,

for instance, in breast cancer (Leikola, Toivonen et al. 2005). A recent review provides further details on the lymphatic system's role in cancer progression (Padera, Meijer et al. 2016). Harnessing the mechanisms involved in cancer cells approaching, entering, and trafficking within the initial lymphatics would be a major step in cancer treatment. DcNPs could be used to deliver combination chemotherapies to lymphatic metastases.

The significance of the lymphatic system in metabolic diseases such as obesity, heart disease, and diabetes has just begun to emerge (Haemmerle, Keller et al. 2013, Martel and Randolph 2013, Kutkut, Meens et al. 2015, Scallan, Hill et al. 2015). Using clearance of ^{99m}Tc-labeled human albumin to investigate adipose tissue lymphatic drainage, lymph drainage was found to be significantly lower in obese human subjects compared to lean controls (Arngrim, Simonsen et al. 2013). Thus, obese subjects have a reduced ability to remove macromolecules from the interstitial space through the lymphatic system. Atherosclerosis—chronic inflammatory disease of the arterial wall—is sustained in part by deposition of cholesterol crystals and unhelpful immunity against cholesterol-associated apolipoproteins (Shi, Bot et al. 2015). Removal of cholesterol esters by lipoprotein acceptors such as apoAI, which results in formation of high-density lipoprotein (HDL), helps regress atherosclerosis (Small, Bond et al. 1984). It was recently shown that HDL primarily uses lymphatic vessels to reach the bloodstream from the interstitium (Lim, Thiam et al. 2013, Martel, Li et al. 2013). Thus, functional lymphatics appear to be required to facilitate the removal of atherosclerotic plaques. Therefore, the lymphatics are now known to play a key role in the pathogenesis of atherosclerosis, which leads to complications that are the most common cause of morbidity and mortality in Western societies.

In the field of rheumatology, new insights on the link between the lymphatic system and rheumatoid arthritis (RA) are also emerging. Mouse studies have showed a critical role of the lymphatic system for the removal of inflammatory factors and cells from inflamed synovium. Initially, lymphatic drainage increases at the onset of inflammatory-erosive arthritis, then as inflammation becomes more chronic, nearby lymph vessels and nodes become damaged and contribute to the eventual severe synovitis and joint erosion. Thus, there is strong rationale for targeting the lymphatics for therapeutic interventions for RA. These studies are discussed in more detail in a recent review (Bouta, Bell et al. 2018).

1.3 Factors Affecting Lymphatic Drug Distribution and Retention

For small molecule and macromolecule drugs to distribute directly from the subcutaneous space to the lymphatics, there are certain anatomical and physiological factors, as well as experimental factors (e.g., injection site, volume, and rate) to consider. Understanding these factors is important for targeting drug to the lymphatics for therapeutic interventions. This section will examine these factors and how they may promote or impede the distribution pathways of DcNPs from the subcutaneous space.

1.3.1 *Anatomical and Physiological Factors*

1.3.1.1 Interstitium, Lymphatic Endothelial Cells (LECs), and Lymph

A fundamental physiological mechanism of the lymphatics is the uptake of interstitial fluid. Under normal conditions, the volume of interstitial fluid is maintained at ~20% of body weight (Aukland and Reed 1993). Major components of the interstitium are a collagen fiber framework,

a gel phase of negatively charged glycosaminoglycans (GAGs), a salt solution, and plasma proteins (Wiig and Swartz 2012), which present a navigational challenge to molecules, proteins, and particles. Structurally, the extracellular matrix is composed of pores and channels that range in size from 10 nm to hundreds of nanometers that create a sterical impedance to large molecules and particles (> ~100 nm) (Chauhan and Jain 2013). Additionally, the faster rate of blood flow (~100-500-fold > lymph flow (Swartz 2001)) and superior sink conditions in blood capillaries stimulate small molecule drug absorption into the blood.

The negative charge of the interstitium causes positively charged molecules to stick and negatively charged entities to move in the direction of least resistance. Much of the negative charge is derived from the GAGs, which are polyanionic polysaccharide chains of repeating disaccharide units of hexosamine and uronic acid or galactose (Comper and Laurent 1978). There are four main classes of GAGs: heparin/heparan sulfate, chondroitin/dermatan sulfate, keratin sulfate, and hyaluronan (Raman, Sasisekharan et al. 2005). All except hyaluronan are covalently bound to a protein backbone to form a proteoglycan (Aukland and Reed 1993).

The oak leaf-shaped endothelial cells of initial lymphatic capillaries overlap while being anchored to the extracellular matrix by collagen VII (Swartz 2001, Negrini and Moriondo 2011). Unlike blood capillaries, lymphatic capillaries are devoid of pericytes. Mechanical forces in the extracellular matrix pull on interstitial anchoring filaments connected to lymphatic endothelial cells and open these flap openings of lymphatic capillaries, allowing interstitial fluid and its constituents to enter the lymphatic system. In mice, the size of the flap openings between vascular endothelial (VE)-cadherin button junctions in lymphatic capillaries is ~2-3 μm (Baluk, Fuxe et al.

2007, Murfee, Rappleye et al. 2007). This is in contrast to the reported ~5-12 nm pore size of continuous and fenestrated (non-sinusoidal) human blood capillaries perfusing >95% of the body (e.g., skeletal muscle, skin) (Sarin 2010). Therefore, the lymphatics have an architecture suited to uptake large molecules, proteins, particles, as well as small cells, bacteria, and viruses, while blood capillaries do not.

Both paracellular (passive) and transcellular (active) transport mechanisms have been described for the lymphatic endothelium, however, the exact mechanisms and relative importance of passive versus active transendothelial transport in lymph formation and drug targeting remain to be determined. It is well accepted that cyclically variable hydraulic pressure gradients between the interstitium and initial lymphatic capillaries drive lymph formation, and vesicular transcellular transport does occur (Wiig and Swartz 2012). Classic electron microscopy studies have shown intracellular vesicles carrying large solutes, lipids, and particles across lymphatic endothelium (Dobbins and Rollins 1970, Azzali 1982, Feng, Nagy et al. 2002), and more recent studies have shown active regulation of transendothelial transport of solute, lipid, and water (Breslin, Yuan et al. 2007, Dixon, Raghunathan et al. 2009, Miteva, Rutkowski et al. 2010, Triacca, Guc et al. 2017). Also, transport of chylomicrons from the interstitium to the lymphatic vessel lumen is actively regulated, and the basal-to-apical transport is much more efficient than the apical-to-basal pathway (Dixon, Raghunathan et al. 2009). Recent studies in mouse models have demonstrated the importance of lymphatic vasculature in lipid homeostasis and SR-B1-receptor mediated uptake of HDL into the lymphatics (Lim, Rutkowski et al. 2009, Lim, Thiam et al. 2013). Albumin is transported across blood vascular endothelial cells by gp60 and caveolae (Schubert, Frank et al. 2001, John, Vogel et al. 2003), however, this remains to be investigated for lymphatic endothelial

cells. More research is warranted to elucidate the details of the transcellular transport mechanisms involved in the lymphatics.

In general, the protein concentration in lymph is ~50% of that in plasma in skin and muscle (Aukland and Reed 1993), but for lung and spleen, the percentages are much higher at ~65% (Fishman, Fisher et al. 1985) and 90% (Kaufman and Deng 1993, Nanjee, Cooke et al. 2000), respectively. Levels of lipoproteins and lipids in lymph are ~10% of those in plasma (Nanjee, Cooke et al. 2000).

The filtration rate of fluid from blood to interstitium and into lymphatics is governed by the Starling principle of fluid exchange. It states that filtration of fluid from blood capillaries to the interstitium is driven by the hydraulic (water) pressure gradient across the blood vessel wall (P_c-$P_{i,}$ where P_c is capillary pressure and P_i is interstitial pressure) and opposed by the osmotic pressure gradient (π_p-π_i, where π_p is the plasma osmotic pressure and π_i is the interstitial osmotic pressure from tissue proteins), which is the suction force that keeps fluid within blood vessels. The traditional view that 90% of interstitial fluid is reabsorbed at the venous end of the capillary is not supported by modern evidence if all Starling forces (interstitial colloid osmotic and hydraulic pressures) are considered (Mortimer and Rockson 2014). In most vascular beds, there is a net and decreasing filtration along the entire length of well-perfused capillaries and no venous reabsorption. Recent data from 12 human tissues at steady state confirm that the sum of pressures opposing filtration is consistently less than venular blood pressure (Levick 2004, Levick and Michel 2010). The importance of the lymphatics in absorbing capillary filtrate is highlighted with the development of tissue edema due to either an intrinsic (genetic) defect in the structure or

function of the lymphatics (primary lymphedema) or trauma, surgery, or infection interrupting the lymphatic structure (secondary lymphedema). Unfortunately, recent reviews still propagate the dogma that the majority of plasma exudate in the interstitial fluid is reabsorbed in post-capillary venules (Richter, Bhansali et al. 2012).

Interstitial fluid flows into lymph capillaries at an average rate of ~10 mL/min, whereas the rate of return of lymph to the blood is lower at ~1 mL/min due to reabsorption of water from the lymphatic vessels and lymph nodes (Swartz 2001, Rowland and Tozer 2011). Lymph flow averages ~1-3 L/day through the human thoracic lymphatic duct, which returns lymph to the blood circulation at anastomoses with the left subclavian vein near the heart (**Figure 1.1**). The greatest producer of lymph is the liver, which contributes ~30-50% of thoracic duct flow (Levick 2010).

Thoracic duct lymph is a mixture of peripheral and intestinal lymph and the two differ from each other in composition and function. Intestinal lymph transports newly synthesized chylomicrons (~200-1,000 nm in diameter) from the ilium to the bloodstream during the absorption of ingested fat. It is thought that the tip of each lacteal contains large pores that are sufficient in size to allow chylomicron entry (Lee 1986). Importantly, a rich macrophage and DC network presides in intestinal villi that uptake macromolecules via endocytosis; this endocytic network has been shown to protect lacteals from tracer antigens (fluorescently labeled ovalbumin) in mice (Chang, Song et al. 2013). It is notable that intestinally-absorbed chylomicrons and lymph-derived lipoproteins transit through mesenteric lymph nodes, the thoracic duct, then heart, vasculature of the lungs, and subsequently to organs prior to being exposed to hepatic metabolism and

elimination. This strongly contrasts with non-fatty nutrients and small molecules that directly enter the portal venous circulation from intestinal villi and are immediately exposed to the liver.

Massive lipid deposits are present in the edematous tissue of patients with lymphedema (Schirger, Harrison et al. 1962, Brorson, Ohlin et al. 2006). This suggests the lymphatic system is vital for transport of lipid from the interstitial space. In fact, the lymphatic system is key to a physiological process known as reverse cholesterol transport (RCT). This concept was first postulated in 1966 (Glomset, Janssen et al. 1966) and was termed RCT in 1976 (Weinstein, Carew et al. 1976). It is the removal of excess cholesterol from tissues and transfer to the plasma and then the liver, where this cholesterol is processed and packaged into bile acids for excretion into the gut. In other words, it is a multistep process of cholesterol mobilization from extravascular tissues to biliary and nonbiliary excretion. It specifically involves high-density lipoprotein (HDL), the anti-atherogenic "good" cholesterol, and these particles (~7-11 nm in diameter (Blanche, Gong et al. 1981, Cheung and Albers 1984)) require lymphatic transport to return to the bloodstream from the interstitium (Randolph and Miller 2014). In summary, DcNPs (~60 nm) in the interstitium likely transit through the <100 nm interstitial fluid channels and preferentially transport across lymphatic endothelial cells into the lymph rather than across blood endothelial cells into the blood.

1.3.1.2 Lymph Vessel and Node Networks

As a whole, the lymphatic system is central to fluid homeostasis, immune function, fat absorption in the gut, reverse cholesterol transport, and disease (Trevaskis, Kaminskas et al. 2015). It is not merely a passive transit system from the interstitial space to the blood circulation (for the clearance of fluid, proteins, and debris from the interstitial space, as well as transport of dietary

fat), but it actively regulates numerous physiological and pathological processes. It is important to understand the lymphatic network architecture and how DcNPs may transit through this tortuous organ system.

The lymphatics are organized into primary and secondary lymphoid tissues. Primary lymphoid tissues include the thymus and bone marrow, while secondary lymphoid tissues include the tonsils, spleen, Peyer's patches and mucosal lymphocytes in the gut, and the distributed network of lymph vessels and nodes throughout the body. Thus, it is a complicated and disperse organ system. Gaspare Aselli of Italy is credited with discovering the visceral lymphatic circulation in 1627 when he first documented "milky veins" (lacteis venis) in the mesentery of a dog that had just been fed (Aselli 1627). Searching back 2000 years, Hippocrates (c. 460 to c. 370 BC), the Father of Medicine, recognized the lymphatic vessels as "white blood," and even created the term *chyle* (Choi, Lee et al. 2012). In about every tissue and organ in the body (Leak, Schannahan et al. 1978, Holstein, Orlandini et al. 1979, Leak and Jamuar 1983, Eliska 1984, Listrom and Fenoglio-Preiser 1987, Kivela, Havas et al. 2007, Vainionpaa, Butzow et al. 2007, Matsumoto, Soh et al. 2008, Ohtani and Ohtani 2008, Red-Horse 2008, Thomson, Heinen et al. 2014, Cesmebasi, Malefant et al. 2015), including the brain and spinal cord (Schwalbe 1869, Brierley and Field 1948, Foldi, Csanda et al. 1968, Aspelund, Antila et al. 2015, Louveau, Smirnov et al. 2015), but not the placenta (Castro, Tony Parks et al. 2011), cartilage, and optic cornea and lens, lymphatic capillaries absorb fluids, salts, small and large molecules, and cells from the interstitial space. Lymph is presented to a network of lymphoid organs via lymph vessels (**Figure 1.2**) and a fraction is recycled back into the blood circulation.

Lymph nodes are interconnected through lymphatic endothelial vessels. Type I lymph nodes are present in the periphery where afferent vessels release lymph into the LN subcapsular sinus and efferent vessels carry lymph away (Engeset 1959, Kubik 2003), and Type II lymph nodes are more centrally located where afferent vessels can pass completely through or bypass lymph nodes (Kubik 2003). In humans, the anatomy of lymph flow through vessels and nodes is described as asymmetrical. Lymph from the right arm, the right side of the head and neck, and the right side of the thorax drains into the ~2 cm right lymphatic duct, which empties into the right subclavian vein by the heart. Lymph from all other parts of the body drains via the ~40 cm thoracic duct into the left subclavian vein (Margaris and Black 2012). In chronic inflammatory pathologies such as obesity, diabetes, atherosclerosis, and cancer, tertiary lymphoid organs with architectures closely resembling those of lymph nodes develop in inflamed tissues (Ruddle 2014).

Collecting lymphatic vessels, unlike initial lymphatic capillaries, are coated with a layer of smooth muscle cells very similar to cardiac muscle, and they contain a series of one-way semilunar valves that prevent backflow. Each section between consecutive intraluminal valves is called a lymphangion. The number of valves per vessel segment varies depending on the tissue type, and is generally highest in tissues with high hydrostatic pressure (e.g., legs in humans) (Schulte-Merker, Sabine et al. 2011). An action potential complex initiates contraction of these lymphatic collectors and thus an electrical impulse propagated by pacemaker cells is required for efficient pumping (Schmid-Schonbein 1990, Muthuchamy and Zawieja 2008). Therefore, calcium influx is important for the pacemaker potential, and calcium channel antagonists could interfere with lymphatic pumping (Toland, McCloskey et al. 2000, Mortimer and Rockson 2014). Moreover, collecting lymphatic vessels have a different molecular signature than initial lymphatic endothelial

cells (LECs). For example, after development, lymphatic vessel endothelial hyaluronan receptor (LYVE-1) is not expressed on collecting lymphatics and prospero homeobox protein 1 (PROX1) is only expressed on valves (Norrmen, Ivanov et al. 2009). All LECs, however, express podoplanin, a 36-43-kDa mucin-type integral transmembrane glycoprotein (Karaman and Detmar 2014).

1.3.1.3 Lymph Node Architecture and Cellular Composition

Lymph nodes (~500 in the human body) are roughly oval-shaped glandular organs (**Figure 1.3**). They provide a highly organized microenvironment that promotes interaction between antigen-specific lymphocytes and their cognate antigen. They are connected by a system of lymphatic vessels that allows immune cells and antigen to drain from sites of infection, resulting in an efficient adaptive as well as innate immune response to immunological challenge. It is key to understand how DcNPs enter, interact with, and clear from lymph node tissues and cells.

Classically, lymph nodes are described as having three main anatomic compartments: the cortex, paracortex, and medulla. Lymph nodes consist of an outer capsule of dense irregular connective tissue surrounded by adipose tissue. At the convex surface of the lymph node, several afferent lymph vessels (containing intraluminal valves to prevent efflux of lymph) penetrate the capsule. Underlying the capsule is a subcapsular sinus lined with LECs and subcapsular macrophages. The capsule invaginates inward toward the cortex forming trabeculae of connective tissue over paratrabecular sinuses. Between adjacent trabeculae and below the subcapsular and paratrabecular sinuses are organized compartments (“lymphoid lobules”) with (1) lymphatic follicles containing proliferating B cells (or lymphoblasts) in germinal centers, resident follicular

dendritic cells (FDCs), migrating dendritic cells, macrophages, and supporting fibroblastic reticular cells (FRCs) that produce type III reticular fibers to form conduits from the subcapsular sinus to high endothelial venules (HEVs), (2) a deep or inner cortex containing CD4+ T cells and postcapillary venules (the sites of entry of most lymphocytes—particularly naïve lymphocytes—from the blood) lined by high endothelial cells, and (3) medullary cords containing mainly macrophages and plasma cells surrounding medullary sinuses. Lymph in the subcapsular sinus flows to the paratrabecular sinuses and percolates to the medullary sinuses, which gather into a single efferent (exiting) lymphatic vessel that penetrates the capsule at the hilum on the concave surface of the lymph node (Willard-Mack 2006).

In a 71 kg human male, the total volume of lymph nodes in the body is estimated to be 274 mL (Shah and Betts 2012) and human lymph nodes vary in diameter between 0.5 to 2 cm (Treuting, Dintzis et al. 2012). Afferent lymph vessel anastomoses with lymph nodes are greater in number per lymph node in large species (e.g., humans) versus small species (e.g., rodents). In the rat, the low amount of lymph vessel-lymph node anastomoses results in transfer of lymph to sub-portions of the node rather than the node as a whole (Sainte-Marie, Peng et al. 1982), whereas in humans, lymph nodes demonstrate a more uniform drainage pattern that exposes more nodal compartments to the lymph (Haley 2003). Moreover, compared to humans, rodent lymph nodes are relatively few totaling ~30-50 (Tilney 1971, Van den Broeck, Derore et al. 2006) and are organized into low numbers of simple chains and connections (Dunn 1954). Lymph nodes of young mice (< 4 mo) often lack germinal centers and there are few obvious HEVs (Treuting, Dintzis et al. 2012). Although swine have fixed skin with tight attachment to subcutaneous tissues (Swindle 2012), which may limit wide lateral expansion after SC administration, and their skin and SC space are

structurally and biochemically similar to that of humans (Eaglstein and Mertz 1978, Swindle, Makin et al. 2012), their skin has reduced vasculature and their lymph nodes have a unique inverted architecture (McFarlin and Binns 1973, Swindle 2012) that could impact SC drug absorption and lymph node delivery. Despite the differences in swine lymph vessel density and lymph node architecture compared to humans, minipigs have been endorsed as a suitable model for therapeutic protein pharmacokinetics (Richter, Bhansali et al. 2012, Richter and Jacobsen 2014). Although mouse lymph nodes are small (1-4 mm) compared to human lymph nodes (0.5-2 cm), they have similar architecture in terms of cell organization and regional distribution of parenchymal cells (Treuting, Dintzis et al. 2012). These are important distinctions to consider when studying drug distribution to lymphoid tissue in preclinical models.

1.3.1.4 Pathobiology of HIV-1 in Lymphoid Tissues

HIV patients with progressive infection present with microscopic changes in secondary lymphoid tissue that includes diffuse augmentation of collagen II, elastic fibers, laminin, fibronectin, and proteoglycans, and patients with the most severe lymph node damage had the most marked reduction in $CD4^+$ T cells (Biberfeld, Ost et al. 1987, Paiva, Morais et al. 1996). In the lymph nodes of HIV-infected patients, the extent of lymph node fibrosis was inversely correlated with the size of the $CD4^+$ T-cell population in the T-cell zone (Schacker, Nguyen et al. 2002, Diaz, Alos et al. 2010, Diaz, Garcia et al. 2011, Wight and Potter-Perigo 2011). These pathological changes in HIV-infected lymph nodes may significantly impact the exposure and efficacy of DcNPs, however, this requires further investigtion.

Virtually all *treated* HIV patients have evidence of persisting lymphoid tissue abnormalities (i.e., follicular absence, regression and hyperplasia, abnormal CD4+ T-cell population size, and damaged lymphoid tissue architecture) (Schacker, Nguyen et al. 2002). These lymphoid tissue abnormalities that result from HIV infection can lead to the development of acquired immunodeficiency syndrome (AIDS), which is defined as less than 200 peripheral blood $CD4^+$ T cells per μL of blood and/or the development of an opportunistic infection. Even when peripheral blood $CD4^+$ T cell count significantly recovers, $CD4^+$ T-cell populations in secondary lymphoid tissues remain markedly reduced (Schacker, Nguyen et al. 2002, Estes 2009). The amount of collagen deposited in the T-cell zone of lymph nodes at the time of initiating suppressive antiretroviral therapy (ART) predicts the magnitude of recovery of the peripheral $CD4^+$ T-cell pool with treatment (Schacker, Nguyen et al. 2002, Schacker, Reilly et al. 2005).

Extensive collagen deposition, which happens initially in the T cell zone and then extends to all lymphoid tissue compartments as disease progresses (Schacker, Nguyen et al. 2002, Estes, Wietgrefe et al. 2007), leads to lymph node fibrosis, which is caused by an increase in extracellular matrix constituents (primarily collagen I and III and fibronectin) produced by resident tissue fibroblasts (Wight and Potter-Perigo 2011). As a part of the fibrotic process, normal tissue is replaced by fine scar-like structure that create obstructions that limit lymph drainage, which leads to further accumulation of extracellular matrix proteins that stimulates more fibrosis (Estes 2009). Lymph nodes in end-stage AIDS patients can have over 30% of the parenchyma replaced by fibrotic collagen (Zeng, Haase et al. 2012). This could present a major barrier for drug delivery to these tissues.

1.3.1.5 Lymphocytes: The Host Cells for HIV Infection

Lymphocytes are a form of small leukocytes (white blood cells) with a single round nucleus and are key players in immunological processes in the body. They reside especially in the lymphatic system, where they circulate between lymphoid tissues and the blood to respond to antigen. They consist of T cells, B cells, and natural killer (NK) cells. T and B cells are part of the adaptive immune system, while NK cells are classified as part of the innate immune system. It is especially important that DcNPs deliver their drug combination payload to $CD4^+$ T lymphocytes, which are the major host cells for HIV infection.

In the blood of healthy adult humans, there are 3,500-10,500 white blood cells (WBCs) per μL. Within these WBCs, ~15-34% are T cells, ~2-10% are B cells, and ~2% are NK cells. The rest are largely neutrophils and monocytes. Of the T cells, ~70% are $CD4^+$ T cells, the main host cells for HIV infection (Ioachim, Lerner et al. 1983). This equates to about 613-1,840 $CD4^+$ T cells per μL of blood. Based on single-photon emission computed tomography (SPECT) imaging of ^{111}In-labeled anti-CD4 mAbs dosed by IV infusion in macaques, ~85% of $CD4^+$ T lymphocytes are located in lymph nodes and gut lymphoid tissue, while 15% are in the spleen, and only ~0.3-0.5% are in the blood (Di Mascio, Paik et al. 2009). It has also been estimated that up to 85% of lymphoid tissue is in the gut (Cerf-Bensussan and Guy-Grand 1991, Mowat and Viney 1997). This clearly illustrates the importance of measuring drug and HIV levels in lymphoid tissues as well as the blood for understanding pharmacokinetic and pharmacodynamic relationships for HIV treatment.

T cells in the gut are known to have phenotypic, functional, and survival properties that are distinct from those of T cells in other tissues (Khan, Telwatte et al. 2017). In gut tissue, it has been

consistently shown that HIV DNA levels per million $CD4^+$ T cells are considerably higher than those in the blood, even when patients are adherent to daily oral cART. In patients on cART with sustained, undetectable plasma viremia, HIV DNA levels per million $CD4^+$ T cells were on average 5-6-fold higher in the gut than the blood (Chun, Nickle et al. 2008, Eriksson, Graf et al. 2013). Poles *et al.* calculated from quantitative PCR on endoscopic biopsies that the gut contained over 2-fold as many HIV DNA^+ cells as the blood in cART-suppressed patients (Poles, Boscardin et al. 2006). Yukl *et al.* estimated that in cART-suppressed patients up to 95% of all HIV-infected $CD4^+$ T cells (or 1.9×10^9 cells) are in the gut (Yukl, Gianella et al. 2010).

Therefore, these data strongly suggest that it is critical to not only target cART to lymph nodes peripherally located in the body (e.g., axillary, inguinal, popliteal, etc.), but also and most importantly to the lymphoid tissues in the gut. However, currently, there exists a gap in knowledge on the specific lymphocyte subsets in the gut that harbor replication-competent virus or integrated viral DNA, where these cells are located, and where they traffic to in the body during suppressive daily oral cART and no treatment. With a deeper understanding of this pathobiology, more specific drug targeting strategies may be developed.

1.3.2 *Experimental Factors: Injection Site, Volume, and Rate*

Depending on where a subcutaneous injection is located on the body, the injection volume, and the rate of its application, the rate and extent of drug absorption into the blood and subsequent distribution into lymph and lymph nodes can be highly variable. Moreover, as shown in **Figure 1.1**, motility, sleep, and anesthesia can significantly impact lymph flow (Hiller, Ismail et al. 2016). Heat can also increase lymphatic flow (Olszewski, Engeset et al. 1977). Most studies have assessed

the impact of the SC injection site on blood exposure; very few have assessed the impact on lymph node uptake or the time course of drug levels in lymph nodes. Considering the factors that influence the lymphatic uptake of DcNPs will be important for the first-in-human studies of DcNPs and may impact the lymphocyte-targeting and long-acting PK of DcNPs.

Some of the earliest studies that looked at the impact of the SC injection site involved insulin (~6 kDa). Nora *et al.* administered ^{131}I-labeled lente insulin SC in the thigh or upper arm of healthy adults and found insulin absorbed faster from the arm (arm and thigh absorption half-lives were on average 232 and 310 minutes, respectively) (Nora, Smith et al. 1964). This was confirmed in studies that assessed the abdomen, arm, and thigh SC injection sites and found insulin absorption was the fastest from the abdomen, intermediate from the arm, and slowest from the thigh (Binder 1969, Koivisto and Felig 1980). A study on human growth hormone (hGH; ~22 kDa; ~5 nm) found similar results in humans where the area under the curve (AUC) after SC abdominal injection was 528 ± 86 and after SC thigh injection was 239 ± 34 mU/L•hr (Beshyah, Anyaoku et al. 1991). Thus, the injection site likely impacted the bioavailability of hGH. However, with a different but similarly sized protein—erythropoietin (EPO; 30.4 kDa; ~5 nm)—Macdougall *et al.* administered ^{125}I-labeled EPO in the arm, abdomen, and thigh of healthy volunteers and found the thigh AUC_∞ was 60 ± 13, the arm AUC_∞ was 54 ± 8, and the abdomen AUC_∞ was 46 ± 9 (Macdougall, Jones et al. 1991). Kota *et al.* administered 36 kDa hyperglycosylated darbapoietin alfa to sheep SC and found the rate of absorption into the blood differed according to the injection site: interdigital (0.15 hr^{-1}), shoulder (0.08 hr^{-1}), and abdomen (0.02 hr^{-1}) (Kota, Machavaram et al. 2007). Thus, with smaller proteins, there appears to be differences in the rate and extent of

absorption into the blood according to the SC injection site. The main contributing factors at present remain unclear.

For larger proteins such as monoclonal antibodies (~150 kDa, ~10 nm), the literature is sparse. Xu *et al.* administered 1 mL of 100 mg of golimumab (an anti-TNFα IgG_1 mAb) SC to healthy adults into the upper arm, abdomen, or thigh and found no statistically significant differences in any PK parameters (Xu, Wang et al. 2010). However, it's very likely that soon (and possibly later) after injection, local draining lymph vessels and lymph nodes had the highest concentration of mAb. In a study in rats dosed SC with ~400 μL of 1-10 mg/kg rituximab in the foot, back, or abdomen, the foot had the highest T_{max} and C_{max} compared to the back and abdomen sites, and the abdomen had slightly higher overall blood exposure than the back injection site (Kagan, Turner et al. 2012). These results were later reproduced in mice by the same group (Kagan, Zhao et al. 2014).

For lipid membrane-based vesicles, Oussoren *et al.* administered non-PEGylated ~100 nm [^{3}H]-labeled liposomes SC to rats in the foot or side flank (slightly below the ribcage) and measured radioactivity at the 2-day terminal time point at the injection site and draining lymph nodes (Oussoren, Zuidema et al. 1997). At 2 days post-injection, ~60-100% of the injected dose remained at the injection site, indicating that these liposomes have difficulty clearing from the injection site. They showed the foot injection site enabled higher draining lymph node uptake than the side flank injection site. This limited lymph node uptake from the SC flank injection site is consistent with the results from Moon *et al.* that showed that SC immunization with ~300 nm anti-malarial vaccine particles in the mouse's tail base elicited ~10-fold higher antibody responses than

the SC flank injection site (Moon, Suh et al. 2012). In the most detailed study to date on the lymph node pharmacokinetics in rats, Pitoirre *et al.* administered 500 μL of ~40 nm PEGylated fluorescent nanoparticles SC above the tail, in the right and left flanks, and behind the neck (Pitorre, Bastiat et al. 2015). The found that SC injection above the tail drained efficiently to bilateral inguinal and axillary lymph nodes and had levels at 1-7 days that were ~3-10-fold higher than other injection sites. The other injection sites drained mostly to local lymph nodes and accumulated in nodes at much lower levels. This study did not assess the abdominal injection site. The results of the study by Pitoirre *et al.* is consistent with the finding by Moon *et al.* that the highest antibody response resulted from the tail base administration, although different nanoparticles were used between the studies.

While it remains to be determined for DcNPs which SC injection site is most convenient for patients and provides the safest and most effective lymphatic distribution, the results above suggest a more centrally located injection site, such as the abdomen, may promote the most extensive lymphatic distribution.

In addition to the SC injection site location, the injection volume and rate should be carefully considered when tuning the amount of drug delivered to the lymphatics from the SC space. Unlike scruff animals such as rodents where the loose SC space is more forgiving by allowing lateral expansion of an SC-injected dose, thereby promoting a larger surface area and dampening hydrostatic pressure buildup, humans have more fixed subcutaneous tissue with tight attachments within the matrix of adipocytes and extracellular milieu. Thus, larger injection volumes (>1 mL) administered at a rapid rate (e.g., 360 mL/hr) in human subcutaneous tissue can

lead to pressure buildup. This pressure buildup could artificially force injected fluid into draining lymph vessels, which could be beneficial or negative for therapeutic applications depending on the desired outcome. In pigs, a 1 mL SC injection in 10 seconds (360 mL/hr flow rate) generated a pressure of 24 ± 3.4 kPa, while 10 mL delivered over 10 minutes (60 mL/hr flow rate) generated a pressure of 7.4 ± 7.8 kPa (Doughty, Clawson et al. 2016). Over several seconds after the injection, the pressure decayed to 0.

In dogs with a thoracic lymph duct cannula to collect lymph, 5 mL of horse serum was injected subcutaneously and lymph and blood were sampled at time points to detect the first appearance of horse serum (Lewis 1921). When massage was performed on the injection site, the first appearance of horse serum in the lymph was 15-20 minutes (shortened from 40 minutes in dogs without massage), and the first appearance in the blood was 2 hours (shortened from 3.5 hours in dogs without massage). Moreover, when a high-pressure injection was performed by injecting 200 mL of horse serum with compressed air into the SC abdominal space, horse serum appeared in the lymph in less than 5 minutes, and in the blood in 40 minutes. Thus, pressure at the subcutaneous injection site can significantly influence the absorption rate of subcutaneously administered macromolecules into the lymph.

Some inferences can be made from recent studies in rats dosed with rituximab via different SC injection volumes. Kagan *et al.* dosed rats SC in the foot with 1 mg/kg rituximab in a volume of either 0.1 or 0.3 mL/kg (Kagan, Turner et al. 2012). They also dosed SC in the back with 10 mg/kg in a volume of either 1.0 or 4.0 mL/kg. In both instances, the higher injection volume promoted a higher plasma C_{max} but the AUCs were generally the same. The higher injection

volumes could have forced more antibody via the lymphatics into the blood to create the higher C_{max} levels, much like increasing the rate of an IV infusion. However, no lymphatic drug levels were collected. Lastly, an early study illustrates the impact of vigorous massage of an SC injection site (which increases the pressure) to boost anaphylactic symptoms by horse serum appearing quicker and at higher levels in the blood of guinea pigs (Lewis 1921). After first priming two guinea pigs with 100 μL of horse serum SC, then 17 days later administering 20 mL SC and vigorously massaging the injection site of one but not the other, the guinea pig that had vigorous massage died rapidly while the other showed anaphylactic symptoms but eventually recovered.

1.4 Drug Distribution and Retention in Lymph Nodes and Lymphocytes

1.4.1 *Small Molecule Distribution and Retention*

For most small molecules (<1000 Da) in the interstitial space, drainage occurs primarily through the blood capillaries due to blood flow rates in these vessels ~100-500-fold higher than lymph flow (Swartz 2001), which creates higher mass transport. For drug that does reach lymph nodes via the lymph or blood, the slow-rate perfusion of lymph filtering through nodes and removal by post-nodal (efferent) lymph vessels and nodal blood vessels promotes clearance of these small molecules from nodes. Thus, lymph flow acts as a counteracting force against retention of these drugs in the nodes, making it unlikely that drug levels will persist for long durations in nodes. Thus, approaches such as the one employed by DcNPs need to be taken to improve the drug *retention* in nodes. This section will discuss the pharmacokinetics of small molecules in lymph nodes and lymphocytes so that one can appreciate the challenge and significance of enhancing and retaining levels of small molecule drug combinations in these cells and tissues. The studies reviewed are summarized in **Table 1.1**.

One of the earlier reports in the literature of targeting small molecules to lymph nodes and evaluating the impact of a liposomal formulation on this did so for the purpose of treating lymph node metastases. Khato *et al.* encapsulated the amphiphilic alkylating agent melphalan into ~24 nm liposomes and administered SC liposomal melphalan or free melphalan at 0.125 mg/kg into the left thigh in rats (Khato, Priester et al. 1982). Tritiated melphalan levels and ^{14}C in liposomes were quantified in the ipsilateral (draining) and contralateral (distal) inguinal lymph nodes over 24 hours. Results clearly showed that in ipsilateral draining lymph nodes after SC administration, free drug levels peaked at 30 minutes then rapidly cleared, while liposomal drug also peaked at 30 minutes, fell gradually, then steadily accumulated and maintained persistently high drug levels in the node between 2 and 24 hours. In the ipsilateral node, liposomal melphalan levels strikingly paralleled the levels of the ^{14}C lipid marker of the liposomes, suggesting intact liposomal drug was carried from the injection site to the node by lymphatic channels. Interestingly, while the contralateral inguinal lymph nodes had consistently lower drug levels than the ipsilateral lymph nodes in both groups, the contralateral node after free drug had drug levels approximately 2-fold higher than those after liposomal drug, indicating the free drug was more available in the blood and accessible to more distant nodes than liposomal drug. Thus, the overall results suggest free drug administered SC was absorbed primarily via the blood capillaries, making it available to distant nodes, but some free drug distributed to regional lymph nodes early-on (via direct lymph uptake). However, free drug that did reach nodes was rapidly cleared. On the other hand, liposomes enhanced and maintained local lymph node drug levels via direct lymph delivery, but they retarded absorption of drug from the injection site and consequently did not enable as efficient distribution

of drug to other lymph nodes in the body. This was one of the first studies to probe lymphatic uptake and the distribution pathways of drug from the SC space.

Based on this same concept of interstitially administered liposomes transferring small molecules to regional lymph nodes through lymph vessels, Akamo *et al*. recruited 34 gastric carcinoma patients and administered equal doses of liposomal doxorubicin (~4 μm in diameter) by gastric submucosal injection or intravenously, then quantified drug levels in gastric lymph nodes over 7 hours using HPLC (Akamo, Mizuno et al. 1994). Over the first 4 hours, drug levels in regional gastric lymph nodes were 30- to 50-fold higher after gastric submucosal injection than after IV administration. All lymph nodes around the stomach had similar low levels following IV administration, while regional draining nodes had much higher drug levels than other nodes after submucosal dosing. Thus, this study further supports that in humans systemically administered nanoparticle-associated drug has a relatively low but even distribution into all lymph nodes compared to locally administered nanoparticle-associated drug, which distributes highly into the nearest draining lymph nodes.

A similar study evaluated the uptake and retention of drug in axillary lymph nodes in 60 breast cancer patients (totaling 275 axillary lymph nodes sampled). Following SC or IV administration of carboplatin in carbon particles, Chen *et al.* found that after SC injection the axillary lymph nodes that drained the tumor had drug levels over the first 36 hours that were about 200-fold higher than after IV administration (Chen, Wang et al. 2004). At day 2, lymph node drug levels persisted in the SC group while none was detected in the IV group. This study again supports the idea that SC administration of small molecules encased in particles enhances drug levels and

slows down the clearance of drug in regional draining lymph nodes, thus providing lymph node-targeting and long-acting behavior of small molecules in lymph nodes. In contrast, small molecules given IV (in free form or nanoparticle-associated) supplies lower levels in lymph nodes and distributes more extensively throughout the body, which could lead to toxicity.

In a study in non-human primates that assessed lymph node distribution of the anti-HIV drug indinavir in lymph nodes throughout the body (axillary, inguinal, mesenteric, ileocecal, Peyer's patch, tonsil, bronchial, submandibular, and popliteal), Kinman *et al.* administered 10 mg/kg of either free indinavir or ~100 nm lipid-nanoparticle indinavir in a 20 mL SC injection on the lower back (Kinman, Bui et al. 2006). Compared to lymph node drug levels at 24 hours after SC administration of soluble indinavir, lymph node drug levels were 3- to 16-fold higher after injecting lipid nanoparticle indinavir. Importantly, the drug levels in the *inguinal* lymph nodes were dramatically higher (6- to 48-fold) after nanoparticle administration than all other nodes analyzed, likely because the inguinal nodes were the closest to the lower back injection site. Another important finding from this study was the persistence of high indinavir levels in the plasma over 2 days with the nanoparticle formulation, whereas soluble indinavir was cleared from the plasma by 15 hours. Thus, the overall results of this study showed the ability of lipid-nanoparticles to enhance lymph node drug levels in nodes throughout the body and to provide long-acting plasma drug levels. However, the distribution pathways that contribute to the lymph node drug accumulation (via lymph or blood channels) could not be clearly discerned from this study, and the mechanism that contributed to the long-acting plasma pharmacokinetics remained unknown.

Recently, elegant studies out of the laboratory of Christopher J. Porter at Monash University in Australia have used rats fitted with both thoracic lymph duct and venous blood cannulas to assess the lymph versus blood uptake of SC administered soluble small molecules. These studies, which also have an IV control arm, have helped refine our understanding of the distribution pathways small molecules take to reach lymph node tissues from the SC injection site. They have also helped to more clearly understand the impact that drug formulation has on subcutaneous drug distribution.

Of note, thoracic lymph sampling is one of the furthest downstream sites one can assess along the lymph vessel and node channel between the SC injection site and the entry of lymph into the venous blood near the heart. Thus, the processes and pathways that drug encounters between the injection site and the cannula tip cannot be precisely elucidated. Drug collected in the thoracic duct after SC administration could take two possible pathways: (1) it either travels directly through lymph vessels to get there or (2) it first enters the blood from the SC injection site, or from another point along the lymph vessel and node chain, then extravasates into the interstitium, where it then is taken up by lymph vessels and follows lymph flow to reach the thoracic lymph. This makes the IV control arm informative because any drug injected IV that is then collected in the thoracic lymph must have taken pathway #2 above (i.e., it extravasated from the blood into the interstitium followed by lymph uptake and drainage into the thoracic lymph).

In rats fitted with a thoracic lymph duct cannula, Ryan *et al.* dosed free doxorubicin either SC or IV at 1 mg/kg and continuously collected thoracic lymph (Ryan, Kaminskas et al. 2013). The cumulative amount of drug recovered over 0-30 hours in the thoracic lymph was quantified

by HPLC. After SC and IV dosing of free doxorubicin, only 0.063% and 0.082% of the injected dose was recovered in the thoracic lymph, respectively. The bioavailability in the blood after SC dosing using only area under the concentration-time curve (AUC) data from 0-30 hours was 64%. Overall, these results suggest that soluble doxorubicin hardly distributed at all to the thoracic lymph after SC and IV administration, and primarily absorbed into the blood from the SC space.

This limited lymph and lymph node distribution of free small molecules has recently been shown in HIV-infected humans taking oral small molecule combination antiretroviral therapy (cART) who have achieved undetectable levels of virus in their blood. Importantly, these lower lymphatic drug levels can be subtherapeutic concentrations and induce drug resistance. Fletcher *et al.* showed that in 12 prospectively-treated subjects with no plasma viremia, drug concentrations of tenofovir diphosphate (TFV-DP), emtricitabine triphosphate (FTC-TP), atazanavir (ATZ), darunavir (DRV), and efavirenz (EFV) in lymph node lymphocytes (LNMCs) were all significantly lower than in blood lymphocytes (PBMCs), and these low lymph node lymphocyte levels correlated with continued virus replication (Fletcher, Staskus et al. 2014). In a follow-up study by the same group, Lorenzo-Redondo *et al*. used mathematical modeling that incorporated the data in the Fletcher *et al.* study to further show that insufficient drug concentrations in lymph node cells is associated with ongoing HIV-1 replication and viral trafficking between the lymph nodes and the blood (Lorenzo-Redondo, Fryer et al. 2016). A separate group reported that in 6 patients on cART with suppressed plasma viremia, the median (2.5^{th}-97.5^{th} percentile) lymph node/plasma ratios for raltegravir (RAL) and darunavir (DRV) were 0.17 (0.14-0.25) and 0.30 (0.26-0.35), respectively, indicating that lymph node drug levels were about 30% or less than those in the blood (Lee, Hatano et al. 2017). More recently, Estes *et al.* showed that in 6 rhesus macaques

infected with SIVmac251 and chronically treated with cART, the median LNMC/PBMC ratios for TFV-DP and FTC-TP were 0.84 and 0.26, respectively (Estes, Kityo et al. 2017). This group also quantified drug levels in the gut-associated lymphoid tissue (GALT) and rectal-associated lymphoid tissue (RALT), which had similar drug levels as those in LNMCs. These reports confirm the original hypothesis set forth by our laboratory in 2003 that orally-dosed small molecules have a tendency to achieve inconsistent and insufficient drug levels in lymph nodes and lymphocytes in lymph nodes relative to the plasma and blood lymphocytes, and this could limit the pharmacological efficacy at the lymphoid tissue target sites of HIV replication (Kinman, Brodie et al. 2003).

The small molecules incorporated into some nanocarriers described above have been shown to target naturally to regional draining lymph nodes. Preferentially drug carrier accumulation is likely due to the anatomy and physiology of the subcutaneous space in which (1) lymph capillaries preferentially take up nanosized solute, and (2) the pores between blood endothelial cells are generally too small to allow uptake of these particles (excluding out the larger nanocarrier sizes). By altering the drug distribution profile, this carrier-enhanced drug exposure has shown clear advantages in terms of lymph node drug targeting compared to soluble free small molecule formulations. However, certain nanoparticle systems dosed subcutaneously have shown the ability to distribute to lymph nodes throughout the body (Kinman, Bui et al. 2006, Rao, Forrest et al. 2010), and others have not (Akamo, Mizuno et al. 1994). It is not clear exactly why and which factors contribute the most to differential lymphatic distribution. Taking a different approach, a recently clinically-approved small molecule is dosed orally and distributes systemically to boost lymph node and lymphocyte drug levels throughout the body and is known

as tenofovir alafenamide (TAF; formerly known as GS-7340). It is an amidate prodrug that is derivatized with a cleavable linker that *actively* targets the parent drug molecule, tenofovir (TFV), to lymphocytes.

Tenofovir alafenamide (TAF) works by: (1) passively diffusing into lymphocytes, (2) its ester is hydrolyzed by lysosomal carboxypeptidase cathepsin A (CatA) to form an intermediate of tenofovir (TFV) with a conjugated alanine, (3) the alanine is released by phosphonamidase enzymatic cleavage or chemical degradation to form TFV, and (4) TFV is phosphorylated by kinases to its pharmacologically active metabolite and nucleotide purine analog TFV-diphosphate (TFV-DP) (Ray, Fordyce et al. 2016). CatA is ubiquitously expressed in human tissues with high levels in lymphoid cells (Birkus, Wang et al. 2007). The rapid/initial cleavage of TAF by CatA in lymphocytes creates a sink in lymphocytes, and coupled with the formation of poorly permeable metabolites that are effectively trapped in cells, this allows for substantial accumulation of pharmacologically active TFV-DP in cells. In human whole blood, TAF preferentially loads peripheral blood mononuclear cells (PBMCs) over red blood cells (RBCs) with TFV-DP (Eisenberg, He et al. 2001). TAF also has potent antiviral activity in human donor CD4+ T cells and monocyte derived macrophages (EC_{50} ~10 nM) (Bam, Birkus et al. 2014), making TAF 10-fold more active against HIV than its clinical precursor, the ester prodrug tenofovir disoproxil fumarate (TDF) (Lee, He et al. 2005). In dogs, TAF enhanced drug distribution to lymph nodes compared to TDF, with 24-hour concentrations of ^{14}C-labeled TAF in axillary, iliac, inguinal, and mesenteric lymph nodes approximately 5- to 15-fold higher than those with ^{14}C-labeled TDF after oral dosing of each at 10 mg-eq/kg (Lee, He et al. 2005). In humans at steady-state drug levels resulting from multiple oral doses, TAF achieved intracellular PBMC levels of TFV-DP that were

~7-fold higher than those after TDF (Ruane, DeJesus et al. 2013). These properties have made TAF likely the first example of a clinically-approved small molecule for HIV treatment that is designed to target drug specifically to lymphocytes.

Pharmaceutical scientists have also taken a creative approach to preferentially distribute small molecule drugs to lymph nodes in the proximal gut by focusing on routing lipophilic prodrugs to the lacteals in gut microvilli, rather than to the portal venous blood, through incorporating into the process of intestinal lipoprotein assembly and transport into the intestinal lymphatics. This effectively bypasses liver metabolism and delivers drug to mesenteric lymph nodes and the thoracic duct lymph, which then merges into the systemic venous circulation and can lead to increased oral bioavailability. This prodrug approach leverages the ability of medium- (C_{8-10}) and long-chain (C_{18}) lipids to associate with intestinal lipoproteins (primarily chylomicrons) in enterocytes, which are then selectively taken up by lacteals that drain lymph into mesenteric lymph nodes. Although fenestrated villous blood capillaries are highly permeable and in the path of chylomicrons, blood capillary chylomicron absorption is probably prevented by size exclusion. A striking example is with oral testosterone, which results in a minimal increase in blood testosterone levels due to complete first-pass metabolism (Daggett, Wheeler et al. 1978). By contrast, testosterone modified with a medium-chain acyl group (testosterone undecanoate) results in increased intestinal lymphatic absorption, thus avoiding first-pass metabolism and, as a result, enhancing systemic distribution (Coert, Geelen et al. 1975, Horst, Holtje et al. 1976).

In summary, the literature to date on small molecule distribution and retention in lymph nodes and lymphocytes demonstrates that free small molecules (without a prodrug moiety that

drives their accumulation in these tissues and cells) are insufficient at achieving and maintaining effective drug levels in lymphoid tissues and cells. Nanoparticulate formulations of single agents administered subcutaneously, or oral prodrugs (e.g., TAF or long-chain lipids), are approaches that have been taken to overcome this drug insufficiency in lymphoid tissue. Yet, only TAF has specifically focused on boosting intracellular lymphocyte drug levels for HIV treatment; nanoparticle approaches have mainly focused on overall lymph node levels without delineating specific lymph node spaces or cell types in which these nanocarriers preferentially accumulate. The long-chain lipid prodrug research has focused mainly on improving systemic bioavailability rather than boosting drug levels in mesenteric lymph nodes; however, a few studies have developed antiretroviral glyceride prodrugs to target HIV drugs to gut lymphoid tissues (Lalanne, Paci et al. 2007, Skanji, Andrieux et al. 2011).

While the literature on free and nanoparticle-bound small molecule lymph node delivery can help us form hypotheses, because our DcNP platform is an entirely novel nanoparticle, that is uniquely able to stabilize and deliver drug combinations to lymphoid tissues, there is a need to understand the mechanisms that drive the widespread lymph node and lymphocyte targeting that specifically results from DcNPs (Freeling and Ho 2014). The unique irregular nanoparticle structures of DcNPs, in which transmission electron microscopy (TEM) images revealed oblong discoidal-shaped particles approximately 15 by 60 nm without complete lipid bilayer membranes, are drastically different than the spherical membranous structures of other nanoparticle drug carriers such as liposomes. TEM images show the unique particle shape of DcNPs is shared by both our indocyanine green (ICG) nanoparticles and DcNPs with lopinavir, ritonavir, tenofovir,

and ICG. Next, we will examine the literature on macromolecule distribution and retention in lymphoid tissues.

1.4.2 *Macromolecule Distribution and Retention*

Macromolecules (soluble proteins and nanoparticulate colloidal carrier systems) have an inherent structural makeup, namely size, that precludes ready access to the blood but does not restrict lymph access. Thus, lymphatic-targeting strategies have centered on macromolecule constructs that are transported from the interstitium to the lymphatics rather than the blood. Many studies have reported preferential distribution of macromolecules to the lymphatic system from the subcutaneous space, and it is well established that certain macromolecules distribute from the blood, to the interstitium, and then to the lymph and repeat this cycle. DcNPs are unique in that to our knowledge, they are the first nanoparticles reported in the literature to boost and sustain levels of drug combinations in lymphocytes. This thesis research has discovered how this novel lymphocyte targeting comes about, and how this is related to the observed long-acting pharmacokinetics. Below, we will examine the first studies that showed lymphatic uptake and lymph node retention of subcutaneous macromolecules, how nanoparticle size and surface charge impacts lymph node distribution and retention, and how lymphatic recirculation of macromolecules in the blood can contribute to long-acting persistence of the agent in the blood. These studies, which are outlined in **Table 1.2**, provide insight on how DcNPs likely behave *in vivo*.

Following SC administration, drug can be transported to the systemic circulation either by the blood capillaries or by the lymphatics. In the early 1900s it was established that soluble

macromolecules in the SC space can enter the bloodstream indirectly via the lymphatics. Lewis injected 5 mL of horse serum subcutaneously into dogs with a thoracic lymph duct cannula and concluded the main route of absorption was via the lymphatics since horse serum was detected in the thoracic lymph 40 minutes after injection, and in the blood 3.5 hours after injection (Lewis 1921). Field and Drinker confirmed this when they injected 15-18 mL horse serum subcutaneously in dogs, ligated and cannulated all thoracic lymph ducts that anastomose with the venous blood, and sampled blood. Horse serum was detected exclusively in the thoracic lymph and not the blood, showing the lymphatics is the major absorption pathway of serum proteins from the SC space (Field and Drinker 1931). In the studies by Lewis (Lewis 1921), in the dogs without a thoracic lymph duct cannula (which allowed lymph to circulate into the blood as it would normally), the time horse serum was first detected in the blood shortened from 3.5 to 1.5 hours. Thus, having the lymph-blood circulation intact promoted earlier appearance of horse serum in the blood because the serum proteins could take the lymphatic pathway with no removal by a cannula.

Overall, these studies established that the lymphatic vasculature is important for the absorption of macromolecules from the SC space, and soluble macromolecules in the SC space largely enter the bloodstream indirectly via the lymphatics, with limited direct absorption into blood capillaries. However, it is important to note that there is significant interspecies variability in lymphatic uptake and systemic bioavailability of subcutaneously administered proteins (~3-150 kDa) reported in the literature. The species differences and major factors that contribute to this are poorly understood. Recent reviews discuss the interspecies pharmacokinetics for SC proteins in detail (Richter, Bhansali et al. 2012, Richter and Jacobsen 2014).

Once an agent enters lymphatic vessels, it may be carried by lymph flow towards the thoracic lymph ducts, and then deposit into the venous blood, or it may become trapped in lymph nodes that it encounters along the way. Drinker *et al.* showed that India Ink (~1-10 μm in diameter) injected into the afferent popliteal lymph vessel in dogs accumulated in the cortical and medullary sinuses within the popliteal node, which were ~1-500 μm wide (Drinker, Field et al. 1934). Steller *et al.* showed that much smaller monoclonal antibodies (mAbs; ~10 nm in diameter) administered subcutaneously in mice enter local lymphatic capillaries and exhibit a dose-dependence in their stepwise accumulation in the first and downstream lymph nodes if a mAb binds to a target receptor in the node. Without binding, mAbs pass through nodes and follow the lymph flow to eventually reach the bloodstream via the thoracic duct (Steller, Parker et al. 1986).

In the 1970s when liposomes were first being recognized as a useful platform for drug delivery, researchers first investigated the optimal structural characteristics of liposomes (e.g., size and charge) for lymph node delivery from the interstitial space. In rat testicles, Segal *et al.* injected 50 μL of small (~24 nm in diameter) or large (~2 μm in diameter) liposomes that contained [4-^{14}C] cholesterol and entrapped ^{125}I-labeled albumin and had a neutral, negative, or positive surface charge (Segal, Gregoriadis et al. 1975). They found that small liposomes were significantly more efficient at clearing from the injection site and trafficking to the draining inguinal lymph node, and surface charge didn't impact small liposome clearance from the injection site. Surface charge, however, did impact the clearance of the large liposomes from the injection site, with negative particles clearing most efficiently.

More recently, Rao and colleagues extended these findings in rats in a unique study that is one of the few to look at the *uptake* and *retention* of SC nanoparticles among multiple lymph nodes in the body (Rao, Forrest et al. 2010). They quantified by HPLC a marker small molecule (1-pyrenemethylamine, PMA) conjugated to PEGylated poly(D,L-lactic-co-glycolic) acid (PLGA) nanoparticles of different size (50, 100, 200 nm in diameter) and charge (neutral, less anionic, more anionic). Over 48 hours, PMA levels were measured at (1) the hind foot SC injection site, (2) in a chain of 4 lymph nodes in the lower half of the body that drained the injection site (popliteal, inguinal, iliac, and renal), and (3) in serum. For size, they found that the sum of each lymph node's area under the concentration-time curve ($AUC_{0\text{-}48h}$) for 50 nm particles was 1.3-fold higher than that of 100 nm particles, and 2.2-fold higher than that of 200 nm particles, indicating the smallest nanoparticle size displayed the highest lymph node uptake and retention in the 4-lymph node network. They also found the 50 nm particles (1) cleared the fastest from the SC injection site, (2) exhibited the highest serum $AUC_{0\text{-}48h}$ levels (1.2- and 1.9-fold higher than 100 and 200 nm particles, respectively), and (3) exhibited long-acting persistent drug levels in the plasma over 48 hours. For particle surface charge, they found that the more negative the surface charge was, the more rapidly particles cleared from the SC injection site, and the higher the lymph node uptake, distribution, and retention was, which also resulted in higher plasma levels. The rapid clearance out of the injection site of more negatively charged particles is likely due to the slight negative charge carried by the interstitium under physiological conditions (Wiig and Swartz 2012); this electrostatic repelling force propels more negatively charged particles through the interstitium. Overall, these results indicate that approximately 50 nm negatively-charged nanoparticles are optimal to rapidly clear from the SC injection site, distribute widely through lymph nodes along a network and to accumulate in these nodes, and to promote blood absorption by more efficient

transport through the lymphatics from the SC space. These findings have been confirmed with PEGylated liposomes in rats with particles approximately 70 nm in diameter (Oussoren and Storm 2001).

Another insight that can be gained from the literature on the distribution and retention of macromolecules in the lymphatics is the potential for recirculation between the lymph and the blood for certain macromolecules, which contributes to their persistence in the blood circulation. In effect, the lymphatic system acts as a depot to continually resupply the blood with infusions of an agent each time the agent cycles from the blood, to the lymphatics, and back again to the blood. This can be most clearly seen with monoclonal antibodies (mAbs).

As discussed above, mAbs in the SC space are efficiently taken up into the lymphatics and efficiently distribute through lymph vessels and nodes (Steller, Parker et al. 1986). It has been clearly shown with IgG mAbs dosed IV that the interaction between IgG and the neonatal Fc receptor (FcRn), and subsequent cellular recycling and release of IgG, contributes significantly to the persistence of IgG proteins in the plasma. For instance in mice, the plasma terminal elimination half-life for 7E3, an anti-platelet IgG_1 mAb, after 8 mg/kg IV dosing was 20 ± 2 days in wild-type mice and 0.78 ± 0.07 days in FcRn-knockout mice (Hansen and Balthasar 2002). However, recently, Dhalberg *et al.* showed in rats fitted with and without a thoracic lymph duct cannula that trastuzumab (an anti-HER-2 IgG_1 mAb) also leverages the lymphatic circulation and recycling of trastuzumab between the blood and lymph to produce its long plasma half-lives (Dahlberg, Kaminskas et al. 2014). This nontrivial role of the lymphatics in the absorption and disposition of trastuzumab in rats is clearly seen in the increased $AUC_{0\text{-}30h}$ in the non-cannulated rats (controls;

intact lymph-blood circulation) versus the lymph cannulated rats (disrupted lymph-blood circulation) following both IV and SC administration. Following SC, the $AUC_{0\text{-}30h}$ was 143 ± 112 and 44.9 ± 17.9 in control rats vs. lymph-cannulated rats, respectively. Following IV, the $AUC_{0\text{-}30h}$ was 776 ± 193 and 700 ± 133 in control rats vs. lymph-cannulated rats, respectively. Because the lymph cannula continuously removes mAb from the body, the collected mAb in the lymph was not available to redistribute into the blood, resulting in the reduced plasma exposure levels. This group used their data to build a PK model with a lymphatic component, and their simulations estimated that after IV administration 464% of the mAb dose flows through the lymphatics in the control rats. This suggests that in rats trastuzumab flows through the lymph approximately 4-5 times before it is eliminated.

A similar lymph-blood recycling concept may contribute to the persistence in the blood of smaller nanoparticles (~10-100 nm in diameter), however, the relevance of this likely diminishes as nanoparticle size increases (e.g., >10 nm in diameter) because then their larger size would increasingly prohibit the crossing of the blood endothelial barrier to reach the lymph. Here again, it is illustrative to look at studies in thoracic lymph duct cannulated rats. Ryan *et al*. dosed rats IV with either ~12 nm dendrimer nanoparticles or ~100 nm liposomes, both containing doxorubicin (Ryan, Kaminskas et al. 2013). Over 0-30 hours, 24% of the dendrimer dose was continuously collected in the lymph, while only 14% of the liposome dose appeared in the lymph. When comparing the plasma $AUC_{0\text{-}30h}$ values between the control and lymph-cannulated rats after IV dosing, the plasma $AUC_{0\text{-}30h}$ was reduced 12% for the smaller dendrimers, and only 7% for the larger liposomes, reflecting the more limited access of the larger liposomes to the lymph compared to the smaller dendrimers. The decreased plasma $AUC_{0\text{-}30h}$ values with both nanoparticle systems

indicates that lymphatic recycling of the IV dose does contribute to some extent to the persistence of these nanoparticles in the blood.

In summary, certain macromolecules in the subcutaneous space clearly exhibit the ability to be taken up and retained by the lymphatic system. They must not be too large or too small (~10-80 nm in diameter), and they must not stick or aggregate in the subcutaneous space (a slight negative surface charge is preferred). Certain macromolecules such as mAbs and some nanoparticles can efficiently distribute through the lymphatic network and into the blood and repeat this cycle before being eliminated; this cycling creates persistent levels in the blood. While the site(s) of extravasation from the blood to the interstitium are not well defined, it is likely this transfer occurs across more permeable fenestrated or sinusoidal endothelium. A main purpose of this thesis is to understand in which ways DcNPs achieve their novel *in vivo* pharmacokinetics of persistent levels of small molecule drug combinations in a) lymphocytes in lymph nodes, b) lymphocytes in the blood, and c) the plasma. The above literature suggests potential mechanisms that could contribute to this *in vivo* behavior of DcNPs.

1.5 Long-Acting Drug Regimens and the TLC-ART Platform

Single-agent long-acting drug regimens have existed for decades. However, never before have drug combinations been made to be long-acting and targeted in one embodiment as with DcNPs. Prior to the work in this thesis, it was not clear how the specific lymphocyte-targeting and long-acting behavior of the drug combinations in DcNPs occurred. This section will briefly review some long-acting drug regimens used clinically, the mechanisms by which they enable long-acting pharmacokinetics, and how DcNPs are a new evolution of long-acting regimens with novel

mechanisms for their long-acting behavior. One of the significant contributions of this thesis is uncovering these novel long-acting mechanisms that are employed by DcNPs.

Long-acting is defined here as a drug formulation that permits dosing on a weekly, monthly, yearly, or more infrequent basis. To achieve this, most long-acting regimens involve a suspension for injection or an implant; very few are dosed orally. Long-acting injectable and implantable formulations have been marketed for decades for indications such as contraception and schizophrenia (Makarainen, van Beek et al. 1998, Westhoff 2003, De Berardis, Marini et al. 2013). The thrust for this development was mainly to improve medication adherence and patient convenience. The pharmacokinetic mechanisms behind the persistent plasma drug levels that are achieved with these long-acting formulations involve slow release of drug from the injection site depot such that the rate of absorption into the blood circulation is slow. This creates pharmacokinetics where the absorption rate constant (k_a) is much slower than the elimination rate constant (k_e) (Wagner and Nelson 1964). The downward terminal part of the plasma concentration-time curve is a reflection of the much slower k_a (producing sustained, slowly-declining drug levels), while the initial upward part of the curve reflects k_e. This is much like a slow, constant-rate infusion of drug into the blood where steady-state levels are achieved and consistently maintained.

Recently, interest in long-acting regimens for HIV prevention and treatment has gained momentum because many patients have difficulty sticking to their lifelong daily pill regimens. This non-adherence contributes to the rise of drug-resistant forms of HIV and treatment failure. In the United States, of all the HIV-infected individuals—those taking and not taking oral

combination antiretroviral therapy (cART)—only 30% have viral suppression (Bradley, Hall et al. 2014). It is believed that long-acting anti-HIV regimens could help improve patient adherence, and thus increase the percentage of patients with suppressed viral replication.

The two most advanced long-acting anti-HIV formulations in clinical development are rilpivirine LA and cabotegravir LA (Margolis, Gonzalez-Garcia et al. 2017). Rilpivirine (RPV) is a non-nucleoside reverse transcriptase inhibitor (NNRTI) with a very low water solubility (<100 μg/mL) and an *in vitro* half maximal inhibitory concentration (IC_{50}) of 0.22 and 0.34 nM against HIV-1 BAL and NL432, respectively (Spreen, Margolis et al. 2013). Cabotegravir (CAB), an analog of FDA-approved dolutegravir, is an HIV integrase strand transfer inhibitor (INSTI) also with a very low water solubility (<10 μg/mL) and an *in vitro* IC_{50} for wild-type virus of 0.51 nM (Garvey and Winston 2009). Due to the nanomolar potencies of these drugs, effective drug levels are achieved in HIV patients with < ~50 mg/day orally. This high potency (and low mass dose) is a key attribute for a drug molecule to be a candidate for formulating it into a long-acting injectable with a practical injection volume, especially for lipophilic compounds. The only other two anti-HIV small molecules that meet this criterium are tenofovir alafenamide (TAF, 25 mg once a day) and dolutegravir (DTG; 50 mg once a day).

Rilpivirine LA and cabotegravir LA are each formulated as single drugs in their own separate nanosuspension using similar excipients. The nanoparticles for both are made through a process of wet bead milling (nanomilling) and have a particle diameter of about 200 nm (Trezza, Ford et al. 2015, Williams, Crauwels et al. 2015). For HIV treatment, rilpivirine LA and cabotegravir LA are currently administered at two separate intramuscular (IM) injection sites (two

2-3 mL injections) (Margolis, Gonzalez-Garcia et al. 2017). While the apparent terminal plasma half-lives of these long-acting formulations are on the order of ~25-54 days (Spreen, Ford et al. 2014), allowing monthly to bi-monthly dosing intervals (Margolis, Gonzalez-Garcia et al. 2017), it takes several days to reach maximum plasma concentrations (T_{max}) (median T_{max}: 9-69 days for cabotegravir (Spreen, Ford et al. 2014), 6-11 days for rilpivirine (McGowan, Dezzutti et al. 2016). Thus, an oral lead-in or loading dose is required to provide effective plasma levels soon after injection to prevent the development of viral resistance from sub-therapeutic concentrations. Based on magnetic resonance imaging (MRI) and matrix-assisted laser desorption ionization (MALDI) imaging mass spectrometry (IMS) of intramuscular (IM) and subcutaneous (SC) depots of cabotegravir LA in rats, a majority of the injected dose remained at the injection site still at 7 days after injection (Jucker, Alsaid et al. 2017). Thus, with the injected drug not readily clearing from the injection site, the long-acting behavior of rilpivirine and cabotegravir is likely due to free drug being slowly released from the injection site depot and slowly absorbing directly into blood capillaries. This creates pharmacokinetics where the slow absorption rate constant (k_a) dictates the slow terminal decline of drug levels in the plasma, much like that of earlier long-acting contraceptives and antipsychotics.

Because a cornerstone of HIV therapy is drug combinations in a single regimen to inhibit HIV replication by multiple mechanisms of action and supply a high barrier to developing drug resistance, it would be advantageous and user friendly if a long-acting HIV treatment combined drug combinations into a single injectable formulation. It would also be advantageous if such a formulation specifically delivered the drug mixture together as one unit to tissues that harbor residual HIV during oral cART, such as lymphoid tissues (Fletcher, Staskus et al. 2014, Lorenzo-

Redondo, Fryer et al. 2016). Our laboratory has successfully developed such a formulation called Targeted Long-Acting Antiretroviral Therapy (TLC-ART) that consists of drug combination nanoparticles (DcNPs), which can stably combine small molecule drug mixtures with diverse physicochemical properties (hydrophobic and hydrophilic) into a single nanosuspension for injection (Freeling, Koehn et al. 2014, Freeling, Koehn et al. 2015). This formulation is unique because it can be used to formulate long-acting cART injectables using multiple different FDA-approved antiretroviral agents (Duan, Freeling et al. 2014, McConnachie, Kinman et al. 2018). Thus, it is not necessarily restricted to only highly potent agents such as CAB, RPV, TAF, and DTG, as the cabotegravir LA and rilpivirine LA intramuscular formulations are. This is highly significant because it means this formulation is applicable to not only HIV prevention and treatment regimens, but to a wide range of drug classes that treat a wide range of diseases with drug combinations, such as cancer and infection. Moreover, the TLC-ART formulation is not only long-acting—providing persistent plasma and PBMC levels in NHPs after a single injection (Freeling, Koehn et al. 2014)—but it also has the ability to target drug to HIV host cells (lymphocytes) within lymph nodes throughout the body (Freeling and Ho 2014). This is unlike other long-acting nanoformulations in development.

As shown in **Figure 1.4**, the intracellular drug levels in blood lymphocytes (PBMCs) compared to plasma levels are consistently lower in the cells than the plasma after a single IM injection of a long-acting dolutegravir formulation in monkeys (McMillan, Szlachetka et al. 2018). In contrast, TLC-ART in monkeys consistently produced the opposite: persistent higher blood lymphocyte drug concentrations than plasma for all three drugs. **Table 1.3** looks as this from a different perspective by comparing PBMC-to-plasma ratios between conventional oral cART and

TLC-ART. In it, the ratios of the three drugs are all greater than 1 with TLC-ART and less than 1 with oral cART. This again illustrates the ability of TLC-ART to target drug combinations to lymphocytes. *How could these high and sustained levels of drug combinations in lymphocytes be happening?*

A proposed sequence of hypothesized mechanisms is presented in **Figure 1.5**. First, DcNPs are likely sufficiently stable *in vivo* and resist forming aggregations, and thus behave as small macromolecules of about 50 nm in diameter. This allows DcNPs to readily clear from the subcutaneous space and not stick at the injection site. Because DcNPs are too large to be taken up rapidly by blood capillaries, and because the lymphatics are optimized to readily absorb macromolecules such as DcNPs, DcNPs preferentially distribute from the subcutaneous space to lymph capillaries (not blood capillaries). Once in lymph vessels, because DcNPs do not readily breakdown and release their drug cargo, they are retained by lymph vessels and distribute through lymph vessel and node pathways. When DcNPs reach lymph nodes, they have optimal size and surface properties to become trapped in lymph nodes. This lymph node trapping is key to the resulting lymphocyte-targeting and long-acting pharmacokinetics because it enables an opportunity for loading of drug into lymphocytes in nodes. From there, drug can then be slowly released into the plasma by multiple pathways: (1) DcNPs/free drug can be released from lymph nodes directly into the blood, (2) DcNPs/free drug in lymph nodes can be released into lymph, which then flows into blood, and/or (3) lymphocytes loaded with DcNPs/free drug traffic from lymph nodes to the blood then slowly release drug into plasma. Overall, the lymph node trapping of DcNPs leads to lymphocyte-targeting, and the drug retention in lymph nodes and lymphocytes lead to the persistent levels of drug combinations in lymph nodes, lymphocytes, and the plasma.

1.6 Hypotheses and Aims

Therefore, the overall hypothesis of this thesis research is: the formation of body-wide drug depots in lymph nodes and lymphocytes by anti-HIV drug combination nanoparticles (DcNPs) injected subcutaneously results in lymphocyte-targeting and long-acting pharmacokinetics (PK) of small molecule drug combinations. It is the distinct lymph node drug distribution and exposure profile—enabled by the unique DcNP formulation—that makes possible the lymphocyte-targeting and long-acting pharmacokinetics of small molecule drug combinations.

To test the first sub-hypothesis that the unique DcNP formulation enables lymphocyte-targeting and long-acting pharmacokinetics of anti-HIV small molecule drug combinations, the pharmacokinetics of DcNP-associated drugs are evaluated in the lymph node lymphocytes, blood lymphocytes, and plasma in non-human primates (NHPs) following a single subcutaneous dose.

To then test the second sub-hypothesis that DcNPs in the SC space undergo lymphatic first-pass distribution and lymph vessel and node retention, a tool to visualize the *in vivo* distribution pathways of DcNPs is engineered and evaluated in mice. To further elucidate the driving forces that enable the long-acting pharmacokinetics and lymphocyte-targeting of DcNPs, mechanism-based pharmacokinetic models are developed and evaluated.

The following chapters in this thesis begin with a description of the pharmacokinetics of three antiretrovirals (lopinavir [LPV], ritonavir [RTV], and tenofovir [TFV]) combined in DcNPs in plasma, peripheral blood mononuclear cells (PBMCs), and lymph node mononuclear cells

(LNMCs) following a single dose in non-human primates (NHPs) (**Chapter 2**). This was the first proof-of-principle showing that DcNPs enable both lymphocyte-targeting and long-acting pharmacokinetics in LNMCs, PBMCs, and plasma in NHPs. The next chapter describes the development of a clinically-relevant fluorescent marker for DcNPs to track the *in vivo* distribution of DcNPs in real-time (**Chapter 3**). The following chapter describes the use of these fluorescently-tagged DcNPs to elucidate the *in vivo* distribution pathways of DcNPs throughout the body from the SC space in mice (**Chapter 4**). Finally, we describe the development and validation of a mathematical mechanism-based pharmacokinetic (MBPK) model of DcNP absorption and disposition in NHPs, which elucidated the underlying mechanisms that drive the lymphocyte-targeting and long-acting pharmacokinetics of DcNPs (**Chapter 5**). A complete list of peer-reviewed manuscripts and academic meeting abstracts authored by John C. Kraft, which include reviews and research collaborations related to this thesis research, can be found in **Appendix A.**

Understanding the lymphocyte-targeting and long-acting mechanisms is key to optimizing the efficacy and safety profiles for the TLC-ART formulation, which is planned to advance into first-in-human testing as an HIV treatment. It has significant implications for further development of the DcNP formulation for other lymphatic diseases that are treated with drug combinations.

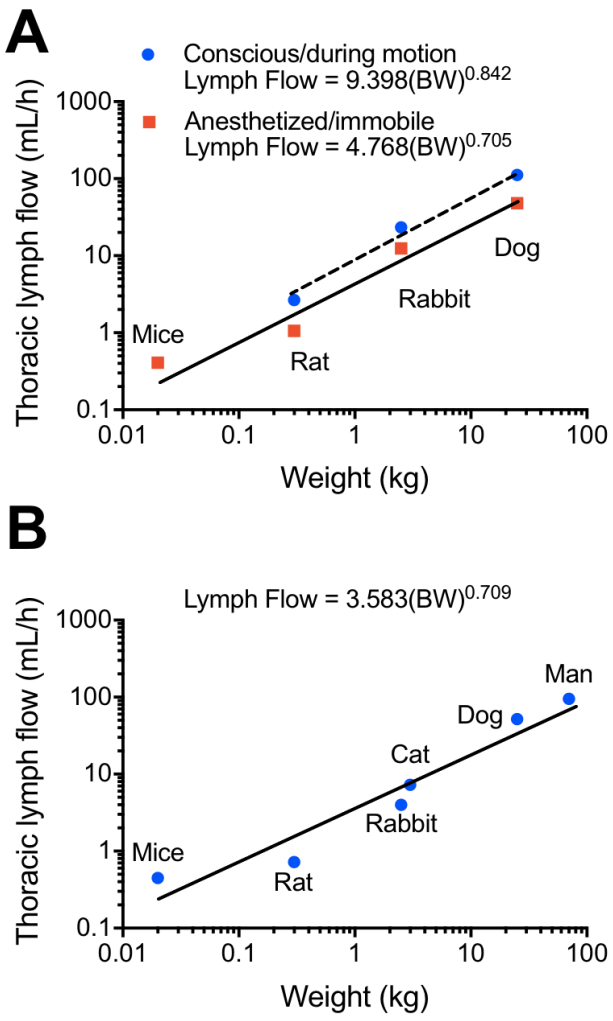

Figure 1.1. Allometric relationship between lymph flow in the thoracic duct (mL/hr) and the body weight of different animal species.

(A) The difference in the thoracic lymph flow as a function of the mobility state of the animal. Data for mice, rats, rabbits, and dogs were extracted from (Lindena, Kupper et al. 1986). (B) Average data for multiple species are summarized from (Lindena, Kupper et al. 1986).

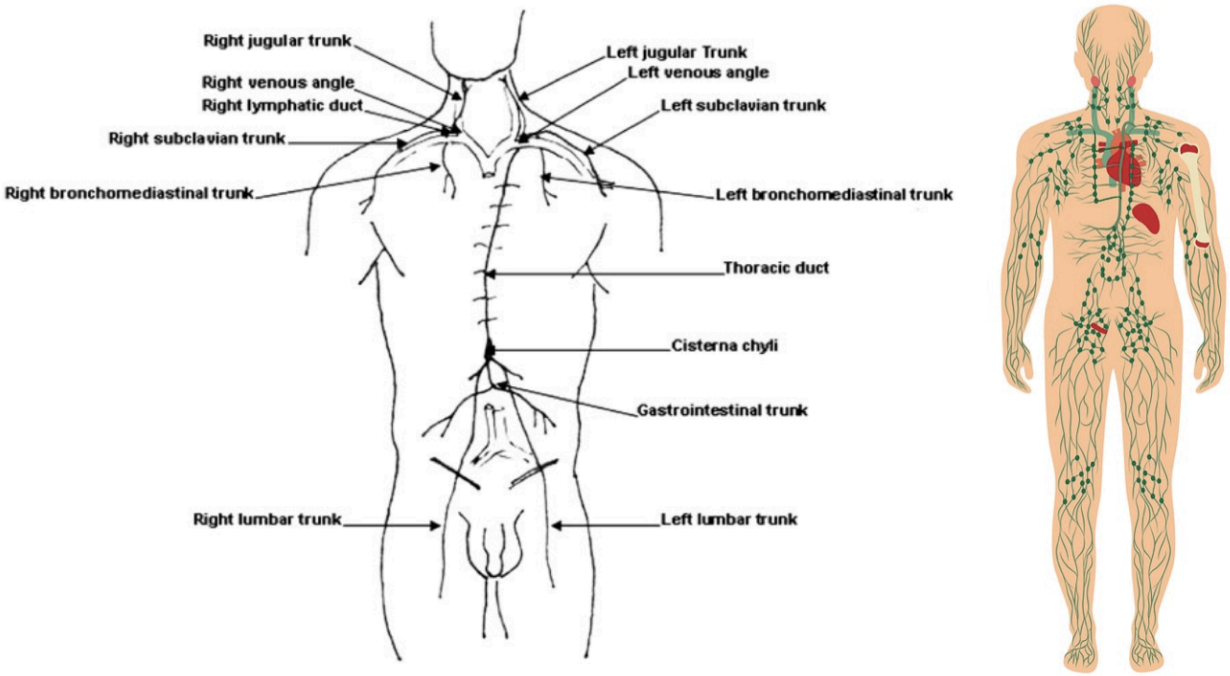

Figure 1.2. Schematic of the human lymphatic system network in the body.

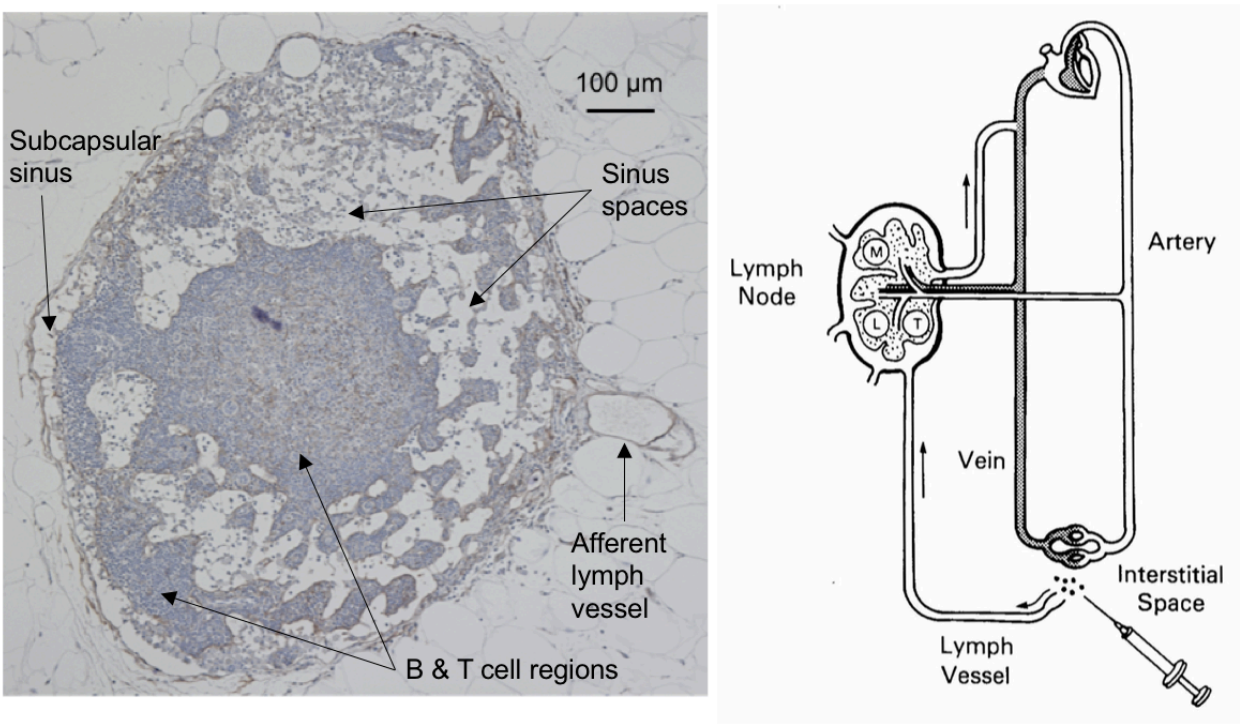

Figure 1.3. Basic lymph node architecture and blood flow relative to lymph flow.

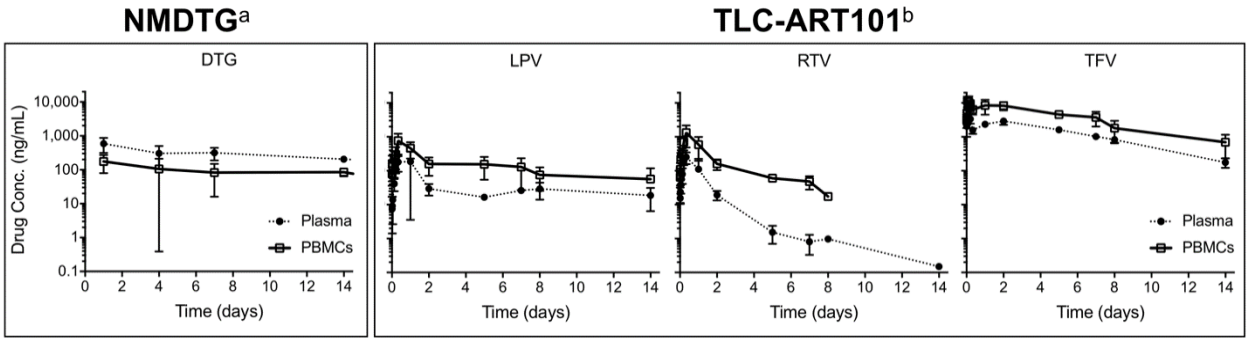

[a] NMDTG, nanoformulated myristoylated dolutegravir prodrug. Dolutegravir plasma and intracellular PBMC concentration values were derived from McMillan J *et al.* (McMillan, Szlachetka et al. 2018), in which macaques (N=3) received a single intramuscular dose of 38.5 mg/kg MDTG (25.5 mg of DTG equivalents/kg). To convert units of ng/10^8 cells to units of ng/mL, the PBMC cell volume was assumed to be 0.2829 pL/cell (Simiele, D'Avolio et al. 2011).

[b] TLC-ART101, targeted long-acting combination antiretroviral therapy formulation 101. Lopinavir, ritonavir, and tenofovir plasma and intracellular PBMC concentrations were derived from Kraft JC *et al.* (Kraft, McConnachie et al. 2017), in which macaques (N=4) received a single subcutaneous dose of 25.0 mg/kg LPV, 7.0 mg/kg RTV, and 10.6 mg/kg TFV.

Abbreviations: DTG, dolutegravir; LPV, lopinavir; RTV, ritonavir; TFV, tenofovir; PBMCs, peripheral blood mononuclear cells.

Figure 1.4. Comparison of long-acting anti-HIV nanoformulations (NMDTG vs. TLC-ART101).

TLC-ART101 has a greater ability to boost drug levels in HIV host cells in the blood (PBMCs) relative to the plasma following a single injection in primates compared to that of NMDTG.

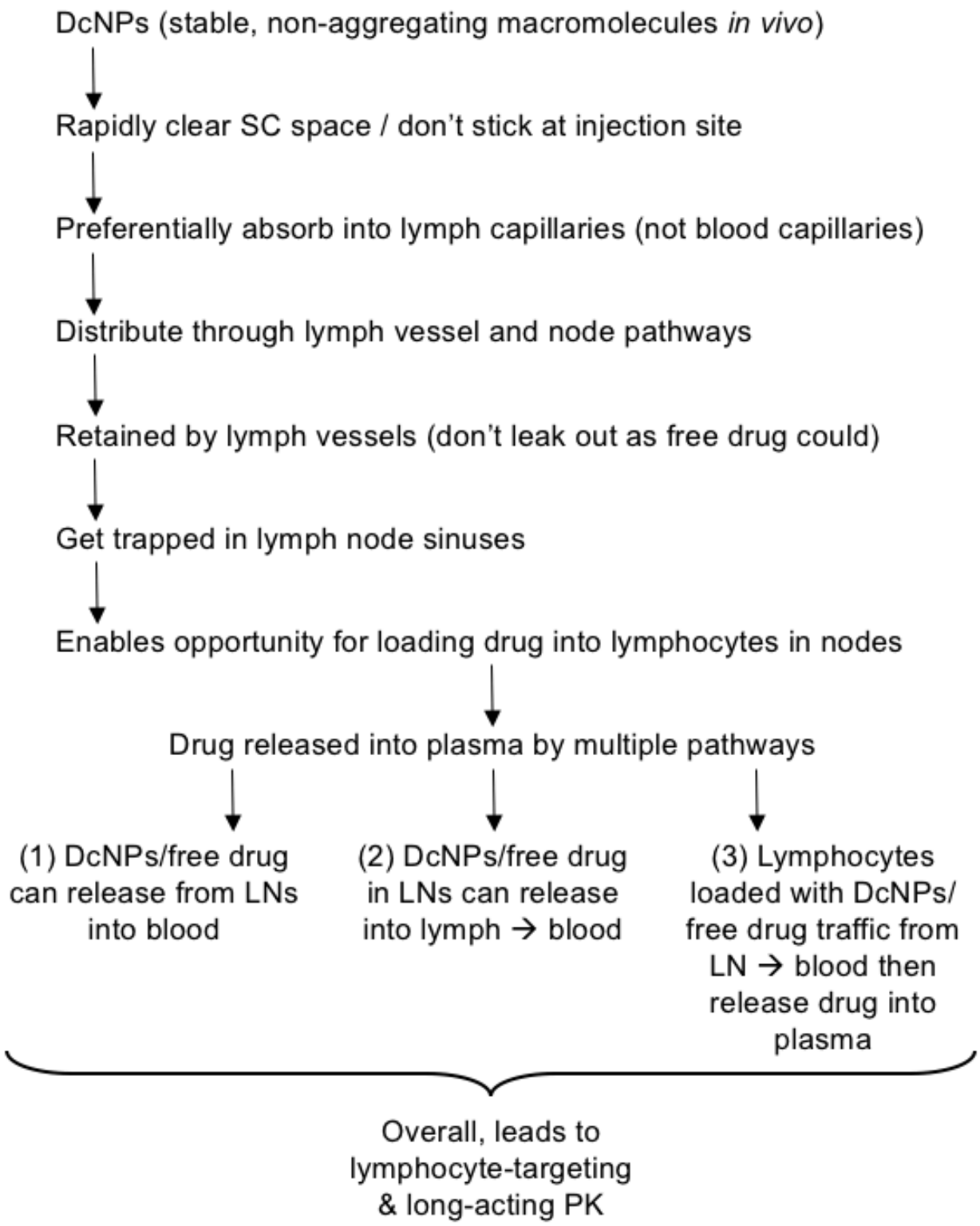

Figure 1.5. Sequence of potential mechanisms for the lymphocyte-targeting and long-acting pharmacokineitcs resulting from subcutaneous administration of DcNPs.

Table 1.1. Distribution and retention of small molecules in lymph nodes and lymphocytes.

Drug	MW (Da)	Dosage Form	Admin Route(s)	Species	Findings (Reference[s])
Melphalan	305.2	Free drug; Liposomal (~24 nm)	SC	Rats	• Free drug cleared readily from LNs, liposomal drug persisted in LNs • From SC space, free drug entered blood, liposomal drug entered lymph (Khato, Priester et al. 1982)
Doxorubicin	544.5	Liposomal (~4 μm)	IV Gastric submucosal	Humans	• Draining LN levels 30-50-fold higher after submucosal than IV over 4h • All LNs had equivalent low drug levels following IV (Akamo, Mizuno et al. 1994)
Carboplatin	371.3	Carbon particles	IV SC	Humans	• Draining axillary LN levels 200-fold higher after SC than IV over 36h • Drug levels persisted in LNs @48h only in the SC group (Chen, Wang et al. 2004)
Indinavir	613.8	Free LNPs (~100 nm)	SC	Monkeys	• LNs throughout body had 3-16-fold higher levels with LNPs vs. free @24h • Plasma levels persisted w/ LNPs @48h, free drug was cleared @15h (Kinman, Bui et al. 2006)
Doxorubicin	544.5	Free	IV SC	Rats	• Total doxorubicin collected in thoracic lymph was only 0.063-0.082% of the injected dose @30h after SC or IV • ~0% of dose reached thoracic lymph (Ryan, Kaminskas et al. 2013)
Atazanavir Darunavir Efavirenz FTC-TP TFV-DP	704.9 547.7 315.7 487.2 447.2	Free	PO	Humans	• Drug conc. in LN lymphocytes (LNMCs) were significantly lower than in blood lymphocytes (PBMCs) for all 5 drugs; this was inversely linked to viral levels in LNs (Fletcher, Staskus et al. 2014)
Tenofovir alafenamide	476.5	Free	PO	Dogs Humans	• TFV-DP levels 5-15-fold higher in LNs @24h w/ TAF vs. TDF (dogs) • TFV-DP levels 7-fold higher in PBMCs @steady-state w/ TAF vs. TDF (humans) (Lee, He et al. 2005, Ruane, DeJesus et al. 2013)
Testosterone undecanoate	456.7	Free medium-chain fatty acid	PO	Humans	• Exogenous testosterone detected in blood only w/ testosterone undecanoate • Fatty acid conjuate routes testosterone via lymph lacteals to increase bioavailabilty (Coert, Geelen et al. 1975, Daggett, Wheeler et al. 1978)

Abbreviations: FTC-TP, emtricitabine triphosphate; IV, intravenous; LNPs, lipid-nanoparticles; LN, lymph node; LNMCs, lymph node mononuclear cells; PBMCs, peripheral blood mononuclear cells; SC, subcutaneous; TAF, tenofovir alafenamide; TDF, tenofovir disoproxil fumarate; TFV-DP, tenofovir diphosphate

Table 1.2. Distribution and retention of macromolecules in lymph nodes and lymph.

Macromolecule	Size	Admin Route(s)	Species	Findings (Reference)
Horse serum	~1-100 nm	SC	Dogs	• Horse serum detected in thoracic lymph duct in dogs much sooner than in blood • Thus, horse serum travels more readily to lymph from SC space than to blood (Lewis 1921)
India Ink	~1-10 µm	Intra-afferent lymph node vessel	Dogs	• India Ink collected in ~1-500 µm wide sinus spaces in the dog lymph node (Drinker, Field et al. 1934)
mAb	10 nm	SC	Mice	• From SC space, mAbs enter local lymph vessels • SC mAbs accumulate stepwise in a dose-dependent manner in the 1st, 2nd, etc. draining LNs (Steller, Parker et al. 1986)
Trastuzumab (mAb)	10 nm	IV SC	Rats	• Plasma $AUC_{0\text{-}30h}$ was higher in control (non-lymph cannulated) vs. cannulated rats after IV/SC • Thus, lymph cannula removes mAb that comes from blood, and decreases mAb blood exposure (Dahlberg, Kaminskas et al. 2014)
Liposomes	24 nm 2 µm	Intra-testicular	Rats	• 24 nm liposomes cleared injection site more readily and trafficked to draining LN than 2 µm • Negatively charged large 2 µm liposomes cleared the injection site faster than positive or neutral (Segal, Gregoriadis et al. 1975)
PEGylated PLGA NPs	50 nm 100 nm 200 nm	SC	Rats	• 50 nm negatively-charged particles cleared fastest from SC site and had highest plasma $AUC_{0\text{-}48h}$ and high LN $AUC_{0\text{-}48h}$ in 4 draining LNs (Rao, Forrest et al. 2010)
PEGylated Liposomes	70 nm 200 nm	SC	Rats	• 70 nm negatively-charged particles cleared fastest from the SC injection site and had the highest distributed to and retention in draining LNs (Oussoren and Storm 2001)
PEGylated Dendrimers Liposomes	12 nm 100 nm	IV	Rats	• 24% of dendrimer dose collected in lymph 0-30h • 14% of liposome dose collected in lymph 0-30h • Thus, larger particles in the blood can access lymph circulation less than smaller particles can (Ryan, Kaminskas et al. 2013)

Abbreviations: AUC, area under the concentration-time curve; LN, lymph node; mAb, monoclonal antibody; PLGA NPs, poly(D,L-lactic-co-glycolic) acid; SC, subcutaneous

Table 1.3. The PBMC-to-plasma drug ratios after oral dosing compared to after subcutaneous TLC-ART101.

Species	**Humans**			**Monkeys**		
Reference	(van Kampen, Reedijk et al. 2010)	(van Kampen, Reedijk et al. 2010)	(Louissaint, Cao et al. 2013)	(Kraft, McConnachie et al. 2017)		
Route	PO	PO	PO	SC		
Formulation	*Kaletra*®	*Kaletra*®	*Viread*®	TLC-ART101		
Drug	LPV	RTV	TFV	LPV	RTV	TFV
Dose (mg/kg)	22.9[a]	5.7[a]	2.4[b]	25.0	7.0	10.6
Time	16 hr	16 hr	24 hr	$AUC_{(0\text{-}336hr)}$[c]	$AUC_{(0\text{-}336hr)}$[c]	$AUC_{(0\text{-}336hr)}$[c]
PBMC Drug Level	2.7 μg/mL	0.23 μg/mL	26 ng/mL[d]	44 hr•μg/mL	35 hr•μg/mL	1.3 hr•mg/mL
Plasma Drug Level	10 μg/mL	0.45 μg/mL	40 ng/mL	11 hr•μg/mL	4.8 hr•μg/mL	0.42 hr•mg/mL
Ratio of PBMC/Plasma Drug Levels	**0.27**	**0.52**	**0.65**	**4.02**	**7.40**	**3.01**

[a] The median age of patients in the van Kampen *et al.* 2010 study was 10 years old. Since dose and median weight were not reported in this study, we used the recommended dose of 800 mg LPV/200 mg RTV administered once daily as *Kaletra*® for children weighing 35 kg (which is the median weight of children 10 years old) to calculate the mg/kg dose for LPV and RTV given in this study.

[b] The oral dose for TFV in humans was calculated for 300 mg tenofovir disoproxil fumarate (TDF; 519.44 g/mol) and assuming 70 kg human weight as follows: (300 mg TDF/70 kg) x (287.21 g/mol TFV/519.44 g/mol TDF) = 2.4 mg/kg.

[c] Because complete drug concentration-time course profiles over two weeks (0-336 hr) were characterized for LPV, RTV, and TFV in monkeys after TLC-ART101 dosing, $AUC_{(0\text{-}336h)}$ values were used to calculate the PBMC/Plasma Ratio for each drug.

[d] Since only tenofovir diphosphate (TFV-DP) drug levels in PBMCs were reported in (Louissaint, Cao et al. 2013), the steady-state fraction of 61% of total intracellular TFV being TFV-DP was used to estimate the total intracellular TFV level reported in the table (26 ng/mL) (Durand-Gasselin, Van Rompay et al. 2009, Ruane, DeJesus et al. 2013, Massud, Mitchell et al. 2016, PMDA (Pharmaceutical and Medical Device Agency of Japan) http://www.pmda.go.jp/drugs/2014/P201400148/800155000_22600AMX01325_H100_1.pdf Accessed Jan 31, 2018). For these calculations, the PBMC cell volume was assumed to be 0.2829 pL/cell (Simiele, D'Avolio et al. 2011).

$AUC_{(0\text{-}336hr)}$, area under the concentration-time curve between time 0 to 336 hours; PBMC, peripheral blood mononuclear cell; PO, oral; SC, subcutaneous; LPV, lopinavir; RTV, ritonavir; TFV, tenofovir.

Chapter 2. **Drug Combination Nanoparticles (DcNPs) Target Lymphocytes in Lymph Nodes and Blood and Exhibit Long-Acting Pharmacokinetics**

Chapter 2 was published

in

AIDS. 2017;31(6):765-770.

2.1 ABSTRACT

Objective: To determine if a combination of anti-HIV drugs—tenofovir (TFV), lopinavir (LPV), and ritonavir (RTV)—in a lipid-stabilized nanosuspension (called TLC-ART101) could enhance and sustain intracellular drug levels and exposures in lymph node and blood cells above those in plasma.

Design: Four macaques were given a single dose of TLC-ART101 subcutaneously. Drug concentrations in plasma and mononuclear cells of the blood (PBMCs) and lymph nodes (LNMCs) were analyzed using a validated combination LC-MS/MS assay.

Results: For the two active drugs (TFV, LPV), plasma and PBMC intracellular drug levels persisted for over two weeks; PBMC drug exposures were 3-4-fold higher than those in plasma. Apparent terminal half-lives ($t_{1/2}$) of TFV and LPV were 65.3 hr and 476.9 hr in plasma, and 169.1 hr and 151.2 hr in PBMCs. At 24 and 192 hr, TFV and LPV drug levels in LNMCs were up to 79-fold higher than those in PBMCs. Analysis of PBMC intracellular TFV and its active metabolite TFV-diphosphate (TFV-DP) indicated that intracellular exposures of total TFV and TFV-DP were markedly higher and persisted longer than in humans and macaques dosed with oral TFV prodrugs—tenofovir disoproxil fumarate (TDF) or tenofovir alafenamide (TAF).

Conclusions: A simple, scalable three-drug combination lipid-stabilized nanosuspension exhibited persistent drug levels in cells of lymph nodes and the blood (HIV host cells) and in plasma. With appropriate dose adjustment, TLC-ART101 may be a useful HIV treatment with potential to impact residual virus in lymph nodes.

2.2 INTRODUCTION

In the U.S., of all HIV-infected individuals—those taking and not taking oral combination antiretroviral therapy (cART)—only 30% have viral suppression (Bradley, Hall et al. 2014). We first proposed (Kinman, Brodie et al. 2003) and others confirmed in prospective studies (Fletcher, Staskus et al. 2014, Lorenzo-Redondo, Fryer et al. 2016) that orally administered drugs exhibit drug insufficiency in lymph nodes (LNs) (Fletcher, Staskus et al. 2014, Freeling and Ho 2014, Lorenzo-Redondo, Fryer et al. 2016). We recently reported a stable, scalable triple-drug anti-HIV formulation sustained drug levels in non-human primate (NHP) plasma and PBMCs for over one week, and enhanced drug levels in LNMCs (Freeling, Koehn et al. 2014). This strategy holds promise as a long-acting injectable that could improve patient adherence—by retaining patients who have challenges with oral therapy in care—and enhance viral suppression in blood and lymphoid tissues.

While several long-acting injectables, including cabotegravir and rilpivirine, are in development, these are currently formulated as separate agents (Owen and Rannard 2016). Having drug combinations in a fixed dosage formulation could improve patient acceptability and potentially better address concerns about viral resistance. However, incorporating multiple drugs into a single long-acting injectable formulation poses considerable challenges with respect to pharmaceutics (formulation, scalability), pharmacokinetics (absorption, disposition, safety), and pharmacodynamics (efficacy against disease).

Previously, we described a lymphatic-targeted HIV drug combination (TFV, LPV, RTV) (Freeling, Koehn et al. 2014, Freeling, Koehn et al. 2015). In this report, we further validate and

characterize the long-acting intracellular and plasma exposure over two weeks using a similar but optimized injectable combination formulation called TLC-ART101.

2.1 Materials and Methods

2.1.1 *Reagents*

DSPC, DSPE-mPEG2000 phospholipids (GMP grade) (Corden Pharma, Liestal, Switzerland). TFV (PMPA), LPV, RTV (Waterstone, Carmel, IN).

2.1.2 *TLC-ART101 TFV-LPV-RTV Combination*

TLC-ART101 composed of DSPC, DSPE-mPEG2000, TFV, LPV, and RTV was prepared as described (Kinman, Brodie et al. 2003, Freeling, Koehn et al. 2015). TLC-ART101 contained 17.1 mM TFV, 18.3 mM LPV, and 4.5 mM RTV; fraction in particle-associated form was 11.2, 92.2, and 91.1%, respectively. Mean particle diameter was 69.0 ± 8.3 nm.

2.1.3 *Pharmacokinetic Study*

Four male macaques (*Macaca nemestrina*, 10.5, 9.8, 6.5, 8.3 kg) were enrolled under an approved Institutional Animal Care and Use Committee protocol. No adverse events occurred. Macaques were dosed 10.6, 25.0, 7.0 mg/kg TFV, LPV, RTV, subcutaneously (SC) once in the back mid-scapular region. Blood was collected at 0, 0.25, 0.5, 1, 3, 5, 8, 24, 48, 120, 168, 192, 336 hr; an inguinal LN was excised at 24, 192 hr. Plasma, PBMCs, and LNMCs were isolated as described (Freeling, Koehn et al. 2015); LPV, RTV, TFV concentrations were analyzed with a

validated LC-MS/MS assay (Koehn and Ho 2014, Koehn, Ding et al. 2015). A non-compartmental model was used to estimate pharmacokinetic (PK) parameters with Phoenix® v6.4 (Certara, Mountain View, CA). Intracellular TFV and its active metabolite TFV-diphosphate (TFV-DP) were analyzed in the context of reported values after TFV, TDF, and TAF dosing.

2.1.4 *Statistical Analysis*

All statistical tests were two-tailed t-tests with $\alpha = 0.05$.

2.2 RESULTS

To determine the time-course of TFV, LPV, and RTV, macaques were dosed with SC TLC-ART101. **Figure 2.1** shows the concentrations of TFV, LPV, and RTV in plasma and PBMCs. The two active drugs (TFV, LPV) in TLC-ART101 exhibited sustained plasma and intracellular (PBMC) levels for 336 hr (two weeks), with higher intracellular TFV and LPV levels than in plasma (**Figure 2.1**). PBMC intracellular exposures to TFV and LPV over two weeks ($AUC_{0\text{-}336h}$) were 3.01- to 4.02-fold higher than in plasma ($p<0.0001$, $p=0.0522$, respectively) (**Figure 2.1**, table insert). Peak drug concentrations (C_{max}) of TFV and LPV were also higher in PBMCs than in plasma ($p=0.0076$, $p=0.0539$, respectively). In plasma and PBMCs, TFV concentrations peaked initially at ~2 hr post-dose prior to rebounding to a secondary peak level at ~24-48 hr. LPV and RTV levels in plasma and PBMCs peaked between 8-14 hr (**Figure 2.1**). Plasma apparent terminal half-lives ($t_{1/2}$) were ~2.7 days for TFV and ~20 days for LPV; PBMC $t_{1/2}$ were ~7 days for TFV and ~6.3 days for LPV (**Figure 2.1**). Unlike TFV and LPV, RTV levels fell below the detection limit in plasma by two weeks and PBMCs after eight days (**Figure 2.1**).

As TLC-ART101 is designed to accumulate drug combinations in LNs, we evaluated LNMC intracellular drug levels. Intracellular TFV and LPV levels in LNMCs persisted at days one and eight; TFV and LPV levels in LNMCs were 0.9- to 79.2-fold higher than in PBMCs, and 3.1- to 197.8-fold higher than in plasma (**Table 2.1**). Even the booster RTV exhibited enhanced intracellular drug levels in LNMCs versus those in PBMCs.

Data in **Table 2.2** indicate that compared to SC TFV, oral TDF, and oral TAF, a single SC TLC-ART101 dose provided higher PBMC intracellular exposures to TFV and estimated TFV-DP (even after dose-normalization).

2.3 DISCUSSION

Here, we describe a further optimized formulation with a fixed dose LPV/RTV molar ratio of 4:1. This optimized TLC-ART101 preparation provided sustained levels of two active drugs (TFV, LPV) in plasma and PBMCs for over two weeks (**Figure 2.1**). Additionally, intracellular TFV and LPV concentrations in LNMCs were higher than in PBMCs (**Table 2.1**). Thus, this treatment strategy could potentially overcome drug insufficiency in LNs with oral regimens (Fletcher, Staskus et al. 2014, Freeling and Ho 2014, Lorenzo-Redondo, Fryer et al. 2016). PBMC intracellular concentrations of TFV and LPV were also consistently higher than plasma levels in all NHPs throughout the two-week study. Collectively, SC TLC-ART101 enhanced intracellular LPV and TFV levels in LNMCs for at least eight days, and extended PBMC and plasma drug

levels for over two weeks. Thus, TLC-ART101 could be considered for development as a long-acting fixed-dose injectable combination for HIV treatment for adults and children.

The exact mechanism of TLC-ART101 enhancing LNMC drug levels and sustaining levels in plasma and PBMCs is not clear. It is likely, however, that from the subcutaneous space, TFV, LPV, and RTV associated in TLC-ART101 nanoparticles are too large to penetrate blood capillary endothelial cells. Instead, they are preferentially taken up together by more permeable lymphatic capillaries as a single drug combination unit. Subsequently, each drug particle could be retained in lymph vessels, and due to the stability of the drug-nano complex, they are likely to be transported throughout the lymphatic system as stable units. Without significant degradation, the size of the drug combination particles (60-80 nm) likely prevents extravasation of drug from lymph vessels, thus delaying drug appearance in the blood. This size of TLC-ART101 particles could fill LN sinus spaces (~1-500 μm) (Drinker, Field et al. 1934) to capacity before moving to other nodes interconnected by lymphatic vessels. Uptake of TFV, LPV, and RTV into cells as a stable particle unit may have contributed to higher intracellular drug concentrations in LNMCs and PBMCs than in the plasma; the time to peak levels in PBMCs for all drugs being ~12-24 hr support this hypothesis (**Figure 2.1**, table insert). Should the drug-lipid particle disintegrate, the released soluble drugs would be cleared into nearby blood vessels (where flow is ~100-500-fold faster than the lymph system) and eliminated within hours (akin to the ~1-12 hr half-life of respective parent soluble drugs). The hypothesis of preferential lymph vessel uptake and LN retention, followed by redistribution of the drug combination in TLC-ART101 to the blood, is consistent with the higher LNMC intracellular concentrations (**Table 2.1**) where the first exposure to drug particles occurs (versus their PBMC counterparts). Regardless of the exact mechanisms, the PK data indicate that

preferential lymphatic drug-combination particle uptake, distribution, retention, and cellular uptake may have contributed to the early peak drug levels followed by sustained drug levels for over two weeks.

Given the long-standing clinical experience with LPV and TFV (including TDF and TAF), development of TLC-ART101 could leverage available *in vitro* antiviral potency data and target plasma drug levels. Compared to equivalent free drug formulations, a drug-lipid fixed dose combination exhibited ~30-fold lower EC_{50} (higher potency); EC_{50}s for TFV and LPV in TLC-ART101 against HIV-infected CEM-174 cells were 1.5 ± 0.1 nM and 3.0 ± 0.8 nM, respectively (Freeling, Koehn et al. 2015). Macaque PBMC intracellular concentrations at 0-336 hr were ~100-10,000-fold higher than these EC_{50} values after one TLC-ART101 dose. Dose-response and efficacy studies in a NHP HIV treatment model are planned.

Long-acting injectable drugs, including cabotegravir and rilpivirine, are in development. However, none to our knowledge are co-formulated. Cabotegravir and rilpivirine (two different dosage forms), injected in separate intramuscular sites, allow drug release predominantly from each injection site. As a result, it takes days to build up plasma drug levels in humans and the T_{max} of each is variable (median 9-69 days (Spreen, Ford et al. 2014), 6-11 days (McGowan, Dezzutti et al. 2016), depending on the dose). Among other considerations, the delay in reaching therapeutic levels requires an initial dose supplement for these formulations. In contrast, TFV and LPV levels after TLC-ART101 peaked in plasma at ~1.5 hr and ~12.3 hr and likely reach therapeutic levels (above EC_{50}) within hours (**Figure 2.1**). These early peak plasma and cell levels may overcome the need to have a lead-in oral dose for TLC-ART101.

Previously, we used a LPV/RTV molar ratio of 2:1 (Freeling, Koehn et al. 2014, Freeling, Koehn et al. 2015) and TFV and LPV levels in NHP plasma and PBMCs persisted for over one week. In this study, TLC-ART101, with a LPV/RTV molar ratio of 4:1 (as in *Kaletra*® tablets (Kaletra Product Lablel (AbbVie Inc.) Accessed 3-2-2017)), extended TFV and LPV levels in plasma and PBMCs to over two weeks. However, inexplicably, at one week post-dosing there were no significant differences for LPV plasma and PBMC $AUC_{0\text{-}168h}$, C_{max}, and T_{max} between LPV/RTV 2:1 vs. 4:1, yet, the LPV/RTV 4:1 formulation exhibited a significantly higher PBMC intracellular TFV $AUC_{0\text{-}168h}$ ($p<0.005$). In this study, as with our previous study (Freeling, Koehn et al. 2015), markers of renal and hepatic function remained within normal levels. Cerebral spinal fluid drug levels in macaques 24 hr after TLC-ART101 dosing were 16- to 1,660-fold lower than those in plasma.

In TLC-ART101, we used TFV as bioavailability of TFV via the SC route is not limited by oral absorption. Prodrugs TDF and TAF are intended to overcome limited oral bioavailability of TFV. Interestingly, PBMC intracellular TFV exposures after a single SC TLC-ART101 dose were much higher than equivalent or recommended doses of SC TFV, oral TDF, and oral TAF in NHPs (**Table 2**). At steady-state, the intracellular TFV-DP ratio was about 61% in both human and macaque PBMCs (Durand-Gasselin, Van Rompay et al. 2009, Ruane, DeJesus et al. 2013, Massud, Mitchell et al. 2016, PMDA Accessed Oct 11, 2016). Even with TFV, which exhibits 10-100-fold lower cell uptake *in vitro* (Taneva, Crooker et al. 2015), our data suggest TLC-ART101 enhanced intracellular TFV and TFV-DP drug concentrations in NHP PBMCs and LNMCs, and substantially enhanced exposure. Even after weight-based adjustments, TLC-ART101 still

provided a several-fold increase in intracellular drug exposure versus TDF or TAF. The increase in TFV exposure enabled by TLC-ART101 may allow use of a lower TFV dose. This may improve safety of TFV, an important consideration for adults and children.

In summary, subcutaneous TLC-ART101 (TFV, LPV, and RTV in a nanosuspension) enabled persistent drug levels in LNMCs, PBMCs, and plasma in NHPs; significant enhancements were noted in overall intracellular drug exposures of hydrophilic TFV over two weeks. The long-acting behavior and higher intracellular levels in LNs and blood over plasma levels may address adherence issues and drug insufficiency reported in lymph nodes after current oral HIV regimens. These data support TLC-ART101 development as a potential platform for a SC long-acting combination antiretroviral regimen.

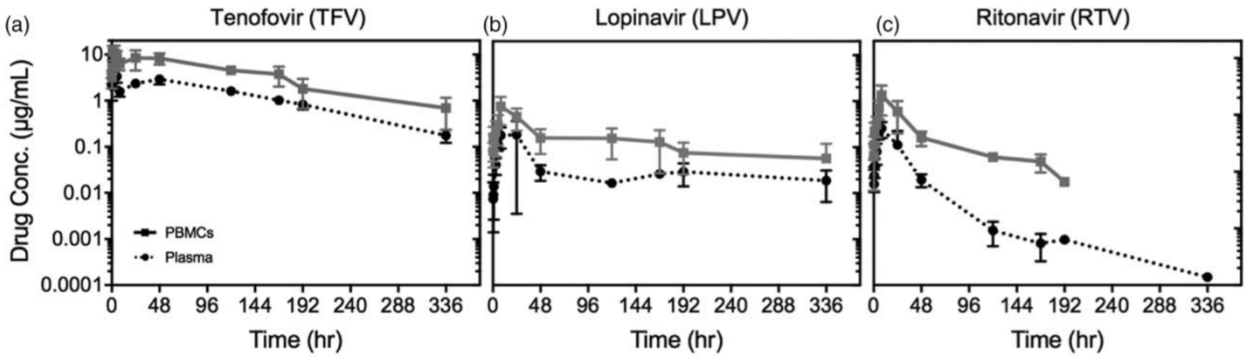

	Tenofovir (TFV)		Lopinavir (LPV)		Ritonavir (RTV)	
	Plasma	PBMCs	Plasma	PBMCs	Plasma	PBMCs
$AUC_{0\text{-}336h}$ (hr•µg/mL)	**416.6** (15.4)	**1,255.7** (5.7)	**11.0** (48.1)	**44.1** (49.4)	**4.8** (57.1)	**35.5** (27.7)
C_{max} (µg/mL)	**4.4** (8.2)	**13.2** (21.2)	**0.2** (44.0)	**0.8** (49.8)	**0.3** (33.1)	**1.2** (61.4)
T_{max} (hr)	**1.5** (100.0)	**2.9** (154.6)	**12.3** (66.7)	**10.5** (66.7)	**7.1** (20.7)	**10.5** (66.7)
$t_{1/2}$ (hr)	**65.3** (10.9)	**169.1** (133.0)	**476.9** (172.8)	**151.2** (51.6)	**44.1** (45.8)	**61.0** (57.2)

Figure 2.1. Time-course of plasma and PBMC intracellular concentrations of TFV, LPV, and RTV after a single SC dose of the TLC-ART101 drug combination nanosuspension; descriptive PK parameters are summarized in the table.

Panels **A**, **B**, and **C** show consistently higher TFV, LPV, and RTV concentrations in peripheral blood mononuclear cells (PBMCs) at each time point compared to those in plasma. The squares (■) represent PBMC intracellular drug concentrations, and circles (●) represent plasma drug concentrations. Each time point represents arithmetic mean ± SD of plasma and PBMC intracellular drug concentrations from N=4 male pigtail macaques. PBMC cell volume assumed to be 0.2829 pL/cell (Simiele, D'Avolio et al. 2011). Limit of detection (LOD) = plasma/PBMCs, TFV: 100/110; LPV: 5/2; RTV: 25/2.5 pg/mL. Limit of quantification (LOQ) = plasma/PBMCs, TFV: 250/250; LPV: 10/5; RTV: 50/5 pg/mL. RTV (intended as a booster for LPV PK) in plasma was <LOQ in N=2 at 192 hr and 336 hr, and was <LOQ in PBMCs of N=3 at 192 hr and N=4 at 336 hr. The summary table lists PK parameter estimates based on non-compartmental analysis (NCA) using Phoenix®. Each PK parameter is presented as the geometric mean (% coefficient of variation) of the individual PK parameters from N=4 macaques. The PBMC TFV $AUC_{0\text{-}366h}$ of 1,255.7 hr•µg/mL was converted to the molar equivalent value (equal to 4,372.06 hr•µM) for data comparisons presented in Table 1B. $AUC_{0\text{-}336h}$, area under the concentration-time curve from 0 to 336 hr; C_{max}, maximum drug concentration reached; T_{max}, time at which C_{max} was reached; $t_{1/2}$, apparent terminal elimination half-life.

Table 2.1. Enhanced TFV, LPV, and RTV intracellular concentrations in inguinal lymph nodes excised one and eight days after a single SC dose of TLC-ART101, and comparisons to drug levels at the same time points in PBMCs and plasma.

	Tenofovir (TFV)		**Lopinavir (LPV)**		**Ritonavir (RTV)**	
SC Dose (mg/kg)	10.58		25.00		6.96	
LNMCs						
C_{24h} (µg/mL)	**7.12**	(56.5)	**9.02**	(89.2)	**4.50**	(28.7)
C_{192h} (ug/mL)	**5.49**	(175.8)	**5.16**	(127.0)	**0.98**	(157.6)
LNMCs/PBMCs						
C_{24h}	**0.93**	(79.6)	**23.04**	(162.7)	**8.88**	(44.3)
C_{192h}	**4.41**	(198.0)	**79.20**	(65.9)	**531.37**	(NA)
LNMCs/Plasma						
C_{24h}	**3.05**	(50.4)	**89.41**	(119.3)	**77.94**	(95.9)
C_{192h}	**6.77**	(165.3)	**197.78**	(93.7)	**3,068.15**	(111.2)

Geometric Mean (% coefficient of variation).

NA, not available due to three macaques having RTV levels <LOQ in PBMCs.

LNMC and PBMC cell volume assumed to be 0.2829 pL/cell (Simiele, D'Avolio et al. 2011).

C_{24h} and C_{192h}, drug concentration at 24 hr and 192 hr; LNMCs, lymph node monnuclear cells; PBMCs, peripheral blood mononuclear cells; SC, subcutaneous.

Table 2.2. Comparison of intracellular TFV-DP and total TFV exposure in PBMCs after dosing with TFV, TDF, TAF, or TLC-ART101 formulations.

Drug Formulation	Route	Dose (mg/kg)	TFV-DP	TFV (total)	Ref
TFV	SC	4	4.65	8.67	(Durand-Gasselin, Van Rompay et al. 2009)
TDF	PO	30	36.60	53.43	
TAF	PO	1.5	32.15	130.98	(Massud, Mitchell et al. 2016)
TAF	PO	4.5	504.60	973.07	
TFV in TLC-ART101*	SC	10.6	2,666.96	4,372.06	Figure 1, table insert

Intracellular drug exposure (AUC in hr•μM) after a single dose in NHPs is estimated based on intracellular concentration (μM) measured over time in PBMCs as TFV-DP, total TFV, or both.

*The steady-state fraction of 61% of total TFV is used to estimate the fraction of TFV-DP (Durand-Gasselin, Van Rompay et al. 2009, Ruane, DeJesus et al. 2013, Massud, Mitchell et al. 2016, PMDA Accessed Oct 11, 2016) (e.g., 1,255.70 hr•μg/mL • [(1,000 μmol•mL) / (287.21 μg•L)] = 4,372.06 hr•μM; 0.61 • 4,372.06 hr•μM total TFV = 2,666.96 hr•μM TFV-DP).

AUC, area under the concentration-time curve; NHPs, non-human primates; PBMCs, peripheral blood mononuclear cells; PO, *per os* (oral); SC, subcutaneous; TAF, tenofovir alafenamide; TDF, tenofovir disoproxil fumarate; TFV, tenofovir; TFV-DP, tenofovir diphosphate.

Chapter 3. **Development of a Near-Infrared Marker to Track the *In Vivo* Distribution of DcNPs in Real-Time**

Chapter 3 was published

in

Biochemistry. 2014;53(8):1275-83.

3.1 ABSTRACT

Indocyanine green (ICG) is a near-infrared (NIR) contrast agent commonly used for *in vivo* cardiovascular and eye imaging. For medical diagnosis, ICG is limited by its aqueous instability, concentration-dependent aggregation, and rapid degradation. To overcome these limitations, scientists have formulated ICG in various liposomes, which are spherical vesicles of lipid membrane with an aqueous core. Some encapsulate ICG while others mix it with liposomes. There is no clear understanding of lipid-ICG interactions. Therefore, we investigated lipid and ICG interactions by fluorescence and photon correlation spectroscopy. These data were used to design stable and maximally fluorescent ICG lipid-nanoparticles for NIR optical imaging of the lymphatic system. We found that ICG binds to and incorporates completely and stably into lipid-nanoparticles. At lipid-ICG molar ratio 250:1 mol/mol, maximal fluorescence intensity was detected. ICG incorporated in lipid-nanoparticles enhanced fluorescence intensity detectable across 1.5 cm of muscle tissue while free ICG only allowed 0.5 cm detection. When administered subcutaneously in mice, lipid-bound ICG in lipid-nanoparticles exhibited higher intensity, NIR image resolution, and enhanced lymph node and lymphatic vessel visualization. It also reduced fluorescence quenching due to light exposure and degradation in storage. Lipid-bound ICG could provide additional medical diagnostic value with NIR optical imaging for early intervention of lymphatic abnormalities.

A graphical abstract is shown in **Figure 3.0**.

3.2 INTRODUCTION

Indocyanine green (ICG) is the only near-infrared (NIR) fluorescent dye approved by the US Food and Drug Administration (FDA) and European Medicines Agency (EMA) for human use (FDA 2013). With its 820 nm NIR emission wavelength, ICG is considered a good *in vivo* contrast agent with minimal interference from blood and tissue autofluorescence (~500-600 nm). It is indicated for determining cardiac output, hepatic function and liver blood flow, and for ophthalmic angiography. ICG is used off-label or in research to visualize anatomical structures filled with fluid (for example, blood, cerebrospinal fluid, lymph, or urine) or as a contrast agent for vascular, renal, or excretory pathways (Nguyen and Tsien 2013). In aqueous environments, ICG molecules aggregate and ICG fluorescence readily degrades (Baker 1966, Zhou, Chin et al. 1994, Mordon, Devoisselle et al. 1998, Saxena, Sadoqi et al. 2003). In blood, ICG binds to plasma proteins, enhancing its fluorescence intensity. *In vivo* ICG fluorescence intensity and duration may vary with fluctuating plasma protein and lipoprotein concentrations and interindividual variation.

To overcome protein binding dependency, scientists have attempted to add ICG to hydrophobic polymers, serum albumin, and nanoparticles, including liposomes. Recent reports on ICG and liposomes with diverse physiochemical characteristics and prepared by various procedures have demonstrated the potential of ICG-lipid particles for optical imaging of lymphatic function (Proulx, Luciani et al. 2010, Proulx, Luciani et al. 2013), sentinel lymph nodes (SLNs) (Jeong, Lee et al. 2013), vascular permeability (Sandanaraj, Gremlich et al. 2010), and angiogenesis (Hua, Gross et al. 2012). However, most of these liposomes with varying compositions containing ICG were prepared without a full understanding of the interactions between ICG and lipids. Under certain conditions, ICG can physically interact with phospholipids

in the liposome membrane and modify the stability and quantum yield of ICG as well as the structure and stability of the lipid membrane. ICG may also be encapsulated in the aqueous compartment of liposomes. These properties and variations could profoundly impact optical NIR imaging quality and the ability to provide medical diagnostic value.

Not all liposomes and lipid-nanoparticles are alike and some may consist of phospholipids of different head groups and fatty acyl chains while others may include cholesterol or other additives, all of which can alter a liposome's physiochemical properties (Kraft, Freeling et al. 2014). Due to a high degree of overlap between the absorption and emission spectra of ICG, ICG exhibits concentration-dependent fluorescence quenching (self-quenching). It is therefore important to define not only the lipid-ICG interactions, but also the optimal density of ICG molecules within a lipid bilayer that exhibits both maximal fluorescence intensity per ICG molecule and minimal self-quenching. Based on the biochemical characteristics of ICG and lipid-ICG interactions, a stoichiometric range of the lipid-ICG molar ratio that avoids self-quenching and maximizes fluorescence yield can be achieved through systematic studies. ICG binding to lipid has been assumed through indirect evidence to stabilize ICG fluorescence and protect the ICG molecule from oxidation, resulting in enhanced fluorescence intensity (Devoisselle, Soulie et al. 1997, Chang, Morse et al. 1998, Mordon, Devoisselle et al. 1998, Yoneya, Saito et al. 1998, Zheng, Xing et al. 2011, Jeong, Lee et al. 2013). However, the interactions between ICG and lipid have yet to be studied.

Therefore, the goal of this study is to elucidate the lipid-ICG interactions that influence ICG fluorescence intensity and ICG-lipid complex stability, and to evaluate lipid-nanoparticle ICG

as an *in vivo* imaging agent. We found that ICG binds to lipid and in the process stabilizes and enhances its fluorescence properties, overcoming the dependency on protein binding. Compared to free ICG, ICG embedded in lipid-nanoparticles enhanced visualization of the popliteal lymph node and downstream lymph nodes in mice, and enabled light transmittance through 1.5 cm of muscle tissue. In addition, these ICG lipid-nanoparticles, produced by an efficient and scalable preparation procedure that incorporates nearly 100% of ICG, had excellent light exposure and storage stability.

3.3 MATERIALS AND METHODS

3.3.1 *Chemicals*

Indocyanine green (ICG; $C_{43}H_{47}N_2NaO_6S_2$; sodium 2-[7-[3,3-dimethyl-1-(4-sulfonatobutyl)benz[e]indolin-2-ylidene]hepta-1,3,5-trien-1-yl]-3,3-dimethyl-1-(4-sulfonatobutyl)benz) was purchased from Sigma-Aldrich (St. Louis, MO). 1,2-distearoyl-sn-glycero-3-phosphocholine (DSPC), 1,2-distearoyl-sn-glycero-3-phosphoethanolamine-N-methoxy-polyethylene glycol-2000 ($DSPEmPEG_{2000}$), and L-α-phosphatidylcholine (Egg PC) were purchased from Avanti Polar Lipids (Alabaster, AL). Other reagents were analytical grade or higher.

3.3.2 *Lipid-Nanoparticle Preparation*

Control or empty lipid-nanoparticles and lipid-nanoparticle ICG were prepared by thin film hydration and sonication. Briefly, DSPC dissolved in $CHCl_3$ and $DSPEmPEG_{2000}$ dissolved in $CHCl_3$:CH_3OH (3:1 v/v) were mixed (9:1 mol/mol) in a sterile test tube. The mixture was then

dried under N_2 gas and reduced pressure into a thin film, which was vacuum desiccated overnight at room temperature. The thin film was rehydrated with 0.9% NaCl, 20 mM $NaHCO_3$ buffer at pH 7 (20 mM final lipid concentration) at 60°C for 3 hours. The lipid-nanoparticle diameter was reduced to approximately 50-80 nm with 15 minutes of bath sonication at 55°C. For lipid-nanoparticle ICG, ICG dissolved in 100% CH_3OH was added to the lipid mixture prior to drying into a thin film. ICG self-quenching[17] was accounted for and the density of ICG in the lipid-nanoparticle was optimized. The mean diameters of lipid-nanoparticles and lipid-nanoparticle ICG were obtained by particle size analysis with photon correlation spectroscopy (PCS) on a PSS-NICOMP 380 ZLS (Particle Sizing Systems; Port Richey, FL, USA). Zeta potential was measured on the same instrument. ICG incorporation efficiency was evaluated by separation of lipid-bound and free ICG by equilibrium dialysis. All experiments were performed under dark conditions and light exposure was avoided.

3.3.3 *90° Light Scattering of ICG Adsorbed to Lipid-Nanoparticles*

ICG dissolved in 100% CH_3OH was incubated with lipid-nanoparticles in plastic micronic tubes at lipid-ICG molar ratios of 25:1 to 500:1 for 20 minutes before diluting 25-fold with 0.9% NaCl, 20 mM $NaHCO_3$ buffered at pH 7 to minimize ICG-lipid interactions. Ninety degree light scattering was then measured on a Hitachi F-4500 fluorescence spectrophotometer (Troy, MI). The set parameters were $\lambda_{ex/em}$ = 660/660 nm and slit $width_{ex/em}$ = 2.5/5 nm. Samples were stored away from light at room temperature during observation.

3.3.4 *Fluorescence*

Fluorescence measurements were performed on a Victor^3 V 1420-040 Multilabel Plate Reader (Perkin Elmer; Waltham, MA) with a tungsten-halogen continuous wave lamp (75 w, spectral range 320-800 nm) and excitation (769 ± 41 nm) and emission (832 ± 37 nm) filters (Semrock; Rochester, NY) using 100 μL of sample in flat bottom, untreated 96-well plates (Grenier Bio-one; Monroe, NC).

3.3.5 *Light Exposure and Storage Stability*

For light exposure stability, samples of free ICG and lipid-nanoparticle ICG at 2.0 μM ICG were exposed to overhead fluorescent tube lighting for 12 hours. Fluorescent measurements were recorded at 0, 6, and 12 h. For storage stability, samples were placed in the dark at 4°C for up to 313 days. Fluorescent measurements were recorded at five different time points for free ICG, and at 10 different time points for lipid-nanoparticle ICG. The time-dependent decay of ICG fluorescence was analyzed based on an exponential decay model with GraphPad Prism version 6.0 Software (San Diego, CA). The data were expressed as $t_{1/2}$ (half-life) and k (rate constant).

3.3.6 *Tissue Depth Penetration*

Cuboid chicken breast tissue phantoms of three different depths (0.5, 1.0, 1.5 cm) were used to assess ICG fluorescence detection through tissue. Tissue cuboids were placed over capillary tubes (70 μL capacity, 75 mm length, 1.2 mm inner diameter; Fisher Scientific; Hampton, New Hampshire) filled with 50 μL of 30 μM of free ICG or lipid-nanoparticle ICG. White light and NIR images were captured within 15 minutes of preparing capillary tubes and tissue cuboids

using a custom NIR charge-coupled device (CCD) camera built by Hamamatsu Photonics K. K. (Hamamatsu, Japan). Fluorescence intensity mean values of select areas, on a scale of 0 to 255 with 255 maximal brightness, were obtained with the analysis function in Adobe Photoshop CS4 software (Adobe Systems Inc.; San Jose, California).

3.3.7 *In Vivo NIR Lymphatic Imaging in Mice*

Mice were maintained in pathogen-free conditions, exposed to a 12-hour light/dark cycle, and received food ad libitum prior to imaging. All procedures were approved by the University of Washington Institutional Animal Care and Use Committee.

Three mice were anesthetized with 1.5% isoflurane, shaved to remove fur, and placed in a supine position on a 37˚C heat pad underneath a custom NIR CCD camera. Precontrast images were taken to confirm absence of autofluorescence. Forty microliters of lipid-bound ICG in lipid-nanoparticles (250:1 lipid-ICG molar ratio) or free ICG was injected subcutaneously into the top of both rear feet (12.5 μM ICG in 0.9% buffered saline in each foot, totaling 1.0 nmol of ICG/mouse). Immediately following injections, both feet were placed under gentle even pressure. Images were acquired for up to 120 minutes prior to euthanasia by cervical dislocation under anesthesia, upon which surgical opening of the skin was performed.

3.4 RESULTS

3.4.1 *Lipid-Nanoparticle Lipid-ICG Interactions*

To evaluate the interactions between ICG and lipid, we incubated empty (no ICG) lipid-nanoparticles with varying concentrations of ICG. If ICG molecules in solution bind to lipids in the particle structure, it will cause lipid-nanoparticles to crosslink and aggregate, resulting in an increase in its apparent size detectable by a change in 90° light scattering and an increase in particle size. In a preliminary experiment, we first tested lipid-nanoparticles composed of egg-derived phosphatidylcholine (Egg PC) (containing mixed-length fatty acyl chains) and observed an increase in light scattering intensity as ICG concentration was increased, indicating that ICG induced lipid-nanoparticle aggregations. We next used lipid-nanoparticles with a well-defined phospholipid composition—DSPC containing two symmetrical C18 fatty acyl chains and $DSPEmPEG_{2000}$ (9:1 mol/mol)—to perform systematic studies. A fixed 10 μM lipid concentration in lipid-nanoparticles with varying ICG concentrations were allowed to interact for 20 min at 25°C; the reaction was stopped by 25-fold dilution with buffered solution. The mixture was subjected to 90° light scattering analysis and photon correlation spectroscopy (PCS) to estimate particle size.

Ninety degree light scattering intensity is expected to be low when particles are in single, non-aggregated form and increase with aggregation. However, when lipid aggregates become too large they may fall off the light path or electrons in a particle may not oscillate together in phase and cause intraparticle destructive interference, resulting in apparent decline of scattering intensity. As shown in **Figure 3.1A**, empty lipid-nanoparticles (lipid only) have a low scattering intensity and free ICG (ICG only) has a consistent scattering intensity near zero regardless of the varying ICG concentration. When lipid-nanoparticles and ICG (L-ICG) were mixed together, at low ICG

concentrations (20-30 nM) a minimum light scattering intensity similar to the empty lipid-nanoparticle control (lipid only) was detected. The scattering intensity of L-ICG increased approximately 1.5-fold when the ICG concentration increased from 30 to 70 nM (**Figure 3.1A**). There was a minor decline in scattering intensity at 40 nM ICG, however, it was still significantly higher than at 20-30 nM ICG. At high concentrations (100-400 nM ICG), the scattering intensity declined as aggregates grew larger. **Figure 3.1B** depicts a schematic drawing of the proposed aggregate formation that leads to an initial increase in light scattering intensity followed by a decrease in intensity as the particle size becomes exceedingly large. These data were confirmed by aggregate size analysis with PCS. As shown in **Figure 3.1C**, at an initial ICG concentration of 20 nM, the particle diameter was similar to that of empty lipid-nanoparticles (~100 nm). The apparent ICG lipid-nanoparticle size increased about 2-fold at ICG concentrations of 20 to 100 nM. The apparent size fluctuated around 300 nm diameter at ICG concentrations between 30-100 nM, and then grew to about 400 nm at 400 nM ICG. In the region of 30-400 nM ICG, we detected a small population of smaller but distinct ICG lipid-nanoparticles with consistent diameters of 60-90 nm (data not shown).

Collectively, these data indicate that ICG binds to lipid presented in empty pre-formed lipid-nanoparticles and leads to lipid-nanoparticle aggregates, detected as apparent increase in particle size, and a discontinuous increase in light scattering intensity. Based on the lipid concentration of 10 μM and ICG concentrations 20-50 nM, these data give rise to a lipid-ICG molar ratio estimated to be between 200:1 to 500:1 that produces maximal lipid aggregation and apparent increase in particle size.

3.4.2 *Impact of Lipid-nanoparticle Lipid-ICG Interactions on ICG Fluorescence*

We next determined the impact on fluorescence intensity due to ICG binding to lipid. We used the lipid-ICG molar ratio range of 125:1 to 25,000:1. Due to the self-quenching property of ICG, the reaction mixture was diluted 20-fold with buffered solution to the linear ICG concentration range of 0.01-2.0 μM. As shown in **Figure 3.2**, the presence of lipid in the mixture increased the fluorescence intensity of ICG at equivalent ICG concentrations. As ICG concentration increased from 0.01 to 1.0 μM, the fluorescence intensity progressively widened for the mixture containing lipid vs. control. At 0.1, 0.5, and 1.0 μM ICG, fluorescence intensity increased by 10.0-fold (65,720 vs. 6,600), 4.3-fold (261,640 vs. 61,360), and 2.8-fold (346,610 vs. 122,530), respectively. At 2.0 μM ICG, the lipid-mediated enhancement in ICG fluorescence intensity was less and only a 1.4-fold increase (275,820 vs. 199,420) was observed. At a fixed 250 μM lipid concentration and 0.5, 1.0, and 2.0 μM ICG, the equivalent lipid-ICG molar ratios for these values are 500:1, 250:1, and 125:1, respectively (**Figure 3.2**). Therefore, the optimal lipid-ICG molar ratio that exhibits the highest fluorescence intensity is estimated to be 125:1 to 500:1. This estimate is consistent with data collected from 90° light scattering and PCS size analysis. These values, derived from ICG and pre-formed lipid-nanoparticle interactions, were used as the target range for subsequent ICG lipid-nanoparticle preparation and characterization studies.

3.4.3 *Incorporation of ICG into Lipid-nanoparticles to Stabilize and Maximize ICG Fluorescence*

Instead of adding ICG in solution to lipid as admixtures in buffered solution, we mixed ICG and lipid together in an organic solution, first, then removed the solvent and rehydrated in buffer to form lipid-nanoparticles inserted or embedded with ICG. ICG has a significant overlap

in absorption and emission spectra (**Figure 3.3A**) and consequently exhibits self-quenching potential at high concentrations. Thus, we made lipid-nanoparticles embedded or incorporated with different concentrations (densities) of ICG incorporated into the lipid-nanoparticle. If ICG density is too high, the close proximity between ICG molecules may induce self-quenching due to concentration-dependent molecular interactions (MacDonald 1990). Moreover, ICG incorporated into lipid without exposure to water would provide higher fluorescence than ICG molecules exposed to water, which quenches ICG fluorescence. Eight lipid-ICG molar ratios ranging from 100:1 to 500:1 were evaluated. **Figure 3.3B** represents the fluorescence intensity per unit of ICG slope at typical ICG concentrations for three lipid-bound ICG samples (equivalent to 100:1, 250:1, and 350:1 mol/mol) and a soluble ICG control. At 0.01-2.0 μM ICG, the fluorescence intensity appears to increase linearly. Note that the slope of the 250:1 line is the steepest, followed by 350:1, 100:1, and ICG only. To determine the optimum lipid-ICG molar ratio, we evaluated the slope of the line for each formulation (for clarity, only three of eight total lines are presented in **Figure 3.3B**).

The slope equals fluorescence intensity per μM ICG. As shown in **Figure 3.3C**, due to a reduction in ICG density and self-quenching, the fluorescence intensity per ICG (slope) increased as the lipid-ICG molar ratio increased from 100:1 to 250:1, at which point the maximum was reached. The fluorescence intensity per ICG then decreased at 300:1 and 350:1, followed by a significant decrease at 500:1. Thus, we observed the peak fluorescence intensity per ICG at lipid-ICG molar ratio 250:1.

As the 250:1 lipid-ICG molar ratio exhibits the highest fluorescence intensity per ICG, we characterized the 250:1 formulation using particle size analysis by photon correlation spectroscopy (PCS) and particle surface charge (zeta potential) analysis by electrophoretic light scattering (ELS). The 250:1 formulation consisted of a monodisperse population of particles with a 56.8 ± 4.4 nm diameter and a -33.1 ± 3.1 mV zeta potential. Equilibrium dialysis indicated the ICG incorporation efficiency was 97.8 ± 0.6%. Due to reproducible and almost complete incorporation of ICG, this formulation was selected without further purification for subsequent *in vitro* and *in vivo* studies.

3.4.4 *Effects of Lipid Incorporation on Enhancing ICG Stability for Light Exposure and Storage*

We next evaluated the stability of lipid-nanoparticle ICG in 4°C storage and under light exposure to simulate the environment in clinical settings. As shown in **Figure 3.4**, the fluorescence intensity of lipid-nanoparticle ICG decreased to 87.6 ± 0.5% of the initial value after 6 hours of light exposure and experienced no further decrease after 12 hours ($t_{1/2}$ = 67.5 ± 11.8 h, k = 0.011 ± 0.002 h^{-1}). In contrast, the fluorescence intensity of free ICG in solution droped to 2.5 ± 0.5% of its initial value after 6 hours of light exposure ($t_{1/2}$ = 0.036 ± 0.005 h, k = 19.2 ± 2.7 h^{-1}), indicating the light instability of ICG in aqueous solutions.

To evaluate longer-term storage stability, we kept lipid-nanoparticle ICG in the dark at 4°C and measured the fluorescence intensity multiple times over 313 days. As shown in **Figure 3.5** and **Table 3.1**, about 78.2 ± 2.8% of the initial fluorescence intensity was recorded after eight months of storing lipid-nanoparticle ICG ($t_{1/2}$ = 394 days [95% CI: 360, 434], $k = 1.76 \times 10^{-3}$ $days^{-}$

[1] [95% CI: 1.60×10^{-3}, 1.93×10^{-3}]). However, for free ICG in buffer, only 0.3 ± 0.2% of the initial ICG fluorescence was observed after eight months of storage ($t_{1/2}$ = 1.19 days [95% CI: 1.14, 1.25], $k = 582 \times 10^{-3}$ days^{-1} [95% CI: 554×10^{-3}, 609×10^{-3}]).

3.4.5 *Enhanced NIR Imaging of Lipid-nanoparticle ICG In Vitro*

To compare fluorescence signal intensity between lipid-nanoparticle ICG (250:1 lipid-ICG molar ratio formulation) and free ICG, we prepared chicken breast cuboids with increasing muscle tissue thicknesses of 0.5, 1.0, and 1.5 cm (**Figure 3.6F**). We filled all capillary tubes (75 mm in length, 1.2 mm inner diameter) with 50 μL of 30 μM ICG (1.5 nmol ICG) (**Figure 3.6B**). As shown in **Figure 3.6A**, the intensity of the capillary tube filled with lipid-nanoparticle ICG was 3.2-fold higher than that of free ICG (intensity mean = 111.7 vs. 34.5, respectively). When placed under three tissue cuboids, with increasing depth from left to right, free ICG fluorescence (top three cuboids) was only detectable across 0.5 cm depth (top left cuboid; intensity mean = 9.0) but not through thicker depths; lipid-nanoparticle ICG fluorescence (bottom three cuboids) was detectable across 0.5 cm, 1.0 cm, and 1.5 cm depths (intensity mean = 112.1, 77.3, 10.0, respectively) (**Figure 6C**). Further analysis indicates that only lipid-nanoparticle ICG in capillary tubes can be detected across 1.5 cm of muscle tissue (intensity mean for 0.5, 1.0, 1.5 cm depths = 100.9, 68.0, 15.2, respectively) (**Figures 3.6E** and 3.**6F**).

3.4.6 *Effects of Lipid-nanoparticle-bound ICG on NIR Lymphatic Image Resolution in Mice*

With the stable and optimized lipid-nanoparticle ICG formulation, we performed *in vivo* proof of principle optical imaging experiments in mice. To compare free versus lipid-nanoparticle

ICG, we subcutaneously administered ICG in 40 μL (0.5 nmol of ICG), either in free or lipid-nanoparticle-bound form, to the mouse's left or right foot (**Figure 3.7A**). At six minutes, only the foot that received lipid-nanoparticle ICG (but not free ICG) exhibited a detectable popliteal node through the skin (**Figure 3.7A**). Only when the image was collected below the skin, both popliteal lymph nodes became detectable. The ICG intensity mean of the popliteal lymph node that received free ICG was 37.0 compared to 208.1 for that treated with lipid-nanoparticle ICG (data not shown). To further compare the lymphatic image resolution of free ICG versus lipid-nanoparticle ICG, in another set of mice, we administered ICG to both feet either in free or lipid-nanoparticle form with the same dose. As shown in **Figure 3.7B**, at six minutes post administration and after removal of the skin, the animal receiving free ICG showed diffusion of ICG into the blood (saphenous vein). In this case, ICG was clearly detectable in the local popliteal node (**Figure 3.7B**). In contrast, in the mouse treated with lipid-nanoparticle ICG, not only the popliteal lymph node intensity was much higher, but also a lymphatic track leading to ventral pelvic and genital/regional nodes was readily visible (**Figure 3.7C**). Distribution of free ICG to this lymphatic track was not observed.

3.5 DISCUSSION

Based on the ability of ICG to bind to and insert into lipid-nanoparticles, we have systematically characterized these interactions that confer ICG molecular and fluorescence stability. Our results show that ICG binds to and incorporates completely and stably into lipid-nanoparticles at ICG densities as high as in a 3:1 lipid-ICG molar ratio. At the 250:1 optimal lipid-ICG ratio, we detected a 4.5-fold enhancement in lipid-bound ICG fluorescence intensity over that of aqueous ICG. At this optimum ratio, lipid-nanoparticle ICG exhibited nearly complete (98%) incorporation efficiency of ICG and fluorescence intensity was independent of plasma protein

binding. In 4°C storage away from light, ICG in lipid-nanoparticles was stable ($t_{1/2}$ = 394 days [95% CI: 360, 434], $k = 1.76 \times 10^{-3}$ days^{-1} [95% CI: 1.60×10^{-3}, 1.93×10^{-3}]; **Figure 3.4** and **Table 3.1**). Lipid-nanoparticle ICG is also stable when exposed to several hours of room light at 25°C ($t_{1/2}$ = 67.5 ± 11.8 h, k = 0.011 ± 0.002 h^{-1}; **Figure 3.5**). When administered subcutaneously in mice, preliminary data suggests that lipid-bound ICG exhibited higher intensity, NIR image resolution, and enhanced lymph node and lymphatic vessel visualization. In contrast, free ICG in mice readily distributes into the blood with lower image resolution.

Although ICG in solution can induce lipid-nanoparticle aggregation, the exact mechanism is not clear. It is possible that ICG with its high LogP value (6.05 at pH 7.4; low water solubility) (Chemicalize.org accessed Jan 6, 2014) may bind to lipid and cause the lipid-nanoparticle surface to become sticky, thus forming lipid-nanoparticle aggregations, detected by 90° light scattering and photon correlation spectroscopy as ICG induced an increase in light scattering and apparent diameter (**Figure 1**). Others have mixed ICG with pre-formed lipid-nanoparticles composed of various lipids and observed aggregation (Verkade, de Bruijn et al. 1996) or fluorescence enhancement (Devoisselle, Soulie et al. 1997, Portnoy, Lecht et al. 2011). However, these studies did not probe concentration dependent effects. In our studies, we evaluated and found non-linear concentration effects and used the information of ICG-lipid-nanoparticle admixtures related to ICG-lipid binding and fluorescence enhancement to fine-tune an optimal composition to construct ICG incorporated completely in lipid-nanoparticles. We used well-characterized lipid-nanoparticles composed of 90 mol% DSPC and 10 mol% DSPEmPEG$_{2000}$, which is based on a validated and scalable formulation for *in vivo* lymphatic drug delivery (Kinman, Brodie et al. 2003). With this lipid composition, we achieved complete incorporation of ICG by mixing ICG

and lipids together in organic solvent, producing stable ICG lipid-nanoparticles. This is in contrast to other preparations using various lipids where ICG was added in aqueous solution to encapsulate 50-88.2% of ICG within liposomes (Proulx, Luciani et al. 2010, Suganami, Toyota et al. 2012, Turner, Moshkelani et al. 2012, Zhuang, Ma et al. 2012, Jeong, Lee et al. 2013, Proulx, Luciani et al. 2013). In such situations, some ICG may be trapped within the aqueous compartment while a small fraction may be bound to the lipid membrane.

The ICG fluorescence yield enhancement observed may be related to insertion of ICG within the hydrophobic domains of the lipid bilayer. In hydrophobic organic microenvironments such as methanol, the ICG fluorescence spectrum is reported to have photo and thermal stability (Holzer, Mauerer et al. 1998). However, the precise ICG-lipid binding configuration that leads to this stabilization is not clear nor is it known how deep ICG inserts into the lipid-nanoparticle. ICG vertical depth in lipid-nanoparticle could be elucidated by quenching ICG fluorescence with extramembranal iodide ions (KI) (Bronshtein, Afri et al. 2004), or by the parallax method where quenching of ICG is compared between two strategically placed quenchers at different known carbon positions of the lipid fatty acyl chains (Chattopadhyay and London 1987). Given the fluorescent enhancement that results from lipid-bound ICG, it is likely ICG inserts at a depth where its interaction with water, which quenches fluorescence and degrades ICG, is minimized. While it is possible that some regions of ICG may be accessible to water and aligned with the phosphate head group, it is clear that such interactions did not have a significant impact on the fluorescence yield of ICG. Regardless, ICG embedded in lipid-nanoparticles assumes a conformation that minimizes negative effects on fluorescence properties and the chemical degradation caused by

aqueous microenvironments (Saxena, Sadoqi et al. 2003), light, and heat (Holzer, Mauerer et al. 1998).

While it is clear that insertion into the lipid-nanoparticle enhances fluorescence, this enhancement is not unlimited. The non-linear relationship of fluorescence intensity per ICG versus lipid-ICG molar ratio (**Figure 3.3C**) is parabolic with the optimal 250:1 lipid-ICG molar ratio exhibiting peak fluorescence yield. The decrease in fluorescence yield to the right side of the vertex correlates with decreasing ICG density and amount of ICG available to emit fluorescence. As density of ICG in the lipid-nanoparticle increases, concentration-dependent quenching of ICG may become significant, leading to the observed decline at higher ICG-to-lipid ratios (or lower lipid-to-ICG ratios). Due to the significant overlap of the ICG excitation and emission spectra between about 780 and 820 nm (**Figure 3.3A**), ICG can undergo self-quenching at high concentrations. However, self-quenching through molecular collision-dependent quenching is unlikely for two reasons—first, ICG is immobilized in lipid-nanoparticles and does not easily collide with other ICG molecules, and second, the experimental concentrations of ICG (40-200 μM ICG in methanol, 0.1-2.0 μM ICG in aqueous solution) were well below those reported to induce ICG aggregates (dimers). In water, ICG forms dimers at concentrations around 5 μM (Baker 1966, Li, Beauvoit et al. 1995, Philip, Penzkofer et al. 1996, Rajagopalan, Uetrecht et al. 2000), and in methanol, ICG forms dimers above 4.2 mM (Philip, Penzkofer et al. 1996). There may be other molecular interactions that need to be explored further to address the discrepancies. Such studies, however, are beyond the scope of this report.

In addition to optimizing the formulation of lipid-nanoparticle ICG to achieve maximal fluorescence yield, stability against environmental effects is also necessary. Light causes ICG to produce singlet oxygen that chemically decomposes ICG through a dioxetane reaction (the polymethine chain of ICG cleaves into two carbonyl products, which may be cytotoxic) (Holzer, Mauerer et al. 1998, Engel, Schraml et al. 2008). With clinical settings and surgical fields normally well lit, such light decomposition is challenging to avoid. In its currently supplied form, free ICG in aqueous solution decomposes from light in a matter of seconds. Our results show that incorporation of ICG into lipid-nanoparticles shields against light degradation. Lipid-nanoparticle ICG can be exposed to light for several hours at room temperature and retain nearly all of its original fluorescence intensity (**Figure 3.5**). To our knowledge, this is the first report of light stability for lipid-bound ICG, and the mechanism for such stability remains to be explored. When stored in the dark at 4°C in aqueous suspension, lipid-nanoparticle ICG maintains fluorescence integrity for at least eight months (**Table 3.1**). This exceeds other reports of 42-days at room temperature (Proulx, Luciani et al. 2010) and 70-days at 4°C (Sandanaraj, Gremlich et al. 2010). Further stabilization of lipid-nanoparticle ICG could be achieved by lyophilization with a cryoprotectant such as trehalose or sucrose that retains the particle characteristics upon hydration with water. Lipid-bound ICG appeared to be stable in serum as lipid-nanoparticle ICG exposed to 10% heat-inactivated rat serum for six hours retained 94 ± 0.6% of initial ICG fluorescence. Taken together, the observed light, storage, and serum stability indicate lipid-nanoparticle ICG has robust stability for clinical use, especially for imaging the lymphatic system where lymph contains lower serum protein content than blood.

The advantage of NIR fluorescence for biological imaging arises from the minimal autofluorescence of deoxy- and oxyhemoglobin, lipid, and water in the 700-900 nm range. This range is known as the NIR or therapeutic window, and ICG, with its 820 nm emission, is the only FDA- and EMA-approved fluorophore for human use to leverage this property. At the time of writing this paper, at least ten other groups have developed liposomes with ICG incorporated (Sandanaraj, Gremlich et al. 2010, Hua, Gross et al. 2012, Zanganeh, Xu et al. 2013, Murata, Tahara et al. 2014), encapsulated (Proulx, Luciani et al. 2010, Suganami, Toyota et al. 2012, Turner, Moshkelani et al. 2012, Zhuang, Ma et al. 2012, Jeong, Lee et al. 2013), or adsorbed (Portnoy, Lecht et al. 2011) with lipid membranes of various compositions and physiochemical properties for *in vivo* NIR optical imaging. The polar head group of a lipid affects the particle surface charge and degree of hydration, which impacts the level of *in vivo* opsonization and complement binding that induces clearance, and the amount of saturation and chain length of the lipid fatty acyl tails affect the lipid phase transition temperature (T_c) through altering the rigidity, thickness, and uniformity of the lipid bilayer (Kraft, Freeling et al. 2014). Therefore, each variable not only may impact the stability and interactions between ICG and lipid, but also the *in vivo* behavior of the particles.

In summary, taking advantage of the ability of ICG to incorporate completely and stably into lipid-nanoparticles and understanding ICG-lipid interactions, we developed lipid-nanoparticle ICG that maximizes ICG fluorescence intensity and stability. These scalable particles are designed to exhibit physiochemical characteristics suitable for *in vivo* imaging as demonstrated with NIR visualization of lymph nodes. Unlike that of free ICG, due to the physiochemical characteristics of subcutaneously given lipid-bound ICG, lipid-nanoparticle ICG predominantly localizes and

distributes within the lymphatics without initial distribution through the blood. Lipid-nanoparticle ICG could be further developed with surface ligands or antibodies to target to diseased cells and tissues in the lymphatic system not only to visualize these cells, but also this lipid-nanoparticle platform may be used to deliver therapeutics. With high storage and light stability, fluorescence intensity, and lymph node imaging resolution compared to that of free ICG, lipid-bound ICG could provide additional medical diagnostic value with NIR optical imaging for early intervention of lymphatic abnormalities.

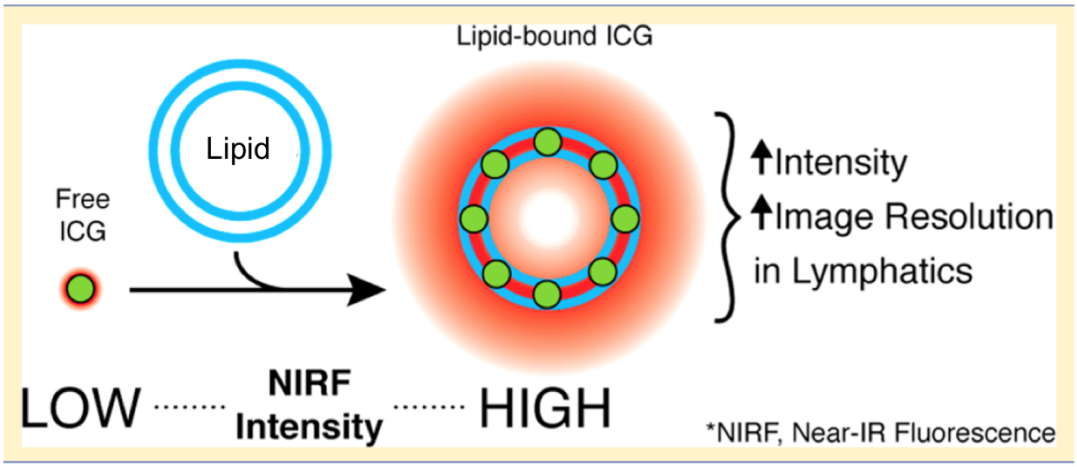

Figure 3.0. Graphical abstract.

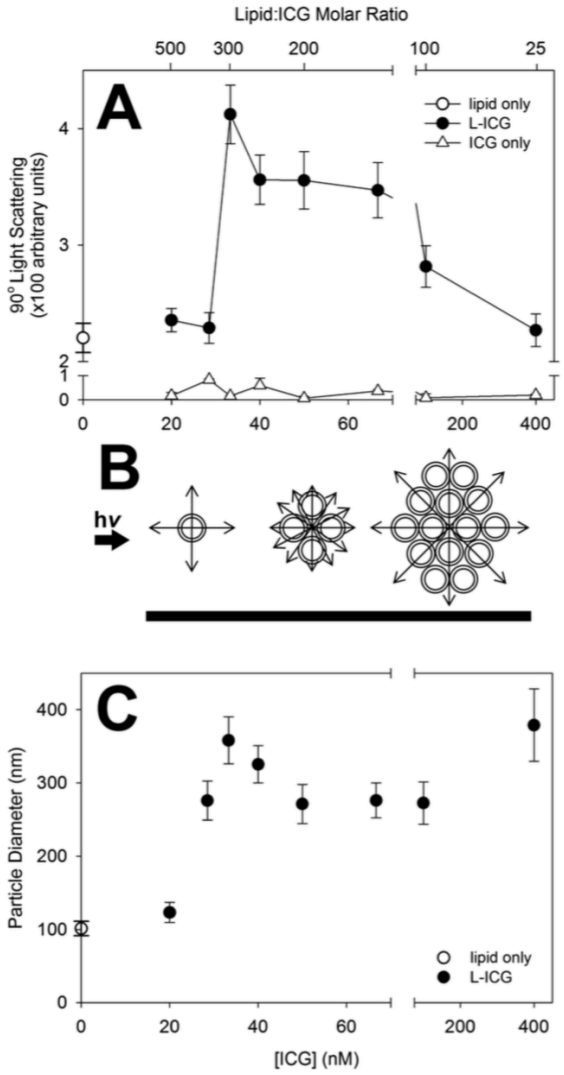

Figure 3.1. ICG concentration-dependent lipid-nanoparticle aggregation and apparent size increase.

Panel A: The effect of ICG concentrations on 90° light scattering intensity of lipid-nanoparticles. A fixed concentration of lipid-nanoparticles was incubated with varying ICG concentrations in a fixed volume. At 20 minutes, mixtures were diluted to stop the reaction and 90° light scattering intensity was measured with a fluorometer as described in Experimental Procedures. Open circle symbol indicates empty lipid only lipid-nanoparticles, closed circle symbol indicates lipid-bound ICG (L-ICG), and open triangle symbol indicates free ICG only. Each data point is the mean ± SD of ten replicates. **Panel B**: Schematic drawing of light scattering efficiency detected by the photomultiplier tube (PMT; bold horizontal bar) 90° to the incident light (hν) path as lipid-nanoparticles aggregate and increase the particle size diameter. **Panel C**: The effect of ICG concentrations on particle size analysis by photon correlation spectroscopy of lipid-nanoparticles. Following collection of Panel A data, particle size analysis was performed as described in Experimental Procedures. Open circle symbol indicates empty lipid only lipid-nanoparticles and closed circle symbol indicates lipid-bound ICG (L-ICG). Each data point is the mean ± SD result from digital autocorrelation calculations following eight minutes of data collection.

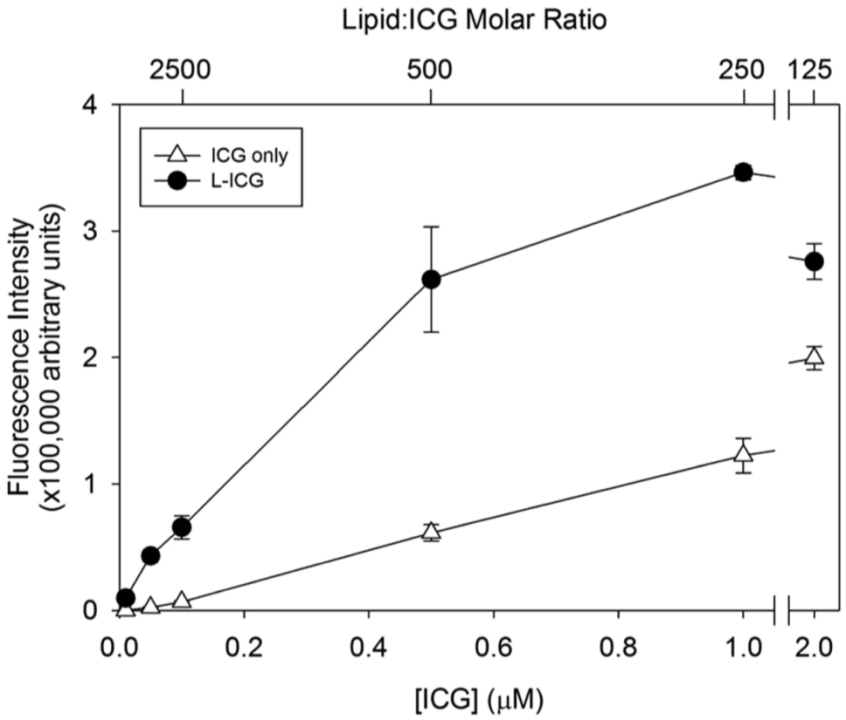

Figure 3.2. Increased fluorescence intensity of lipid-associated ICG.

A fixed concentration of lipid-nanoparticles was incubated with varying ICG concentrations in a fixed volume. At 20 minutes, mixtures were diluted 20-fold with buffered solution to stop the reaction and fluorescence intensity was measured with a fluorometer as described in Experimental Procedures. Open triangle symbol indicates free ICG only and closed circle symbol indicates lipid-bound ICG (L-ICG). Each data point is the mean ± SD of eight replicates.

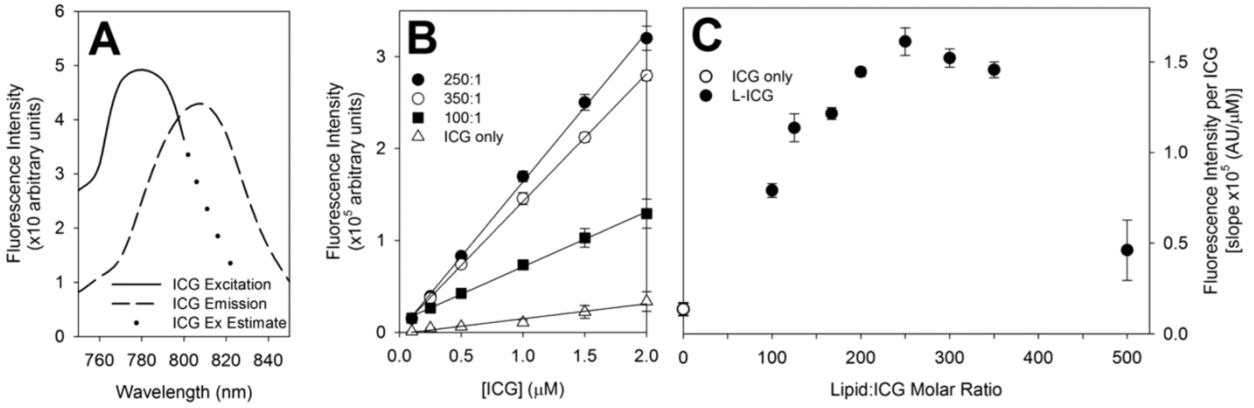

Figure 3.3. Optimization of lipid-ICG molar ratio to maximize ICG fluorescence yield.

Panel A: Excitation (solid line) and emission (dashed line) spectra of ICG in aqueous buffer. The dotted line extending the excitation spectra solid line is an estimate based on Reference 3.[3] **Panel B**: Effects of lipid-ICG molar ratio on the ICG fluorescence yield (fluorescence intensity/μM ICG). Lipid-bound ICG with varying lipid-ICG molar ratios were prepared and their fluorescence intensity per unit ICG was measured at indicated concentrations. Only three of eight lipid-nanoparticle ICG formulations are presented for clarity; their data points are labeled according to their lipid-ICG molar ratio. Closed circle symbol indicates 250:1 lipid-ICG, open circle symbol indicates 350:1 lipid-ICG, closed square symbol indicates 100:1 lipid-ICG, and open triangle symbol indicates ICG only. Each fluorescence intensity data point is the mean ± SD of eight replicates. **Panel C**: Effects of lipid-ICG molar ratio on fluorescence yield. The data from Panel B were used to calculate the slope (fluorescence intensity/μM ICG) and plotted against the lipid-ICG molar ratio. Open circle symbol indicates free ICG only, closed circle symbol indicates lipid-bound ICG (L-ICG) in lipid-nanoparticles of varying molar ratios. Each data point is the mean ± SD of six replicates.

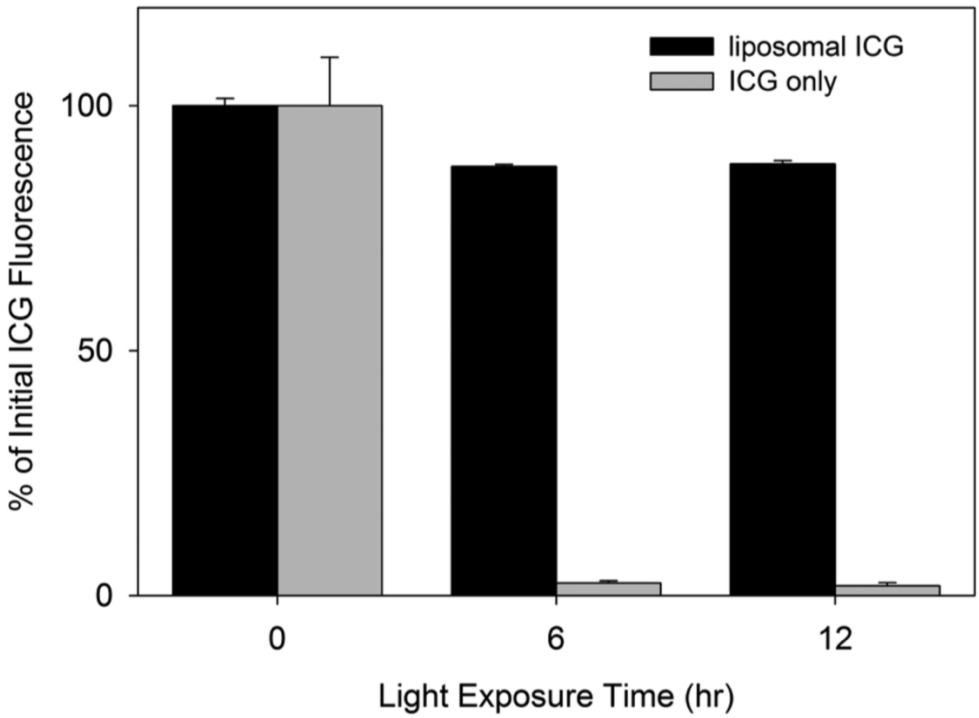

Figure 3.4. Lipid-bound ICG in lipid-nanoparticles reduces ICG fluorescence quenching due to light exposure.

Lipid-nanoparticle ICG and free ICG were exposed to overhead fluorescent light for 12 hours. ICG fluorescence was recorded at six- and 12-hours as described in Experimental Procedures. Black bars represent lipid-nanoparticle ICG and grey bars represent ICG only. Each data point is the mean ± SD of eight replicates.

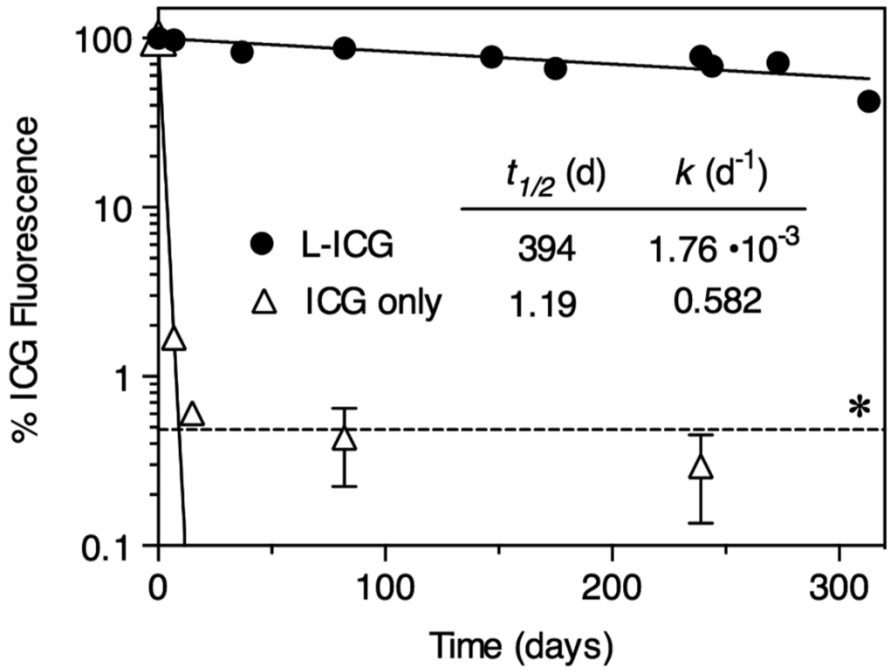

Figure 3.5. Stability of lipid-bound ICG in storage.

Lipid-bound ICG in lipid-nanoparticles and free ICG were stored in the dark at 4ºC for up to 313 days and ICG fluorescence was analyzed at indicated time points. Open triangle symbol represents free ICG, and closed circle symbol represents lipid-bound ICG (L-ICG). The time-course data were analyzed based on an exponential decay model and the half-life, $t_{1/2}$ (days), and rate constant, k (days^{-1}), values are listed. *Dashed line indicates limit of detection. Each data point is the mean ± SD of three to eight replicates.

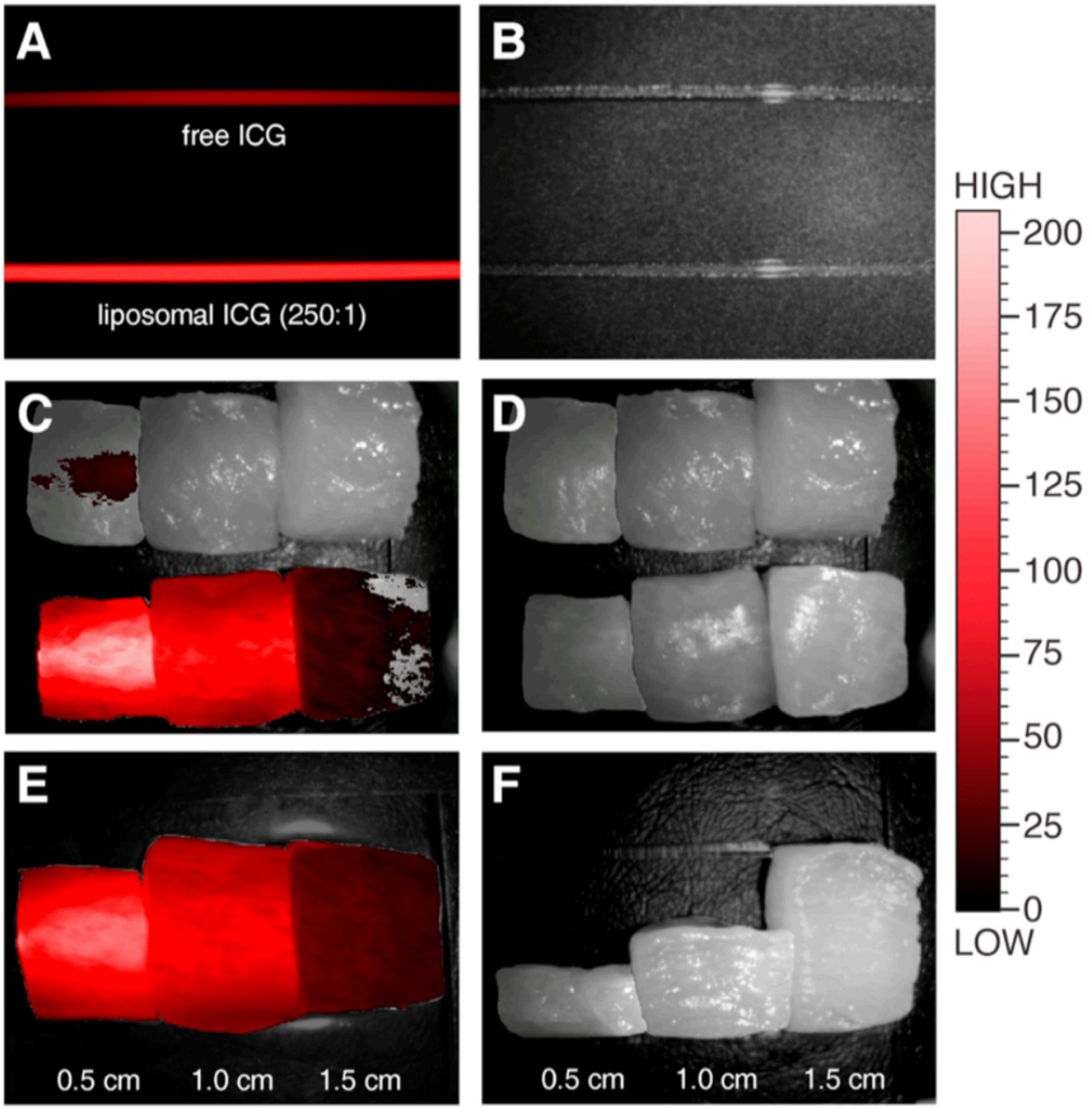

Figure 3.6. Fluorescence intensity of lipid-bound versus free ICG detected through muscle tissue.

NIR fluorescence image intensity of capillary tubes filled with 30 μM free ICG (top) and lipid-bound ICG (bottom). **Panel B**: White light image of the two identical capillary tubes filled with different formulations of ICG in Panel A. **Panel C**: NIR fluorescence image overlaid on visual light photograph of capillaries filled with free (top) or lipid-bound (bottom) ICG and placed underneath 0.5, 1.0, and 1.5 cm (left to right) chicken breast tissue cuboids. **Panel D**: Visible light image of chicken breast tissue cuboids in Panel C. **Panel E**: NIR fluorescence image overlaid on visual light background of lipid-bound ICG capillary placed underneath 0.5, 1.0, and 1.5 cm chicken breast tissue cuboids. **Panel F**: A side view of tissue cuboid thickness.

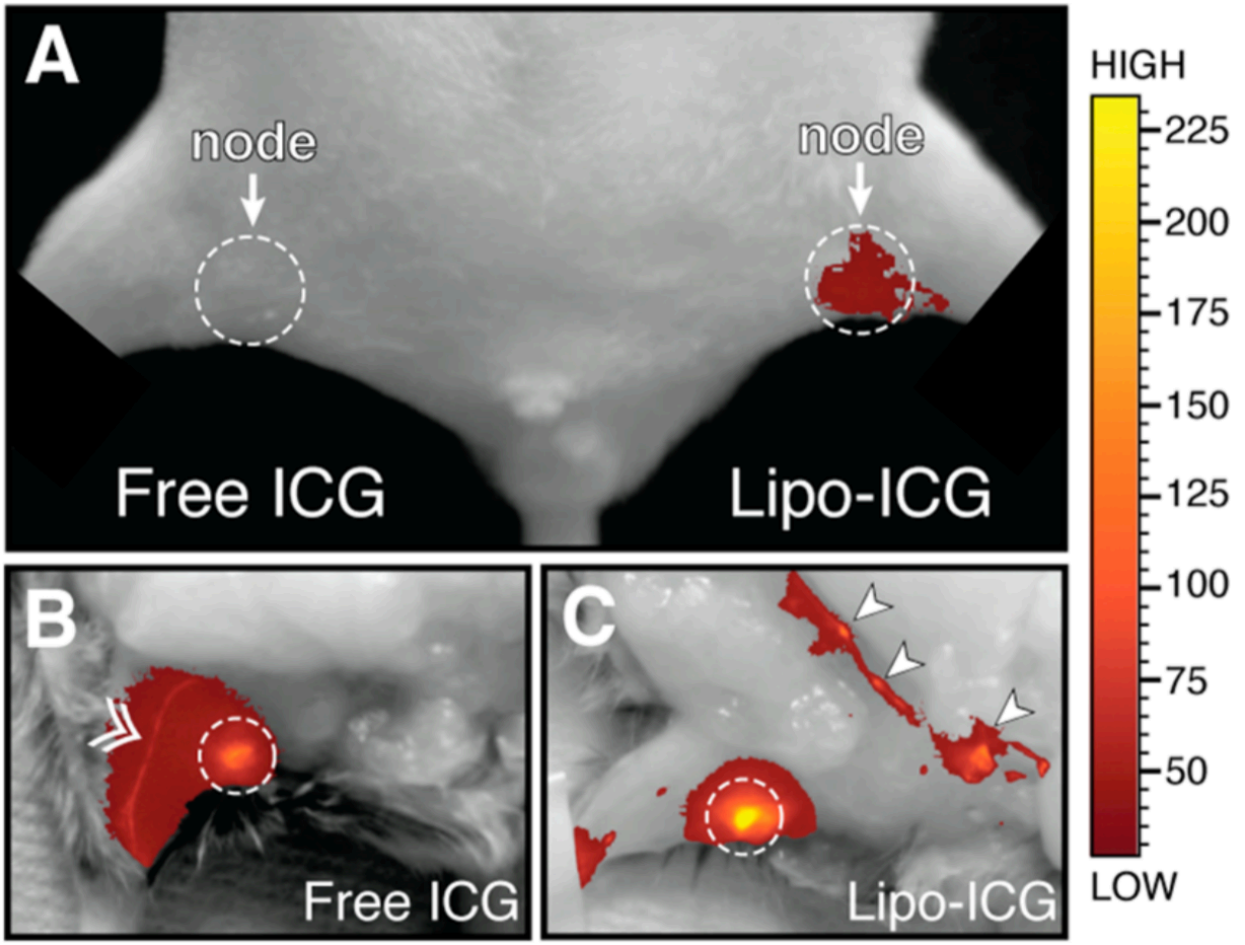

Figure 3.7. Comparison of lipid-bound ICG and free ICG NIR image behavior in mice after subcutaneous injection.

Lipid-bound ICG in lipid-nanoparticles (Lipo-ICG; left foot) or free ICG (right foot) were subcutaneously injected and NIR fluorescence image was collected at six minutes. Fluorescence image is overlaid on visual light photograph for anatomical representation. Dashed circle indicates the local popliteal node. Mouse is viewed in supine position. In another set of mice treated only with free (**Panel B**) or lipid-bound (**Panel C**) ICG for six minutes, the skin was removed and analyzed further. **Panel B**: Visible light photograph is the image collected of the right leg of a mouse treated with free ICG in its right foot. Corresponding fluorescence image is overlaid. Double arrow (>>) indicates saphenous vein where free ICG appears to diffuse throughout the muscle tissue and the popliteal lymph node (dashed circle). Mouse is viewed in supine position. **Panel C**: Visible light photograph is the image collected of the right leg of a mouse treated with lipid-bound ICG in its right foot. Corresponding fluorescence image is overlaid. Dashed circle indicates popliteal lymph node and bold arrowheads indicate ventral pelvic and genital/regional lymph nodes. Mouse is viewed in supine position.

Table 3.1. Storage stability kinetics.[a]

	% ICG Fluorescence[b] (8 months)	$t_{1/2}$ (days)	k (10^{-3} days^{-1})
Lipid-nanoparticle ICG[c]	78.2 ± 2.8	394 (360, 434)	1.76 (1.60, 1.93)
Free ICG[d]	0.3 ± 0.2	1.19 (1.14, 1.25)	582 (554, 609)

[a] Stored in dark at 4°C.
[b] Mean ± SD of samples (N=2 each) stored for eight months.
[c] $t_{1/2}$ (95% CI) and k (95% CI) calculated from multiple time points (N=10) over 313 days.
[d] $t_{1/2}$ (95% CI) and k (95% CI) calculated from multiple time points (N=5) over 239 days.

Chapter 4. **Elucidation of DcNP Targeting and Retention in Lymph Nodes Enabled by ICG-Labeled DcNPs**

Chapter 4 was published

in

Journal of Drug Targeting. 2018;Feb 12:1-11.

4.1 ABSTRACT

The distributed network of lymph vessels and nodes in the body, with its complex architecture and physiology, presents a major challenge for whole-body lymphatic-targeted drug delivery. To gather physiological and pathological information of the lymphatics, near-infrared (NIR) fluorescence imaging of NIR fluorophores is used in clinical practice due to its tissue-penetrating optical radiation (700-900 nm) that safely provides real-time high-resolution *in vivo* images. However, indocyanine green (ICG), a common clinical NIR fluorophore, is unstable in aqueous environments and under light exposure, and its poor lymphatic distribution and retention limits its use as a NIR lymphatic tracer. To address this, we investigated in mice the distribution pathways of a novel nanoparticle formulation that stabilizes ICG and is optimized for lymphatic drug delivery. From the subcutaneous space, ICG particles provided selective lymphatic uptake, lymph vessel and node retention, and extensive first-pass lymphatic distribution of ICG, enabling 0.2 mm and 5-to-10 cell resolution of lymph vessels, and high signal-to-background ratios for lymphatic vessel and node networks. Soluble (free) ICG readily dissipated from lymph vessels local to the injection site and absorbed into the blood. These unique characteristics of ICG particles could enable mechanistic studies of the lymphatics and diagnosis of lymphatic abnormalities.

4.2 INTRODUCTION

The lymphatic vasculature is a distributed, whole-body network of vessels and nodes that converges toward the thoracic duct, which runs ventrally up the spine in the thoracic cavity. While blood capillaries deliver oxygen and nutrients to cells via the interstitial space, most of the interstitial fluid and its solutes are drained by lymphatic capillaries rather than being reabsorbed into the blood through venous capillaries (Levick and Michel 2010). As a whole, the lymphatic system is central to fluid homeostasis, immune function, fat absorption in the gut, reverse cholesterol transport, and disease (Trevaskis, Kaminskas et al. 2015). Blockages of lymph drainage and flow (e.g., due to surgical interventions such as mastectomy) can lead to peripheral edema (lymphedema), which afflicts 4% of the world's population (Ruddle 2014). Moreover, cancer and microbes exploit and block lymphatic pathways (Alitalo 2011), and HIV infects cells of lymph nodes (LNs) throughout the body (Estes 2013). Despite the prevalence of occluded lymph flow and the lymphatic system being central to devastating diseases, there exists a gap in our ability to safely and efficiently visualize in detail and deliver drug to the extensive and distributed network of lymph vessels and nodes in the body. This is largely because current imaging and drug targeting agents do not widely distribute through and are not sufficiently retained within lymph vessels, nodes, and overall lymphatic networks.

It is now becoming appreciated that small molecules in the systemic blood circulation have difficulty penetrating into and being retained in lymph nodes throughout the body. As a result, subcutaneous (SC) injection as opposed to intravenous (IV) or oral (PO) dosing has been leveraged to transiently increase small molecule drug levels in lymph nodes (Chen, Wang et al. 2004), however, these elevated drug levels rarely persist for extended durations. In 2003, we first

hypothesized and verified (Kinman, Brodie et al. 2003), and others recently confirmed in prospective clinical studies (Fletcher, Staskus et al. 2014, Lorenzo-Redondo, Fryer et al. 2016, Lee, Hatano et al. 2017), that orally dosed antiretroviral small molecule drug combinations fail to maintain sufficient lymph node levels (Freeling and Ho 2014). To overcome this insufficiency of small drug molecules in lymph nodes, our laboratory has developed a novel nanoparticle platform that enables targeted localization of drug combinations in lymph nodes. We found that multiple drugs formulated in this nanoparticle platform are not only capable of distributing widely to lymph nodes throughout the body, but also provide exposure in cells of lymph nodes and the blood for an extended time. Thus, long-acting delivery of small molecule drug combinations (containing three or more hydrophilic and hydrophobic drugs) to lymph nodes throughout the body is feasible (Freeling and Ho 2014, Freeling, Koehn et al. 2014, Kraft, McConnachie et al. 2017).

Recently, we leveraged this nanoparticle platform with its unique formulation and preparation methods to stabilize the near-infrared (NIR) fluorophore indocyanine green (ICG) (Kraft and Ho 2014). NIR fluorescence imaging using non-ionizing 700-900 nm optical radiation affords real-time in vivo imaging with high resolution and tissue penetration due to reduced photon scattering, light absorption, and autofluorescence of biological tissues (Frangioni 2003), and is an emerging technology in clinical practice (Nguyen and Tsien 2013). The unique ICG particles we developed maximally boost the ICG fluorescence emission intensity (Kraft and Ho 2014) with a formulation optimized for widespread lymphatic distribution following subcutaneous (SC) administration (Kinman, Bui et al. 2006, Freeling and Ho 2014). The *in vivo* stability of these particles minimizes the rapid release of free ICG, which reduces the likelihood of potential off-target toxicities. Moreover, reduction of free ICG improves the signal-to-noise ratio as the presence

of free ICG, which binds nonspecifically to interstitial and tissue proteins, and contributes to background fluorescence signal. Injectable NIR protein- and nanoparticle-based lymphatic tracers have been reported (Davies-Venn, Angermiller et al. 2012, Proulx, Luciani et al. 2013), and free ICG is commonly used off-label in the clinic for lymphatic visualization and sentinel lymph node dissection (Polom, Murawa et al. 2011). However, in preclinical models (Davies-Venn, Angermiller et al. 2012, Proulx, Luciani et al. 2013) and humans (Burrows, Gonzalez-Garay et al. 2013), these agents, including those reported for nanoparticle and liposome formulations, dissipate quickly from lymph vessels and nodes near the injection site and do not provide sufficient detail of lymph vessel and node networks (Xie, Xin et al. 2017). Moreover, studies show radiotracers such as subcutaneously administered ^{99m}Tc and blue dyes readily diffuse out of lymph vessels and deposit into nearby tissues or enter the blood (Zhang, Niu et al. 2011, Smedley, Turkbey et al. 2014). As a result, blue dye tracers may leave tattoos for months, and furthermore, they carry a risk of skin necrosis and anaphylaxis (Verbeek, Troyan et al. 2014).

We hypothesized that these limitations of current lymphatic imaging agents may be largely overcome if our novel ICG particles enabled widespread lymphatic distribution and retention of ICG specifically within lymph vessels and nodes. In this report, we show that following subcutaneous administration in mice, ICG particles provided selective lymphatic uptake, lymph vessel and node retention, and extensive first-pass lymphatic distribution of ICG, enabling 0.2 mm and 5-to-10 cell resolution of lymph vessels, and high signal-to-background ratios for lymphatic vessel and node networks. Soluble (free) ICG readily dissipated from lymph vessels local to the injection site and absorbed into the blood. Due to the widespread lymphatic distribution and retention of ICG particles, coupled with the maximally enhanced ICG fluorescence quantum yield,

the safety of ICG and the nanoparticle formulation, as well as the convenience and cost-effectiveness of NIR imaging, these novel ICG particles are likely a useful tool for assessing lymphatic anatomy and function.

4.3 Materials and Methods

4.3.1 *Reagents*

Phospholipids 1,2-distearoyl-sn-glycero-3-phosphocholine (DSPC) and 1,2-distearoyl-sn-glycero-3-phosphoethanolamine-N- methoxy-polyethylene glycol-2000 (DSPE-mPEG$_{2000}$) were purchased from Avanti Polar Lipids (Alabaster, AL). Indocyanine green (ICG, $C_{43}H_{47}N_2NaO_6S_2$, sodium 2-[7-[3,3-dimethyl-1-(4-sulfonatobutyl)benz[e]indolin- 2-ylidene]hepta-1,3,5-trien-1-yl]-3,3-dimethyl-1-(4- sulfonatobutyl)benz) was purchased from Sigma-Aldrich (St. Louis, MO). Qtracker 800 non-targeted quantum dots (PEGylated, ~20 nm diameter) were purchased from Invitrogen (Q21071MP, Molecular Probes; Eugene, OR). Other reagents were analytical grade or higher.

4.3.2 *Optical Imaging*

Methods described previously were used to prepare ~60 nm ICG nanoparticles (ICG particles) where ICG molecules are complexed and stabilized by lipid excipients DSPC and DSPE-mPEG$_{2000}$ (Kraft and Ho 2014). Free ICG was prepared in saline with 8% (v/v) DMSO. All animal procedures complied with and were approved by the University of Washington Institutional Animal Care and Use Committee. Male and female two- to 24-month old C57BL/6 mice were used, originally obtained from Charles River Laboratories (Wilmington, MA). Mice were kept

under pathogen-free conditions, exposed to a 12 h light/dark cycle, and received food *ad libitum* prior to imaging. Mice were anesthetized with 1.5% isoflurane, shaved to remove fur, and placed on a 37°C platform in an IVIS Lumina II (Caliper Life Sciences, PerkinElmer; Waltham, MA). IVIS imaging settings were: fluorescence, 3 sec exposure (except 0.5 sec exposure for **Figure 4.1** data only), small binning, 2 F/stop, Ex/Em 745/ICG (for ICG) and 570/ICG (For QD800). 25-40 µL of ICG particles or free ICG in buffered saline or 25 µL of QD800 in PBS were injected subcutaneously (SC) into the top (dorsum) of hind feet to avoid the medial tarsal and lateral marginal blood vessels (0.5 nmol ICG/foot; 5 pmol QD800/foot). QD800 dose is equivalent to ICG particle dose at ~100 ICG molecules/particle. For the plasma pharmacokinetic study, mice were injected SC in the inner hind left leg about 0.5 cm above the ankle with 400 µM ICG solutions of free ICG or ICG particles at a dose of 3.0 mg/kg. Whole blood was collected via cardiac puncture at terminal time points (2.5 and 5 min), placed into K2 EDTA (7.2 mg) vacutainer tubes, before isolating plasma by centrifuging at 2,348 g (5,000 rpm) for 10 min and storing at -80ºC. Room temperature whole plasma samples were measured for ICG fluorescence intensity using a fluorescence plate reader [Victor3 V 1420-040 Multilabel Plate Reader (PerkinElmer, Waltham, MA) with a tungsten−halogen continuous wave lamp (75 W, spectral range of 320−800 nm) and excitation (769 ± 41 nm) and emission (832 ± 37 nm) filters (Semrock, Rochester, NY) using 100 µL of sample in flat bottom, untreated 96-well plates (Grenier Bio-one, Monroe, NC)]. Plasma ICG fluorescence intensity was converted into plasma ICG concentration (ng/mL) using standard curves of blank neat plasma spiked with fresh free ICG or ICG particles. All mice tolerated the injections well and were monitored for respiratory rate and heart rate. No changes related to the injections were observed. Experiments were performed with at least three independent replicates (specified in figure legends). Data collection methods were predetermined for all experiments, and

animals were assigned randomly to treatment groups. No outliers were excluded. For region of interest (ROI) analysis of the foot injection site (**Figure 4.1B**) and of lymph nodes and the thoracic lymph duct (**Figure 4.3C-4.3E**), 0.401 cm^2 and 0.441 cm^2 circles were used, respectively, to collect Total Efficiency (a.u.) values using Living Image 4.5 (Caliper Life Sciences, PerkinElmer; Waltham, MA).

4.3.3 *Immunohistochemistry*

Podoplanin: The University of Washington's Histology and Imaging Core performed the immunohistochemistry optimization and staining for podoplanin, using syrian hamster polyclonal anti-mouse podoplanin (1:250 dilution; BioLegend, catalog number 127402). We used 5 μm thick formalin-fixed paraffin-embedded sections for the staining. First, the slides were baked for 30 minutes at 60°C and deparaffinized on the Leica Bond Automated Immunostainer (Leica Microsystems, Buffalo Grove, IL). Antigen Retrieval was performed with citrate buffer, pH 6.0, at 100°C for 20 minutes. All subsequent steps were performed at room temperature. Blocking consisted of Leica peroxide block for 5 minutes. Additional blocking was performed with 10% normal donkey serum (Jackson ImmunoResearch Laboratories, catalog number 017-000-121) in tris-buffered saline (TBS) for 20 minutes. The primary antibody, podoplanin, was diluted in Leica Primary Antibody Diluent and was applied for 30 minutes. A peroxidase-conjugated secondary antibody, goat anti-syrian hamster IgG (1:500 dilution; Jackson ImmunoResearch Laboratories, Inc., catalog number 107-035-142) in 5% normal donkey serum and TBS for 30 minutes was applied. Antibody complexes were visualized using Leica Bond Mixed Refine (DAB, 3,3'-diaminobenzidine) detection 2X for 10 minutes. Tissues were counterstained with hematoxylin for 4 minutes followed by two rinses in water and dehydrated through graded alcohol to xylene. Slides

were mounted with a synthetic mounting media. Slides were imaged using a Nikon Eclipse 90i automated microscope and a 20X objective lens. Unless otherwise specified all reagents were obtained from Leica Microsystems.

4.3.4 *Statistical Analysis*

Statistical analyses were performed with GraphPad Prism (GraphPad Software, Inc., La Jolla, CA). All statistical comparisons were performed with the two-tailed *t*-tests with significance probability α set at 0.05.

4.4 RESULTS

4.4.1 *Small Molecule vs. Nanoparticle Uptake and Distribution*

In a preliminary study, we observed soluble ICG (free ICG) in the SC space readily distributed equally well into lymph and blood vessels while ICG bound to novel nanoparticles (ICG particles) preferentially distributed to lymph but not blood vessels. Unlike free ICG, which readily redistributed to adjacent tissues and blood capillaries, the fraction of ICG particles in lymph vessels was retained without leaking into neighboring tissues. Thus, to characterize the differential uptake and distribution of free ICG versus ICG particles, equal doses of free ICG and lipid-bound ICG were injected SC in the dorsal foot of mice and NIR fluorescence imaging over the skin was performed at 5, 30, and 60 min. As a control, we compared these results with quantum dot nanoparticles (QDs) that emit NIR wavelengths similar to those of ICG and have the same PEGylated exposed surface as ICG particles (**Figure 4.1A, 4.1B**). Rapid clearance of ICG particles from the SC site is detectable as a steep rate of decline in NIR intensity, while NIR intensity

increased in mice treated with free ICG (k = -2.07 vs. +1.41 x 10-2 min-1) (**Figure 4.1B**). This increased NIR intensity for free ICG is due to nonspecific protein binding of soluble ICG in the interstitial space and nearby tissues (Hong, Antaris et al. 2017), instead of draining into blood or lymph vessels. In mice treated with the smaller QDs (~20 nm vs. ~60 nm ICG particles), QDs cleared from the SC injection sites at a much slower rate (k = -1.01 x 10-2 min-1) than ICG particles (**Figure 4.1B**), verifying the unique property of these ICG particles to rapidly clear from the SC space and distribute into lymph vessels.

4.4.2 *Differential Lymphatic and Blood Distribution of Free ICG vs. ICG Particles*

We then followed the movement of free ICG and ICG particles from the SC foot injection site to the nearby tissue in the mouse hind leg. To differentiate the distribution of free vs. nanoparticle-bound ICG into blood, adjacent tissue, and lymph, mice were dosed SC with free ICG or ICG particles in the dorsal foot and detailed ICG distribution was analyzed. ICG appeared in the blood (saphenous vein) and nearby tissue more extensively in mice treated with free ICG (**Figure 4.2A-C, 4.2G**) than with ICG particles, which remained localized to the popliteal LN (**Figure 4.2D-F, 4.2H, 4.2I**). Mice with ICG particles in their popliteal LN did not have ICG in the nearby saphenous vein (**Figure 4.2D-F, 4.2H**) and the vessel connecting the popliteal and sciatic LNs was clearly delineated (**Figure 4.2I**). To further verify the extent that free ICG and ICG particles enter the blood from the SC space, we measured the plasma ICG concentration in mice following a 3.0 mg/kg dose of ICG given as free ICG or ICG particles, soon after drug administration. As shown in **Table 4.1**, ICG concentrations were significantly higher in plasma at early time points following free ICG dosing than after dosing ICG particles. These data suggest that ICG particles given SC remain in and distribute via the lymphatics (vessels and nodes) with

minimal dissociation (or release of ICG from particles) without entering blood vessels as free ICG; whereas free ICG can readily enter the blood circulation from the SC space and may leak out of the lymphatics and enter nearby tissues and blood. Such movement of ICG solute in and out of lymph vessels would greatly diminish the signal resolution (due to increased background fluorescence in nearby tissue) and the distribution of ICG throughout the lymphatics, which in turn would reduce the ability to target ICG specifically to the extensive network of lymph vessels and nodes.

4.4.3 *Extensive Distribution and Retention of ICG Particles in the Lymphatic System*

To visualize the whole-body lymphatic distribution of free ICG and ICG particles after a single SC dose in mice, we systematically analyzed the ICG fluorescence intensity in the mouse lymphatic network that drains the right hind foot at 1, 5, and 30 min following SC injection. As shown in **Figure 4.3A**, free ICG was visualized only in the lower part of the mouse lymphatic system (popliteal LN, sciatic LN, medial iliac LN, and lumbar LN) at 30 min, whereas with ICG particles, this lower lymphatic portion was clearly visualized at 1 min post-injection, and the thoracic duct was clearly visualized at 5 min post-injection (**Figure 4.3B**). At 30 min post-injection, the signal from ICG particles detailing the lymphatic network did not readily fade from the signal previously observed at 5 min (**Figure 4.3B**), suggesting ICG particles are retained within the lymph vessels and nodes and do not readily leak out into nearby tissue and blood vessels. Thus, downstream lymph vessels, nodes, and the thoracic duct maintain signal and continue to exhibit higher ICG fluorescence signal over time. At 72 hr, ICG fluorescence was still observed in lymph nodes following ICG particle dosing while no lymph node fluorescence signal following free ICG dosing was detected (data not shown).

To quantify the differences in lymphatic exposure to ICG after SC dosing of free ICG or ICG particles, we measured the ICG fluorescence intensity at different locations along the mouse lymphatic system at each of the three post-injection time points (1, 5, 30 min). The structures in the lymphatics that were assayed, with their approximate distances away from the right hind foot SC injection site, are as follows: popliteal LN (2 cm), sciatic LN (2.5 cm), medial iliac LN (3.8 cm), lumbar LN (5.4 cm), inferior thoracic lymph duct (5.7 cm), medial thoracic lymph duct (6.5 cm), and superior thoracic lymph duct (7.3 cm). The ICG fluorescence intensities at each of these lymphatic structures at 1, 5, and 30 min following free ICG and ICG particle dosing are shown in **Figure 4.3C-4.3E**. For ICG particles, ICG fluorescence was consistently highest in all of these lymphatic structures at all three time points (**Figure 4.3C-4.3E**). The drop in the fluorescence intensity in the sciatic LN (2.5 cm from the SC injection site) for both free ICG and ICG particles (**Figure 4.3C-4.3E**) is due to the sciatic LN being deeper within muscle tissue and relatively small in volume compared to the other lymphatic structures analyzed. These data confirm ICG particles enable more rapid distribution of ICG throughout the lymphatic system and promote more extensive lymphatic retention of ICG and exposure to ICG than the soluble formulation of ICG.

4.4.4 *Ability of ICG Particles to Verify Small and Abnormal Lymph Vessels*

Leveraging the ability of ICG particles to be retained in lymph vessels with minimal penetration into nearby tissues (**Figure 4.2, 4.3**), as well as undergo extensive lymphatic first-passage throughout the lymphatic network of vessels and nodes following SC administration (**Figure 4.3**), we determined if the small lymph vessel connecting the subiliac and axillary LNs could be visualized. As schematically presented in **Figure 4.1C** and 4.**4A insert**, ICG particles

clearly delineated this lymph vessel adjacent to blood vessels, which were devoid of ICG signal (**Figure 4.4A**). This small mouse lymph vessel is estimated to be ~0.2 mm in diameter (**Figure 4.4A**). This lymph vessel was not visible in mice treated with control free ICG. In addition, the high degree of lymphatic resolution from ICG particles detected a lymph vessel abnormality in a 23-month old mouse that was resolved down to a level of approximately 5-to-10 cells in two dimensions via histopathology (**Figure 4.4B**). This abnormality was verified by histopathology to be an enlarged lymph vessel with significant perivascular mononuclear cell infiltrations (**Figure 4.4B insert**). Collectively, these data verify that ICG particles rapidly clear from the SC space, are preferentially taken up into the lymphatics from the SC space, and undergo widespread distribution and retention within the lymphatic system throughout the body prior to entering the blood at the lymph-blood anastomoses near the heart. These properties enabled delineation of small normal and lesioned lymph vessels.

4.5 DISCUSSION

Unlike the free and soluble ICG counterpart, ICG particles exhibited rapid lymphatic uptake, retention, and widespread distribution through the body within the lymphatic path between the foot SC injection site and the entry into the blood circulation by the heart (**Figure 4.1-4.4A**). These ICG particles, likely due to the stable association of ICG to the particles, provided a high signal-to-noise ratio as a result of low surrounding tissue and blood background fluorescence signal, which enabled detection of a 0.2 mm thin and long lymph vessel connecting the subiliac and axillary LNs (**Figure 4.4A**). The high-resolution NIR imaging enabled by ICG particles also allowed detection of abnormal lymph vessels down to a resolution confirmed by histopathology to be approximately 5-to-10 cells (**Figure 4.4B**).

The detailed mechanisms of differential free/soluble vs. nanoparticle ICG distribution from the SC space and the subsequent widespread lymphatic distribution and retention of ICG particles are not fully understood and remain to be investigated further. It is likely, however, that free/soluble small molecules (e.g., free ICG) in the SC space can penetrate across endothelial cells lining lymphatic or blood capillaries. Small molecules absorbed into the initial lymph capillaries in the SC space can egress back into the interstitium and be rapidly cleared into the systemic blood circulation by rapid blood flow in capillaries (~100-500-fold > than lymph flow in capillaries (Wiig and Swartz 2012)). In contrast, the same molecules (i.e., ICG) stably bound to much larger nanoparticles are not permeable to blood capillaries but are permeable to lymph capillaries from the SC space. Once inside the lymph vessels, ICG particles remain in and distribute throughout the interconnected lymphatic system from local to distal LNs without leaking out of lymph vessels. As long as small molecules remain bound to nanoparticles and particles do not readily adsorb to lymph components, become endocytosed by cells in lymph vessels and nodes, or disintegrate, they circulate through lymph vessels and nodes before entering the blood at anastomoses between the thoracic lymphatic ducts and subclavian veins near the heart. This size-dependent differential blood vs. lymphatic uptake-retention-distribution hypothesis is consistent with the observations that free ICG was taken up by lymphatics near the injection site (**Figure 4.2A-C, 4.2G**), but did not travel extensively to downstream lymph vessels and nodes (**Figure 4.3**) and leaked out of lymphatics into proximal tissue and absorbed into the saphenous vein (blood circulation) (**Figure 4.2A-C, 4.2G**). The more extensive early entry into the blood circulation after free ICG dosing was confirmed by plasma ICG pharmacokinetics (**Table 4.1**), which to our knowledge is the first plasma PK data reported for ICG dosed SC in mice (IV has been the predominant administration route reported for ICG in

mice [e.g., 10 mg/kg ICG dose] (Milesi-Halle, Abdel-Rahman et al. 2011) and humans [e.g., 0.5-2.0 mg/kg ICG dose] (Meijer, Weert et al. 1988)). Mice administered with ICG particles did not exhibit detectable plasma ICG in blood (**Table 4.1**); it is likely due to the stability of ICG particles that very little if any free ICG was released from the lymph or the SC space and appeared in the blood, which would have been detectable in the plasma. Moreover, ICG particles did not diffuse to nearby tissues and blood vessels, but localized to and distributed widely throughout the lymphatics (**Figure 4.2D-F, 4.2H, 4.2I, 4.3, 4.4A**). In contrast, there was appreciable leakage of free ICG out of lymph vessels, which is consistent with studies that have shown healthy lymph vessels constitutively leak a portion of the fluid and solute (albumin) that they transport into the surrounding tissue (Scallan and Huxley 2010).

These data in mice are consistent with higher indinavir levels in multiple macaque lymph nodes (popliteal, inguinal, mesenteric, ileocecal, Peyer's patch, bronchial, axillary, tonsil, and submandibular) after SC injection of the same lipid-drug nanoparticle formulation used in ICG particles compared to an oral free drug formulation (Freeling and Ho 2014). Thus, it is clear that ICG particles enter and remain in lymph vessels, traversing from local to distal lymph nodes as their first-pass through the body without requiring blood recirculation to help promote widespread lymph node distribution. While additional cellular and molecular mechanisms remain to be elucidated and may contribute to lymph node accumulation of drug, the data collected in mice using free ICG and ICG particles are consistent with the above proposed mechanisms that drive the differential small-molecule solute and particle flow within the interconnected lymphatic vasculature.

Given the increased use of the SC route to reduce infection risk as well as healthcare cost of protein biotherapeutics intended for blood exposure (Pivot, Gligorov et al. 2013), a fuller understanding of the role of molecular characteristics that drive distribution into the blood versus the lymph is needed. Molecular or particle size, shape, elasticity, surface properties (e.g., charge, hydrophilicity), receptor-ligand mediated processes at cell or tissue targets, opsonization, and even the injection site and injection volume, each individually or in combination, likely play a role in regulating blood vs. lymphatic uptake, retention, and distribution. Size, presented as hydrodynamic diameter of most globular proteins, has a significant impact on the differential diffusion rate across blood vs. lymph vessels as well as through the SC space. For example, permeability (p=1-0.01) through blood capillaries in human skeletal muscle has been reported to diminish with size (~0.3-5 nm): water (18 Da, ~0.3 nm) p=1.0, glucose (180 Da, ~0.7 nm) p=0.6, sucrose (342 Da, ~0.9 nm) p=0.4, hemoglobin (64 kDa, ~5 nm) p=0.01 (Pappenheimer 1953). Furthermore, leveraging the well-defined physicochemical characteristics of gadolinium (Gd) conjugated to dendrimer particles, effects of increasing particle size (G2-10, 4-14 nm) on blood vasculature (capillary) permeability were systematically investigated in mice using MRI. These studies found that the majority of Gd-dendrimers <5 nm (G2-3) quickly leaked out of the vasculature into surrounding tissues, while most dendrimers >8 nm (G6-10) showed minimal leakage from blood vessels (Kobayashi and Brechbiel 2003). These data are consistent with the reported ~5-12 nm pore size of continuous and fenestrated (non-sinusoidal) human blood capillaries perfusing >95% of the body (e.g., skeletal muscle, skin) (Sarin 2010). Recent mouse studies with larger 30 nm magnetic particles given IV demonstrated almost exclusive blood vasculature retention in healthy mice but allowed extravascular tumor accumulation through leaky blood vessels (Miller, Gadde et al. 2015).

These accumulated data support the hypothesis that molecules with hydrodynamic diameters >5-8 nm do not readily permeate in and out of blood vessels. In contrast, much larger molecules (even bacteria and viruses) can readily cross lymphatic capillaries from the SC space, partly due to the 2-3 μm fenestrations between lymphatic endothelial cells (Baluk, Fuxe et al. 2007). As the estimated size of the interstitial water channels in the SC space is ~100 nm, molecules or particles should be < ~100 nm to readily transit through these channels and gain access to lymphatic capillaries (Wiig and Swartz 2012). With ICG associated to particles ~60 nm in size, they are small enough to rapidly transit through the interstitial water channels, but are too large to penetrate blood capillaries; thus, they appeared predominantly in and were retained by lymph vessels. It is possible that the nanoparticles that penetrated into lymph vessels were carried subsequently by lymph flow and were retained by specific retentive forces within the lymphatic system. Elucidation of these processes, while important, is beyond the scope of this report and is a topic of future investigation.

In addition to molecular size-dependent differentiation of lymph and blood vessel penetration, there are other physiological differences between lymph and blood that could contribute to treatment effectiveness. It is well-documented that human blood capillaries exhibit a flow rate ~100-500-fold faster than lymph capillaries. Thoracic duct lymph flow has been reported to range from 0.001-0.013 mL/min in mice, 0.008-0.017 mL/min in rats, and 0.67-2.5 mL/min in humans, and depends upon mobilization (e.g., anesthetized vs. ambulatory) (Lindena, Kupper et al. 1986). Moreover, total blood volume is larger than lymph volume (~5 vs. ~3 L), and protein and lipid levels are higher in blood than lymph. Also total protein concentration is much higher in blood than in lymph fluid; lipoprotein and lipid levels in lymph are ~10% of those in plasma

(Nanjee, Cooke et al. 2000). Since many orally administered HIV drugs such as the protease inhibitors indinavir, ritonavir, and lopinavir are highly protein bound, a majority of the fraction of oral HIV drug molecules found in the blood are protein bound, which further retards their ability to penetrate and distribute into lymph capillaries and nodes via extravasation from the blood into the interstitium or via penetration through high endothelial venules (HEVs) in lymph nodes. As a result, the concentration of oral HIV drugs in lymph is expected to be lower than that in blood. This concept, referred to as lymphatic drug insufficiency (LDI), was initially proposed and validated in our 2003 report (Kinman, Brodie et al. 2003), and recently confirmed in prospective studies in HIV patients that showed LDI of oral small-molecule antiretrovirals (Fletcher, Staskus et al. 2014, Lorenzo-Redondo, Fryer et al. 2016, Lee, Hatano et al. 2017). This is consistent with other reports in preclinical models and humans that showed the anti-cancer small molecules methotrexate (Kaminskas, McLeod et al. 2015), doxorubicin (Ryan, Kaminskas et al. 2013), and platinum-based chemotherapeutics (Zor, Yildirim et al. 2012) displayed limited lymphatic availability after IV and SC injection. This can result in negative clinical outcomes, particularly for antiviral therapy, as LDI in HIV patients on oral drug therapy has been associated with persistent HIV-1 RNA in LNs (Fletcher, Staskus et al. 2014).

Approaches to improve lymphatic drug exposure include a number of drug carrier platforms (e.g., nanoparticles, polymers, and liposomes), or *in situ* association with endogenous lipoproteins, proteins, or cells (leukocytes) with lymphotropic properties. Macromolecules and carriers can also be derivatized with targeting agents that bind to lymphatic targets. Recently, the US Food and Drug Administration approved [^{99m}Tc] Tilmanocept (*Lymphoseek*) for lymphatic mapping. Its polymeric dextran backbone that accumulates in draining LNs by selectively binding

to mannose receptors (CD206) on macrophage and dendritic cell surfaces prevents lymphatic egress of soluble ^{99m}Tc into the SC space and subsequent blood uptake (Wallace, Han et al. 2013). However, only local draining lymph nodes are visualized at low resolution with this agent. Other nanoparticles without targeting to macrophages also show very limited lymphatic distribution, primarily to local nodes, and content redistributed to local blood vessels (Davies-Venn, Angermiller et al. 2012, Burrows, Gonzalez-Garay et al. 2013, Proulx, Luciani et al. 2013).

Even without selective binding, the design of ICG particles (based on the early discovery that 40-80 nm black ink particles access the LN interstitium (Drinker, Field et al. 1934)) enables lymphatic homing from the SC space and widespread lymphatic retention/distribution (no blood redistribution is necessary) (**Figure 4.3**). Furthermore, no targeting moiety on the particle surface is required to enable high-resolution lymphatic imaging of LNs and vessels. The ability of ~60 nm ICG particles to distribute throughout and remain in lymph vessels (**Figure 4.4A**) when given SC is novel and could provide invaluable diagnostic and drug targeting (theranostic) possibilities. Full tissue distribution studies for ICG particles and free ICG are under our current investigation, and are also beyond the scope of this report.

Using this approach that specifically accesses the lymph vasculature throughout the body, we can probe in detail the anatomy and physiological state of the lymphatics (e.g., extent of lymph vessel leakiness or diminished clearance due to tumors). Recently reported carbon nanoparticles intended for lymphatic mapping only collect in lymph nodes and do not provide detailed resolution of the interconnecting lymph vessels or the thoracic duct (Xie, Xin et al. 2017). Other recent lymphatic targeting approaches using nanoparticles (~20-60 nm) relied on the blood (after IV

administration) to distribute to multiple LNs in mice (Xiong, Shuhendler et al. 2012, Pu, Shuhendler et al. 2014). With high background and limited blood-to-lymph transfer of nanoparticles in these studies, the ability to resolve small lymph vessels was low and thus derivation of pharmacokinetic and physiologic parameters required to develop and validate *in silico* physiologically based pharmacokinetic (PBPK) models would be limited. Our novel lymphatic first-passage approach using ICG particles given SC is a simplified experimental process and would likely provide a higher signal-to-noise ratio, and thus more efficient derivation of key parameters. With some optimization, the use of ICG particles could provide real-time, direct physiological measurements and could overcome the inability of other nanostructures to resolve small lymph vessels widely throughout the lymphatic network. This may enable physiological measurements without using more invasive procedures that can perturb the biologic system (Ryan, Kaminskas et al. 2013). With higher resolution and more confident derivation of key parameters, validated PBPK models may serve to predict lymphatic drug disposition and accelerate therapeutic product development.

The *in vivo* stability of ICG particles appeared to be an essential characteristic. *In vivo* stability of ICG association to the nanoparticles is evident by widespread and specific lymphatic distribution (**Figure 4.3**) and vascular retention (**Figure 4.4A**), suggesting these particles remained intact. Should small molecule contrast agents come apart in biological milieu, the dissociated molecules would behave as the solute free form and would leak out of the lymphatics, diminishing fluorescence signal and the signal-to-noise ratio, as shown in **Figure 4.3**. Stable binding between ICG and nanoparticles enabled detection of delicate (**Figure 4.4A**) and abnormal or inflamed lymph vessels (**Figure 4.4B**). To our knowledge, this is the first demonstration of ICG

nanoparticles being used to detect lymphatic vessels with confirmed inflammatory cell accumulations.

Abnormal lymph vessels such as those detected can permit lymph leakage, which is associated with the development of obesity, atherosclerosis, oedema, type 2 diabetes, and is thought to facilitate cancer cell entry into these vessels (Harvey, Srinivasan et al. 2005, Alitalo 2011, Stacker, Williams et al. 2014, Scallan, Hill et al. 2015). Thus, the ICG molecular-binding stability of particles and preferential lymphatic uptake/retention and widespread lymphatic distribution characteristics may be useful for convenient, real-time early diagnosis of abnormal lymph vessels and occluded lymph flow. Lymph flow is central to how well the lymphatic system functions, since functional transport of fluid and cells through lymph vessels maintains a properly functioning immune system by facilitating interactions between antigen presenting cells (APCs and DCs) and cognate lymphocytes. Defective lymphatic transport has been linked to impaired reverse cholesterol transport from tissues (Lim, Thiam et al. 2013) and exacerbates atherosclerosis (Martel, Li et al. 2013, Randolph and Miller 2014). In addition, ICG particles could be used to guide intranodal immunization injections, which have been shown to be ~100-fold more potent for eliciting an immune response for peptide and DNA vaccines than the same vaccine administered SC (Maloy, Erdmann et al. 2001). Furthermore, since solid tumors commonly induce an expansion of the surrounding lymphatic network (Skobe, Hawighorst et al. 2001, Stacker, Williams et al. 2014), and functional lymphatic vessels are restricted to tumor margins and peritumoral regions surrounding tumors (Padera, Kadambi et al. 2002), ICG particles could be used to detect the margins of tumors and tumor lymphatic networks. The limited depth range of non-invasive NIR diagnostic imaging with ICG particles may be enhanced by using a NIR-II imaging device that

could detect ICG's fluorescence emission in the 1,000-1,600 nm range (Carr, Franke et al. 2017, Starosolski, Bhavane et al. 2017) (NIR-II wavelengths demonstrate reduced photon scattering and tissue autofluorescence compared to the traditional 700-900 nm NIR-I range (Hong, Antaris et al. 2017)) or by complementing these particles with similar Gd particles and MRI (Bui, Stevenson et al. 2010) to provide high-resolution 3D imaging analysis for early diagnosis of lymphatic malignancies. Our novel Gd particles exhibit ~5-10-fold greater Gd particle accumulation in tumor-infiltrated LNs in mice and much higher resolution than any available Gd MRI contrast agent (Partridge, Kurland et al. 2015). In addition, more sensitive imaging devices (Zhu and Sevick-Muraca 2015) could provide further enhancement of NIR imaging capabilities with these ICG particles. Also, with surface coating of targeting biomarkers on ICG or Gd particles, resolution of these particles for abnormal LNs and vessels could be enhanced further.

4.5.1 *Conclusion*

In summary, we have shown that the lymphatics can be accessed widely and selectively when small molecules are stably bound to novel nanoparticles introduced into the SC space. Unlike parent soluble small molecules that readily permeated blood and lymph vessels, the same molecules bound to and stably associated with particles were preferentially taken up and retained by lymph vessels and nodes. These robust tracer nanoparticles allow high-resolution (~0.2 mm, 5-to-10 cells) NIR imaging of superficial lymph vessels and nodes and show higher resolving power of lymphatic anatomy than free ICG. Collectively, the properties of these particles may be used to diagnose as well as treat lymphatic abnormalities—particularly cancer metastases and residual HIV—by enhancing drug exposure in lymph nodes and vessels. These particles may also be further

developed to specifically interact with cell populations and signaling pathways in the lymphatic system to mediate immune responses.

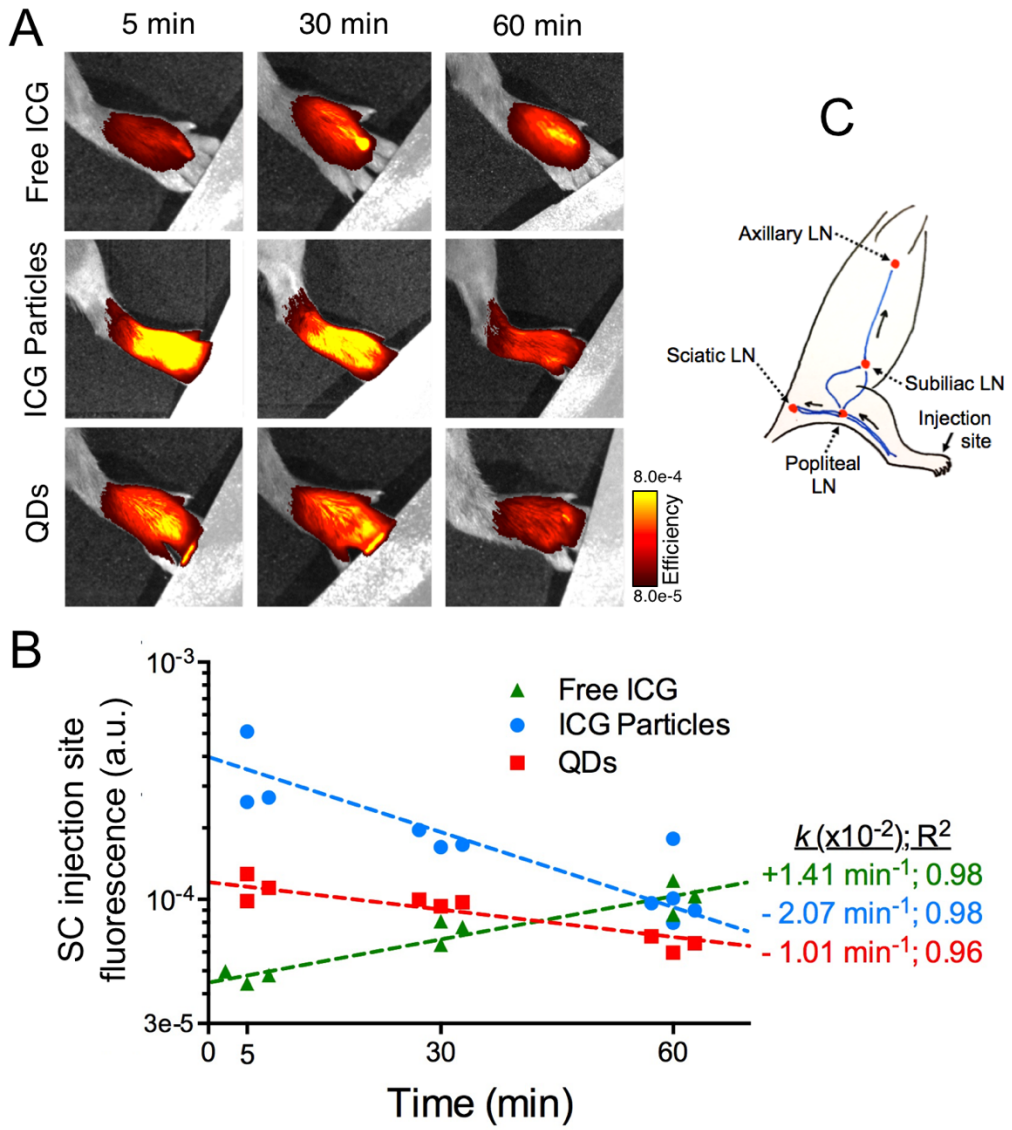

Figure 4.1. Comparison of free ICG, ICG particle, and quantum dot (QD) clearance from the SC foot injection site.

(***A***) Representative NIR fluorescence images of the injection site (N=3-5). (***B***) Time course of the foot SC injection site NIR fluorescence intensity (arbitrary units, a.u.). Rate constants (min^{-1}) and R^2 values for trendlines are listed. (***C***) Schematic representation of the superficial lymphatic vessels and nodes (popliteal, sciatic, subiliac, and axillary) on the right side of the mouse in relation to the dorsal right hind foot SC injection site.

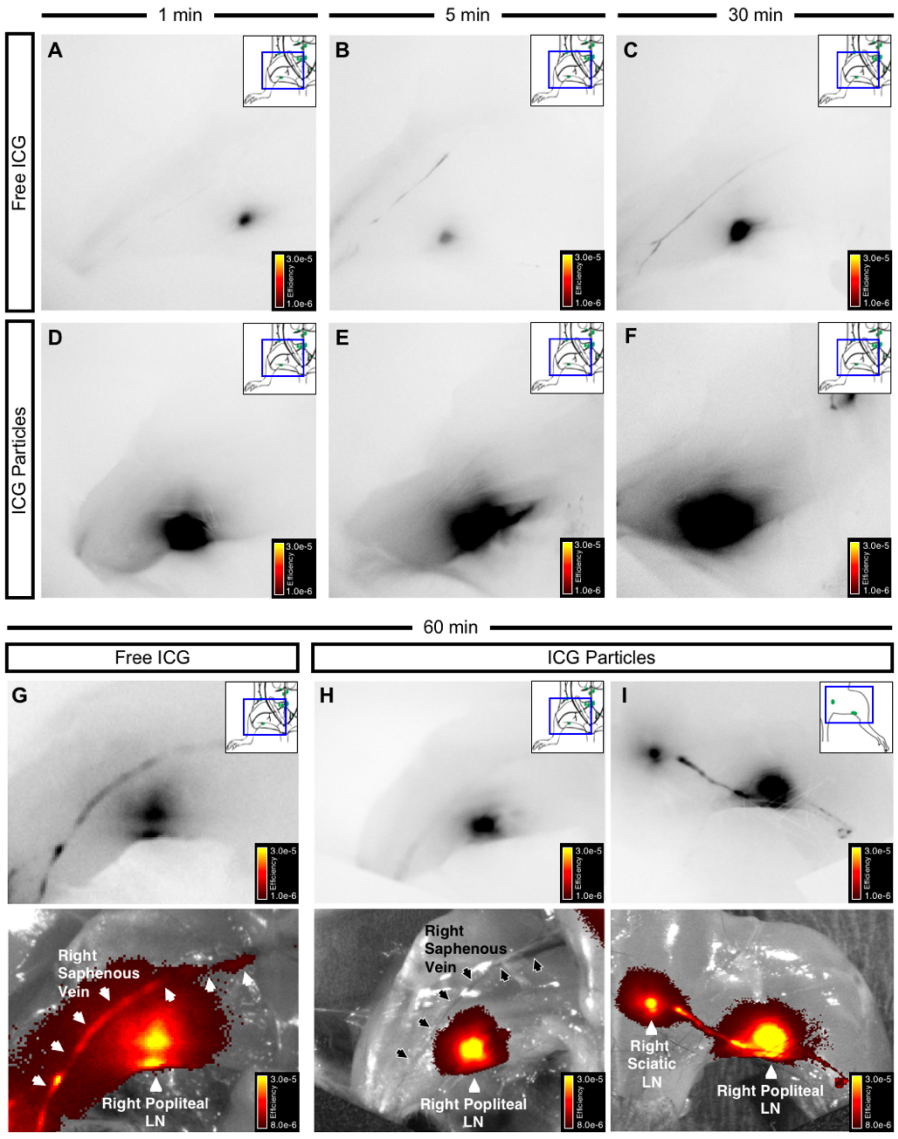

Figure 4.2. Comparison of ICG localization following SC dosing of free ICG or ICG particles.

NIR fluorescence images (top three rows) and corresponding bright field images with false color fluorescence overlay (bottom row) of the *ventral* right hind leg muscle tissue and saphenous vein (arrows) with skin removed 1, 5, 30, and 60 min post-SC foot injection of (***A-C, G***) free ICG or (***D-F, H, I***) ICG particles.

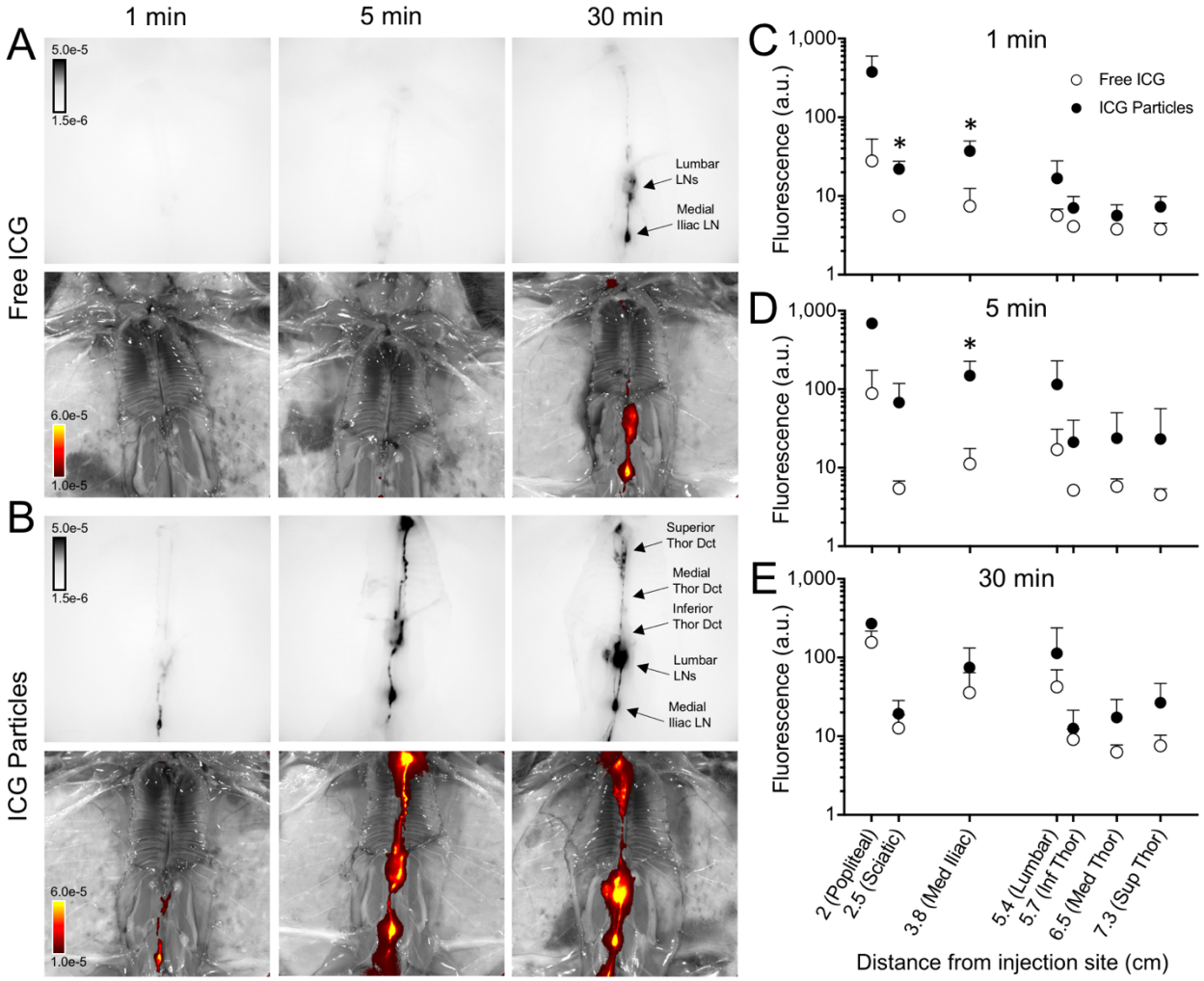

Figure 4.3. Time course of ICG distribution in the lymphatic system following a single SC dose of free ICG or ICG particles.

NIR fluorescence images (top) and corresponding bright field images with false color fluorescence overlay (bottom) showing the lymphatic distribution of ICG at 1, 5, and 30 min following SC dosing of (***A***) free ICG or (***B***) ICG particles. Comparison of the ICG fluorescence intensity versus distance from the SC injection site of the lymph node or thoracic lymph duct at (***C***) 1 min, (***D***) 5 min, and (***E***) 30 min following SC injection of free ICG (open circles) or ICG particles (solid circles). The structures in the lymphatics that were assayed and their approximate distance away from the right hind foot SC injection site, which is listed on the x-axis of (***C-E***), are as follows: popliteal LN (2.0 cm), sciatic LN (2.5 cm), medial iliac LN (3.8 cm), lumbar LN (5.4 cm), inferior thoracic lymph duct (5.7 cm), medial thoracic lymph duct (6.5 cm), and superior thoracic lymph duct (7.3 cm). *, P-value < 0.05.

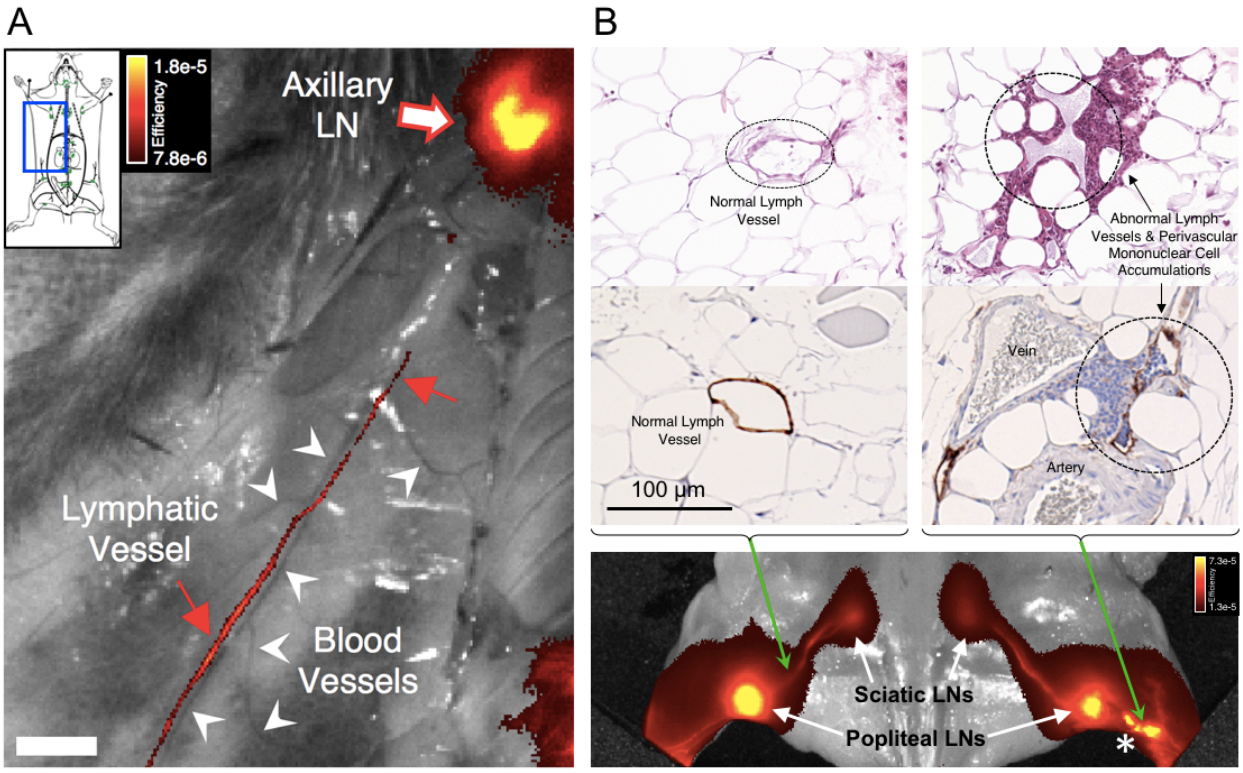

Figure 4.4. ICG particles verify small and abnormal lymph vessels.

(***A***) ICG particles detected a small lymph vessel adjacent to blood vessels. NIR fluorescence image of mouse skin opened with ICG particles post-SC foot injection tracing a small lymph vessel (red arrows) connecting the right subiliac and axillary LNs without egressing from the lymph vessel into nearby tissue or the parallel dark blood vessel (white arrows). Scale bar, 3 mm. (***B***) Lymphatic retention of ICG particles permitted detection of a lymphatic abnormality. NIR fluorescence image of ICG particles in the hind limbs of a mouse exhibiting abnormal, enlarged afferent popliteal lymph vessels (*). H&E histology (*top*) and anti-podoplanin immunohistochemistry (*bottom*) of control (*left*) and abnormal (*right*) lymph vessels that correspond to the locations in the mouse indicated by arrows. Histological analysis shows perivascular and intravascular mononuclear cell accumulations for the abnormal lymph vessels (*right*) but not for the normal lymph vessels (*left*).

Table 4.1. Early time course of indocyanine green (ICG) concentration (ng/mL) in mouse plasma following a single subcutaneous dose of ICG (3.0 mg/kg) formulated as either free ICG or ICG particles.

Time (min)	ICG Plasma Conc. (ng/mL)	
	Free ICG	**ICG Particles**
2.5	61.03 ± 8.50	BLOQ
5	74.06 ± 29.93	BLOQ

Arithmetic Mean ± SD of 3-4 mice per time point. BLOQ, below limit of quantification. Free ICG and ICG particles were dosed at 3.0 mg/kg ICG via identical SC injection volumes to the inside of the left hind leg.

Chapter 5. **Development and Validation of Mechanism-Based Pharmacokinetic (MBPK) Models for DcNPs**

Chapter 5 was published

in

Journal of Controlled Release. 2018:275:229-24.

5.1 ABSTRACT

Existing oral antiretroviral (ARV) agents have been shown in human studies to exhibit limited lymph node penetration and lymphatic drug insufficiency. As lymph nodes are a reservoir of HIV, it is critical to deliver and sustain effective levels of ARV combinations in these tissues. To overcome lymph node drug insufficiency of oral combination ARV therapy (cART), we developed and reported a long-acting and lymphocyte-targeting injectable that contains three ARVs—hydrophobic lopinavir (LPV) and ritonavir (RTV), and hydrophilic tenofovir (TFV)—stabilized by lipid excipients in a nanosuspension. A single subcutaneous (SC) injection of this first-generation formulation of drug combination nanoparticles (DcNPs), named TLC-ART101, provided persistent ARV levels in macaque lymph node mononuclear cells (LNMCs) for at least 1 week, and in peripheral blood mononuclear cells (PBMCs) and plasma for at least 2 weeks, demonstrating long-acting pharmacokinetics for all three drugs. In addition, the lymphocyte-targeting properties of this formulation were demonstrated by the consistently higher intracellular drug concentrations in LNMCs and PBMCs versus those in plasma. To provide insights into the complex mechanisms of absorption and disposition of TLC-ART101, we constructed novel mechanism-based pharmacokinetic (MBPK) models. Based upon plasma PK data obtained after single administration of TLC-ART101 (DcNPs) and a solution formulation of free triple-ARVs, the models feature uptake from the SC injection site that respectively routes free and nanoparticle-associated ARVs via the blood vasculature and lymphatics, and their eventual distribution into and clearance from the systemic circulation. The models provided simultaneous description of the complex long-acting plasma and lymphatic PK profiles for all three ARVs in TLC-ART101. The long-acting PK characteristics of the three drugs in TLC-ART101 were likely due to a combination of mechanisms including: (1) DcNPs undergoing preferential lymphatic uptake from the

subcutaneous space, (2) retention in nodes during lymphatic first-pass, (3) subsequent slow release of ARVs into blood circulation, and (4) limited extravasation of DcNP-associated ARVs that resulted in longer persistence in the circulation.

A graphical abstract is shown in **Figure 5.0**.

5.2 INTRODUCTION

There is growing interest in developing long-acting (LA) antiretroviral (ARV) injectable formulations that provide persistent, effective drug levels in plasma and/or HIV target cells (in the blood) for weeks to months, for HIV prevention and treatment (Owen and Rannard 2016). Currently, intramuscular (IM) LA cabotegravir and LA rilpivirine are in Phase III trials; each contains one anti-HIV drug. As single agents, their use is limited to prevention. For treatment, which requires ARV combinations, the two long-acting agents (cabotegravir and rilpivirine) are currently administered in two separate injections (Margolis, Gonzalez-Garcia et al. 2017). Because LA cabotegravir and LA rilpivirine both take several days to reach maximum plasma concentrations (T_{max}) (median T_{max}: 9-69 days (Spreen, Ford et al. 2014) or 6-11 days (McGowan, Dezzutti et al. 2016)), an additional oral lead-in or loading dose may be needed to provide effective plasma levels soon after injection to prevent the development of viral resistance from subtherapeutic concentrations. There is a need for injectables that can deliver a combination of ARVs in a single dosage form that can quickly achieve effective levels at times similar to the oral T_{max}, and from thereon sustain therapeutic drug levels for extended durations.

In addition to long-acting characteristics, the combination ARV injectable should also allow targeting of HIV reservoir sites. Since HIV infects T-cells in lymph nodes throughout the body (Lederman and Margolis 2008, Horiike, Iwami et al. 2012, Estes 2013), sustained and effective ARV levels in these host cells should be a key objective of any strategy for HIV eradication. In 2003, we first proposed and verified (Kinman, Brodie et al. 2003), and others later confirmed in prospective clinical studies (Fletcher, Staskus et al. 2014, Lorenzo-Redondo, Fryer et al. 2016, Lee, Hatano et al. 2017), that most orally dosed ARVs fail to achieve sufficient levels

in lymph nodes (Freeling and Ho 2014). This is consistent with reports showing rats and humans having limited lymphatic exposure to intravenous (IV) anti-cancer small molecules (e.g., doxorubicin, methotrexate, and carboplatin) (Chen, Wang et al. 2004, Ryan, Kaminskas et al. 2013, Kaminskas, McLeod et al. 2015). To overcome this lymphatic HIV drug insufficiency, we previously developed an indinavir-lipid nanosuspension and demonstrated that it provided indinavir accumulation in lymph nodes throughout the body (in addition to local draining lymph nodes) (Kinman, Bui et al. 2006, Freeling and Ho 2014) and reduced lymph node viral levels in HIV-infected macaques (Kinman, Brodie et al. 2003). With this drug delivery platform, we have now developed a novel long-acting and lymphocyte-targeting drug-combination injectable for subcutaneous (SC) administration. It contains multiple classes of ARVs in a single formulation that is intended to deliver the ARV combinations to HIV-infected lymph nodes and cells at much enhanced and more sustained levels of each ARV. Notably, this approach permits combining three ARV small molecules with different physicochemical properties (i.e., two hydrophobic drugs [LPV, LogD = 4.7; RTV, LogD = 5.2] and one hydrophilic drug [TFV, LogD = -3.6])–all together– into a single drug combination nanoparticle (DcNP) suspension (Freeling, Koehn et al. 2014, Freeling, Koehn et al. 2015). In macaques, a single SC injection produced enhanced and persistent drug levels in not only lymph node mononuclear cells (LNMCs) in lymph nodes local to the SC injection site, but in nodes throughout the body (Freeling and Ho 2014) for over a week (Kraft, McConnachie et al. 2017). Moreover, in peripheral blood mononuclear cells (PBMCs) and plasma, measurable drug levels were maintained longer than the two-week test period (Kraft, McConnachie et al. 2017). Plasma T_{max} values occurred within hours, apparent terminal plasma half-lives for the active drugs ranged from 65 to 477 hr, and intracellular LNMC drug concentrations were consistently higher than those in PBMCs, which were consistently higher than

those in plasma (i.e., drug concentrations in LNMCs > PBMCs > plasma) (Kraft, McConnachie et al. 2017). However, the pharmacokinetic (PK) mechanisms responsible for this enhanced, widespread lymphatic uptake and drug persistence in LNMCs, PBMCs, and plasma remained to be elucidated. Moreover, the published literature describing in general the lymphatic absorption, distribution, and elimination mechanisms of HIV drugs and drug combinations after SC dosing is limited.

To gain an understanding of the PK mechanisms governing SC absorption, distribution into lymphatics, lymph node-targeting, and sustained drug levels in lymphocytes and plasma following administration of our long-acting triple-ARV DcNP formulation—TLC-ART101 (Kraft, McConnachie et al. 2017)—we developed compartmental PK models based on a mechanistic framework that describe the kinetic processes governing the complex plasma concentration-time course of all three ARVs following SC injection of TLC-ART101 in macaques. We leveraged plasma concentrations in macaques dosed with the solubilized (free) triple-ARV combination to inform the parameterization of the free drug component of our TLC-ART101 models. This approach not only accounted for the complex long-acting plasma drug concentration-time profiles for all three ARVs in TLC-ART101, but also allowed for prediction of first-pass drug retention in the lymphatics. These mechanistic PK models are applicable to optimizing dosing for future efficacy and safety studies of TLC-ART101 in macaques, and comparing disposition profiles between the current and future generations of long-acting drug combination formulations.

5.3 MATERIALS AND METHODS

5.3.1 *Reagents and Animals*

1,2-distearoyl-*sn*-glycero-3-phosphocholine (DSPC) and 1,2-distearoyl-sn-glycero-3-phosphoethanolamine-N-[methoxy(polyethylene glycol)-2000] (ammonium salt) (DSPE-mPEG$_{2000}$) were purchased from Corden Pharma (Liestal, Switzerland). Lopinavir (LPV), ritonavir (RTV), and tenofovir (TFV, PMPA) were purchased from Waterstone (Carmel, IN, USA). All other reagents used were of analytical grade or higher.

Eleven adult male macaques (*Macaca nemestrina*, 5.6-14.9 kg) were housed and cared for by the Washington National Primate Research Center (WaNPRC) under an approved Institutional Animal Care and Use Committee protocol.

5.3.2 *TLC-ART101 and Free Triple-ARV Combination Formulations*

The long-acting drug combination nanoparticle (DcNP) formulation (TLC-ART101) composed of DSPC and DSPE-mPEG$_{2000}$ (9:1 molar ratio) that contained a combination of three antiretrovirals (ARVs) (LPV, RTV, and TFV) was prepared as previously described (Kinman, Brodie et al. 2003, Freeling, Koehn et al. 2015). The nanosuspension used in this study contained 18.3 mM LPV, 4.5 mM RTV, and 17.1 mM TFV. The pharmacokinetics (PK) of this formulation in macaques was recently reported (Kraft, McConnachie et al. 2017). The mean fraction of DcNP-associated LPV, RTV, and TFV was 92.2%, 91.1%, and 11.2%, respectively, as assessed by equilibrium dialysis using a 6-8 kDa molecular weight cut-off dialysis membrane. This mixture of lipid-associated and free ARVs constitutes the delivered drug content of TLC-ART101 (Kraft,

McConnachie et al. 2017). Mean diameter of the DcNPs was 69.0 ± 8.3 nm, as assessed by photon correlation spectroscopy.

The solution formulation of free LPV, RTV, and TFV was prepared in 20 mM $NaHCO_3$-buffered water (pH 7.4) with 0.7% NaCl, 8% DMSO, and 0.1% Tween20 and had the same final drug concentrations as those listed above for TLC-ART101.

5.3.3 *Pharmacokinetic Study*

Macaques were given a single subcutaneous (SC) bolus dose in the back mid-scapular region of 25.0 mg/kg LPV, 7.0 mg/kg RTV, and 10.6 mg/kg TFV, either as TLC-ART101 or free ARV formulation. In four animals dosed with TLC-ART101, blood was collected at 0, 0.25, 0.5, 1, 3, 5, 8, 24, 48, 120, 168, 192, and 336 hr for full PK profiling; in another four animals designated for lymph node biopsy, blood was only collected at 0, 0.5, and 24 hr. In three animals dosed with the free ARV formulation, blood was collected at 0, 0.5, 8, 12, 18, and 24 hr. LPV, RTV, and TFV concentrations in plasma were simultaneously analyzed using a validated LC-MS/MS method (Koehn and Ho 2014). The following descriptive PK parameters were estimated using the non-compartmental analysis module in Phoenix v6.4 (Certara, Mountain View, CA, USA): AUC, area under the plasma drug concentration-time curve; CL/F, apparent total clearance; MBRT, mean body residence time; $t_{1/2}$, apparent terminal plasma drug half-life.

5.3.4 *Free ARV Compartmental Models*

Structural Models and Parameter Estimation

A linear one-compartment model (1CM) with first-order absorption was fit to LPV and RTV plasma concentration-time data after SC dosing (**Figure 5.3A**). A two-compartment model (2CM) with first-order absorption was deemed to best fit the plasma concentration-time data for TFV (**Figure 5.3B**). For the 1CM analysis, the absorption rate constant k_{21}, the elimination rate constant k_{02}, and the apparent volume of distribution (V/F) were estimated, where F is the subcutaneous bioavailability. For the 2CM analysis, the following parameters were estimated: absorption rate constant (k_{21}), rate constants for the exchange of drug between central and peripheral compartments (k_{32}, k_{23}), and the elimination rate constant from the central compartment (k_{02}), along with the apparent volume of the central compartment (Vc/F). Secondary parameter estimates for apparent volumes in the terminal phase (V_β/F) and at steady state (V_{ss}/F) were computed from the primary parameter estimates (Gibaldi and Perrier 1982). It should be noted that subscript notations for all rate constants followed the engineering convention of k_{ji} with j = receiving compartment and i = originating compartment. See **Appendix B** for a full description of model parameters and their interpretation.

The average or typical value of the aforementioned 1CM or 2CM parameters were estimated by subjecting the plasma concentration-time datasets from each of the macaques to an iterated two-stage (ITS) analysis using the Popkinetics module of SAAM II v2.3 (18) (The Epsilon Group, Charlottesville, VA, USA). Briefly, the first stage involves estimating the PK parameters of each macaque through nonlinear regression; the second stage involves estimating the population PK parameters across macaques (e.g., mean, variance) based upon individual estimates from the first stage. SAAM II then uses the resulting population PK parameter estimates as Bayesian priors, and iterates the two-stage process until model convergence is reached (Bell and Schumitzky 1997).

Apparent terminal half-life ($t_{1/2}$) and apparent plasma clearance (CL/F) were then calculated using the population PK parameter values.

5.3.5 *TLC-ART101 ARV Compartmental Models*

Structural Models

The compartmental models for TLC-ART101 conceptualize the formulation-driven and physiological processes (i.e., mechanisms) underlying the absorption and disposition of DcNPs. As such, the mechanism-based pharmacokinetic (MBPK) models consist of two submodels: one for DcNP-associated ARV absorption and disposition (part above the dashed line in **Figure 5.3C**, 3D), and one for free ARV absorption and disposition (part below the dashed line in **Figure 5.3C**, 3D). This composite organization of two separate but linked submodels allows the accounting of differential absorption and disposition pathways between DcNP-associated ARVs and free ARVs from the subcutaneous space. In total this model structure has eleven parameters for LPV and RTV and thirteen parameters for TFV (**Figure 5.3C, 5.3D; Table 5.2**). See **Appendix B** for differential equations that define these models and a description of model parameters.

The lymphatic system draws interstitial fluid containing cells and solutes to lymph nodes and eventually drains into the thoracic lymphatic duct, which deposits its contents into the blood circulation via valves at the subclavian veins near the heart. Following SC injection, ARVs associated with DcNPs are taken up exclusively into the lymphatics (i.e., no uptake into the blood capillaries at the injection site) and transit through the lymphatic network where they may either: (1) transit as solutes through the lymph as it flows through lymph vessel and node networks before entering the systemic circulation via the thoracic lymph duct, (2) fill and become trapped in lymph

node sinuses, or (3) be taken up by lymph node parenchymal cells, such as lymphocytes. This exclusive lymphatic uptake, distribution, and retention is supported by preclinical studies with SC injection of large proteins and nanoparticles in the literature (Oussoren and Storm 2001, Kaminskas, Kota et al. 2009, Ryan, Kaminskas et al. 2013, Dahlberg, Kaminskas et al. 2014, Kaminskas, McLeod et al. 2015, Trevaskis, Kaminskas et al. 2015) and confirmed by our *in vivo* imaging studies in mice (Kraft, Treuting et al. 2018). These processes are depicted in the submodel above the dashed line in **Figure 5.3C, 5.3D**. In contrast, free ARVs in the subcutaneous space are absorbed entirely via blood capillaries into the circulation, which is depicted in the submodel below the dashed line in **Figure 5.3C, 5.3D**.

The two hydrophobic protease inhibitors (LPV, RTV) with LogP ~5 are nearly 100% incorporated into the core of DcNPs, as evidenced by complete retention in the nanoparticles despite exposure to sink conditions for 24 hr via equilibrium dialysis at 25ºC. The hydrophilic nucleotide reverse transcriptase inhibitor (TFV) with LogP -3.4 is mostly associated to the surface of DcNPs; equilibrium dialysis measurements indicate up to 90% of TFV in TLC-ART101 is effectively free under sink conditions and no significant release from the DcNPs occurs after 90% of free drug is dialyzed away, which indicates stable interactions between TFV and lipid and/or PEG in DcNPs for a minor fraction of the total amount of TFV. For DcNP-associated LPV and RTV, since 100% of the dose is assumed to be associated to DcNPs in the subcutaneous space, the entire SC dose of the protease inhibitors undergoes first-pass through the lymphatic system and is handled exclusively by the DcNP-associated ARV disposition submodel (above the dashed line in **Figure 5.3C**). For DcNP-associated TFV, since 10% of the dose is assumed to be associated to

DcNPs, and 90% is assumed to be free in the subcutaneous space, these percentages of the total dose were available for each respective submodel (**Figure 5.3D**).

In the MBPK models (**Figure 5.3C, 5.3D**), DcNP-associated ARVs are absorbed from the SC injection site (compartment q1) into the lymphatics via three parallel first-order pathways described by rate constants k_{21}, k_{31}, and k_{41}. Transit of DcNPs through the lymphatic system occurs through three parallel delay compartments (d2, d3, d4)—representing a fast, intermediate, and slow pathway, respectively. The decision to set the minimum number of delay compartments to three was based upon trial-and-error simulations to achieve reasonable visual fits of observed plasma concentration-time data. Only one or two lymphatic delay compartments, or a single uptake rate constant into one lymphatic delay compartment with three different release rate constants from this lymphatic delay compartment into the systemic circulation, were not sufficient to account for the complex and multiphasic persistent plasma levels for all three ARVs. Physiologically, the three different "waves" of drug entering the plasma from the lymph vessel and node network could result from: (1) DcNPs appearing in the plasma through more rapid flow of DcNPs and lymph through the lymphatics soon after injection, (2) DcNPs that are initially lodged in the sinus spaces in lymph nodes being eventually carried away and into the blood by slower lymph flow, and/or (3) DcNPs being taken up by lymphocytes in lymph nodes and then these lymphocytes trafficking into the blood where they could release intracellular drug into the plasma. Each delay compartment, which consisted of three sub-compartments in series, is defined by a transit time (*tlag*1, *tlag*2, or *tlag*3) and first-order exit rate constant (k_{52}, k_{53}, k_{54}), by which DcNP- or lymphocyte-associated ARVs are directed into the central compartment (q5). Once ARVs in DcNPs or lymphocytes enter the systemic compartment, release of free ARV would commence. Free ARVs are released from

DcNPs and lymphocytes in central compartment q5 by a first-order process into the free ARV central compartment (q7, described by first-order rate constant k_{75}). We assumed free ARV PK is the same whether it is administered as such or released from DcNPs *in vivo*. Moreover, we assumed DcNPs do not undergo significant degradation during the two-week period (i.e., no physical clearance of DcNPs), as evidenced by their long circulation lifetimes (Kraft, McConnachie et al. 2017). We also assumed no significant fraction of drug is released from DcNPs during their stay in the SC injection site and while transiting through the lymphatics (i.e., there is no dissociation or release of free ARV prior to entry into the systemic circulation), as evidenced by (1) our *in vitro* release assays that showed stable association of both hydrophobic and hydrophilic ARVs to DcNPs under sink conditions and (2) our *in vivo* imaging studies that showed only DcNPs undergo preferential, rapid, and widespread lymph vessel and node distribution and retention following SC administration in mice, whereas free drug does not (Kraft, Treuting et al. 2018). Re-entry into the lymphatic system following systemic distribution of DcNPs is not explicitly recognized, as evidenced by preclinical IV studies using nanoparticles (Ryan, Kaminskas et al. 2013).

For free ARVs at the subcutaneous injection site (compartment q6), they are absorbed into the blood by a first-order process into the central compartment (q7, described by the first-order rate constant k_{76}) (**Figure 5.3C, 5.3D**). Free TFV distributes in and out of the peripheral compartment q8 by first-order processes described by the rate constants k_{87} and k_{78} (**Figure 5.3D**). Free ARVs are cleared from the central compartment (q7) by a first-order process described by the rate constant k_{07}. The entire SC dose, either in free or DcNP-associated form, is assumed to be bioavailable from the subcutaneous space.

5.3.6 *Parameter Estimation*

As with free ARV model fitting, residual error for the observed plasma concentrations was described by a proportional error model for each dependent variable. Since the LC-MS/MS assay for plasma ARV concentration quantifies both DcNP-associated, protein-bound, and free ARV, the model output is the sum of predicted concentrations in compartments 5 (DcNP-associated ARVs) and 7 (DcNP-dissociated ARVs). Free ARV PK parameter estimates, including k_{76}, k_{78}, k_{87}, V7_Free, and k_{07}, were set to Bayesian priors based upon the mean and standard deviation of the population estimates derived from modeling of free drug formulation. To establish the lag times for each ARV through each of the three different lymphatic pathways (*tlag*1, *tlag*2, *tlag*3), we first fixed each of the lymphatic entry rate constants (k_{21}, k_{31}, k_{41}) equal to 0.1. Lag times (*tlag*1, *tlag*2, *tlag*3) were then set to "adjustable," as well as well as the apparent volume of distribution of DcNPs from the blood compartment (V5_DcNP) and the rate constant for release of free ARV from DcNPs (k_{75}). Initial estimates for "adjustable" parameters were obtained through visual fits of geometric mean data. Once lag times were established, for all subsequent model development these lag times served as Bayesian prior estimates with a 30% relative standard deviation. Next, lymphatic entry and exit rate constants ($k_{21} = k_{52}$, $k_{31} = k_{53}$, $k_{41} = k_{54}$) were manually adjusted based upon trial-and-error simulations to achieve reasonable visual fits of observed plasma concentration-time data. Final parameter estimates of the lymphatic entry rate constants were "fixed" to account for the proportion of subcutaneous ARV available for the rise and fall in plasma concentrations during early, mid, and late periods. Remaining model parameters (V5_DcNP and k_{75}) were set to "adjustable" and the model was fit to the plasma data. Finally, fits for plasma data from individual animals were loaded into the ITS SAAM II engine as described above to derive population PK parameter estimates.

Total lymphatic ARV exposure as a percentage of the subcutaneously injected dose (%ID) was estimated by adding together the ARV amounts in each of the three lymphatic delay compartments (d2, d3, d4) at each time point, and then dividing this sum by the total ARV amount administered in the SC dose.

$$\frac{d2\ (ng)+d3(ng)+d4(ng)}{Total\ SC\ Dose\ (ng)} = \%ID\ in\ Lymphatic\ System\ at\ each\ time\ point \quad (1)$$

Sensitivity analysis was performed on all TLC-ART101 model parameters by taking the parameter value that best fit the geometric mean plasma data, increasing and decreasing each value by 10-fold from the optimal value, and inspecting the impact on the estimated plasma ARV levels versus observed levels.

5.3.7 *Statistical Analysis*

Statistical analyses were performed with GraphPad Prism (GraphPad Software, Inc., La Jolla, CA). All statistical comparisons were performed with the two-tailed *t*-tests with significance probability α set at 0.05.

5.4 RESULTS

5.4.1 *Long-Acting Plasma PK of LPV, RTV, and TFV Following TLC-ART101*

We reported previously that SC dosing of LPV, RTV, and TFV stabilized in a DcNP suspension in macaques exhibited plasma PK profiles markedly different than those of the free drug combination—while the same three ARVs in the free formulation cleared in ~24 hr, DcNP-

associated ARVs persisted for the 1-week duration of the experiment (Freeling, Koehn et al. 2014). The plasma time course of these three ARVs in another DcNP formulation with a slight variation in the fixed dose molar ratio of LPV-to-RTV, called TLC-ART101, is presented in **Figure 1**. RTV is typically included in oral dosage forms to inhibit CYP3A-mediated metabolism and thus boost the oral bioavailability of protease inhibitors (Sham, Kempf et al. 1998). RTV is included in the TLC-ART101 injectable formulation containing LPV to preserve the protease inhibitor combination and possibly slow down the metabolic clearance of LPV. Measurable plasma levels of the two active ARVs of interest—LPV and TFV—persisted for over 2 weeks (**Figure 1A, 1C**). Compared to the free drug formulation, which cleared rapidly, the area under the plasma concentration-time curve (AUC) for LPV, RTV, and TFV in TLC-ART101 was 2.5-, 3.5-, and 28.9-fold higher, respectively (P-value = LPV, 0.0871; RTV, 0.0878; TFV, 0.0001) (**Table 1**). LPV and TFV in TLC-ART101 had apparent terminal half-lives ($t_{1/2}$) of ~20 and ~3 days. In comparison to free drug, $t_{1/2}$ of LPV, RTV, and TFV in TLC-ART101 was 55.1-, 5.5-, and 8.2-fold longer, respectively (P-value = LPV, 0.3814; RTV, 0.0306; TFV, <0.0001) (**Table 1**).

Following injection of the free drug formulation, the two hydrophobic protease inhibitors, LPV ($LogD_{7.4}$ 4.69) and RTV ($LogD_{7.4}$ 5.22), exhibited similar plasma PK profiles: time of maximum concentration (T_{max}) occurred between 30 min and 8 hr, and plasma levels declined in a monoexponential fashion out to 24 hr (**Figure 5.1A, 5.1B**). Free LPV and RTV also had similar $t_{1/2,}$ apparent clearance (CL/F), and mean body residence time ($MBRT_{0\text{-}24h}$) (**Table 5.1**). In contrast, free hydrophilic TFV exhibited a plasma PK profile resembling an IV bolus and declined in a biphasic fashion over 24 hr (**Figure 5.1C**), which was consistent with other studies in macaques given free TFV subcutaneously (Van Rompay, Babusis et al. 2012). Initial decline of

free TFV was rapid; levels fell to ~1% of their peak by 10 hr, followed by a slower terminal phase of decline (**Figure 5.1C**). Free TFV was eliminated from the body more rapidly than free LPV and RTV, as $MBRT_{0\text{-}24h}$ for free TFV was ~5-fold shorter than those of free LPV and RTV, and CL/F followed a similar trend (**Table 5.1**).

While the PK of free LPV (25 mg/kg) and RTV (7 mg/kg) were remarkably similar, the PK of an equivalent dose of LPV and RTV in TLC-ART101 were different in significant ways (**Figure 5.1A, 5.1B; Table 5.1**). Following their injection in TLC-ART101, both LPV and RTV had a very rapid initial phase of absorption that resulted in a small first peak within 0.5 to 1 hr; thereafter, plasma concentrations rose to a second peak or plateau at ~8 hr, followed by a slow but steady decline over the next 16 to 40 hr (**Figure 5.1A, 5.1B**). T_{max} of ~8 hr for LPV and RTV suggested a moderate rate of absorption with the DcNP-associated dose (**Figure 5.1A, 5.1B**). After 48 hr, the decline of plasma LPV concentration slowed to a near plateau at ~20 ng/mL that persisted out to 336 hr (2 weeks) (**Figure 5.1A**); RTV levels declined in a multiphasic fashion and were mostly eliminated by 2 weeks (**Figure 5.1B**). Although $MBRT_{0\text{-}24h}$ for free LPV and RTV were nearly identical, following TLC-ART101 administration $MBRT_{0\text{-}336h}$ of LPV was ~4.6-fold longer than that of RTV (**Table 5.1**). Delivery of TFV as DcNPs resulted in remarkable transformation of its PK compared to free TFV (**Figure 5.1C**). TFV levels persisted out to 336 hr, with an initial peak within 1 hr after injection, a subsequent gradual decline, followed by a rebound at ~8 hr that peaked at ~2,800 ng/mL around 24-48 hr, before declining in a log-linear fashion to ~170 ng/mL at 336 hr (**Figure 5.1C**). $MBRT_{0\text{-}336h}$ of TFV following injection of TLC-ART101 was ~39-fold longer than the $MBRT_{0\text{-}24h}$ of free TFV, and was comparable to that of LPV (**Table 5.1**). CL/F for all three ARVs decreased in TLC-ART101, most dramatically for TFV with an ~36-

fold drop in CL/F (**Table 5.1**), reflecting its striking high and persistent plasma concentration profile (**Figure 5.1C**). In sum, these differences in plasma PK between free and TLC-ART101 ARVs illustrate the marked effect that the TLC-ART101 formulation had on plasma persistence for both the hydrophobic (LPV, RTV) and hydrophilic (TFV) ARVs.

5.4.2 *Mechanism-Based PK (MBPK) Models*

Mechanism-based compartmental PK models were developed that can provide kinetic insights into the physiological processes of subcutaneous uptake, lymphatic transit, and systemic disposition of the three ARVs delivered by the TLC-ART101 formulation. As depicted in **Figure 2**, we assumed the following scenario for subcutaneously administered LPV, RTV, and TFV collected into a DcNP form (69.0 ± 8.3 nm): (1) the DcNPs have appropriate particle sizes and surface properties to move via convection through the <100 nm interstitial water channels in the SC space (between the skin and muscle) (Wiig and Swartz 2012), (2) they are too large to move paracellularly between or through the 5-12 nm intercellular gaps between capillary blood endothelial cells (Sarin 2010), and as a result, (3) the three drugs in DcNPs preferentially enter lymphatic capillaries, which have an architecture that promotes uptake of larger particulate matter (Trevaskis, Kaminskas et al. 2015). Once in lymphatic capillaries, these DcNPs travel throughout the lymphatic vessels and nodes. A fraction of the DcNPs taken up into the lymphatics is retained in lymph node sinuses, and a fraction eventually enter the blood circulation either through lymph that flows into the venous blood through the right and left thoracic ducts, or as cargo within lymphocytes in lymph nodes that traffic out of lymph nodes into the blood via the thoracic duct or high endothelial venules (HEVs) in lymph nodes. If DcNPs prematurely released drug and disintegrated *in vivo* (in the lymphatics or the blood), the released ARVs would be rapidly cleared

as shown with free ARVs (**Figure 5.1, Table 5.1**). In contrast, free drugs in the SC space are small enough to penetrate or diffuse through the capillary endothelium; while a fraction can enter the lymphatics, overall, free drug molecules are preferentially absorbed via the blood capillaries due to the ~100- to 500-fold faster flow in blood compared to lymphatic capillaries (Wiig and Swartz 2012), i.e., a more effective "sink" condition. Unlike DcNP-associated ARVs that experience retentive forces that trap them in lymph vessels and nodes, free ARVs that enter the lymph could readily diffuse out and redistribute back into the blood. As a result, free ARVs would follow drug distribution and clearance mechanisms mediated by blood carriage, whereas ARVs associated to DcNPs, following their preferential uptake into the lymphatics, would first encounter distribution and retention mechanisms within the lymphatics, before being subject to those in the blood. Taken together, DcNPs in TLC-ART101 would likely undergo first-passage through the lymphatic system before entering the blood circulation, whereas free ARVs in the SC space would be preferentially absorbed directly into the blood vasculature. These processes are schematically illustrated in **Figure 5.2** and featured in the compartmental models in **Figure 5.3C, 5.3D**.

These assumptions are based on *in vivo* animal studies with nanoparticulate drug carriers reported in the literature. For instance, in rats, a major fraction of radiolabeled liposomes ~50-100 nm in diameter preferentially entered the lymphatics versus the blood following SC injection (Oussoren, Zuidema et al. 1997). Also, in sheep, proteins <16-20 kDa (~4-5 nm) in the SC space were absorbed primarily by blood capillaries draining the SC injection site (Supersaxo, Hein et al. 1990). Based on these observations, we propose differential absorption mechanisms between free and DcNP-associated ARVs from the SC space in accordance to their differences in physical size. Thus, we developed composite compartmental PK models that would feature parallel uptake of (1)

DcNP-associated ARVs into and transit through the lymphatics, eventually making their way to the systemic circulation (submodel above the dashed line in **Figure 5.3C, 5.3D**) and (2) free ARVs directly into the blood for systemic distribution (submodel below the dashed line in **Figure 5.3C, 3D**). It is further assumed that once the DcNP-associated ARVs reach systemic circulation, free drug can be release from the DcNPs.

5.4.3 *Models of Plasma PK of Free LPV, RTV, and TFV*

We assumed that the model structure and parameter estimates derived from analysis of PK data obtained after SC injection of the free ARV formulation apply equally to the PK of free drug either absorbed directly or released from DcNPs following administration of TLC-ART101. This lessened the burden of parameter estimation for the full MBPK models and allayed some concerns of model complexity. Thus, for the initial step in model development, we analyzed the plasma ARV concentration-time data in macaques given a SC dose of the free ARV combination (**Figure 5.1**) according to a conventional one- or two-compartmental PK model (1CM or 2CM) with first-order absorption from the SC injection site (**Figure 5.3A, 5.3B**). Population estimates of free drug PK parameters obtained using an iterated two-stage approach are presented in **Table 5.2**. Excellent model fits were observed with individual and mean plasma concentration-time data from the cohort of macaques (**Figure 5.4**).

All three free ARVs were assumed to have a rapid absorption following SC injection (i.e., $k_{21} > k_{52}$, k_{53}, and k_{54}) (**Table 5.2**) (Gibaldi and Perrier 1982). CL/F and $t_{1/2}$ values in **Table 5.2** agreed with their corresponding estimates derived from non-compartmental analysis in **Table 5.1**. The rather high ~4 L/(hr•kg) CL/F values for free LPV and RTV (**Table 5.2**) are comparable to

reported macaque liver blood flow (Bourne 1975, pgs. 52, 61), indicating a high hepatic extraction and clearance of these two protease inhibitors. The 0.60 L/(hr•kg) CL/F for free TFV (**Table 5.2**) matched macaque renal plasma flow (Bourne 1975, pgs. 52, 61), which is consistent with avid renal tubular clearance of this nucleotide reverse transcriptase inhibitor. The population parameter estimates for free ARV PK were entered as Bayesian priors in the MBPK models for TLC-ART101-associated ARVs (**Figure 5.3C, 5.3D**).

5.4.4 *Models of Plasma and Lymphatic PK of DcNP-associated LPV, RTV, and TFV*

As mentioned above, we designed the MBPK models for TLC-ART101 to consist of: (1) a submodel for disposition of DcNP-associated ARV following its absorption from the SC space that features first-passage through the lymphatics (lymph vessels and nodes), that is linked to (2) a submodel for disposition of free ARV either absorbed directly from the SC space or released from DcNPs during their systemic distribution phase (**Figure 5.3C, 5.3D**). Based on equilibrium dialysis results, the "free-to-DcNP-associated" fractions of TFV in TLC-ART101 were 90:10 (mol%/mol%); hence, 10% of the TLC-ART101 dose was assigned to the SC compartment (q1) for DcNPs and 90% was assigned to the SC compartment for free drug (q6). LPV and RTV were 100% associated to DcNPs; hence, the entire LPV and RTV dose in TLC-ART101 was assigned to the SC compartment for nanoparticles (q1).

We first characterized the lymphatic transit kinetics for each ARV using the geometric mean plasma values from N=8 animals (four of these eight only contributed blood samples at 30 min and 24 hr). Fitting the plasma concentration-time data to these models resulted in lag time estimates for the three ARVs that range from 0.1 to 2.2 hr with the fast lymphatic pathway, 10.9

to 38.8 hr with the intermediate pathway, and 122.1 to 262.2 hr for the slow pathway (**Table 5.2**). As the initial plasma levels for LPV and RTV were similar over 0-48 hr (**Figure 5.1A, 5.1B**), *tlag*1 for both of these ARVs was nearly identical at ~2 hr (**Table 5.2**). However, because LPV plasma levels were sustained at essentially a steady-state during 48-336 hr while RTV plasma concentration declined steadily over 48-336 hr (**Figure 5.1A, 5.1B**), *tlag*3 for LPV (260 hr) was much longer than that for RTV (180 hr) (**Table 5.2**). RTV, at ¼ of the dose of LPV (i.e., LPV-to-RTV ratio of 4:1 mol%/mol%), showed a slight rebound in levels around 1 week (168 hr) (**Figure 5.1B**), which accounts for its *tlag*3 value (**Table 5.2**). TFV, due to its very early first peak (which likely corresponded to absorption of the free fraction in DcNPs), then second peak (which likely corresponded to the DcNP-associated fraction), and gradual but persistent terminal decline (**Figure 5.1C**), had the most rapid *tlag*1 (0.1 hr) and the shortest *tlag*3 (120 hr) amongst the three DcNP-associated ARVs (**Table 5.2**). Thus, taken together, each ARV exhibited characteristically short, medium, and long lag times that may be thought of as "waves" of DcNPs being released into the blood circulation from the lymphatics. These three different "waves" of DcNPs appearing in the plasma may occur either through a faster and a slower flow of DcNPs through the lymph into the blood (the faster flow through lymph occurring soon after injection and the slower flow through lymph resulting from DcNPs initially trapped in lymph node sinuses eventually being carried away by lymph), or through lymph node lymphocytes that have taken up DcNPs and then trafficked into the blood and slowly releasing ARVs into the plasma. These lag times were entered as Bayesian estimates for further model refinement.

Next, we performed a manual search for the guess-estimates of k_{21}, k_{31}, and k_{41}, the rate constants for entry of the three ARVs into each of the three lymphatic pathways (**Figure 5.3C,**

5.3D). Since entry of DcNPs into the different lymphatic pathways operate in parallel, the sum total of the entry rate constants k_{21}, k_{31}, and k_{41} for DcNP-associated ARV uptake from the SC space into the respective lymphatic delay compartments d2, d3, and d4 (**Figure 5.3C, 5.3D**) ought to be about the same for each ARV. This is consistent with our observations that DcNPs cleared from the SC space within ~24 hr and were predominantly taken up into lymph vessels and nodes. Through systematic adjustment of k_{21}, k_{31}, and k_{41}, the minimum sum for each ARV was determined to be ~0.45 hr^{-1} (i.e., $k_{21} + k_{31} + k_{41} = \sim 0.45\ hr^{-1}$) and constrained to this value (i.e., fixed) during regression runs (**Table 5.2**). The sum for final estimates of the entry rate constants for LPV, RTV, and TFV equaled 0.46, 0.44, and 0.47 hr^{-1}, respectively (**Table 5.2**). However, despite constraining the sum total of lymphatic entry rate constants to be the same value for all three ARVs, the optimal estimates of k_{21}, k_{31}, and k_{41} differed among ARVs in the final model fits (**Table 5.2**). For LPV, the rank order for the lymphatic entry rate constants was $k_{41} >> k_{31} >> k_{21}$; for RTV, $k_{21} > k_{31} >> k_{41}$; and for TFV, $k_{41} \geq k_{31} \geq k_{21}$ (**Table 5.2**), suggesting that LPV was most available for the slow lymphatic pathway (d4), RTV was most available for the fast lymphatic pathway (d2), while hydrophilic TFV entered into all three lymphatic pathways to nearly equal extent, despite the fact that all three ARVs were tightly associated with DcNPs and presumably then transit together as single entities through lymph vessels and nodes. This could be due to uneven incorporation of the three ARVs into DcNPs—creating different subpopulations of DcNPs—and retention of DcNPs within the lymphatic network being influenced by the drug payload. Alternatively, there may be different rates of intracellular metabolism/anabolism and efflux from lymphocytes for each ARV, which would impact their lymphatic transit kinetics. More investigation is required to understand the underlying mechanisms for this apparent differential lymphatic transit of each ARV, the details of which are beyond the scope of this report. In

summary, although the total sum of the lymphatic entry rate constants could be set to a value comparable for all three ARVs, each DcNP-associated ARV had its own unique uptake distribution into the three lymphatic pathways (**Table 5.2**). After the best estimates of lymphatic entry rate constants were determined for each ARV using geometric mean data, they were fixed as we proceeded to the iterated two-stage population analysis of the cohort macaque data.

For all three ARVs, the TLC-ART101 MBPK model fits to observed plasma concentration-time data were excellent (**Figure 5.5**) and %CV for the regression estimates were within a reasonable range considering the limited sample size (N=8) (**Table 5.2**). Sensitivity analysis, where the optimal parameter value was increased or decreased by 10-fold, showed that *tlag*3, V7_DcNP, and k_{75} impacted the predicted plasma ARV concentration-time profile the most. We have used these MBPK models for dose selection for TLC-ART101 multi-dosing studies in healthy and SHIV-C-infected macaques, and the models predicted the observed plasma concentrations extremely well (personal observation), which demonstrates the validity and robustness of these models.

The apparent volume of distribution of DcNP-associated ARVs in the q5 plasma compartment (V5_DcNP) (**Figure 5.3C, 5.3D**) was ~7-10 L/kg for the lipophilic ARVs LPV and RTV, while V5_DcNP for hydrophilic TFV was much smaller at 0.17 L/kg (**Table 5.2**). These distribution volumes were about 6.7- to 12.8-fold smaller than those of free ARVs in q7 (V7_Free) (**Table 5.2**), suggesting much more limited extravascular distribution for DcNP-associated ARVs. The rate constant for release of free ARV from DcNPs in the plasma (k_{75}) was similar for LPV and RTV at ~0.4-0.7 hr^{-1} ($t_{1/2}$ ~1.0-1.7 hr), while k_{75} was much slower for TFV at ~0.02 hr^{-1} ($t_{1/2}$

~35 hr) (**Table 5.2**). As expected, the final mean parameter estimates for free ARV (k_{76}, k_{78}, k_{87}, V7_Free, and k_{07}) matched the assigned Bayesian priors (**Table 5.2**). Next, we used the models to evaluate the ARV exposure in the lymphatic system.

5.4.5 *Lymphatic Exposure to LPV, RTV, and TFV Following TLC-ART101*

Based on single-photon emission computed tomography (SPECT) imaging of ^{111}In-labeled anti-CD4 mAbs dosed by IV infusion in macaques, ~75% of CD4+ T lymphocytes (the main target cell of HIV) are located in lymph nodes (~15% are in the spleen, ~10% are in Peyer's patches, and ~0.3-0.5% are in the blood) (Di Mascio, Paik et al. 2009). These data are corroborated by a separate study in macaques infected with simian immunodeficiency virus (SIV) that were dosed IV with ^{64}Cu-labeled anti-SIV Gp120 PEGylated mAbs and imaged with immunoPET (antibody-targeted positron emission tomography), which showed predominant SIV localization in lymphoid tissues in chronically viremic animals and still measurable viral levels in lymph nodes after 5 weeks of combination antiretroviral therapy (Santangelo, Rogers et al. 2015). This pattern of HIV infection in lymphoid tissues in non-human primates mirrors the viral distribution in humans. Thus, it is important to target anti-HIV drugs to lymph nodes throughout the body and sustain ARV levels within lymph node cells infected by HIV. The MBPK models we developed allowed us to simulate the total lymphatic ARV exposure from TLC-ART101. **Figure 5.6** shows the predicted amount of ARVs held in the lymphatics during first-pass over the entire 2 weeks. More than 80% of the LPV dose was held in the lymphatics at peak, and released gradually over the 2 weeks (**Figure 5.6A**). In contrast, less of the RTV dose was withheld and nearly all of it was released from the lymphatics within 96 hr (**Figure 5.6B**). With TFV, while the maximum % of dose withheld in the lymphatics was low (<10%), it accounted for nearly the entire DcNP-associated portion (10%) of the TLC-

ART101 dose (**Figure 5.6C**). Subsequent release of TFV from the lymphatics was gradual, but at a faster pace compared to LPV (**Figure 5.6A, 5.6C**).

5.5 DISCUSSION

Previously, we reported a long-acting ARV combination injectable (TLC-ART101) that provided sustained lymphocyte and plasma ARV concentrations in macaques for longer than the 2-week experiment (Kraft, McConnachie et al. 2017). However, detailed mechanisms leading to this lymphocyte-targeting and persistent intracellular and plasma ARV concentrations were not elucidated. In this study, PK models were developed based on consideration of physiological processes that govern the uptake of DcNPs from the SC interstitium into lymph capillaries, transit through the lymphatic network including retention by the lymph nodes, and eventual drainage into the blood circulation. The models were able to simultaneously capture the complex persistent lymphatic and plasma pharmacokinetics of three ARVs (LPV, RTV, TFV) formulated together in the TLC-ART101 lymphocyte-targeting and long-acting drug combination formulation (**Figure 5.3C, 5.3D, 5.5, 5.6**). Moreover, these mechanism-based models afforded mechanistic insights into the absorption and disposition of DcNP-associated ARVs and enabled prediction of overall ARV levels in the lymphatics (lymph vessels and nodes) following SC injection of TLC-ART101 (**Figure 5.6**). They can also guide the design of dosage regimens for future efficacy and safety studies of TLC-ART101.

To our knowledge, these are the first mechanistic PK models of a nanoparticle-bound drug combination that describe the time-course of plasma concentration and lymphatic retention of multiple ARVs formulated in a single nanosuspension. These models enabled, for the first time,

prediction of the long-acting PK of each ARV in both the plasma and lymphatics. Our mechanism-based PK models were also able to account for the complex, multiphasic plasma-concentration time course of the three DcNP-associated ARVs (**Figure 5.1**) by having multiple (three) delay pathways through the lymphatics after SC injection of TLC-ART101 (**Figure 5.3C, 5.3D**). Only one or two lymphatic delay compartments were not sufficient to account for the complex plasma concentration time courses of each ARV. Previous reports on the disposition of subcutaneously injected large proteins of ~4-10 nm in diameter (Chen, Sawchuk et al. 2000, Ramakrishnan, Cheung et al. 2003, McLennan, Porter et al. 2005, Zhao, Ji et al. 2013, Dahlberg, Kaminskas et al. 2014, Chan, Bulitta et al. 2015, Landersdorfer, Caliph et al. 2015, Chan, Ascher et al. 2016) (reviewed in (Kagan 2014)) and single, small molecule drugs in ~10-100 nm diameter nanoparticles (Ryan, Kaminskas et al. 2013) have reported PK models featuring a lymphatic component. The few PBPK models published to date include single monoclonal antibodies (mAbs) administered SC (Zhao, Ji et al. 2013, Gill, Gardner et al. 2016). Despite evidence of significant absorption of lymphatic fluid into the blood as it flows through lymph nodes in mammalian systems (which leads to concentrating lymph solutes and decreasing the lymph flow rate) (Aukland and Reed 1993, Dahlberg, Kaminskas et al. 2014), and substantial recirculation of mAbs via the lymphatic system after IV administration (Dahlberg, Kaminskas et al. 2014), these PBPK models either assumed reabsorption of drug molecules in lymph tissue and fluid back into the blood was negligible (Gill, Gardner et al. 2016) or no recirculation via the lymphatic system occurred after entry of mAbs into the systemic circulation (Zhao, Ji et al. 2013).

While the detailed mechanisms of how the three DcNP-associated drugs in the TLC-ART101 formulation exhibited long-lasting retention in the lymphatics, particularly in lymph

nodes, and were targeted to lymphocytes, awaits further investigation; a working hypothesis is presented schematically in **Figure 5.2**. We envisioned the mechanisms that lead to the complex plasma time-course of the three ARVs in TLC-ART101 are as follows: first, in the SC space, the ARVs associated to DcNPs readily clear from the interstitium and preferentially enter lymph capillaries (as opposed to free drug with greater propensity to enter blood capillaries), followed by first-pass transit of the DcNPs through the lymphatic network. This exclusive lymphatic uptake and extensive first-pass distribution through lymph vessel and node networks has been confirmed by *in vivo* imaging of DcNP clearance from the SC space and lymphatic uptake, distribution, and retention in mice (Kraft, Treuting et al. 2018). This is consistent with our observation of high levels of drug distribution and accumulation in lymph nodes all throughout the body in macaques following a single SC dose of DcNPs, which was not observed with free drug (Freeling and Ho 2014). This lymphatic first-pass distribution of DcNPs is also consistent with the higher drug concentrations in LNMCs versus those in PBMCs, which are both persistently higher than the drug levels in the plasma (Kraft, McConnachie et al. 2017). These high intracellular levels of ARVs are opposite of the higher plasma versus intracellular levels that are typically observed following oral dosing of the same ARVs in DcNPs (Colombo, Beguin et al. 2005, Colombo, Telenti et al. 2006, van Kampen, Reedijk et al. 2010, D'Avolio, Simiele et al. 2013). Thus, as supported by our *in vitro* release studies under sink conditions, DcNPs must be sufficiently stable and not release a significant fraction of their ARV payloads to be able to make their extensive journey through lymph vessel and node networks, be internalized by LNMCs, and provide long-acting PK; if DcNPs readily degraded and released free ARVs, these free drugs would not be able to transit extensively through lymph vessels and nodes and be retained by the lymphatics, and they would clear from the body rapidly.

As the lymphatic network is composed of nodes with sinuses within the node tissue being able to trap ~70 nm diameter DcNPs (Drinker, Field et al. 1934), they provide a reservoir or depot for sustained drug presence in the lymphatics. Tissue lipases in the nodes as well as those on the surface or within lymph node parenchymal cells could release the drug back into the lymphatic network, or the DcNPs could be taken up by lymphocytes trafficking in and out of the blood via high endothelial venules (HEVs) in lymph nodes. The acid- and base-stable characteristics of LPV and RTV may also contribute to the ability of these drugs to release in acidic intracellular organelles such as endosomes and lysosomes with minimal risk of degradation. Long-acting plasma drug exposure could also arise from gradual release of DcNP- and lymphocyte-associated ARVs from the lymphatics into the blood via lymph-blood vessel anastomoses near the heart. It is likely that a combination of these processes work in concert to provide the long-acting plasma and intracellular kinetics observed for each ARV. These processes are accounted for in the three lymphatic delay compartments in the MBPK models (**Figure 5.3C, 5.3D**), which represent three different "waves" of release of DcNPs from the lymphatics into the systemic circulation. As discussed below, recent data collected in our laboratory and those reported by others support this integrated hypothesis (i.e., preferential DcNP uptake into lymphatics, lymphatic first-pass distribution and retention, extended release into blood, and limited extravasation in blood circulation).

5.5.1 *Preferential Lymphatic (First-Pass) Uptake of DcNP-associated ARVs in TLC-ART101 From the SC Space*

Drugs or vaccines deposited in the SC space may stay there or be taken up by lymph or blood capillaries. Free small molecules, peptides, and small proteins can permeate the ~5-12 nm intercellular pores between capillary blood endothelial cells and/or diffuse across the blood capillary endothelium (Sarin 2010), while ~70 nm DcNPs may be too large to readily enter blood capillaries. Using the near-infrared fluorescence marker indocyanine green (ICG) for real-time imaging in mice, we found that SC administered DcNP-associated ICG, but not free/soluble ICG, predominantly entered lymph vessels rather than blood vessels. Free ICG in mice penetrated into lymph as well as blood vessels, but only distributed to the first few lymph vessels and nodes draining the SC injection site; free ICG rapidly absorbed into the blood to a greater extent than DcNP-associated ICG (Kraft, Treuting et al. 2018). Due to the ~100-500-fold faster capillary blood flow compared to lymph capillary flow (Wiig and Swartz 2012), smaller molecules are preferentially absorbed from the SC space via the blood. This predominant route of absorption via blood for small molecules in the SC space was also observed with SC dosing of free hydrophobic doxorubicin or hydrophilic methotrexate in rats fitted with a thoracic lymph cannula, where ~64-74% of a SC dose was recovered in the blood, while ~0.063-2% was recovered in the lymph (Ryan, Kaminskas et al. 2013, Kaminskas, McLeod et al. 2015). With respect to larger particles, certain particles tend to be retained in the SC space, especially if their large size limits their convection through the ~100 nm interstitial water channels (Wiig and Swartz 2012). For instance, in pigs, ~105 nm negatively charged polymeric particles were mostly confined to the injection site 24 hr post-injection, while smaller ~55 nm counterparts traveled extensively to draining inguinal lymph nodes ~24 cm from the SC injection site (Khullar, Griset et al. 2012). In addition, in rats, ~83 nm PEGylated doxorubicin liposomes (*Doxil*®) mostly remained at the SC injection site for an

extended period (Ryan, Kaminskas et al. 2013). This is in contrast to ~70 nm DcNPs in TLC-ART101 that cleared from the SC injection site in mice, rats, and macaques within ~24 hr (personal observation). Taken together, these data are consistent with free ARVs predominantly clearing from the SC space via blood capillaries, while ~70 nm DcNPs are optimal for lymphatic uptake (**Figure 5.2**).

5.5.2 *Lymphatic First-Passage of DcNP-associated ARVs in TLC-ART101*

Since DcNP-associated ARVs cleared rapidly from the SC space and predominantly absorbed into the lymph capillaries, they are likely to first transit through the lymphatics before entering the blood. This delay in absorption into the systemic circulation is reflected in the longer T_{max} for ARVs in TLC-ART101 (~8-36 hr) versus in free formulation (~1-3 hr) (**Figures 5.4-5.5**); the latter directly enter the blood from the SC space. Importantly, the T_{max} values for all three ARVs in DcNPs (~8-36 hr) were much shorter than the days to weeks it takes for long-acting (LA) cabotegravir and LA rilpivirine to reach peak levels in humans (Spreen, Ford et al. 2014, McGowan, Dezzutti et al. 2016), in which case slow absorption controls the terminal decline of LA cabotegravir and LA rilpivirine over weeks, suggesting sustained release of free drug from an IM depot, and limited lymphatic uptake, distribution, and retention (as depicted in **Figure 5.2**). This is in contrast to DcNP-associated ARVs in TLC-ART101 that cleared readily from the SC injection site, were predominantly taken into lymph capillaries, distributed through lymph vessels to lymph nodes throughout the body, and reached peak plasma levels at ~6-8 hr. A slower rise in LA cabotegravir or LA rilpivirine plasma levels is expected due to the sustained release from slow dissolution of the nanocrystal of hydrophobic cabotegravir or rilpivirine (Owen and Rannard 2016); free drug released into the extracellular fluid is then taken up immediately into blood

capillaries. Thus, these formulations, by design, would require an extended time to reach T_{max} and therapeutic concentrations; as a result, an initial oral (lead-in) dose supplement is essential to more quickly reach target peak levels (Margolis, Gonzalez-Garcia et al. 2017), complicating these IM long-acting regimens. Such an oral lead-in is probably unnecessary for the TLC-ART101 formulation. Avoiding an oral lead-in strategy could simplify treatment and improve patient adherence.

The parallel rise and peak in plasma levels over 8 hr of the lipophilic ARVs (LPV, RTV) associated to DcNPs (**Figure 5.1A, 5.1B**) also suggest ARVs remain associated to DcNPs *in vivo*. If large amounts of ARVs released from DcNPs prematurely, they would clear in a matter of hours as free ARVs are, they would not preferentially distribute throughout and be retained within the lymphatics, and would not exhibit plasma persistence for 2 weeks or more (**Figure 5.1**). TFV in TLC-ART101 exhibited an early T_{max} at ~1 hr, which resembled the free TFV plasma PK profile (**Figure 5.1C**); this suggests a significant fraction of the TLC-ART101 formulation is present in free form (e.g., ~90%), consistent with *in vitro* equilibrium dialysis results. The most remarkable finding was the persistence of plasma TFV that occurred with only ~10% of the TFV dose associated to DcNPs; TFV must be firmly associated to sufficiently stable DcNPs with limited extravascular distribution and long blood circulation lifetimes.

5.5.3 *Widespread Lymphatic Distribution and Retention of ARVs in TLC-ART101*

Our recent data in macaques show widespread lymph node distribution (Freeling and Ho 2014) and long-term LNMC retention (Kraft, McConnachie et al. 2017) of DcNP-associated ARVs. Intracellular ARV levels in LNMCs at 1 and 8 days after a single SC dose were persistently

higher than those in PBMCs, and in turn levels in PBMCs were persistently higher than those in plasma over the 2-week experiment (Kraft, McConnachie et al. 2017), demonstrating the lymphocyte-targeting properties of the TLC-ART101 formulation. These high concentrations of ARVs in LNMCs relative to those in PBMCs and plasma suggest DcNP-associated ARVs are sequestered during lymphatic first-pass and accumulate in lymphocytes.

Such intracellular delivery performance for these ARVs in lymphocytes is unprecedented. In pharmacokinetic studies in rats and humans dosed orally with LPV and RTV, the whole blood/plasma ratio for LPV was 0.44-0.50 and for RTV was 0.26-0.68 (Denissen, Grabowski et al. 1997, Kumar, Jayanti et al. 2004). In these studies, the lymph node/plasma ratio in rats for LPV was 0.19-0.55 (Kumar, Jayanti et al. 2004). In HIV-infected persons, LPV and RTV concentrations in whole blood were reported to be lower than those in plasma (Koal, Burhenne et al. 2005). Collectively, these studies show that LPV and RTV, administered either as a free/soluble injectable or an oral dosage form, are taken up poorly into blood cells, and LPV has limited penetration into lymph nodes. However, since erythrocytes comprise >99% of the whole blood cellular fraction, LPV and RTV penetration in PBMCs may be different than in erythrocytes. Still, in HIV-infected persons, the PBMC/plasma ratio for LPV was 0.34-0.55 and for RTV was 0.46 (Colombo, Beguin et al. 2005, Colombo, Telenti et al. 2006, van Kampen, Reedijk et al. 2010), indicating poor PBMC penetration. For TLC-ART101, a single SC dose in macaques exhibited PBMC/plasma ratios of 4.01 for LPV, 7.40 for RTV, and 3.01 for TFV. Thus, compared to a free/soluble injectable or an oral dosage form, association of LPV and RTV to DcNPs has increased their respective PBMC/plasma ratios by ~7-12-fold and ~16-fold. For hydrophilic TFV, which is negatively charged at physiological pH 7.4, a single SC dose of TLC-ART101 produced a much greater

PBMC exposure (AUC) to the intracellular active metabolite of TFV, TFV-diphosphate (TFV-DP), by ~7-fold compared to a single 1.5 mg/kg oral dose of the TFV prodrug tenofovir alafenamide (TAF) in macaques (Massud, Mitchell et al. 2016, Kraft, McConnachie et al. 2017). The detailed mechanisms behind these strikingly enhanced intracellular ARV levels in LNMCs and PBMCs, the most commonly infected cells, remain to be elucidated. However, it is likely that the preferential lymphatic uptake of DcNPs from the SC space and the widespread lymphatic distribution and retention over long durations promote the uptake of DcNPs by lymphocytes in lymph nodes, which can traffic from lymph nodes to the blood either via lymph flow through the thoracic duct or via HEVs in lymph nodes. The MBPK models reported here could serve as a base model to account for accumulation of ARVs in target intracellular compartments, viz. PBMCs and LNMCs.

As mentioned, within the lymph node, DcNPs could access and be retained in the ~1-500 μm sinus spaces (Drinker, Field et al. 1934), where they could readily be taken up by LNMCs. This deep lymph node retention (e.g., in LNMCs) could be a component of sequestered DcNP-associated ARVs within the lymphatics that contribute to the relatively long lag times and sustained levels in plasma (**Table 5.2**). For the models to sustain persistent plasma ARV levels, we postulated three different "waves" of release (having an early, intermediate, or late transit time) of DcNP-associated ARVs from the lymphatics into the systemic circulation (**Table 5.2**). LPV and RTV concentrations both had a rapid initial peak in the first 0.5 to 1 hr and subsequently continued to rise quickly over the first 6 hr (**Figure 5.1A, 5.1B**), suggesting an initial rapid wave of ARVs in DcNPs entering and exiting the lymphatics. This was followed by an intermediate wave of DcNPs between 8 to 24 hr as evidenced by the rebound in the TFV concentration (**Figure 5.1C**).

Finally, there was a late and protracted emergence of ARVs in DcNPs beyond 48 hr that sustained measurable plasma levels for over 2 weeks (**Figure 5.1**). Thus, it is possible a fraction of the ARVs in DcNPs within the lymphatics moves rapidly through the major lymphatic vessels, another fraction moves less rapidly due to travel through the diffuse branched vessels and/or being trapped temporarily in the sinus spaces in lymph nodes, and a third fraction is retained in lymph nodes where they may be taken up by lymphocytes and then released slowly into the blood. The slow release of ARVs into the blood (the second and third "waves") could occur either by (1) DcNPs being carried by lymph flow or (2) lymphocytes, which have taken up DcNPs in lymph nodes, trafficking into the blood and slowly releasing ARVs into the plasma. It is the second and third fractions that primarily contributed to persistent plasma LPV and TFV levels of TLC-ART101 by continuously supplying DcNP- and lymphocyte-associated ARVs to the blood (**Figure 5.1A, 5.1C**). It is noteworthy that k_{31} and k_{41} (lymphatic entry rate constants) and *tlag*2 and *tlag*3 assumed greater importance than k_{21} and *tlag*1 for LPV and TFV (**Table 5.2**), illustrating that the second and third lymphatic delay compartments contributed the most to the long-acting plasma PK of LPV and TFV.

Thus, more of the LPV dose entered the deeper ("slower") lymphatic pathways to enable the extended persistence of lipophilic LPV in the plasma (see k_{31} and k_{41} versus k_{21} rate constants in **Table 5.2**). In contrast, due to its relatively low dose that is not able to fully leverage the lymphatic system as a sustained release drug depot, lipophilic RTV in TLC-ART101 was mostly eliminated from the plasma by ~100 hr (**Figure 5.1B**); accordingly, the model shows that the main contribution to RTV plasma PK resulted from RTV transit through the "fast" initial lymphatic pathway (i.e., k_{21} was the largest lymphatic uptake rate constant for RTV) (**Table 5.2**).

Interestingly, the k_{31} and k_{41} rate constants for LPV and TFV in TLC-ART101 (**Table 5.2**), which are equal to their respective k_{53} and k_{54} rate constants for release of DcNP- and lymphocyte-associated ARVs from the lymphatics into the systemic circulation, are approximately equal to the 0.204 hr^{-1} rate constant reported in the literature for ^{51}Cr-labeled lymphocytes trafficking out of lymph nodes into the blood in rats (Ganusov and Auerbach 2014). Thus, these k_{31} and k_{41} rate constants for LPV and TFV in TLC-ART101 could reflect the movement of ARV-loaded lymphocytes from lymph nodes into the blood (compartment 5, where ARVs are bound to either DcNPs or lymphocytes, **Figure 5.3C, 5.3D**). This suggests lymphocytes that have internalized DcNPs in lymph nodes and then trafficked into the blood circulation may be a major contributing mechanism to the long-acting PK observed in plasma. Furthermore, the rate constant of release of free ARVs in the systemic circulation is represented by k_{75}, which is a composite rate constant representing ARV release from both DcNPs and lymphocytes. Note that k_{75} for lipophilic LPV and RTV are ~5-9-fold *higher* than the respective elimination rate constant k_{07} for free LPV and RTV from the systemic circulation (**Table 5.2**). This indicates that the lipophilic ARVs are being released from DcNPs and lymphocytes as their free form into the plasma at rates faster than those they are eliminated by, creating an *elimination rate-limited* process that enables the sustained presence of free LPV and RTV in the plasma. In contrast, k_{75} for hydrophilic TFV is ~36-fold *lower* than its free drug elimination rate constant k_{07} (**Table 5.2**), suggesting that TFV must remain tightly bound to DcNPs (perhaps to PEG) and/or is efficiently retained in lymphocytes. It is likely that the stable association of TFV to PEG and the enhanced lymphocyte uptake and retention of TFV enables the dramatically persistent plasma and intracellular levels of TFV.

In sum, the kinetic insights derived from the MBPK models suggest the lymphatic system itself acts as a body-wide drug depot for the DcNP-associated ARVs in the TLC-ART101 formulation. In contrast to reports on lymphatic uptake of SC proteins and nanoparticles that suggest interstitial transit being the rate-limiting step (Porter and Charman 2000, Swartz 2001), lymphatic transit and retention are the more prevalent rate-limiting steps for absorption of TLC-ART101 into the blood. To our knowledge, this is the first suggestion that the lymphatic system itself could serve as a distributed body-wide drug depot to enable long-acting plasma drug exposure. Although lymphatic transit of DcNPs that are sufficiently stable to not prematurely release drug is important, there are a number of questions that remain, for example: (1) how ARVs carried by DcNPs are internalized by lymphocytes, (2) how lymphocytes in the blood release ARVs, and (3) how DcNPs in the blood release ARVs. To address these insights, additional *in vitro* experiments such as those investigating (1) the rate of DcNP and ARV uptake into lymphocytes, (2) the rate of ARV release from DcNPs in blood, and (3) the rate of ARV release from lymphocytes circulating in the blood could begin to discern the role and significance of each of these steps. Investigations are being planned to gain a deeper understanding of these and other processes (such as the impact of the biological identity and protein corona on DcNPs) that drive the long-acting intracellular and plasma PK that result from DcNPs in TLC-ART101 leveraging the lymphatic system as a body-wide drug depot.

5.5.4 *Limited Blood Extravasation of DcNP-associated ARVs in TLC-ART101*

In addition to lymphatic uptake and first-pass lymphatic distribution and retention of DcNP-associated ARVs, followed by slow release of ARVs into the blood from the lymphatics, limited blood extravasation of circulating DcNPs in blood likely contributed to the LPV and TFV

persistence in the plasma (**Figure 5.1A-5.1C**). In **Table 5.2**, the ~7- to 13-fold lower V5_DcNP versus V7_Free for both LPV and TFV indicated limited extravasation of DcNP-associated ARV versus free ARV.

It has been shown in rats with a thoracic lymph duct cannula and dosed IV with ~83 nm of PEGylated liposomal doxorubicin (similar in size to DcNPs in TLC-ART101), ~14% of the IV dose was recovered in lymph at 30 hr (i.e., ~14% extravasated from the blood into the interstitium, and subsequently entered the lymphatics) (Ryan, Kaminskas et al. 2013). Thus, since a minor fraction of the DcNPs circulating in the blood may extravasate and be available for re-entry into the lymphatics, this process should be considered as part of the systemic compartment (q5) for DcNP-associated ARVs (**Figure 5.3C, 5.3D**). Another consideration is that PEGylation of the lipid membrane surface significantly enhanced plasma circulation lifetimes of ~110 nm liposomes (Allen, Hansen et al. 1991). Hence, it is likely that inclusion of $mPEG_{2000}$ on the DcNP surface of slightly smaller particles may impart long-circulation behavior of DcNPs to the TLC-ART101 formulation.

There remains much to learn about the detailed mechanisms of the long-acting PK of TLC-ART101. It is instructive to compare the PK of lipophilic LPV and RTV between the free and TLC-ART101 formulations. While CL/F and MBRT were similar for free LPV and RTV, these statistical moment derived PK parameters were different for LPV and RTV in TLC-ART101 (**Table 5.1**), suggesting LPV and RTV, when associated to DcNPs, could have different cellular uptake and efflux, release from DcNPs, and tissue distribution profiles. Moreover, free LPV and RTV had similar $t_{1/2}$ values (~8 hr), while the $t_{1/2}$ of DcNP-associated LPV was ~11-fold longer

than that of DcNP-associated RTV (**Table 5.1**), further indicating drug release from DcNPs and tissue distribution differed between these two drugs. Elucidating the details of these PK differences between LPV and RTV (as well as TFV) in TLC-ART101 requires further investigation—possibly including sampling of lymph vessel and node drug concentrations throughout the body and defining pre-systemic clearance mechanisms. Many of the uncertainties of the systemic PK of TLC-ART101 could be elucidated in further studies such as an IV study and being able to measure the time-course of free versus DcNP-associated ARV in the plasma (Stern, Martinez et al. 2016). Currently, the plasma PK of DcNP-associated ARVs after dosing TLC-ART101 is unknown.

5.5.5 *Conclusion*

In conclusion, we developed the first mechanism-based PK (MBPK) models to simultaneously describe the complex long-acting plasma and lymphatic PK profiles of three ARVs associated to DcNPs all in one SC injectable formulation called TLC-ART101. These models anchored on plasma PK data are composed of two submodels: one for disposition of ARVs incorporated in DcNPs that undergo first-pass through the lymphatics, and one for free ARVs that are routed directly into the blood circulation. Subsequent model improvements incorporating LNMC and PBMC intracellular compartments (cells in the lymph nodes and blood) would provide additional insights on ARV access to these sites. These additional data may allow for predicting the impact of TLC-ART101 dosing regimens on viral clearance in lymph nodes where ~75% of HIV-infected cells (CD4+ T lymphocytes) reside. At present, these first-generation MBPK models suggest the lymphocyte-targeting and long-acting PK of ARVs associated to DcNPs are due to (1) preferential lymphatic uptake from the SC space, (2) first-pass transit through the lymphatics (throughout the vessels and nodes in the body), (3) lymphatic (lymph vessel and node) retention,

(4) eventual release of ARVs into the blood from the lymphatics, and (5) limited extravascular distribution out of blood vessels of DcNP-associated ARVs.

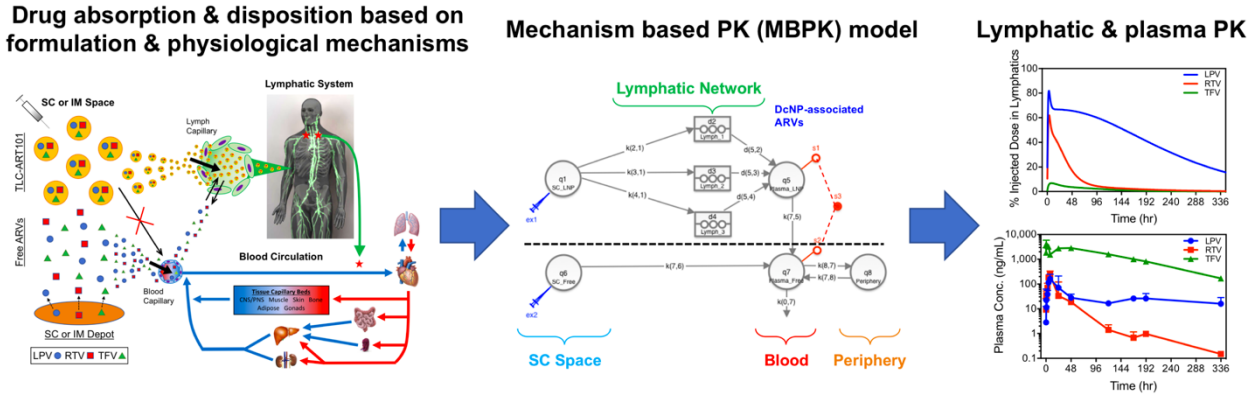

Figure 5.0. Graphical abstract.

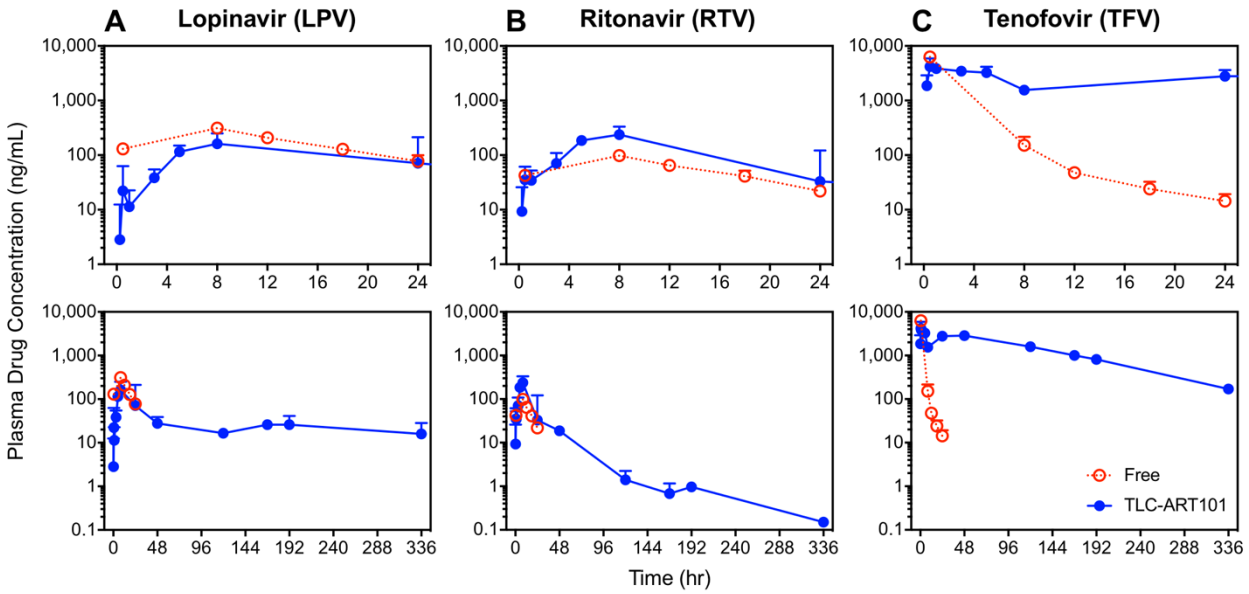

Figure 5.1. Plasma concentration-time profiles of lopinavir (LPV; panel A), ritonavir (RTV; panel B), and tenofovir (TFV; panel C) in macaques following a single SC dose of the triple-drug combination in either the soluble ("free"; red open circles [O] and dotted line) or TLC-ART101 (blue closed circles [•] and solid line) formulation.

The top graphs in panels A, B, and C are plasma concentration-time profiles of the first 24 hr after SC dosing, and the bottom graphs are the entire time course over 336 hr (2 weeks). Please note the differences in the y-axis scales for the top graphs over 24 hr to highlight relevant plasma concentrations for each ARV. Plasma limit of quantification (LOQ)/limit of detection (LOD) = lopinavir: 10/5, ritonavir: 50/25, tenofovir: 250/100 pg/mL. Ritonavir (intended as a PK booster for lopinavir) in plasma after TLC-ART101 dosing was <LOQ in N=2 at 192 and 336 hr. Geometric mean ± SD (N=3-8).

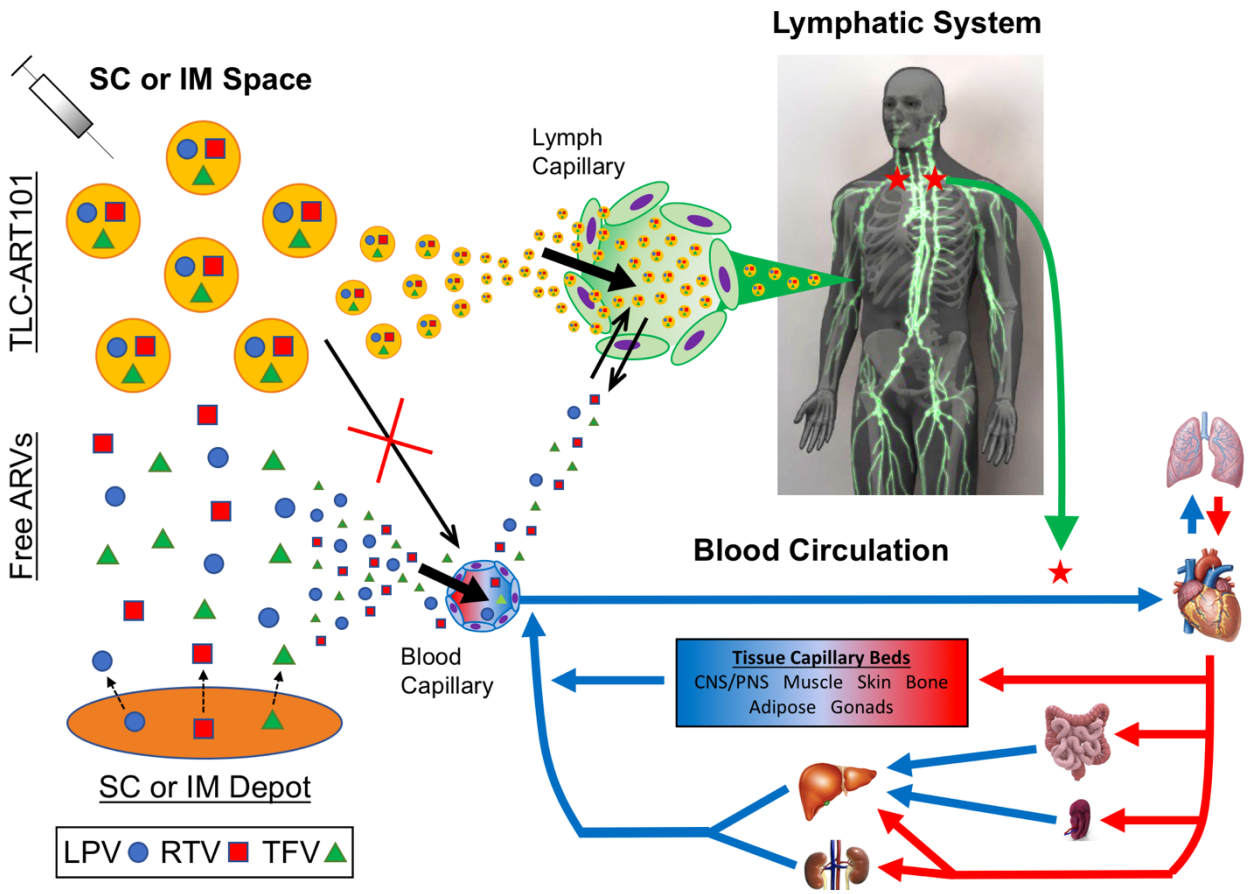

Figure 5.2. Schematic representation of the differential absorption and disposition pathways of ARVs associated to DcNPs in TLC-ART101, free, or in a stationary depot in the SC or IM space.

In the SC space, ARV combinations (e.g., lopinavir [LPV], ritonavir [RTV], and tenofovir [TFV]) associated to drug combination nanoparticles (DcNPs) and referred to as "TLC-ART101," are too large to enter blood capillaries, and thus preferentially enter lymph capillaries. While free ARVs in the SC space can enter lymph capillaries initially due to a strong concentration gradient driving drug out of the SC space, free ARVs are not able to be retained in the lymphatics and can easily diffuse back into the SC space as the diffusion gradient reverses direction over time. Overall, free ARVs preferentially enter the blood from the SC space, largely due to the 100-500-fold faster blood flow via capillaries than lymph flow. A stationary SC or intramuscular (IM) depot that provides a sustained release reservoir of free drug would follow the same principles for free drug and thus would also be predominantly absorbed directly into the blood. Once in lymphatic capillaries, TLC-ART101 particles would undergo first-pass distribution throughout the lymphatic system before entering the systemic blood circulation. In contrast, free drug that mostly enters the systemic circulation would undergo distribution, metabolism, and excretion mechanisms characteristic to the free drug molecule.

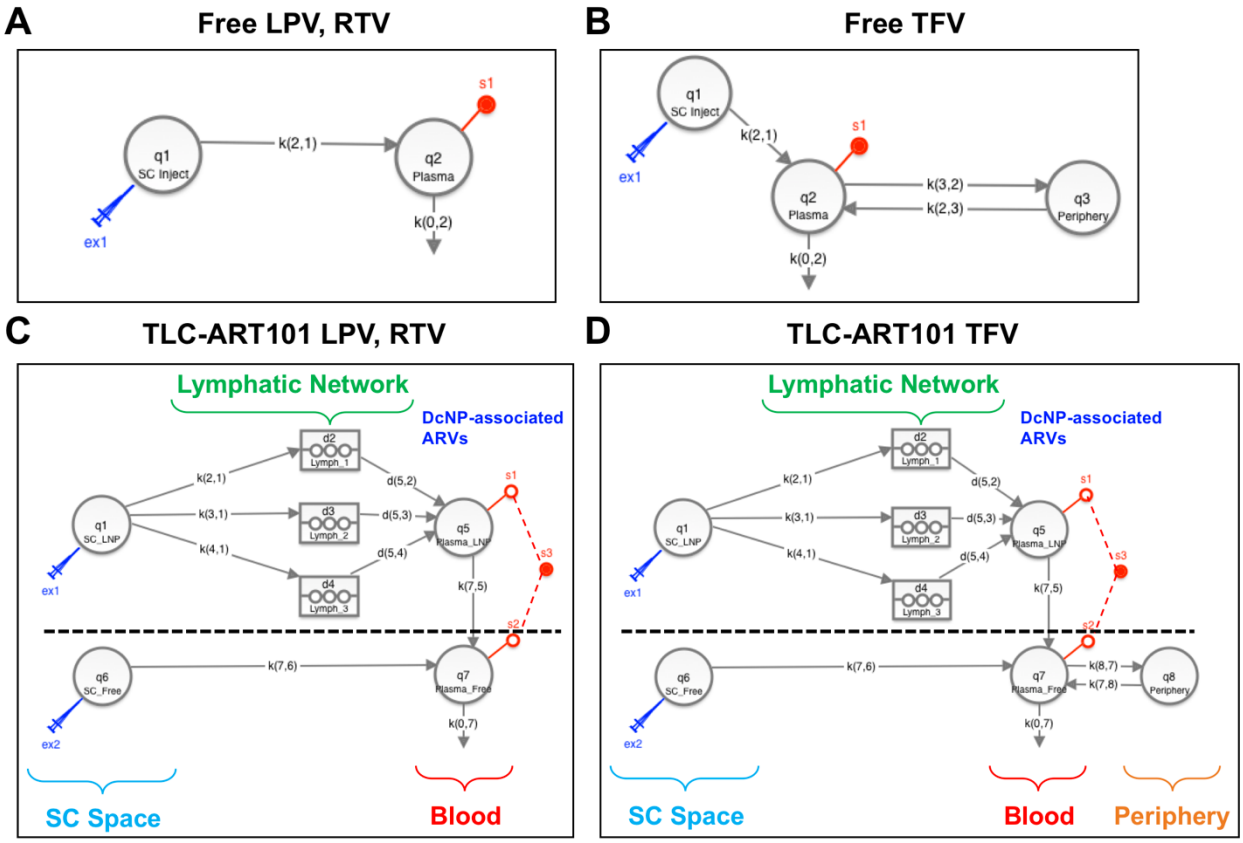

Figure 5.3. Structural models for free drug disposition in the systemic circulation (panels A, B) and TLC-ART101 disposition in the lymphatics and systemic circulation (panels C, D) after SC dosing.

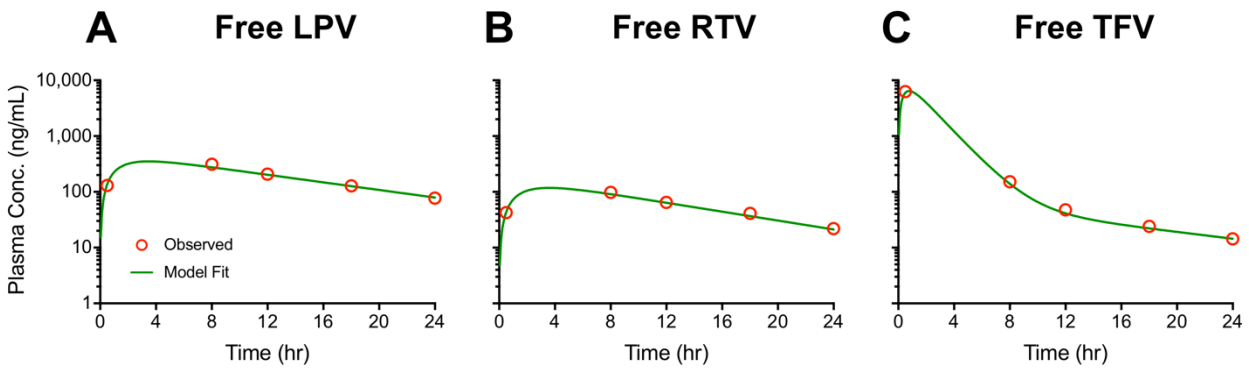

Figure 5.4. Observed (symbols) and fitted (curves) plasma concentration-time profiles of lopinavir (LPV, panel A), ritonavir (RTV, panel B), and tenofovir (TFV, panel C) in macaques after a single SC dose of the free and soluble triple-drug combination (N=3).

Symbols represent the geometric mean plasma concentration, and green curves represent the fits that resulted from population analysis.

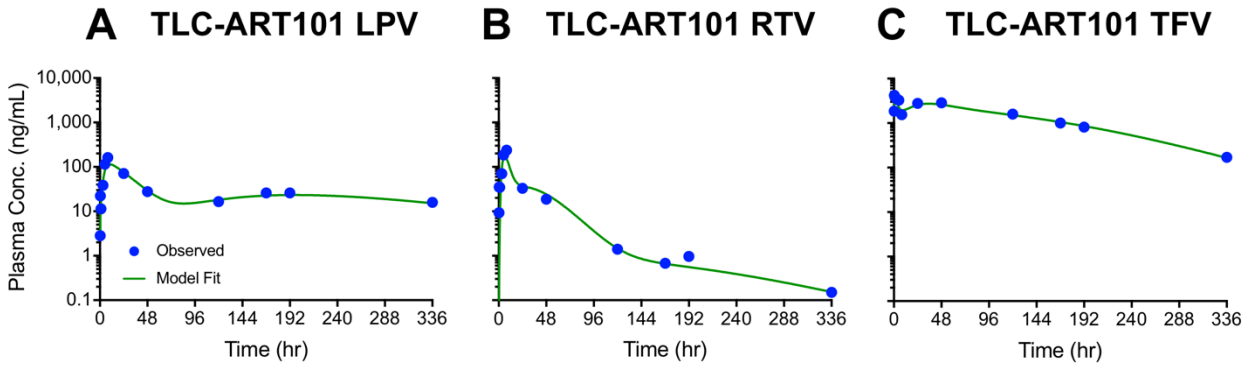

Figure 5.5. Observed (symbols) and fitted (curves) plasma concentration-time profiles of lopinavir (LPV, panel A), ritonavir (RTV, panel B), and tenofovir (TFV, panel C) in macaques after a single SC dose of TLC-ART101 (N=8).

Symbols represent the geometric mean plasma concentration, and blue curves represent the fits that resulted from population analysis.

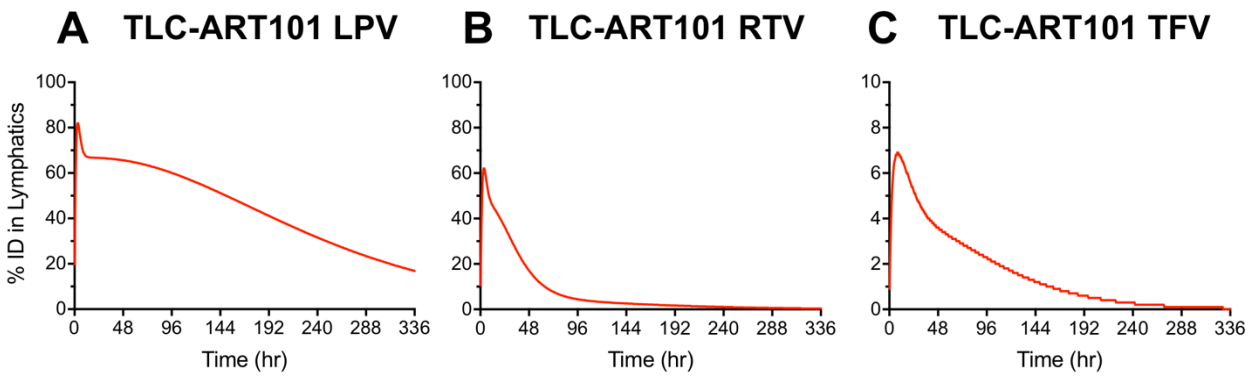

Figure 5.6. Simulated time-course of the percentage of injected dose (%ID) of lopinavir (LPV, panel A), ritonavir (RTV, panel B), and tenofovir (TFV, panel C) in the lymphatics after a single SC dose of TLC-ART101.

Table 5.1. Descriptive non-compartmental plasma pharmacokinetic (PK) parameters for each drug in the triple-drug combination given as a single SC dose in either the free or TLC-ART101 formulation.

	Lopinavir (LPV)		Ritonavir (RTV)		Tenofovir (TFV)	
	Free	**TLC-ART101**	**Free**	**TLC-ART101**	**Free**	**TLC-ART101**
AUC[a] (hr•μg/mL)	**4.35** (7)	**10.98** (48)	**1.37** (9)	**4.80** (57)	**14.4** (4)	**416.55** (15)
Terminal $t_{1/2}$ (hr)	**8.65** (28)	**476.94** (173)	**7.99** (38)	**44.06** (46)	**8.01** (51)	**65.33** (11)
CL/F (L/[hr•kg])	**4.64** (14)	**0.85** (85)	**4.23** (15)	**1.43** (56)	**0.72** (4)	**0.02** (15)
MBRT[b] (hr)	**10.83** (5)	**116.09** (8)	**10.78** (5)	**24.86** (9)	**2.61** (12)	**102.68** (7)

Geometric Mean (% coefficient of variation).
Free, N=3 (M10088, R10125, T10111); TLC-ART101, N=4 (R10125, Z11084, M10068, R10142).
[a] $AUC_{0\text{-}24h}$ for Free, $AUC_{0\text{-}336h}$ for TLC-ART101.
[b] $MBRT_{0\text{-}24h}$ for Free, $MBRT_{0\text{-}336h}$ for TLC-ART101.
AUC, area under the plasma drug concentration-time curve; CL/F, apparent total clearance; MBRT, mean body residence time; $t_{1/2}$, apparent terminal plasma drug half-life.
AUC and $t_{1/2}$ values for TLC-ART101 only (not free drug) were recently reported elsewhere (Kraft, McConnachie et al. 2017). They are included here for comparison to free drug.

Table 5.2. Model-derived pharmacokinetic parameters for each drug in the triple-drug combination given as a single SC dose in either the free or TLC-ART101 formulation.

	Free Lopinavir	**Free Ritonavir**	**Free Tenofovir**
V/F (L/kg)	**54.10** (6)	**42.41** (24)	**1.44**[a]; **8.65**[b]
$\mathbf{k_{21}}$ (1/hr)	**0.7120** (20)	**0.6242** (29)	**2.3423** (38)
$\mathbf{k_{02}}$ (1/hr)	**0.0784** (17)	**0.0919** (22)	**0.5896** (-)
$\mathbf{k_{32}}$ (1/hr)	-	-	**0.0298** (0)
$\mathbf{k_{23}}$ (1/hr)	-	-	**0.0738** (-)
$\mathbf{t_{1/2}}$ (hr)	**8.85**	**7.54**	**1.11**[c]; **9.93**[d]
CL/F (L/[hr•kg])	**4.24**	**3.90**	**0.60**
	TLC-ART101 Lopinavir	**TLC-ART101 Ritonavir**	**TLC-ART101 Tenofovir**
$\mathbf{k_{21}}$ (1/hr)	**0.0278** (-)	**0.2361** (-)	**0.1300** (-)
$\mathbf{k_{31}}$ (1/hr)	**0.1236** (-)	**0.1881** (-)	**0.1588** (-)
$\mathbf{k_{41}}$ (1/hr)	**0.3050** (-)	**0.0198** (-)	**0.1779** (-)
tlag1 (hr)	**2.15** (43)	**2.13** (51)	**0.10** (-)
tlag2 (hr)	**10.85** (29)	**38.83** (13)	**24.04** (19)
tlag3 (hr)	**262.23** (12)	**181.87** (11)	**122.06** (3)
V5_DcNP (L/kg)	**6.53** (3)	**10.09** (27)	**0.17** (22)
$\mathbf{k_{75}}$ (1/hr)	**0.6836** (30)	**0.4336** (5)	**0.0164** (15)
$\mathbf{k_{76}}$ (1/hr)	-	-	**1.4201** (-)
$\mathbf{k_{78}}$ (1/hr)	-	-	**0.0738** (0)
$\mathbf{k_{87}}$ (1/hr)	-	-	**0.0298** (-)
V7_Free (L/kg)	**83.82** (1)	**67.94** (3)	**1.66** (18)
$\mathbf{k_{07}}$ (1/hr)	**0.0788** (3)	**0.0962** (4)	**0.5824** (2)

Parameter value (% coefficient of variation).

[a] V_{ss}/F

[b] V_{β}/F

[c] $t_{1/2,alpha}$

[d] $t_{1/2,beta}$

-, not available due to being "fixed" or not applicable.

Chapter 6. **Summary and Future Directions**

6.1 SUMMARY

The lymphatic system is central to multiple diseases that burden hundreds of millions of individuals worldwide, yet there currently is a lack of effective therapies for lymphatic diseases due to the lymphatic system and its exposure to drugs being poorly understood. In this thesis, we developed tools to sensitively probe and study the complex, body-wide distributed network of lymph vessels and nodes and their exposure to drug. Through employing these tools to understand the lymphatic exposure to HIV drug combinations delivered by drug combination nanoparticles (DcNPs), we discovered novel mechanisms for enhancing and prolonging the lymphatic exposure to drug combinations. These are highly valuable tools for researchers, health providers, and pharmaceutical scientists to help assess the details of drug time course and lymphatic exposure in the complex lymphatic network. Furthermore, these tools, the novel DcNP platform, and the novel pharmacokinetic concepts we discovered can be leveraged together to help develop lymphatic-targeted drug combinations for the treatment of other diseases that exploit the lymphatic system (such as infection, cancer, lymphedema, metabolic diseases, and inflammatory diseases). These tools, concepts, and the lymphoid-tissue targeting ability of DcNPs can also be leveraged for the development of vaccines with higher potency.

In this thesis, our central hypothesis was that the formation of body-wide drug depots in lymph nodes and lymphocytes by DcNPs injected subcutaneously resulted in lymphocyte-targeting and long-acting pharmacokinetics (PK) of small molecule drug combinations. This hypothesis was an outgrowth of our observation that in non-human primates administered DcNPs subcutaneously and studied for two weeks, the concentrations of three drugs in a combination were persistently highest in lymph node lymphocytes, which were higher than those in blood

lymphocytes, which were in turn higher than plasma concentrations (Kraft, McConnachie et al. 2017). Thus, drug levels in HIV host cells in the lymph nodes and the blood were persistently higher than drug levels in the plasma, and levels in lymph node lymphocytes were consistently higher than those in blood lymphocytes. This is opposite of the drug levels achieved after conventional oral antiretroviral therapy (**Table 1.3**) and other leading long-acting anti-HIV injectables (**Figure 1.4**), which result in higher plasma than intracellular drug levels. As a result, our study was the first to show lymphocyte-targeted and long-acting drug levels of multiple drugs in lymph node lymphocytes (LNMCs) for over 1 week after a single dose in primates [previous studies only reported up to 24 hours and did not compare intracellular drug concentrations to plasma concentrations (Freeling, Koehn et al. 2014)]. It was also the first to show lymphocyte-targeted and long-acting drug levels of multiple drugs in blood lymphocytes (PBMCs) for over 2 weeks, and long-acting levels of drug combinations in the plasma for over 2 weeks, following a single dose in primates [previous studies only reported up to 1 week (Freeling, Koehn et al. 2014)]. As shown in **Figure 6.1**, compared to a single 1.5 mg/kg oral dose of tenofovir alafenamide (TAF) in macaques (Massud, Mitchell et al. 2016), the estimated dose-normalized intracellular exposure in PBMCs to tenofovir diphosphate (TFV-DP) was ~7-fold higher after a single dose of DcNPs. This highlights the unprecedented and unique ability of DcNPs to target hydrophilic and negatively-charged drugs such as tenofovir to lymphocytes, and to achieve intracellular TFV-DP levels similar to or higher than those from TAF. These results are highly significant because they were the first proof-of-principle that a single dose of DcNPs targeted and sustained drug levels in the lymphocytes in lymph nodes, and in addition, produced long-acting drug levels in the plasma as well as in lymphocytes in the blood. From the results in this study, we hypothesized that lymphatic first-pass distribution of DcNPs from the subcutaneous space is key to targeting drug

combinations to lymph nodes. We then proceeded to develop tools to elucidate the mechanisms that contributed to these unique pharmacokinetic properties we observed for DcNPs.

To be able to elucidate the *in vivo* distribution pathways of DcNPs from the SC space that enable the observed lymphocyte-targeting and long-acting behavior, we developed a novel near-infrared imaging tool to track in real-time the *in vivo* distribution pathways of DcNPs (Kraft and Ho 2014). We tagged the lipid-stabilized DcNP formulation with the clinically-approved and widely used near-infrared small molecule indocyanine green (ICG). We found the lipid:ICG molar ratio that maximally enhanced and stabilized the fluorescence intensity of ICG *in vitro* was 250:1. This was the first study to systematically characterize the optimal lipid-drug interactions to maximize the brightness and stability of ICG fluorescence. This technology has significant potential to be developed into a clinical tool for near-infrared mapping of the lymphatics during surgery and other procedures. It could be used as a tool for opening up a new treatment approach that involves assessing the impact of disease-mediated and treatment-mediated changes in lymphatic function on lymphatic access of drugs to help guide therapeutic decisions. It can also be used for tracking other DcNP formulations *in vivo*.

In order to test the sub-hypothesis that DcNPs in the SC space are taken up by, distribute throughout, and are retained in lymph vessels and nodes, we used the ICG-tagged DcNPs we developed above to visualize the absorption of DcNPs from the SC space into lymphatic or blood vessels and their subsequent distribution throughout the body in mice (Kraft, Treuting et al. 2018). We found that DcNPs rapidly clear from the SC injection site, they are extensively taken up into lymph capillaries (not blood capillaries), they distribute widely throughout the lymph vessel and

node networks in the whole body, they are retained by lymph vessels, and they are retained for long durations in multiple lymph nodes along the lymphatic network that drains the injection site. This exclusive lymphatic uptake from the SC space, and first-pass lymphatic distribution and lymph node retention, prior to entering the blood, confirmed the hypothesis that DcNPs distribute directly to and widely throughout the lymphatic vessel and node networks as a first step to enable the observed lymphocyte-targeting and long-acting pharmacokinetics of drug combinations.

To further elucidate the underlying formulation- and physiological-based mechanisms of the lymphocyte-targeting and long-acting behavior of DcNPs, we developed mechanism-based pharmacokinetic (MBPK) models using non-human primate plasma pharmacokinetic data following a single dose of DcNPs or a free drug mixture of the same drug combination (Kraft, McConnachie et al. 2018). Based on the experimental validation of the exclusive lymphatic uptake and first-pass lymphatic distribution and retention of DcNP-bound drug combinations (Kraft, Treuting et al. 2018), these models routed SC-injected DcNP-associated drug to the lymphatics before entering the blood, and not directly into blood capillaries from the SC space. We found these MBPK models could simultaneously describe the complex long-acting plasma and lymphatic PK profiles for all three drugs in DcNPs. The modelling revealed that the complex plasma profiles were best described by three "waves"—a rapid, intermediate, and slow wave—being released from the lymphatics into the blood. While the exact mechanisms that contribute to these waves remain to be determined, it is likely that they result from drug entering the plasma through (1) lymph flow, (2) drug being slowly released from lymph nodes into the plasma, and/or (3) lymph node lymphocytes loaded with drug trafficking out of lymph nodes into the blood and then slowly releasing their drug cargo into the plasma.

Overall, results from the modelling suggested the long-acting PK characteristics of these drugs in DcNPs were likely due to a combination of mechanisms including: (1) preferential lymphatic uptake of DcNPs from the SC space, (2) retention in lymph nodes during lymphatic first-pass, (3) subsequent slow release of drugs into the blood circulation, and (4) limited extravasation of DcNP-associated drug that resulted in longer persistence in the circulation. These are the first mechanistic PK models of a nanoparticle-bound drug combination that describe the time-course of plasma concentration and lymphatic retention of multiple drugs formulated in a single nanosuspension. For the first time, these models enabled prediction of the long-acting PK of each drug in both the plasma and lymphatics and closely matched validation data sets. These models revealed the novel concept that loading the lymph nodes in the body with DcNPs can allow the lymph nodes and lymphocytes to serve as body-wide drug depots that then elicit long-acting pharmacokinetics in lymph node and blood lymphocytes as well as the plasma. This was a key finding that supported the central hypothesis of this thesis. In contrast to most long-acting drug formulations where a drug depot resides at the injection site and slowly releases drug into the systemic circulation (Jucker, Alsaid et al. 2017), DcNPs do not predominantly remain at the injection site as a depot. Instead, lymph nodes and lymphocytes become loaded with drug (via lymphatic first-pass distribution and retention of DcNPs). Then, lymph nodes and lymphocytes act as body-wide drug depots that slowly release drug into the plasma over time, and produce the persistent drug levels in the plasma. Overall, these MBPK models serve as a foundation on which detailed characteristics of drug uptake and release from lymphocytes may be added in future, more complex, iterations of these models to further elucidate the targeting and long-acting mechanism.

In summary, the results of this thesis demonstrate for the first time that exclusive uptake of DcNPs from the SC space into the lymphatics, and extensive first-pass lymphatic distribution and lymph node retention—creating body-wide depots in lymph nodes and lymphocytes—produce the lymphocyte-targeting and long-acting behavior of drug combinations in DcNPs. At the heart of this thesis is the discovery that DcNPs leverage lymph nodes and lymphocytes throughout the body as drug depots; this enables the lymphocyte-targeting and long-acting pharmacokinetics of small molecule drug combinations. The unique DcNP formulation enables the stable combination of small molecules with diverse physicochemical properties such as lipophilic lopinavir and ritonavir and hydrophilic tenofovir. By changing the distribution profile of the nanoparticle-bound small molecules to home to the lymphatics in unison, this creates the opportunity for a drug combination to be taken up and retained by lymph node lymphocytes, and subsequently produce long-acting pharmacokinetics, which are not possible with the same small molecules freely soluble in a suspension.

This could be a highly valuable drug formulation platform to target other small molecule drug combinations to the lymphatics and lymphocytes, for example, for the treatment of cancers such as lymphoma, lymph node metastases, or to manipulate immune responses or a host of other diseases that involve the lymphatics. Through this thesis providing a more detailed understanding of the mechanisms that contribute to the *in vivo* behavior of this DcNP platform, one can better optimize its safety and efficacy. In addition, the near-infrared fluorescence imaging tool developed in this thesis could be used for real-time lymphatic mapping during surgery, as this product has clear advantages in terms of brightness, stability, and lymphatic uptake, distribution, and retention over the commonly used free ICG. ICG particles are also a valuable experimental tool for assessing

lymphatic function in health and disease. For example, in preliminary studies using ICG particles, we have characterized the differential lymphatic function and lymphatic drug exposure in diabetic mice treated with dapagliflozin, a clinically-approved sodium glucose co-transporter 2 (SGLT2) inhibitor for treating diabetic patients. Overall, with elucidation of the mechanisms for the long-acting and lymphocyte-targeting properties of DcNPs in this thesis, further work can be done to investigate the potential therapeutic impact of leveraging these mechanisms and this drug delivery platform for a wide variety of relevant drug combinations to treat lymphatic diseases and interact with the immune system for vaccination and promoting immune responses.

6.2 Future Directions[1]

This thesis established novel tools to assess lymphatic drug exposure and it discovered new mechanisms that may be used to enhance and prolong lymphatic drug exposure. These tools and mechanisms can be employed in future studies to develop technologies that detect, prevent, and/or treat lymphatic diseases. The broader next steps—to move the field forward—involve, in no particular order, (1) more detailed characterization of lymphatic drug levels in preclinical and clinical studies to gain a better understanding of lymphatic drug exposure, (2) a better understanding of how drugs and the DcNP carriers are handled by the body and the main factors

[1] The ICG nanoparticle technology developed in this thesis for lymphatic mapping using near-infrared fluorescence has been acquired by TongliBio, in Suzhou, China. Investor funding is currently being sought for IND-enabling studies for developing ICG particles as a clinical lymphatic mapping product. Planning is currently underway by the Targeted Long-Acting Combination Antiretroviral Therapy (TLC-ART) Program to test the DcNPs discussed in this thesis in a proof-of-concept Phase 0 first-in-human study at Harborview Medical Center in Seattle. Work has also begun on developing a novel physiologically-based pharmacokinetic (PBPK) model for DcNPs that incorporates the anatomical and physiological complexities of the lymphatic network. This will be a valuable tool for interspecies scaling and predicting lymphoid tissue pharmacokinetics at different sites in the body after dosing DcNPs as well as other small molecule and macromolecule drug formulations.

that impact their biodistribution and the persistence of drugs, and (3) developing capabilities to scale lymphatic drug exposure between preclinical species and humans.

With respect to the first "next step," the results of this thesis have strong implications for lymphatic drug exposure and long-acting pharmacokinetics in both experimental and clinical settings. Our results show that targeting drug combinations to lymph nodes and lymphocytes, and exhibiting long-acting PK in lymph nodes, lymphocytes, and the plasma, are highly dependent on direct and efficient lymphatic distribution and retention of drug combinations from the SC space. This has important implications for treating lymphatic diseases and vaccine development. A majority of preclinical studies on lymphatic drug delivery do not systematically characterize the clearance of drug from the injection site and the extent of drug distribution and retention in the lymph nodes throughout the body (Trevaskis, Kaminskas et al. 2015). Over decades, studies have focused on drug levels in local draining lymph nodes (Segal, Gregoriadis et al. 1975, Oussoren and Storm 2001, Ryan, Kaminskas et al. 2014) and use smaller animal models such as rodents, which have a much less complicated lymph vessel and node network than humans [e.g., mice and rats have ~30-50 lymph nodes in their body while humans have ~500] (Tilney 1971, Van den Broeck, Derore et al. 2006). They also largely focus on the first absorption step—whether drug enters lymph or blood capillaries—but do not systematically characterize what happens to drug as it transits through the complex lymphatic network of vessels and nodes (Kaminskas, Ascher et al. 2013, Ryan, Kaminskas et al. 2013, Chan, Bulitta et al. 2015). This makes it difficult to interpret the amount of the dose that leaves the injection site and distributes to, retains in, and clears from lymph vessels and nodes that are exposed to drug as it travels through the lymphatics before entering the blood. Through mass balance studies, understanding the fraction of the dose at the

injection site and in the draining lymph node network at different time points is key to the safety and efficacy of drug combination therapies and vaccines. Future studies to assess lymph node drug exposure should assay the injection site and multiple lymph nodes in the body at several time points and use higher species such as non-human primates, which have lymph node networks that more closely resemble that of humans. Although it is challenging to implement these studies, they are necessary to obtain a detailed understanding of lymphatic drug exposure.

In addition, the results of this thesis have strong implications for lymph node drug delivery studies in humans, especially for the treatment of HIV infection and even beyond for other diseases that also exploit the lymphatic system, such as cancer, lymphedema, metabolic diseases, and inflammatory diseases. The results of this thesis provide further evidence that free small molecules have limited ability to maintain drug levels in lymphoid tissues, and higher and more persistent drug levels in these tissues can be achieved with an appropriate drug delivery platform such as DcNPs. Since HIV infects lymphocytes in lymph nodes and lymphoid tissues throughout the body, and since antiretroviral drug levels in these tissues and cells are typically lower than those in the plasma after oral dosing, drug levels in these cells and tissues should be collected whenever possible in healthy and HIV-infected subjects. However, most clinical studies for HIV treatment focus on drug levels in blood lymphocytes and plasma (De Lepeleire 2017, Gallant, Thompson et al. 2017). Only a handful of studies have quantified drug levels in human lymph node mononuclear cells in peripheral lymph nodes, and these studies involve few individuals (Kinman, Brodie et al. 2003, Fletcher, Staskus et al. 2014, Lorenzo-Redondo, Fryer et al. 2016). Also, it is unknown how drug levels in gut lymph nodes and lymphocytes (a major tissue sanctuary for HIV) compare to those in peripheral nodes. Gaining a better understanding of lymphatic drug exposure in HIV

infection and the associated viral levels will likely enable important progress to made in terms of more effective anti-HIV therapies.

Moreover, the long-acting anti-HIV injectable products currently in clinical trials report only plasma drug levels (Margolis, Gonzalez-Garcia et al. 2017). Thus, it is challenging to estimate the drug levels in HIV target cells in blood and in lymph nodes/lymphoid tissues with these new formulations. Furthermore, without demonstrating that the antiviral efficacy is greater with these long-acting products in comparison to conventional oral cART, these new regimens may only extend the dosing interval—and thus improve patient convenience—as well as provide a new prophylactic option, without improving treatment efficacy, which is needed to make strides toward finding a cure for HIV. Similarly, the DcNP platform for HIV treatment will need to demonstrate enhanced efficacy and/or convenience for patients to be able to be translated into a clinically and commercially successful product that competes with existing oral cART regimens and other long-acting anti-HIV platforms in clinical development.

For the second "next step," there is much more to learn about the mechanisms that drive the *in vivo* behavior of DcNPs. A more detailed understanding is needed at the level of the interactions of DcNPs and cells and *in vivo* microenvironments and how these interactions drive the long-acting pharmacokinetics. Studies to gain this understanding could involve investigating the rates and extents that lymphocytes uptake DcNPs and which lymphocyte subsets are mostly involved. It is also not well understood what the major factors are that impact the direct distribution of DcNPs from the SC space to the lymph vessel and nodes and retention of DcNPs in these lymph vessels and nodes—this lymphatic distribution and retention are key to enhancing lymphocyte

drug levels and producing long-acting PK. The unique particle structure, surface properties, and the interactions DcNPs have with the *in vivo* milieu likely play important roles, and require further characterization. DcNP degradation and drug release rates at the SC injection site, during lymphatic transit, while retained in lymph nodes, and during circulation in the blood are other important questions. Quantifying the time course in plasma, following subcutaneous and intravenous administration, of the fractions of free drug versus DcNP- and protein-bound drug, perhaps using an ultrafiltration assay where samples are spiked with stable isotope tracers (Stern, Martinez et al. 2016, Skoczen and Stern 2018), could help elucidate these *in vivo* drug release kinetics and the overall contribution that the free and bound forms have on the total drug exposure in plasma. This would also provide key pharmacokinetic parameters such as absolute bioavailability and clearance of DcNP-bound drugs. In addition, drug formulation factors (e.g., ionic strength, pH, osmolarity, concentration, viscosity, lipophilicity) may affect lymphatic exposure, however, the influence of these factors remains to be elucidated (Kinnunen and Mrsny 2014). Also, the injection site location on the body and injection volume and rate can significantly impact the rate and extent of drug distribution to draining and more distant lymph nodes (Lewis 1921, Pitorre, Bastiat et al. 2015). Preliminary studies in mice that imaged the levels of DcNPs tagged with ICG in the first two draining lymph nodes shows that injection volume can have a significant impact on the lymph node drug levels soon after injection (**Figure 6.2**). Thus, subcutaneous injection volume and rate are important parameters to control when lymphatic drug exposure is of primary concern.

Moreover, to elicit a long-acting effect in lymphocytes and plasma, it is currently not clear the extent to which lymph nodes must be loaded with drug. Do they need to be filled below, at, or

above their loading capacity to produce long-acting pharmacokinetics? How does dose, injection site, injection volume, and injection rate impact this? In the context of HIV infection where large viral sanctuaries reside in gut lymphoid tissues, it is not clear how well DcNPs distribute to and are taken up by lymphocytes in the gut, and the impact injection site, volume, and rate have on this. Detailed distribution studies in nonhuman primates that control for dose, injection site, volume, and rate could lead to a better understanding of the impact of these variables on lymphocyte uptake and long-acting PK. To elucidate the lymphocyte subsets that predominantly accumulate drug delivered by DcNPs, a cell sorting step could be added to these studies. Also, quantifying drug levels in healthy and diseased lymph node histological sections using matrix-assisted laser desorption ionization (MALDI) imaging mass spectrometry (IMS), and ICG-labeled DcNPs, could shed light on the intra-nodal distribution of DcNPs and DcNP-associated drugs.

For the third "next step," other questions that need to be resolved are the correlation between lymph node drug distribution and retention in preclinical species and humans. Currently, species differences in subcutaneous absorption of drug is not fully understood (Richter, Bhansali et al. 2012, Richter and Jacobsen 2014). Also, in the context of disease states, it is unclear how, for example, the fibrotic lymph nodes in HIV patients will impact lymphatic drug exposure and the efficacy of DcNPs. The lymphatic network is complex, and as noted, this complexity varies among species. Developing a physiologically-based pharmacokinetic (PBPK) model that accounts for the anatomical and physiological complexities of the lymphatic system could help significantly with extrapolating between species and predicting lymphatic drug levels. This currently does not exist, and the latest compartmental and PBPK models that involve the lymphatics treat the lymphatics as a black box and ignore the complexity of the lymphatic network (Ryan, Kaminskas

et al. 2013, Kagan 2014, Gill, Gardner et al. 2016). A lymphatic PBPK framework could also help to further elucidate the details of the long-acting mechanisms. For instance, it is not known if the "waves" that mathematically explain the persistent plasma levels are due to (1) sustained DcNP or free drug release from lymph nodes to the blood, (2) lymph node lymphocytes loaded with DcNPs trafficking to the blood and then releasing drug into plasma, (3) cycles of recirculation of DcNPs between the lymph and blood, (4) a combination of these or other unknown factors. Incorporating lymphocyte trafficking patterns in the body and *in vitro* DcNP and drug uptake and release kinetics in lymphocytes into such PBPK models could help further elucidate the drivers of targeting and long-acting PK.

Finally, the tools and concepts developed in this thesis to assess lymphatic drug exposure are also highly valuable for prophylactic and therapeutic vaccine development. Thus far, the only vaccine trial (RV144) that showed any protective effect against HIV infection achieved only modest efficacy (~31%) (Rerks-Ngarm, Pitisuttithum et al. 2009). It could be that providing better control of viral replication in lymphoid tissues through the use of DcNPs for HIV treatment could create an opportunity for partially effective therapeutic vaccines to be even more effective. Moreover, deploying the "shock and kill" strategy using latency reversing agents such as histone deacetylase inhibitors and toll-like receptor 9 ligands, which aims to pharmacologically reactivate viral gene expression to induce immune-mediated elimination of virally infected cells, have failed so far to translate into reductions in viral reservoir size even when combined with therapeutic vaccines designed to activate HIV-1-specific T cells (Leth, Schleimann et al. 2016). Especially since *in vivo* studies demonstrate that reactivation of latent viral gene expression critically depends on the chromosomal position of integrated proviruses (Chen, Martinez et al. 2017), combinations

of different latency reversing agents and enhanced lymphatic exposures using a delivery platform such as DcNPs will likely be needed to mobilize the entire spectrum of integrated proviruses. In short, more effective lymphatic exposure of antiretroviral and latency reversing combinations, coupled with effective vaccination strategies, will likely lead to a significant improvement in anti-HIV efficacy. In addition, as with drug combination therapies for lymphatic diseases, effective subunit vaccines must traffic to lymph nodes and persist/retain in lymph nodes to activate both innate and adaptive arms of the immune system to promote a mature immune response (Moyer, Zmolek et al. 2016). Controlling and optimizing the lymphatic biodistribution and pharmacokinetics of vaccines is key to their potency and safety. The research in this thesis has established a platform that could be used to help tailor the kinetics of vaccine uptake into lymphoid tissues to help shape the immune response, through quantitatively understanding the duration and magnitude of antigen and adjuvant lymphatic exposure. Overall, employing the work in this thesis in the context of vaccine development could lead to a better understanding of how vaccines interact with the lymphatic (immune) system.

In conclusion, the novel mechanisms that DcNPs employ where lymph nodes and lymphocytes in the body serve as drug depots, which results in enhanced and sustained levels of drug combinations in lymphoid tissues, provides a powerful new approach to diagnose, prevent, and/or treat lymphatic abnormalities and lymphatic diseases. Due to the unique ability of DcNPs to target small molecule drug combinations with diverse physicochemical properties to lymphocytes, one opportunity with significant therapeutic potential is incorporation of small molecule combinations into DcNPs that have pharmacological effect on immune checkpoint surface proteins such as CTLA-4 and PD-1 on T cells. Overall, the novel tools and concepts

established in this thesis provide an unprecedented, detailed understanding of lymphatic drug exposure to small molecules—both in free form and in a unique DcNP delivery platform. This in turn has made the pathway for translation of lymphatic therapies clearer and has opened up new diagnostic and therapeutic possibilities.

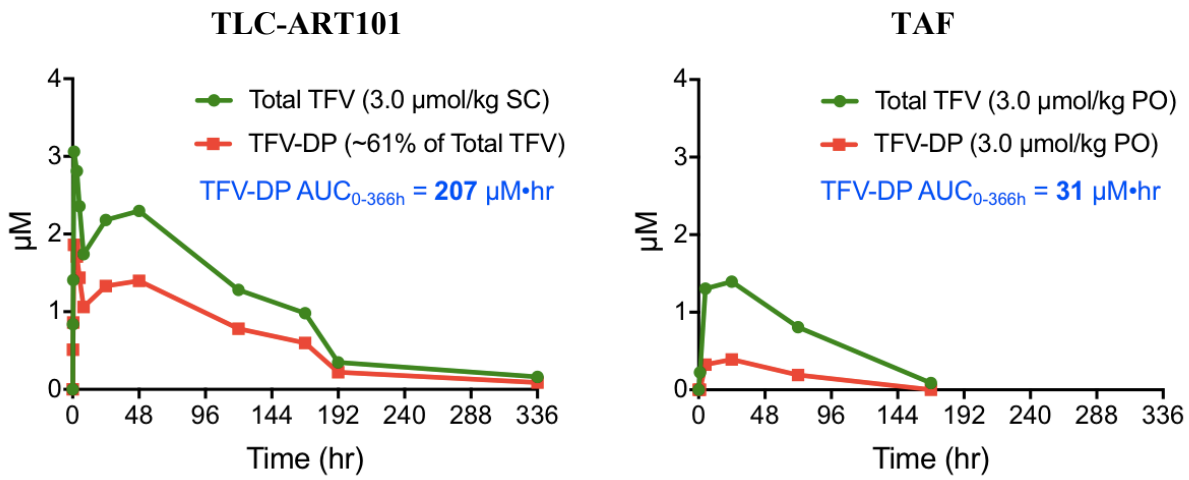

Figure 6.1. Comparison between intracellular PBMC levels in monkeys of tenofovir (TFV) and tenofovir diphosphate (TFV-DP) after a single dose of TLC-ART101 or TAF.

A single TLC-ART101 dose containing 10.6 mg/kg TFV was given subcutaneously as part of a drug combination with 25 mg/kg lopinavir, and 7 mg/kg ritonavir. A single TAF dose of 30 mg/kg was given orally. For comparison, drug concentrations were dose-normalized to 3.0 µmol/kg for each formulation. The TFV-DP levels for TLC-ART101 are estimated as 61% of the total TFV concentration, which is representative of TFV-DP levels in monkey and human PBMCs at steady-state. Total TFV and TFV-DP levels following TAF were extracted from (Massud, Mitchell et al. 2016).

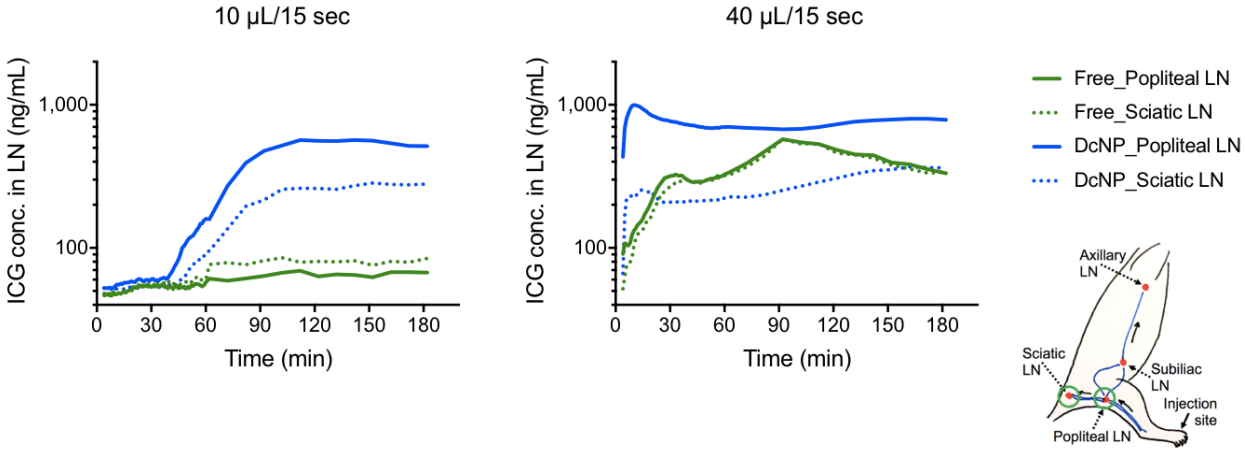

Figure 6.2. Impact of subcutaneous injection volume in the hind foot of a mouse on the uptake of free or nanoparticle-bound indocyanine green (ICG) into the 1st and 2nd draining lymph nodes.

The subcutaneous injection volume on the dorsal hind foot of mice was either 10 µL (left plot) or 40 µL (right plot). Free (green) or nanoparticle-bound (blue) indocyanine green (ICG) was administered. Solid lines represent the 1st draining lymph node (popliteal), dashed lines represent the second draining lymph node (sciatic). The anatomical locations of the injection site and the popliteal and sciatic lymph nodes are indicated in the schematic (bottom right). N=5-6 mice per group. Coefficient of variation (CV%) for the area under the concentration-time curve (AUC) values for each group ranged from 8-262%.

BIBLIOGRAPHY

Akamo, Y., I. Mizuno, T. Yotsuyanagi, T. Ichino, N. Tanimoto, T. Yamamoto, M. Nagata, H. Takeyama, N. Shinagawa, J. Yura and et al. (1994). "Chemotherapy targeting regional lymph nodes by gastric submucosal injection of liposomal adriamycin in patients with gastric carcinoma." Jpn J Cancer Res **85**(6): 652-658.

Alitalo, K. (2011). "The lymphatic vasculature in disease." Nat Med **17**(11): 1371-1380.

Allen, T. M., C. Hansen, F. Martin, C. Redemann and A. Yau-Young (1991). "Liposomes containing synthetic lipid derivatives of poly(ethylene glycol) show prolonged circulation half-lives in vivo." Biochim Biophys Acta **1066**(1): 29-36.

Arngrim, N., L. Simonsen, J. J. Holst and J. Bulow (2013). "Reduced adipose tissue lymphatic drainage of macromolecules in obese subjects: a possible link between obesity and local tissue inflammation?" Int J Obes (Lond) **37**(5): 748-750.

Aselli, G. (1627). De Lactibus Sive Lacteis Venis. Milan, Italy, J.B. Bidellius.

Ashikaga, T., D. N. Krag, S. R. Land, T. B. Julian, S. J. Anderson, A. M. Brown, J. M. Skelly, S. P. Harlow, D. L. Weaver, E. P. Mamounas, J. P. Costantino, N. Wolmark and B. P. National Surgical Adjuvant Breast (2010). "Morbidity results from the NSABP B-32 trial comparing sentinel lymph node dissection versus axillary dissection." J Surg Oncol **102**(2): 111-118.

Aspelund, A., S. Antila, S. T. Proulx, T. V. Karlsen, S. Karaman, M. Detmar, H. Wiig and K. Alitalo (2015). "A dural lymphatic vascular system that drains brain interstitial fluid and macromolecules." J Exp Med **212**(7): 991-999.

Aukland, K. and R. K. Reed (1993). "Interstitial-lymphatic mechanisms in the control of extracellular fluid volume." Physiol Rev **73**(1): 1-78.

Azzali, G. (1982). "The ultrastructural basis of lipid transport in the absorbing lymphatic vessel." J Submicrosc Cytol **14**(1): 45-54.

Baker, K. J. (1966). "Binding of sulfobromophthalein (BSP) sodium and indocyanine green (ICG) by plasma alpha-1 lipoproteins." Proc Soc Exp Biol Med **122**(4): 957-963.

Baluk, P., J. Fuxe, H. Hashizume, T. Romano, E. Lashnits, S. Butz, D. Vestweber, M. Corada, C. Molendini, E. Dejana and D. M. McDonald (2007). "Functionally specialized junctions between endothelial cells of lymphatic vessels." J Exp Med **204**(10): 2349-2362.

Bam, R. A., G. Birkus, D. Babusis, T. Cihlar and S. R. Yant (2014). "Metabolism and antiretroviral activity of tenofovir alafenamide in CD4+ T-cells and macrophages from demographically diverse donors." Antivir Ther **19**(7): 669-677.

Baroni, C. D., F. Pezzella, M. Pezzella, B. Macchi, D. Vitolo, S. Uccini and L. P. Ruco (1988). "Expression of HIV in lymph node cells of LAS patients. Immunohistology, in situ hybridization, and identification of target cells." Am J Pathol **133**(3): 498-506.

Baroni, C. D. and S. Uccini (1990). "Lymph nodes in HIV-positive drug abusers with persistent generalized lymphadenopathy: histology, immunohistochemistry, and pathogenetic correlations." Prog AIDS Pathol **2**: 33-50.

Barre-Sinoussi, F., J. C. Chermann, F. Rey, M. T. Nugeyre, S. Chamaret, J. Gruest, C. Dauguet, C. Axler-Blin, F. Vezinet-Brun, C. Rouzioux, W. Rozenbaum and L. Montagnier (1983). "Isolation of a T-lymphotropic retrovirus from a patient at risk for acquired immune deficiency syndrome (AIDS)." Science **220**(4599): 868-871.

Bell, B. M. and A. Schumitzky (1997). "A Generalization of the Gauss-Newton Method that Solves Extended Least Squares Problems. White Paper: https://www.seanet.com/~bradbell/gauss_newton.pdf."

Beshyah, S. A., V. Anyaoku, R. Niththyananthan, P. Sharp and D. G. Johnston (1991). "The effect of subcutaneous injection site on absorption of human growth hormone: abdomen versus thigh." Clin Endocrinol (Oxf) **35**(5): 409-412.

Betterman, K. L. and N. L. Harvey (2016). "The lymphatic vasculature: development and role in shaping immunity." Immunol Rev **271**(1): 276-292.

Biberfeld, P., A. Ost, A. Porwit, B. Sandstedt, G. Pallesen, B. Bottiger, L. Morfelt-Mansson and G. Biberfeld (1987). "Histopathology and immunohistology of HTLV-III/LAV related lymphadenopathy and AIDS." Acta Pathol Microbiol Immunol Scand A **95**(1): 47-65.

Binder, C. (1969). "Absorption of injected insulin. A clinical-pharmacological study." Acta Pharmacol Toxicol (Copenh) **27 Suppl 2**: 1-84.

Birkus, G., R. Wang, X. Liu, N. Kutty, H. MacArthur, T. Cihlar, C. Gibbs, S. Swaminathan, W. Lee and M. McDermott (2007). "Cathepsin A is the major hydrolase catalyzing the intracellular hydrolysis of the antiretroviral nucleotide phosphonoamidate prodrugs GS-7340 and GS-9131." Antimicrob Agents Chemother **51**(2): 543-550.

Blanche, P. J., E. L. Gong, T. M. Forte and A. V. Nichols (1981). "Characterization of human high-density lipoproteins by gradient gel electrophoresis." Biochim Biophys Acta **665**(3): 408-419.

Bourne, G. H. (1975, pgs. 52, 61). The Rhesus Monkey. New York, Academic Press.

Bouta, E. M., R. D. Bell, H. Rahimi, L. Xing, R. W. Wood, C. O. Bingham, 3rd, C. T. Ritchlin and E. M. Schwarz (2018). "Targeting lymphatic function as a novel therapeutic intervention for rheumatoid arthritis." Nat Rev Rheumatol **14**(2): 94-106.

Bradley, H., H. I. Hall, R. J. Wolitski, M. M. Van Handel, A. E. Stone, M. LaFlam, J. Skarbinski, D. H. Higa, J. Prejean, E. L. Frazier, R. Patel, P. Huang, Q. An, R. Song, T. Tang

and L. A. Valleroy (2014). "Vital Signs: HIV diagnosis, care, and treatment among persons living with HIV--United States, 2011." MMWR Morb Mortal Wkly Rep **63**(47): 1113-1117.

Brenchley, J. M. and D. C. Douek (2008). "The mucosal barrier and immune activation in HIV pathogenesis." Curr Opin HIV AIDS **3**(3): 356-361.

Brenchley, J. M. and D. C. Douek (2012). "Microbial translocation across the GI tract." Annu Rev Immunol **30**: 149-173.

Brenchley, J. M., D. A. Price, T. W. Schacker, T. E. Asher, G. Silvestri, S. Rao, Z. Kazzaz, E. Bornstein, O. Lambotte, D. Altmann, B. R. Blazar, B. Rodriguez, L. Teixeira-Johnson, A. Landay, J. N. Martin, F. M. Hecht, L. J. Picker, M. M. Lederman, S. G. Deeks and D. C. Douek (2006). "Microbial translocation is a cause of systemic immune activation in chronic HIV infection." Nat Med **12**(12): 1365-1371.

Breslin, J. W., S. Y. Yuan and M. H. Wu (2007). "VEGF-C alters barrier function of cultured lymphatic endothelial cells through a VEGFR-3-dependent mechanism." Lymphat Res Biol **5**(2): 105-113.

Brierley, J. B. and E. J. Field (1948). "The connexions of the spinal sub-arachnoid space with the lymphatic system." J Anat **82**(3): 153-166.

Bronshtein, I., M. Afri, H. Weitman, A. A. Frimer, K. M. Smith and B. Ehrenberg (2004). "Porphyrin depth in lipid bilayers as determined by iodide and parallax fluorescence quenching methods and its effect on photosensitizing efficiency." Biophys J **87**(2): 1155-1164.

Brorson, H., K. Ohlin, G. Olsson and M. Nilsson (2006). "Adipose tissue dominates chronic arm lymphedema following breast cancer: an analysis using volume rendered CT images." Lymphat Res Biol **4**(4): 199-210.

Bui, T., J. Stevenson, J. Hoekman, S. Zhang, K. Maravilla and R. J. Ho (2010). "Novel Gd nanoparticles enhance vascular contrast for high-resolution magnetic resonance imaging." PLoS One **5**(9).

Burrows, P. E., M. L. Gonzalez-Garay, J. C. Rasmussen, M. B. Aldrich, R. Guilliod, E. A. Maus, C. E. Fife, S. Kwon, P. E. Lapinski, P. D. King and E. M. Sevick-Muraca (2013). "Lymphatic abnormalities are associated with RASA1 gene mutations in mouse and man." Proc Natl Acad Sci U S A **110**(21): 8621-8626.

Carr, J. A., D. Franke, J. R. Caram, C. F. Perkinson, V. Askoxylakis, M. Datta, D. Fukumura, R. K. Jain, M. G. Bawendi and O. T. Bruns (2017). "Shortwave infrared fluorescence imaging with the clinically approved near-infrared dye indocyanine green." bioRxiv **100768**.

Castro, E., W. Tony Parks and C. Galambos (2011). "Neither normal nor diseased placentas contain lymphatic vessels." Placenta **32**(4): 310-316.

Cerf-Bensussan, N. and D. Guy-Grand (1991). "Intestinal intraepithelial lymphocytes." Gastroenterol Clin North Am **20**(3): 549-576.

Cesmebasi, A., J. Malefant, S. D. Patel, M. Du Plessis, S. Renna, R. S. Tubbs and M. Loukas (2015). "The surgical anatomy of the lymphatic system of the pancreas." Clin Anat **28**(4): 527-537.

Chaffer, C. L. and R. A. Weinberg (2011). "A perspective on cancer cell metastasis." Science **331**(6024): 1559-1564.

Chakradhar, S. (2018). "Sleeper cells." Nat Med.

Chan, L. J., D. B. Ascher, R. Yadav, J. B. Bulitta, C. C. Williams, C. J. Porter, C. B. Landersdorfer and L. M. Kaminskas (2016). "Conjugation of 10 kDa Linear PEG onto Trastuzumab Fab' Is Sufficient to Significantly Enhance Lymphatic Exposure while Preserving in Vitro Biological Activity." Mol Pharm **13**(4): 1229-1241.

Chan, L. J., J. B. Bulitta, D. B. Ascher, J. M. Haynes, V. M. McLeod, C. J. Porter, C. C. Williams and L. M. Kaminskas (2015). "PEGylation does not significantly change the initial intravenous or subcutaneous pharmacokinetics or lymphatic exposure of trastuzumab in rats but increases plasma clearance after subcutaneous administration." Mol Pharm **12**(3): 794-809.

Chang, A. A., L. S. Morse, J. T. Handa, R. B. Morales, R. Tucker, L. Hjelmeland and L. A. Yannuzzi (1998). "Histologic localization of indocyanine green dye in aging primate and human ocular tissues with clinical angiographic correlation." Ophthalmology **105**(6): 1060-1068.

Chang, S. Y., J. H. Song, B. Guleng, C. A. Cotoner, S. Arihiro, Y. Zhao, H. S. Chiang, M. O'Keeffe, G. Liao, C. L. Karp, M. N. Kweon, A. H. Sharpe, A. Bhan, C. Terhorst and H. C. Reinecker (2013). "Circulatory antigen processing by mucosal dendritic cells controls CD8(+) T cell activation." Immunity **38**(1): 153-165.

Chattopadhyay, A. and E. London (1987). "Parallax method for direct measurement of membrane penetration depth utilizing fluorescence quenching by spin-labeled phospholipids." Biochemistry **26**(1): 39-45.

Chauhan, V. P. and R. K. Jain (2013). "Strategies for advancing cancer nanomedicine." Nat Mater **12**(11): 958-962.

Chemicalize.org. (accessed Jan 6, 2014). "http://www.chemicalize.org/structure/ -!mol=indocyanine+green&source=fp."

Chen, H. C., J. P. Martinez, E. Zorita, A. Meyerhans and G. J. Filion (2017). "Position effects influence HIV latency reversal." Nat Struct Mol Biol **24**(1): 47-54.

Chen, J., L. Wang, Q. Yao, R. Ling, K. Li and H. Wang (2004). "Drug concentrations in axillary lymph nodes after lymphatic chemotherapy on patients with breast cancer." Breast Cancer Res **6**(4): R474-477.

Chen, S. A., R. J. Sawchuk, R. C. Brundage, C. Horvath, H. V. Mendenhall, R. A. Gunther and R. A. Braeckman (2000). "Plasma and lymph pharmacokinetics of recombinant human

interleukin-2 and polyethylene glycol-modified interleukin-2 in pigs." J Pharmacol Exp Ther **293**(1): 248-259.

Cheung, M. C. and J. J. Albers (1984). "Characterization of lipoprotein particles isolated by immunoaffinity chromatography. Particles containing A-I and A-II and particles containing A-I but no A-II." J Biol Chem **259**(19): 12201-12209.

Choi, I., S. Lee and Y. K. Hong (2012). "The new era of the lymphatic system: no longer secondary to the blood vascular system." Cold Spring Harb Perspect Med **2**(4): a006445.

Chun, T. W., D. C. Nickle, J. S. Justement, J. H. Meyers, G. Roby, C. W. Hallahan, S. Kottilil, S. Moir, J. M. Mican, J. I. Mullins, D. J. Ward, J. A. Kovacs, P. J. Mannon and A. S. Fauci (2008). "Persistence of HIV in gut-associated lymphoid tissue despite long-term antiretroviral therapy." J Infect Dis **197**(5): 714-720.

Coert, A., J. Geelen, J. de Visser and J. van der Vies (1975). "The pharmacology and metabolism of testosterone undecanoate (TU), a new orally active androgen." Acta Endocrinol (Copenh) **79**(4): 789-800.

Colombo, S., A. Beguin, A. Telenti, J. Biollaz, T. Buclin, B. Rochat and L. A. Decosterd (2005). "Intracellular measurements of anti-HIV drugs indinavir, amprenavir, saquinavir, ritonavir, nelfinavir, lopinavir, atazanavir, efavirenz and nevirapine in peripheral blood mononuclear cells by liquid chromatography coupled to tandem mass spectrometry." J Chromatogr B Analyt Technol Biomed Life Sci **819**(2): 259-276.

Colombo, S., A. Telenti, T. Buclin, H. Furrer, B. L. Lee, J. Biollaz, L. A. Decosterd and H. I. V. C. S. Swiss (2006). "Are plasma levels valid surrogates for cellular concentrations of antiretroviral drugs in HIV-infected patients?" Ther Drug Monit **28**(3): 332-338.

Comper, W. D. and T. C. Laurent (1978). "Physiological function of connective tissue polysaccharides." Physiol Rev **58**(1): 255-315.

D'Avolio, A., M. Simiele, A. Calcagno, M. Siccardi, G. Larovere, S. Agati, L. Baietto, J. Cusato, M. Tettoni, M. Sciandra, L. Trentini, G. Di Perri and S. Bonora (2013). "Intracellular accumulation of ritonavir combined with different protease inhibitors and correlations between concentrations in plasma and peripheral blood mononuclear cells." J Antimicrob Chemother **68**(4): 907-910.

Daggett, P. R., M. J. Wheeler and J. D. Nabarro (1978). "Oral testosterone, a reappraisal." Horm Res **9**(3): 121-129.

Dahlberg, A. M., L. M. Kaminskas, A. Smith, J. A. Nicolazzo, C. J. Porter, J. B. Bulitta and M. P. McIntosh (2014). "The lymphatic system plays a major role in the intravenous and subcutaneous pharmacokinetics of trastuzumab in rats." Mol Pharm **11**(2): 496-504.

Davies-Venn, C. A., B. Angermiller, N. Wilganowski, P. Ghosh, B. R. Harvey, G. Wu, S. Kwon, M. B. Aldrich and E. M. Sevick-Muraca (2012). "Albumin-binding domain conjugate for near-infrared fluorescence lymphatic imaging." Mol Imaging Biol **14**(3): 301-314.

De Berardis, D., S. Marini, A. Carano, A. P. Lang, M. Cavuto, M. Piersanti, M. Fornaro, G. Perna, A. Valchera, M. Mazza, F. Iasevoli, G. Martinotti and M. Di Giannantonio (2013). "Efficacy and safety of long acting injectable atypical antipsychotics: a review." Curr Clin Pharmacol **8**(3): 256-264.

De Lepeleire, I. (2017). "Oral abstracts of the HIV Cure and Reservoir Symposium 2017." J Virus Erad **3**(Suppl 3): 1-5.

Denissen, J. F., B. A. Grabowski, M. K. Johnson, A. M. Buko, D. J. Kempf, S. B. Thomas and B. W. Surber (1997). "Metabolism and disposition of the HIV-1 protease inhibitor ritonavir (ABT-538) in rats, dogs, and humans." Drug Metab Dispos **25**(4): 489-501.

Devoisselle, J. M., S. Soulie, S. R. Mordon, T. Desmettre and H. Maillols (1997). "Fluorescence properties of indocyanin green. I. In-vitro study with micelles and liposomes." Proc SPIE **2980**: 453-460.

Di Mascio, M., C. H. Paik, J. A. Carrasquillo, J. S. Maeng, B. S. Jang, I. S. Shin, S. Srinivasula, R. Byrum, A. Neria, W. Kopp, M. Catalfamo, Y. Nishimura, K. Reimann, M. Martin and H. C. Lane (2009). "Noninvasive in vivo imaging of CD4 cells in simian-human immunodeficiency virus (SHIV)-infected nonhuman primates." Blood **114**(2): 328-337.

Diaz, A., L. Alos, A. Leon, A. Mozos, M. Caballero, A. Martinez, M. Plana, T. Gallart, C. Gil, M. Leal, J. M. Gatell, F. Garcia and H. I. V. i. Study Group of Lymphoid Tissue immunopathogenesis in (2010). "Factors associated with collagen deposition in lymphoid tissue in long-term treated HIV-infected patients." AIDS **24**(13): 2029-2039.

Diaz, A., F. Garcia, A. Mozos, M. Caballero, A. Leon, A. Martinez, C. Gil, M. Plana, T. Gallart, J. M. Gatell and L. Alos (2011). "Lymphoid tissue collagen deposition in HIV-infected patients correlates with the imbalance between matrix metalloproteinases and their inhibitors." J Infect Dis **203**(6): 810-813.

Dixon, J. B., S. Raghunathan and M. A. Swartz (2009). "A tissue-engineered model of the intestinal lacteal for evaluating lipid transport by lymphatics." Biotechnol Bioeng **103**(6): 1224-1235.

Dobbins, W. O., 3rd and E. L. Rollins (1970). "Intestinal mucosal lymphatic permeability: an electron microscopic study of endothelial vesicles and cell junctions." J Ultrastruct Res **33**(1): 29-59.

Domingo, J. and N. W. Chin (1983). "Lymphadenopathy in a heterogeneous population at risk for the acquired immunodeficiency syndrome (AIDS)--a morphologic study." Am J Clin Pathol **80**(5): 649-654.

Doughty, D. V., C. Z. Clawson, W. Lambert and J. A. Subramony (2016). "Understanding Subcutaneous Tissue Pressure for Engineering Injection Devices for Large-Volume Protein Delivery." J Pharm Sci **105**(7): 2105-2113.

Drinker, C. K., M. E. Field and H. K. Ward (1934). "The Filtering Capacity of Lymph Nodes." J Exp Med **59**(4): 393-405.

Duan, J., J. P. Freeling, J. Koehn, C. Shu and R. J. Ho (2014). "Evaluation of atazanavir and darunavir interactions with lipids for developing pH-responsive anti-HIV drug combination nanoparticles." J Pharm Sci **103**(8): 2520-2529.

Dunn, T. B. (1954). "Normal and pathologic anatomy of the reticular tissue in laboratory mice, with a classification and discussion of neoplasms." J Natl Cancer Inst **14**(6): 1281-1433.

Durand-Gasselin, L., K. K. Van Rompay, J. E. Vela, I. N. Henne, W. A. Lee, G. R. Rhodes and A. S. Ray (2009). "Nucleotide analogue prodrug tenofovir disoproxil enhances lymphoid cell loading following oral administration in monkeys." Mol Pharm **6**(4): 1145-1151.

Eaglstein, W. H. and P. M. Mertz (1978). "New methods for assessing epidermal wound healing: the effects of triamcinolone acetonide and polyethelene film occlusion." J Invest Dermatol **71**(6): 382-384.

Eisenberg, E. J., G. X. He and W. A. Lee (2001). "Metabolism of GS-7340, a novel phenyl monophosphoramidate intracellular prodrug of PMPA, in blood." Nucleosides Nucleotides Nucleic Acids **20**(4-7): 1091-1098.

Eliska, O. (1984). "Topography of intrarenal lymphatics." Lymphology **17**(4): 135-141.

Embretson, J., M. Zupancic, J. L. Ribas, A. Burke, P. Racz, K. Tenner-Racz and A. T. Haase (1993). "Massive covert infection of helper T lymphocytes and macrophages by HIV during the incubation period of AIDS." Nature **362**(6418): 359-362.

Engel, E., R. Schraml, T. Maisch, K. Kobuch, B. Konig, R. M. Szeimies, J. Hillenkamp, W. Baumler and R. Vasold (2008). "Light-induced decomposition of indocyanine green." Invest Ophthalmol Vis Sci **49**(5): 1777-1783.

Engeset, A. (1959). "The route of peripheral lymph to the blood stream; an x-ray study of the barrier theory." J Anat **93**(1): 96-100.

Eriksson, S., E. H. Graf, V. Dahl, M. C. Strain, S. A. Yukl, E. S. Lysenko, R. J. Bosch, J. Lai, S. Chioma, F. Emad, M. Abdel-Mohsen, R. Hoh, F. Hecht, P. Hunt, M. Somsouk, J. Wong, R. Johnston, R. F. Siliciano, D. D. Richman, U. O'Doherty, S. Palmer, S. G. Deeks and J. D. Siliciano (2013). "Comparative analysis of measures of viral reservoirs in HIV-1 eradication studies." PLoS Pathog **9**(2): e1003174.

Estes, J. D. (2009). "Role of collagen deposition in lymphatic tissues and immune reconstruction during HIV-1 and SIV infections." Curr HIV/AIDS Rep **6**(1): 29-35.

Estes, J. D. (2013). "Pathobiology of HIV/SIV-associated changes in secondary lymphoid tissues." Immunol Rev **254**(1): 65-77.

Estes, J. D., L. D. Harris, N. R. Klatt, B. Tabb, S. Pittaluga, M. Paiardini, G. R. Barclay, J. Smedley, R. Pung, K. M. Oliveira, V. M. Hirsch, G. Silvestri, D. C. Douek, C. J. Miller, A. T. Haase, J. Lifson and J. M. Brenchley (2010). "Damaged intestinal epithelial integrity linked to microbial translocation in pathogenic simian immunodeficiency virus infections." PLoS Pathog **6**(8): e1001052.

Estes, J. D., C. Kityo, F. Ssali, L. Swainson, K. N. Makamdop, G. Q. Del Prete, S. G. Deeks, P. A. Luciw, J. G. Chipman, G. J. Beilman, T. Hoskuldsson, A. Khoruts, J. Anderson, C. Deleage, J. Jasurda, T. E. Schmidt, M. Hafertepe, S. P. Callisto, H. Pearson, T. Reimann, J. Schuster, J. Schoephoerster, P. Southern, K. Perkey, L. Shang, S. W. Wietgrefe, C. V. Fletcher, J. D. Lifson, D. C. Douek, J. M. McCune, A. T. Haase and T. W. Schacker (2017). "Defining total-body AIDS-virus burden with implications for curative strategies." Nat Med **23**(11): 1271-1276.

Estes, J. D., S. Wietgrefe, T. Schacker, P. Southern, G. Beilman, C. Reilly, J. M. Milush, J. D. Lifson, D. L. Sodora, J. V. Carlis and A. T. Haase (2007). "Simian immunodeficiency virus-induced lymphatic tissue fibrosis is mediated by transforming growth factor beta 1-positive regulatory T cells and begins in early infection." J Infect Dis **195**(4): 551-561.

FDA. (2013). "Product Insert: Indocyanine Green (IC-Green™)." from http://www.accessdata.fda.gov/drugsatfda_docs/label/2006/011525s017lbl.pdf.

Feng, D., J. A. Nagy, H. F. Dvorak and A. M. Dvorak (2002). "Ultrastructural studies define soluble macromolecular, particulate, and cellular transendothelial cell pathways in venules, lymphatic vessels, and tumor-associated microvessels in man and animals." Microsc Res Tech **57**(5): 289-326.

Field, M. E. and C. K. Drinker (1931). "THE PERMEABILITY OF THE CAPILLARIES OF THE DOG TO PROTEIN." American Journal of Physiology-Legacy Content **97**(1): 40-51.

Fishman, A. P., A. B. Fisher and American Physiological Society (1887-) (1985). The Respiratory system. Bethesda, Md., American Physiological Society; Distributed by Williams & Wilkins.

Fletcher, C. V., K. Staskus, S. W. Wietgrefe, M. Rothenberger, C. Reilly, J. G. Chipman, G. J. Beilman, A. Khoruts, A. Thorkelson, T. E. Schmidt, J. Anderson, K. Perkey, M. Stevenson, A. S. Perelson, D. C. Douek, A. T. Haase and T. W. Schacker (2014). "Persistent HIV-1 replication is associated with lower antiretroviral drug concentrations in lymphatic tissues." Proc Natl Acad Sci U S A **111**(6): 2307-2312.

Foldi, M., E. Csanda, M. Simon, F. Obal, I. Schneider, I. Dobranovics, O. T. Zoltan, M. Kozma and M. Poberai (1968). "Lymphogenic haemangiopathy. "Prelymphatic" pathways in the wall of cerebral and cervical blood vessels." Angiologica **5**(4): 250-262.

Frangioni, J. V. (2003). "In vivo near-infrared fluorescence imaging." Curr Opin Chem Biol **7**(5): 626-634.

Freeling, J. P. and R. J. Ho (2014). "Anti-HIV drug particles may overcome lymphatic drug insufficiency and associated HIV persistence." Proc Natl Acad Sci U S A **111**(25): E2512-2513.

Freeling, J. P., J. Koehn, C. Shu, J. Sun and R. J. Ho (2014). "Long-acting three-drug combination anti-HIV nanoparticles enhance drug exposure in primate plasma and cells within lymph nodes and blood." AIDS **28**(17): 2625-2627.

Freeling, J. P., J. Koehn, C. Shu, J. Sun and R. J. Ho (2015). "Anti-HIV drug-combination nanoparticles enhance plasma drug exposure duration as well as triple-drug combination levels in cells within lymph nodes and blood in primates." AIDS Res Hum Retroviruses **31**(1): 107-114.

Gallant, J. E., M. Thompson, E. DeJesus, G. W. Voskuhl, X. Wei, H. Zhang, K. White, A. Cheng, E. Quirk and H. Martin (2017). "Antiviral Activity, Safety, and Pharmacokinetics of Bictegravir as 10-Day Monotherapy in HIV-1-Infected Adults." J Acquir Immune Defic Syndr **75**(1): 61-66.

Gallo, R. C., P. S. Sarin, E. P. Gelmann, M. Robert-Guroff, E. Richardson, V. S. Kalyanaraman, D. Mann, G. D. Sidhu, R. E. Stahl, S. Zolla-Pazner, J. Leibowitch and M. Popovic (1983). "Isolation of human T-cell leukemia virus in acquired immune deficiency syndrome (AIDS)." Science **220**(4599): 865-867.

Ganusov, V. V. and J. Auerbach (2014). "Mathematical modeling reveals kinetics of lymphocyte recirculation in the whole organism." PLoS Comput Biol **10**(5): e1003586.

Garvey, L. and A. Winston (2009). "Rilpivirine: a novel non-nucleoside reverse transcriptase inhibitor." Expert Opin Investig Drugs **18**(7): 1035-1041.

Gibaldi, M. and D. Perrier (1982). Pharmacokinetics. New York, Marcel Dekker, Inc.

Gill, K. L., I. Gardner, L. Li and M. Jamei (2016). "A Bottom-Up Whole-Body Physiologically Based Pharmacokinetic Model to Mechanistically Predict Tissue Distribution and the Rate of Subcutaneous Absorption of Therapeutic Proteins." AAPS J **18**(1): 156-170.

Glomset, J. A., E. T. Janssen, R. Kennedy and J. Dobbins (1966). "Role of plasma lecithin:cholesterol acyltransferase in the metabolism of high density lipoproteins." J Lipid Res **7**(5): 638-648.

Haemmerle, M., T. Keller, G. Egger, H. Schachner, C. W. Steiner, D. Stokic, C. Neumayer, M. K. Brown, D. Kerjaschki and B. Hantusch (2013). "Enhanced lymph vessel density, remodeling, and inflammation are reflected by gene expression signatures in dermal lymphatic endothelial cells in type 2 diabetes." Diabetes **62**(7): 2509-2529.

Haley, P. J. (2003). "Species differences in the structure and function of the immune system." Toxicology **188**(1): 49-71.

Hansen, R. J. and J. P. Balthasar (2002). "Intravenous immunoglobulin mediates an increase in anti-platelet antibody clearance via the FcRn receptor." Thromb Haemost **88**(6): 898-899.

Harvey, N. L., R. S. Srinivasan, M. E. Dillard, N. C. Johnson, M. H. Witte, K. Boyd, M. W. Sleeman and G. Oliver (2005). "Lymphatic vascular defects promoted by Prox1 haploinsufficiency cause adult-onset obesity." Nat Genet **37**(10): 1072-1081.

Hiller, J. G., H. M. Ismail, M. S. Hofman, K. Narayan, S. Ramdave and B. J. Riedel (2016). "Neuraxial Anesthesia Reduces Lymphatic Flow: Proof-of-Concept in First In-Human Study." Anesth Analg **123**(5): 1325-1327.

Holstein, A. F., G. E. Orlandini and R. Moller (1979). "Distribution and fine structure of the lymphatic system in the human testis." Cell Tissue Res **200**(1): 15-27.

Holzer, W., M. Mauerer, A. Penzkofer, R. M. Szeimies, C. Abels, M. Landthaler and W. Baumler (1998). "Photostability and thermal stability of indocyanine green." J Photochem Photobiol B **47**(2-3): 155-164.

Hong, G., A. L. Antaris and H. Dai (2017). "Near-infrared fluorophores for biomedical imaging." Nature Biomedical Engineering **1; DOI:10.1038/s41551-016-0010**.

Horiike, M., S. Iwami, M. Kodama, A. Sato, Y. Watanabe, M. Yasui, Y. Ishida, T. Kobayashi, T. Miura and T. Igarashi (2012). "Lymph nodes harbor viral reservoirs that cause rebound of plasma viremia in SIV-infected macaques upon cessation of combined antiretroviral therapy." Virology **423**(2): 107-118.

Horst, H. J., W. J. Holtje, M. Dennis, A. Coert, J. Geelen and K. D. Voigt (1976). "Lymphatic absorption and metabolism of orally administered testosterone undecanoate in man." Klin Wochenschr **54**(18): 875-879.

Hua, J., N. Gross, B. Schulze, U. Michaelis, H. Bohnenkamp, E. Guenzi, L. L. Hansen, G. Martin and H. T. Agostini (2012). "In vivo imaging of choroidal angiogenesis using fluorescence-labeled cationic liposomes." Mol Vis **18**: 1045-1054.

IARC. (2018). "International Agency for Reserach on Cancer (IARC) - Globocan 2012; http://globocan.iarc.fr/Pages/fact_sheets_cancer.aspx." Retrieved May 29, 2018.

Ioachim, H. L., W. Cronin, M. Roy and M. Maya (1990). "Persistent lymphadenopathies in people at high risk for HIV infection. Clinicopathologic correlations and long-term follow-up in 79 cases." Am J Clin Pathol **93**(2): 208-218.

Ioachim, H. L., C. W. Lerner and M. L. Tapper (1983). "Lymphadenopathies in homosexual men. Relationships with the acquired immune deficiency syndrome." JAMA **250**(10): 1306-1309.

Ioachim, H. L., C. W. Lerner and M. L. Tapper (1983). "The lymphoid lesions associated with the acquired immunodeficiency syndrome." Am J Surg Pathol **7**(6): 543-553.

Jeong, H. S., C. M. Lee, S. J. Cheong, E. M. Kim, H. Hwang, K. S. Na, S. T. Lim, M. H. Sohn and H. J. Jeong (2013). "The effect of mannosylation of liposome-encapsulated indocyanine green on imaging of sentinel lymph node." J Liposome Res **23**(4): 291-297.

Jiang, X., M. R. Nicolls, W. Tian and S. G. Rockson (2018). "Lymphatic Dysfunction, Leukotrienes, and Lymphedema." Annu Rev Physiol **80**: 49-70.

John, T. A., S. M. Vogel, C. Tiruppathi, A. B. Malik and R. D. Minshall (2003). "Quantitative analysis of albumin uptake and transport in the rat microvessel endothelial monolayer." Am J Physiol Lung Cell Mol Physiol **284**(1): L187-196.

Johnson, O. W., J. F. Chick, N. R. Chauhan, A. H. Fairchild, C. M. Fan, M. S. Stecker, T. P. Killoran and A. Suzuki-Han (2016). "The thoracic duct: clinical importance, anatomic variation, imaging, and embolization." Eur Radiol **26**(8): 2482-2493.

Jucker, B. M., H. Alsaid, M. Rambo, S. C. Lenhard, B. Hoang, F. Xie, M. R. Groseclose, S. Castellino, V. Damian, G. Bowers and M. Gupta (2017). "Multimodal imaging approach to examine biodistribution kinetics of Cabotegravir (GSK1265744) long acting parenteral formulation in rat." J Control Release **268**: 102-112.

Kagan, L. (2014). "Pharmacokinetic modeling of the subcutaneous absorption of therapeutic proteins." Drug Metab Dispos **42**(11): 1890-1905.

Kagan, L., M. R. Turner, S. V. Balu-Iyer and D. E. Mager (2012). "Subcutaneous absorption of monoclonal antibodies: role of dose, site of injection, and injection volume on rituximab pharmacokinetics in rats." Pharm Res **29**(2): 490-499.

Kagan, L., J. Zhao and D. E. Mager (2014). "Interspecies pharmacokinetic modeling of subcutaneous absorption of rituximab in mice and rats." Pharm Res **31**(12): 3265-3273.

Kaletra Product Lablel (AbbVie Inc.) (Accessed 3-2-2017). "https://dailymed.nlm.nih.gov/dailymed/drugInfo.cfm?setid=8290add3-4449-4e58-6c97-8fe1eec972e3."

Kaminskas, L. M., D. B. Ascher, V. M. McLeod, M. J. Herold, C. P. Le, E. K. Sloan and C. J. Porter (2013). "PEGylation of interferon alpha2 improves lymphatic exposure after subcutaneous and intravenous administration and improves antitumour efficacy against lymphatic breast cancer metastases." J Control Release **168**(2): 200-208.

Kaminskas, L. M., J. Kota, V. M. McLeod, B. D. Kelly, P. Karellas and C. J. Porter (2009). "PEGylation of polylysine dendrimers improves absorption and lymphatic targeting following SC administration in rats." J Control Release **140**(2): 108-116.

Kaminskas, L. M., V. M. McLeod, D. B. Ascher, G. M. Ryan, S. Jones, J. M. Haynes, N. L. Trevaskis, L. J. Chan, E. K. Sloan, B. A. Finnin, M. Williamson, T. Velkov, E. D. Williams, B. D. Kelly, D. J. Owen and C. J. Porter (2015). "Methotrexate-conjugated PEGylated dendrimers show differential patterns of deposition and activity in tumor-burdened lymph nodes after intravenous and subcutaneous administration in rats." Mol Pharm **12**(2): 432-443.

Karaman, S. and M. Detmar (2014). "Mechanisms of lymphatic metastasis." J Clin Invest **124**(3): 922-928.

Kaufman, S. and Y. Deng (1993). "Splenic control of intravascular volume in the rat." J Physiol **468**: 557-565.

Kearney, M. F., A. Wiegand, W. Shao, W. R. McManus, M. J. Bale, B. Luke, F. Maldarelli, J. W. Mellors and J. M. Coffin (2017). "Ongoing HIV Replication During ART Reconsidered." Open Forum Infectious Diseases **4**(3): ofx173-ofx173.

Khan, S., S. Telwatte, M. Trapecar, S. Yukl and S. Sanjabi (2017). "Differentiating Immune Cell Targets in Gut-Associated Lymphoid Tissue for HIV Cure." AIDS Res Hum Retroviruses **33**(S1): S40-S58.

Khato, J., E. R. Priester and S. M. Sieber (1982). "Enhanced lymph node uptake of melphalan following liposomal entrapment and effects on lymph node metastasis in rats." Cancer Treat Rep **66**(3): 517-527.

Khullar, O. V., A. P. Griset, S. L. Gibbs-Strauss, L. R. Chirieac, K. A. Zubris, J. V. Frangioni, M. W. Grinstaff and Y. L. Colson (2012). "Nanoparticle migration and delivery of Paclitaxel to regional lymph nodes in a large animal model." J Am Coll Surg **214**(3): 328-337.

Kinman, L., S. J. Brodie, C. C. Tsai, T. Bui, K. Larsen, A. Schmidt, D. Anderson, W. R. Morton, S. L. Hu and R. J. Ho (2003). "Lipid-drug association enhanced HIV-1 protease inhibitor indinavir localization in lymphoid tissues and viral load reduction: a proof of concept study in HIV-2287-infected macaques." J Acquir Immune Defic Syndr **34**(4): 387-397.

Kinman, L., T. Bui, K. Larsen, C. C. Tsai, D. Anderson, W. R. Morton, S. L. Hu and R. J. Ho (2006). "Optimization of lipid-indinavir complexes for localization in lymphoid tissues of HIV-infected macaques." J Acquir Immune Defic Syndr **42**(2): 155-161.

Kinnunen, H. M. and R. J. Mrsny (2014). "Improving the outcomes of biopharmaceutical delivery via the subcutaneous route by understanding the chemical, physical and physiological properties of the subcutaneous injection site." J Control Release **182**: 22-32.

Kivela, R., E. Havas and V. Vihko (2007). "Localisation of lymphatic vessels and vascular endothelial growth factors-C and -D in human and mouse skeletal muscle with immunohistochemistry." Histochem Cell Biol **127**(1): 31-40.

Koal, T., H. Burhenne, R. Romling, M. Svoboda, K. Resch and V. Kaever (2005). "Quantification of antiretroviral drugs in dried blood spot samples by means of liquid chromatography/tandem mass spectrometry." Rapid Commun Mass Spectrom **19**(21): 2995-3001.

Kobayashi, H. and M. W. Brechbiel (2003). "Dendrimer-based macromolecular MRI contrast agents: characteristics and application." Mol Imaging **2**(1): 1-10.

Koehn, J., Y. Ding, J. Freeling, J. Duan and R. J. Ho (2015). "A simple, efficient, and sensitive method for simultaneous detection of anti-HIV drugs atazanavir, ritonavir, and tenofovir by use of liquid chromatography-tandem mass spectrometry." Antimicrob Agents Chemother **59**(11): 6682-6688.

Koehn, J. and R. J. Ho (2014). "Novel liquid chromatography-tandem mass spectrometry method for simultaneous detection of anti-HIV drugs Lopinavir, Ritonavir, and Tenofovir in plasma." Antimicrob Agents Chemother **58**(5): 2675-2680.

Koivisto, V. A. and P. Felig (1980). "Alterations in insulin absorption and in blood glucose control associated with varying insulin injection sites in diabetic patients." Ann Intern Med **92**(1): 59-61.

Kota, J., K. K. Machavaram, D. N. McLennan, G. A. Edwards, C. J. Porter and S. A. Charman (2007). "Lymphatic absorption of subcutaneously administered proteins: influence of different injection sites on the absorption of darbepoetin alfa using a sheep model." Drug Metab Dispos **35**(12): 2211-2217.

Kraft, J. C., J. P. Freeling, Z. Wang and R. J. Ho (2014). "Emerging research and clinical development trends of liposome and lipid nanoparticle drug delivery systems." J Pharm Sci **103**(1): 29-52.

Kraft, J. C. and R. J. Ho (2014). "Interactions of indocyanine green and lipid in enhancing near-infrared fluorescence properties: the basis for near-infrared imaging in vivo." Biochemistry **53**(8): 1275-1283.

Kraft, J. C., L. A. McConnachie, J. Koehn, L. Kinman, C. Collins, D. D. Shen, A. C. Collier and R. J. Ho (2017). "Long-acting combination anti-HIV drug suspension enhances and sustains higher drug levels in lymph node cells than in blood cells and plasma." AIDS **31**(6): 765-770.

Kraft, J. C., L. A. McConnachie, J. Koehn, L. Kinman, J. Sun, A. C. Collier, C. Collins, D. D. Shen and R. J. Y. Ho (2018). "Mechanism-based pharmacokinetic (MBPK) models describe the complex plasma kinetics of three antiretrovirals delivered by a long-acting anti-HIV drug combination nanoparticle formulation." J Control Release **275**: 229-241.

Kraft, J. C., P. M. Treuting and R. J. Y. Ho (2018). "Indocyanine green nanoparticles undergo selective lymphatic uptake, distribution and retention and enable detailed mapping of lymph vessels, nodes and abnormalities." J Drug Target: 1-11.

Kubik, S. (2003). Anatomy of the lymphatic system. Textbook of Lymphology. M. Foldi, E. Foldi and S. Kubik. San Francisco, Elsevier GmbH**:** 1-166.

Kumar, G. N., V. K. Jayanti, M. K. Johnson, J. Uchic, S. Thomas, R. D. Lee, B. A. Grabowski, H. L. Sham, D. J. Kempf, J. F. Denissen, K. C. Marsh, E. Sun and S. A. Roberts (2004). "Metabolism and disposition of the HIV-1 protease inhibitor lopinavir (ABT-378) given in combination with ritonavir in rats, dogs, and humans." Pharm Res **21**(9): 1622-1630.

Kuo, H. H. and M. Lichterfeld (2018). "Recent progress in understanding HIV reservoirs." Curr Opin HIV AIDS **13**(2): 137-142.

Kutkut, I., M. J. Meens, T. A. McKee, M. L. Bochaton-Piallat and B. R. Kwak (2015). "Lymphatic vessels: an emerging actor in atherosclerotic plaque development." Eur J Clin Invest **45**(1): 100-108.

Lalanne, M., A. Paci, K. Andrieux, N. Dereuddre-Bosquet, P. Clayette, A. Deroussent, M. Re, G. Vassal, P. Couvreur and D. Desmaele (2007). "Synthesis and biological evaluation of two glycerolipidic prodrugs of didanosine for direct lymphatic delivery against HIV." Bioorg Med Chem Lett **17**(8): 2237-2240.

Landersdorfer, C. B., S. M. Caliph, D. M. Shackleford, D. B. Ascher and L. M. Kaminskas (2015). "PEGylated interferon displays differences in plasma clearance and bioavailability between male and female mice and between female immunocompetent C57Bl/6J and athymic nude mice." J Pharm Sci **104**(5): 1848-1855.

Leak, L. V. and M. P. Jamuar (1983). "Ultrastructure of pulmonary lymphatic vessels." Am Rev Respir Dis **128**(2 Pt 2): S59-65.

Leak, L. V., A. Schannahan, H. Scully and W. M. Daggett (1978). "Lymphatic vessels of the mammalian heart." Anat Rec **191**(2): 183-201.

Lederman, M. M. and L. Margolis (2008). "The lymph node in HIV pathogenesis." Semin Immunol **20**(3): 187-195.

Lee, J. S. (1986). "Tissue fluid pressure, lymph pressure, and fluid transport in rat intestinal villi." Microvasc Res **31**(2): 170-183.

Lee, S., H. Hatano, A. D. Kashuba, M. L. Cottrell, T. J. Liegler, S. Stephenson, M. Somsouk, P. W. Hunt, S. G. Deeks and R. M. Savic (2017). Integrase and protease inhibitor concentrations in lymph node and gut mucosal tissue (Abstract #407). Conference on Retroviruses and Opportunistic Infections (CROI), Seattle, WA.

Lee, W. A., G. X. He, E. Eisenberg, T. Cihlar, S. Swaminathan, A. Mulato and K. C. Cundy (2005). "Selective intracellular activation of a novel prodrug of the human immunodeficiency virus reverse transcriptase inhibitor tenofovir leads to preferential distribution and accumulation in lymphatic tissue." Antimicrob Agents Chemother **49**(5): 1898-1906.

Leikola, J. P., T. S. Toivonen, L. A. Krogerus, K. A. von Smitten and M. H. Leidenius (2005). "Rapid immunohistochemistry enhances the intraoperative diagnosis of sentinel lymph node metastases in invasive lobular breast carcinoma." Cancer **104**(1): 14-19.

Leth, S., M. H. Schleimann, S. K. Nissen, J. F. Hojen, R. Olesen, M. E. Graversen, S. Jorgensen, A. S. Kjaer, P. W. Denton, A. Mork, M. A. Sommerfelt, K. Krogsgaard, L. Ostergaard, T. A. Rasmussen, M. Tolstrup and O. S. Sogaard (2016). "Combined effect of Vacc-4x, recombinant human granulocyte macrophage colony-stimulating factor vaccination, and romidepsin on the HIV-1 reservoir (REDUC): a single-arm, phase 1B/2A trial." Lancet HIV **3**(10): e463-472.

Levick, J. R. (2004). "Revision of the Starling principle: new views of tissue fluid balance." J Physiol **557**(Pt 3): 704.

Levick, J. R. (2010). An introduction to cardiovascular physiology. London, Hodder Arnold.

Levick, J. R. and C. C. Michel (2010). "Microvascular fluid exchange and the revised Starling principle." Cardiovasc Res **87**(2): 198-210.

Lewis, J. H. (1921). "The route and rate of absorption of subcutaneously injected serum: In relation to the occurrence of sudden death after injection of antitoxic horse serum." Journal of the American Medical Association **76**(20): 1342-1345.

Li, X., B. Beauvoit, R. White, S. Nioka, B. Chance and A. Yodh (1995). "Tumor localization using fluorescence of indocyanine green (ICG) in a rat model." Proc. SPIE **2389**: 789-797.

Lim, H. Y., J. M. Rutkowski, J. Helft, S. T. Reddy, M. A. Swartz, G. J. Randolph and V. Angeli (2009). "Hypercholesterolemic mice exhibit lymphatic vessel dysfunction and degeneration." Am J Pathol **175**(3): 1328-1337.

Lim, H. Y., C. H. Thiam, K. P. Yeo, R. Bisoendial, C. S. Hii, K. C. McGrath, K. W. Tan, A. Heather, J. S. Alexander and V. Angeli (2013). "Lymphatic vessels are essential for the removal of cholesterol from peripheral tissues by SR-BI-mediated transport of HDL." Cell Metab **17**(5): 671-684.

Lindena, J., W. Kupper and I. Trautschold (1986). "Catalytic enzyme activity concentration in thoracic duct, liver, and intestinal lymph of the dog, the rabbit, the rat and the mouse. Approach to a quantitative diagnostic enzymology, II. Communication." J Clin Chem Clin Biochem **24**(1): 19-33.

Listrom, M. B. and C. M. Fenoglio-Preiser (1987). "Lymphatic distribution of the stomach in normal, inflammatory, hyperplastic, and neoplastic tissue." Gastroenterology **93**(3): 506-514.

Lorenzo-Redondo, R., H. R. Fryer, T. Bedford, E. Y. Kim, J. Archer, S. L. Kosakovsky Pond, Y. S. Chung, S. Penugonda, J. G. Chipman, C. V. Fletcher, T. W. Schacker, M. H. Malim, A. Rambaut, A. T. Haase, A. R. McLean and S. M. Wolinsky (2016). "Persistent HIV-1 replication maintains the tissue reservoir during therapy." Nature **530**(7588): 51-56.

Louissaint, N. A., Y. J. Cao, P. L. Skipper, R. G. Liberman, S. R. Tannenbaum, S. Nimmagadda, J. R. Anderson, S. Everts, R. Bakshi, E. J. Fuchs and C. W. Hendrix (2013). "Single dose pharmacokinetics of oral tenofovir in plasma, peripheral blood mononuclear cells, colonic tissue, and vaginal tissue." AIDS Res Hum Retroviruses **29**(11): 1443-1450.

Louveau, A., I. Smirnov, T. J. Keyes, J. D. Eccles, S. J. Rouhani, J. D. Peske, N. C. Derecki, D. Castle, J. W. Mandell, K. S. Lee, T. H. Harris and J. Kipnis (2015). "Structural and functional features of central nervous system lymphatic vessels." Nature **523**(7560): 337-341.

MacDonald, R. I. (1990). "Characteristics of self-quenching of the fluorescence of lipid-conjugated rhodamine in membranes." J Biol Chem **265**(23): 13533-13539.

Macdougall, I. C., J. M. Jones, M. I. Robinson, J. B. Miles, G. A. Coles and J. D. Williams (1991). "Subcutaneous erythropoietin therapy: comparison of three different sites of injection." Contrib Nephrol **88**: 152-156; discussion 157-158.

Makarainen, L., A. van Beek, L. Tuomivaara, B. Asplund and H. Coelingh Bennink (1998). "Ovarian function during the use of a single contraceptive implant: Implanon compared with Norplant." Fertil Steril **69**(4): 714-721.

Maloy, K. J., I. Erdmann, V. Basch, S. Sierro, T. A. Kramps, R. M. Zinkernagel, S. Oehen and T. M. Kundig (2001). "Intralymphatic immunization enhances DNA vaccination." Proc Natl Acad Sci U S A **98**(6): 3299-3303.

Margaris, K. N. and R. A. Black (2012). "Modelling the lymphatic system: challenges and opportunities." J R Soc Interface **9**(69): 601-612.

Margolis, D. A., J. Gonzalez-Garcia, H. J. Stellbrink, J. J. Eron, Y. Yazdanpanah, D. Podzamczer, T. Lutz, J. B. Angel, G. J. Richmond, B. Clotet, F. Gutierrez, L. Sloan, M. S. Clair, M. Murray, S. L. Ford, J. Mrus, P. Patel, H. Crauwels, S. K. Griffith, K. C. Sutton, D. Dorey, K. Y. Smith, P. E. Williams and W. R. Spreen (2017). "Long-acting intramuscular cabotegravir and rilpivirine in adults with HIV-1 infection (LATTE-2): 96-week results of a randomised, open-label, phase 2b, non-inferiority trial." Lancet **390**(10101): 1499-1510.

Martel, C., W. Li, B. Fulp, A. M. Platt, E. L. Gautier, M. Westerterp, R. Bittman, A. R. Tall, S. H. Chen, M. J. Thomas, D. Kreisel, M. A. Swartz, M. G. Sorci-Thomas and G. J. Randolph (2013). "Lymphatic vasculature mediates macrophage reverse cholesterol transport in mice." J Clin Invest **123**(4): 1571-1579.

Martel, C. and G. J. Randolph (2013). "Atherosclerosis and transit of HDL through the lymphatic vasculature." Curr Atheroscler Rep **15**(9): 354.

Massud, I., J. Mitchell, D. Babusis, F. Deyounks, A. S. Ray, J. F. Rooney, W. Heneine, M. D. Miller and J. G. Garcia-Lerma (2016). "Chemoprophylaxis With Oral Emtricitabine and Tenofovir Alafenamide Combination Protects Macaques From Rectal Simian/Human Immunodeficiency Virus Infection." J Infect Dis **214**(7): 1058-1062.

Matsumoto, K., S. Soh, T. Satoh, M. Iwamura, Y. Ishikawa, T. Ishii and S. Baba (2008). "Distribution of lymphatic vessel network in normal urinary bladder." Urology **72**(3): 706-710.

McConnachie, L. A., L. M. Kinman, J. Koehn, J. C. Kraft, S. Lane, W. Lee, A. C. Collier and R. J. Y. Ho (2018). "Long-Acting Profile of 4 Drugs in 1 Anti-HIV Nanosuspension in Nonhuman Primates for 5 Weeks After a Single Subcutaneous Injection." J Pharm Sci.

McFarlin, D. E. and R. M. Binns (1973). "Lymph node function and lymphocyte circulation in the pig." Adv Exp Med Biol **29**(0): 87-93.

McGowan, I., C. S. Dezzutti, A. Siegel, J. Engstrom, A. Nikiforov, K. Duffill, C. Shetler, N. Richardson-Harman, K. Abebe, D. Back, L. Else, D. Egan, S. Khoo, J. E. Egan, R. Stall, P. E. Williams, K. K. Rehman, A. Adler, R. M. Brand, B. Chen, S. Achilles and R. D. Cranston (2016). "Long-acting rilpivirine as potential pre-exposure prophylaxis for HIV-1 prevention (the MWRI-01 study): an open-label, phase 1, compartmental, pharmacokinetic and pharmacodynamic assessment." Lancet HIV **3**(12): e569-e578.

McLennan, D. N., C. J. Porter, G. A. Edwards, S. W. Martin, A. C. Heatherington and S. A. Charman (2005). "Lymphatic absorption is the primary contributor to the systemic availability of epoetin Alfa following subcutaneous administration to sheep." J Pharmacol Exp Ther **313**(1): 345-351.

McMaster, P. D. (1942). "Lymphatic Participation in Cutaneous Phenomena: Harvey Lecture, April 16, 1942." Bull N Y Acad Med **18**(11): 731-767.

McMillan, J., A. Szlachetka, L. Slack, B. Sillman, B. Lamberty, B. Morsey, S. Callen, N. Gautam, Y. Alnouti, B. Edagwa, H. E. Gendelman and H. S. Fox (2018). "Pharmacokinetics of a Long-Acting Nanoformulated Dolutegravir Prodrug in Rhesus Macaques." Antimicrob Agents Chemother **62**(1).

Meijer, D. K., B. Weert and G. A. Vermeer (1988). "Pharmacokinetics of biliary excretion in man. VI. Indocyanine green." Eur J Clin Pharmacol **35**(3): 295-303.

Milesi-Halle, A., S. M. Abdel-Rahman, A. Brown, S. S. McCullough, L. Letzig, J. A. Hinson and L. P. James (2011). "Indocyanine green clearance varies as a function of N-acetylcysteine treatment in a murine model of acetaminophen toxicity." Chem Biol Interact **189**(3): 222-229.

Miller, M. A., S. Gadde, C. Pfirschke, C. Engblom, M. M. Sprachman, R. H. Kohler, K. S. Yang, A. M. Laughney, G. Wojtkiewicz, N. Kamaly, S. Bhonagiri, M. J. Pittet, O. C. Farokhzad and R. Weissleder (2015). "Predicting therapeutic nanomedicine efficacy using a companion magnetic resonance imaging nanoparticle." Sci Transl Med **7**(314): 314ra183.

Miteva, D. O., J. M. Rutkowski, J. B. Dixon, W. Kilarski, J. D. Shields and M. A. Swartz (2010). "Transmural flow modulates cell and fluid transport functions of lymphatic endothelium." Circ Res **106**(5): 920-931.

Moon, J. J., H. Suh, M. E. Polhemus, C. F. Ockenhouse, A. Yadava and D. J. Irvine (2012). "Antigen-displaying lipid-enveloped PLGA nanoparticles as delivery agents for a Plasmodium vivax malaria vaccine." PLoS One **7**(2): e31472.

Mordon, S., J. M. Devoisselle, S. Soulie-Begu and T. Desmettre (1998). "Indocyanine green: physicochemical factors affecting its fluorescence in vivo." Microvasc Res **55**(2): 146-152.

Mortimer, P. S. and S. G. Rockson (2014). "New developments in clinical aspects of lymphatic disease." J Clin Invest **124**(3): 915-921.

Mouta Carreira, C., S. M. Nasser, E. di Tomaso, T. P. Padera, Y. Boucher, S. I. Tomarev and R. K. Jain (2001). "LYVE-1 is not restricted to the lymph vessels: expression in normal liver blood sinusoids and down-regulation in human liver cancer and cirrhosis." Cancer Res **61**(22): 8079-8084.

Mowat, A. M. and J. L. Viney (1997). "The anatomical basis of intestinal immunity." Immunol Rev **156**: 145-166.

Moyer, T. J., A. C. Zmolek and D. J. Irvine (2016). "Beyond antigens and adjuvants: formulating future vaccines." J Clin Invest **126**(3): 799-808.

Murata, M., K. Tahara and H. Takeuchi (2014). "Real-time in vivo imaging of surface-modified liposomes to evaluate their behavior after pulmonary administration." Eur J Pharm Biopharm **86**(1): 115-119.

Murfee, W. L., J. W. Rappleye, M. Ceballos and G. W. Schmid-Schonbein (2007). "Discontinuous expression of endothelial cell adhesion molecules along initial lymphatic vessels in mesentery: the primary valve structure." Lymphat Res Biol **5**(2): 81-89.

Muthuchamy, M. and D. Zawieja (2008). "Molecular regulation of lymphatic contractility." Ann N Y Acad Sci **1131**: 89-99.

Nadolski, G. and M. Itkin (2013). "Thoracic duct embolization for the management of chylothoraces." Curr Opin Pulm Med **19**(4): 380-386.

Nanjee, M. N., C. J. Cooke, W. L. Olszewski and N. E. Miller (2000). "Lipid and apolipoprotein concentrations in prenodal leg lymph of fasted humans. Associations with plasma concentrations in normal subjects, lipoprotein lipase deficiency, and LCAT deficiency." J Lipid Res **41**(8): 1317.

Negrini, D. and A. Moriondo (2011). "Lymphatic anatomy and biomechanics." J Physiol **589**(Pt 12): 2927-2934.

Nguyen, Q. T. and R. Y. Tsien (2013). "Fluorescence-guided surgery with live molecular navigation--a new cutting edge." Nat Rev Cancer **13**(9): 653-662.

Nora, J. J., D. W. Smith and J. R. Cameron (1964). "The Route of Insulin Administration in the Management of Diabetes Mellitus." J Pediatr **64**: 547-551.

Norrmen, C., K. I. Ivanov, J. Cheng, N. Zangger, M. Delorenzi, M. Jaquet, N. Miura, P. Puolakkainen, V. Horsley, J. Hu, H. G. Augustin, S. Yla-Herttuala, K. Alitalo and T. V. Petrova (2009). "FOXC2 controls formation and maturation of lymphatic collecting vessels through cooperation with NFATc1." J Cell Biol **185**(3): 439-457.

Ohtani, O. and Y. Ohtani (2008). "Lymph circulation in the liver." Anat Rec (Hoboken) **291**(6): 643-652.

Olszewski, W., A. Engeset, P. M. Jaeger, J. Sokolowski and L. Theodorsen (1977). "Flow and composition of leg lymph in normal men during venous stasis, muscular activity and local hyperthermia." Acta Physiol Scand **99**(2): 149-155.

Oussoren, C. and G. Storm (2001). "Liposomes to target the lymphatics by subcutaneous administration." Adv Drug Deliv Rev **50**(1-2): 143-156.

Oussoren, C., J. Zuidema, D. J. Crommelin and G. Storm (1997). "Lymphatic uptake and biodistribution of liposomes after subcutaneous injection. II. Influence of liposomal size, lipid compostion and lipid dose." Biochim Biophys Acta **1328**(2): 261-272.

Owen, A. and S. Rannard (2016). "Strengths, weaknesses, opportunities and challenges for long acting injectable therapies: Insights for applications in HIV therapy." Adv Drug Deliv Rev **103**: 144-156.

Padera, T. P., A. Kadambi, E. di Tomaso, C. M. Carreira, E. B. Brown, Y. Boucher, N. C. Choi, D. Mathisen, J. Wain, E. J. Mark, L. L. Munn and R. K. Jain (2002). "Lymphatic metastasis in the absence of functional intratumor lymphatics." Science **296**(5574): 1883-1886.

Padera, T. P., E. F. Meijer and L. L. Munn (2016). "The Lymphatic System in Disease Processes and Cancer Progression." Annu Rev Biomed Eng **18**: 125-158.

Paiva, D. D., J. C. Morais, J. Pilotto, V. Veloso, F. Duarte and H. L. Lenzi (1996). "Spectrum of morphologic changes of lymph nodes in HIV infection." Mem Inst Oswaldo Cruz **91**(3): 371-379.

Pantaleo, G., C. Graziosi, J. F. Demarest, L. Butini, M. Montroni, C. H. Fox, J. M. Orenstein, D. P. Kotler and A. S. Fauci (1993). "HIV infection is active and progressive in lymphoid tissue during the clinically latent stage of disease." Nature **362**(6418): 355-358.

Pappenheimer, J. R. (1953). "Passage of molecules through capillary wals." Physiol Rev **33**(3): 387-423.

Partridge, S. C., B. F. Kurland, C. L. Liu, R. J. Ho and A. Ruddell (2015). "Tumor-induced lymph node alterations detected by MRI lymphography using gadolinium nanoparticles." Sci Rep **5**: 15641.

Paskett, E. D., J. A. Dean, J. M. Oliveri and J. P. Harrop (2012). "Cancer-related lymphedema risk factors, diagnosis, treatment, and impact: a review." J Clin Oncol **30**(30): 3726-3733.

Philip, R., A. Penzkofer, W. Baumler, R. M. Szeimies and C. Abels (1996). "Absorption and fluorescence spectroscopic investigation of indocyanine green." J. Photochem. Photobiol. A: Biol. **96**: 137-148.

Pitorre, M., G. Bastiat, E. Chatel and J.-P. Benoît (2015). "Passive and specific targeting of lymph nodes: the influence of the administration route." European Journal of Nanomedicine **7**(2): 121-128.

Pivot, X., J. Gligorov, V. Muller, P. Barrett-Lee, S. Verma, A. Knoop, G. Curigliano, V. Semiglazov, G. Lopez-Vivanco, V. Jenkins, N. Scotto, S. Osborne, L. Fallowfield and G. PrefHer Study (2013). "Preference for subcutaneous or intravenous administration of trastuzumab in patients with HER2-positive early breast cancer (PrefHer): an open-label randomised study." Lancet Oncol **14**(10): 962-970.

PMDA (Accessed Oct 11, 2016). "Complera (FTC/RPV/TFV) Gilead Nonclinical Summary, 2010." (Pharmaceutical and Medical Device Agency of Japan) http://www.pmda.go.jp/drugs/2014/P201400148/800155000_22600AMX01325_H100_1.pdf.

PMDA (Pharmaceutical and Medical Device Agency of Japan) http://www.pmda.go.jp/drugs/2014/P201400148/800155000_22600AMX01325_H100_1.pdf (Accessed Jan 31, 2018). "Complera (FTC/RPV/TFV) Gilead Nonclinical Summary, 2010."

Poles, M. A., W. J. Boscardin, J. Elliott, P. Taing, M. M. Fuerst, I. McGowan, S. Brown and P. A. Anton (2006). "Lack of decay of HIV-1 in gut-associated lymphoid tissue reservoirs in maximally suppressed individuals." J Acquir Immune Defic Syndr **43**(1): 65-68.

Polom, K., D. Murawa, Y. S. Rho, P. Nowaczyk, M. Hunerbein and P. Murawa (2011). "Current trends and emerging future of indocyanine green usage in surgery and oncology: a literature review." Cancer **117**(21): 4812-4822.

Porter, C. J. and S. A. Charman (2000). "Lymphatic transport of proteins after subcutaneous administration." J Pharm Sci **89**(3): 297-310.

Portnoy, E., S. Lecht, P. Lazarovici, D. Danino and S. Magdassi (2011). "Cetuximab-labeled liposomes containing near-infrared probe for in vivo imaging." Nanomedicine **7**(4): 480-488.

Proulx, S. T., P. Luciani, A. Christiansen, S. Karaman, K. S. Blum, M. Rinderknecht, J. C. Leroux and M. Detmar (2013). "Use of a PEG-conjugated bright near-infrared dye for functional imaging of rerouting of tumor lymphatic drainage after sentinel lymph node metastasis." Biomaterials **34**(21): 5128-5137.

Proulx, S. T., P. Luciani, S. Derzsi, M. Rinderknecht, V. Mumprecht, J. C. Leroux and M. Detmar (2010). "Quantitative imaging of lymphatic function with liposomal indocyanine green." Cancer Res **70**(18): 7053-7062.

Pu, K., A. J. Shuhendler, J. V. Jokerst, J. Mei, S. S. Gambhir, Z. Bao and J. Rao (2014). "Semiconducting polymer nanoparticles as photoacoustic molecular imaging probes in living mice." Nat Nanotechnol **9**(3): 233-239.

Rajagopalan, R., P. Uetrecht, J. E. Bugaj, S. A. Achilefu and R. B. Dorshow (2000). "Stabilization of the optical tracer agent indocyanine green using noncovalent interactions." Photochem Photobiol **71**(3): 347-350.

Ramakrishnan, R., W. K. Cheung, F. Farrell, L. Joffee and W. J. Jusko (2003). "Pharmacokinetic and pharmacodynamic modeling of recombinant human erythropoietin after intravenous and subcutaneous dose administration in cynomolgus monkeys." J Pharmacol Exp Ther **306**(1): 324-331.

Raman, R., V. Sasisekharan and R. Sasisekharan (2005). "Structural insights into biological roles of protein-glycosaminoglycan interactions." Chem Biol **12**(3): 267-277.

Randolph, G. J. and N. E. Miller (2014). "Lymphatic transport of high-density lipoproteins and chylomicrons." J Clin Invest **124**(3): 929-935.

Rao, D. A., M. L. Forrest, A. W. Alani, G. S. Kwon and J. R. Robinson (2010). "Biodegradable PLGA based nanoparticles for sustained regional lymphatic drug delivery." J Pharm Sci **99**(4): 2018-2031.

Ray, A. S., M. W. Fordyce and M. J. Hitchcock (2016). "Tenofovir alafenamide: A novel prodrug of tenofovir for the treatment of Human Immunodeficiency Virus." Antiviral Res **125**: 63-70.

Red-Horse, K. (2008). "Lymphatic vessel dynamics in the uterine wall." Placenta **29 Suppl A**: S55-59.

Rerks-Ngarm, S., P. Pitisuttithum, S. Nitayaphan, J. Kaewkungwal, J. Chiu, R. Paris, N. Premsri, C. Namwat, M. de Souza, E. Adams, M. Benenson, S. Gurunathan, J. Tartaglia, J. G. McNeil, D. P. Francis, D. Stablein, D. L. Birx, S. Chunsuttiwat, C. Khamboonruang, P. Thongcharoen, M. L. Robb, N. L. Michael, P. Kunasol, J. H. Kim and M.-T. Investigators (2009). "Vaccination with ALVAC and AIDSVAX to prevent HIV-1 infection in Thailand." N Engl J Med **361**(23): 2209-2220.

Richter, W. F., S. G. Bhansali and M. E. Morris (2012). "Mechanistic determinants of biotherapeutics absorption following SC administration." AAPS J **14**(3): 559-570.

Richter, W. F. and B. Jacobsen (2014). "Subcutaneous absorption of biotherapeutics: knowns and unknowns." Drug Metab Dispos **42**(11): 1881-1889.

Rockson, S. G. (2012). "Update on the biology and treatment of lymphedema." Curr Treat Options Cardiovasc Med **14**(2): 184-192.

Rockson, S. G. (2017). "Lymphatic Medicine: Paradoxically and Unnecessarily Ignored." Lymphat Res Biol **15**(4): 315-316.

Rockson, S. G., D. N. Granger, K. M. Skeff and W. Chaite (2004). "Lymphatic biology and disease: is it being taught? Who is listening?" Lymphat Res Biol **2**(2): 86-95.

Rodrigues, V., N. Ruffin, M. San-Roman and P. Benaroch (2017). "Myeloid Cell Interaction with HIV: A Complex Relationship." Front Immunol **8**: 1698.

Rosenbloom, D. I. S., A. L. Hill, S. B. Laskey and R. F. Siliciano (2017). "Re-evaluating evolution in the HIV reservoir." Nature **551**(7681): E6-E9.

Rowland, M. and T. M. Tozer (2011). Clinical pharmacokinetics and pharmacodynamics: concepts and applications. Baltimore, MD, Lippincott Williams & Wilkins.

Ruane, P. J., E. DeJesus, D. Berger, M. Markowitz, U. F. Bredeek, C. Callebaut, L. Zhong, S. Ramanathan, M. S. Rhee, M. W. Fordyce and K. Yale (2013). "Antiviral activity, safety, and

pharmacokinetics/pharmacodynamics of tenofovir alafenamide as 10-day monotherapy in HIV-1-positive adults." J Acquir Immune Defic Syndr **63**(4): 449-455.

Ruddle, N. H. (2014). "Lymphatic vessels and tertiary lymphoid organs." J Clin Invest **124**(3): 953-959.

Ryan, G. M., L. M. Kaminskas, J. B. Bulitta, M. P. McIntosh, D. J. Owen and C. J. Porter (2013). "PEGylated polylysine dendrimers increase lymphatic exposure to doxorubicin when compared to PEGylated liposomal and solution formulations of doxorubicin." J Control Release **172**(1): 128-136.

Ryan, G. M., L. M. Kaminskas and C. J. Porter (2014). "Nano-chemotherapeutics: maximising lymphatic drug exposure to improve the treatment of lymph-metastatic cancers." J Control Release **193**: 241-256.

Sainte-Marie, G., F. S. Peng and C. Belisle (1982). "Overall architecture and pattern of lymph flow in the rat lymph node." Am J Anat **164**(4): 275-309.

Sandanaraj, B. S., H. U. Gremlich, R. Kneuer, J. Dawson and S. Wacha (2010). "Fluorescent nanoprobes as a biomarker for increased vascular permeability: implications in diagnosis and treatment of cancer and inflammation." Bioconjug Chem **21**(1): 93-101.

Santangelo, P. J., K. A. Rogers, C. Zurla, E. L. Blanchard, S. Gumber, K. Strait, F. Connor-Stroud, D. M. Schuster, P. K. Amancha, J. J. Hong, S. N. Byrareddy, J. A. Hoxie, B. Vidakovic, A. A. Ansari, E. Hunter and F. Villinger (2015). "Whole-body immunoPET reveals active SIV dynamics in viremic and antiretroviral therapy-treated macaques." Nat Methods **12**(5): 427-432.

Sarin, H. (2010). "Physiologic upper limits of pore size of different blood capillary types and another perspective on the dual pore theory of microvascular permeability." J Angiogenes Res **2**: 14.

Saxena, V., M. Sadoqi and J. Shao (2003). "Degradation kinetics of indocyanine green in aqueous solution." J Pharm Sci **92**(10): 2090-2097.

Scallan, J. P., M. A. Hill and M. J. Davis (2015). "Lymphatic vascular integrity is disrupted in type 2 diabetes due to impaired nitric oxide signalling." Cardiovasc Res **107**(1): 89-97.

Scallan, J. P. and V. H. Huxley (2010). "In vivo determination of collecting lymphatic vessel permeability to albumin: a role for lymphatics in exchange." J Physiol **588**(Pt 1): 243-254.

Schacker, T. W., P. L. Nguyen, G. J. Beilman, S. Wolinsky, M. Larson, C. Reilly and A. T. Haase (2002). "Collagen deposition in HIV-1 infected lymphatic tissues and T cell homeostasis." J Clin Invest **110**(8): 1133-1139.

Schacker, T. W., P. L. Nguyen, E. Martinez, C. Reilly, J. M. Gatell, A. Horban, E. Bakowska, B. Berzins, R. van Leeuwen, S. Wolinsky, A. T. Haase and R. L. Murphy (2002). "Persistent abnormalities in lymphoid tissues of human immunodeficiency virus-infected patients successfully treated with highly active antiretroviral therapy." J Infect Dis **186**(8): 1092-1097.

Schacker, T. W., C. Reilly, G. J. Beilman, J. Taylor, D. Skarda, D. Krason, M. Larson and A. T. Haase (2005). "Amount of lymphatic tissue fibrosis in HIV infection predicts magnitude of HAART-associated change in peripheral CD4 cell count." AIDS **19**(18): 2169-2171.

Scharko, A. M., S. B. Perlman, P. W. n. Hinds, J. M. Hanson, H. Uno and C. D. Pauza (1996). "Whole body positron emission tomography imaging of simian immunodeficiency virus-infected rhesus macaques." Proc Natl Acad Sci U S A **93**(13): 6425-6430.

Schirger, A., E. G. Harrison, Jr. and J. M. Janes (1962). "Idiopathic lymphedema. Review of 131 cases." JAMA **182**: 14-22.

Schmid-Schonbein, G. W. (1990). "Microlymphatics and lymph flow." Physiol Rev **70**(4): 987-1028.

Schubert, W., P. G. Frank, B. Razani, D. S. Park, C. W. Chow and M. P. Lisanti (2001). "Caveolae-deficient endothelial cells show defects in the uptake and transport of albumin in vivo." J Biol Chem **276**(52): 48619-48622.

Schulte-Merker, S., A. Sabine and T. V. Petrova (2011). "Lymphatic vascular morphogenesis in development, physiology, and disease." J Cell Biol **193**(4): 607-618.

Schuurman, H. J., W. J. Krone, R. Broekhuizen and J. Goudsmit (1988). "Expression of RNA and antigens of human immunodeficiency virus type-1 (HIV-1) in lymph nodes from HIV-1 infected individuals." Am J Pathol **133**(3): 516-524.

Schwalbe, G. (1869). "Die arachnoidalraum, ein lymphraum und sein zusammenhang mit dem perichoriordalraum." Zentralbl. Med. Wiss. **7**: 465-467.

Segal, A. W., G. Gregoriadis and C. D. Black (1975). "Liposomes as vehicles for the local release of drugs." Clin Sci Mol Med **49**(2): 99-106.

Sengupta, S. and R. F. Siliciano (2018). "Targeting the Latent Reservoir for HIV-1." Immunity **48**(5): 872-895.

Shah, D. K. and A. M. Betts (2012). "Towards a platform PBPK model to characterize the plasma and tissue disposition of monoclonal antibodies in preclinical species and human." J Pharmacokinet Pharmacodyn **39**(1): 67-86.

Sham, H. L., D. J. Kempf, A. Molla, K. C. Marsh, G. N. Kumar, C. M. Chen, W. Kati, K. Stewart, R. Lal, A. Hsu, D. Betebenner, M. Korneyeva, S. Vasavanonda, E. McDonald, A. Saldivar, N. Wideburg, X. Chen, P. Niu, C. Park, V. Jayanti, B. Grabowski, G. R. Granneman, E. Sun, A. J. Japour, J. M. Leonard, J. J. Plattner and D. W. Norbeck (1998). "ABT-378, a highly potent inhibitor of the human immunodeficiency virus protease." Antimicrob Agents Chemother **42**(12): 3218-3224.

Shi, G. P., I. Bot and P. T. Kovanen (2015). "Mast cells in human and experimental cardiometabolic diseases." Nat Rev Cardiol **12**(11): 643-658.

Simiele, M., A. D'Avolio, L. Baietto, M. Siccardi, M. Sciandra, S. Agati, J. Cusato, S. Bonora and G. Di Perri (2011). "Evaluation of the mean corpuscular volume of peripheral blood mononuclear cells of HIV patients by a coulter counter to determine intracellular drug concentrations." Antimicrob Agents Chemother **55**(6): 2976-2978.

Skanji, R., K. Andrieux, M. Lalanne, J. Caron, C. Bourgaux, J. Degrouard, F. Brisset, C. Gueutin, H. Chacun, N. Dereuddre-Bosquet, A. Paci, G. Vassal, L. Bauduin, S. Garcia-Argote, B. Rousseau, P. Clayette, D. Desmaele and P. Couvreur (2011). "A new nanomedicine based on didanosine glycerolipidic prodrug enhances the long term accumulation of drug in a HIV sanctuary." Int J Pharm **414**(1-2): 285-297.

Skobe, M., T. Hawighorst, D. G. Jackson, R. Prevo, L. Janes, P. Velasco, L. Riccardi, K. Alitalo, K. Claffey and M. Detmar (2001). "Induction of tumor lymphangiogenesis by VEGF-C promotes breast cancer metastasis." Nat Med **7**(2): 192-198.

Skoczen, S. L. and S. T. Stern (2018). "Improved Ultrafiltration Method to Measure Drug Release from Nanomedicines Utilizing a Stable Isotope Tracer." Methods Mol Biol **1682**: 223-239.

Small, D. M., M. G. Bond, D. Waugh, M. Prack and J. K. Sawyer (1984). "Physicochemical and histological changes in the arterial wall of nonhuman primates during progression and regression of atherosclerosis." J Clin Invest **73**(6): 1590-1605.

Smedley, J., B. Turkbey, M. L. Bernardo, G. Q. Del Prete, J. D. Estes, G. L. Griffiths, H. Kobayashi, P. L. Choyke, J. D. Lifson and B. F. Keele (2014). "Tracking the luminal exposure and lymphatic drainage pathways of intravaginal and intrarectal inocula used in nonhuman primate models of HIV transmission." PLoS One **9**(3): e92830.

Spreen, W., S. L. Ford, S. Chen, D. Wilfret, D. Margolis, E. Gould and S. Piscitelli (2014). "GSK1265744 pharmacokinetics in plasma and tissue after single-dose long-acting injectable administration in healthy subjects." J Acquir Immune Defic Syndr **67**(5): 481-486.

Spreen, W. R., D. A. Margolis and J. C. Pottage, Jr. (2013). "Long-acting injectable antiretrovirals for HIV treatment and prevention." Curr Opin HIV AIDS **8**(6): 565-571.

Stacker, S. A., S. P. Williams, T. Karnezis, R. Shayan, S. B. Fox and M. G. Achen (2014). "Lymphangiogenesis and lymphatic vessel remodelling in cancer." Nat Rev Cancer **14**(3): 159-172.

Stanton, A. W., S. Modi, T. M. Bennett Britton, A. D. Purushotham, A. M. Peters, J. R. Levick and P. S. Mortimer (2009). "Lymphatic drainage in the muscle and subcutis of the arm after breast cancer treatment." Breast Cancer Res Treat **117**(3): 549-557.

Starosolski, Z., R. Bhavane, K. B. Ghaghada, S. A. Vasudevan, A. Kaay and A. Annapragada (2017). "Indocyanine green fluorescence in second near-infrared (NIR-II) window." PLoS One **12**(11): e0187563.

Steller, M. A., R. J. Parker, D. G. Covell, O. D. Holton, 3rd, A. M. Keenan, S. M. Sieber and J. N. Weinstein (1986). "Optimization of monoclonal antibody delivery via the lymphatics: the dose dependence." Cancer Res **46**(4 Pt 1): 1830-1834.

Stern, S. T., M. N. Martinez and D. M. Stevens (2016). "When Is It Important to Measure Unbound Drug in Evaluating Nanomedicine Pharmacokinetics?" Drug Metab Dispos **44**(12): 1934-1939.

Suganami, A., T. Toyota, S. Okazaki, K. Saito, K. Miyamoto, Y. Akutsu, H. Kawahira, A. Aoki, Y. Muraki, T. Madono, H. Hayashi, H. Matsubara, T. Omatsu, H. Shirasawa and Y. Tamura (2012). "Preparation and characterization of phospholipid-conjugated indocyanine green as a near-infrared probe." Bioorg Med Chem Lett **22**(24): 7481-7485.

Supersaxo, A., W. R. Hein and H. Steffen (1990). "Effect of molecular weight on the lymphatic absorption of water-soluble compounds following subcutaneous administration." Pharm Res **7**(2): 167-169.

Swartz, M. A. (2001). "The physiology of the lymphatic system." Adv Drug Deliv Rev **50**(1-2): 3-20.

Swartz, M. A. and A. W. Lund (2012). "Lymphatic and interstitial flow in the tumour microenvironment: linking mechanobiology with immunity." Nat Rev Cancer **12**(3): 210-219.

Swindle, M. M. (2012). "The development of swine models in drug discovery and development." Future Med Chem **4**(14): 1771-1772.

Swindle, M. M., A. Makin, A. J. Herron, F. J. Clubb, Jr. and K. S. Frazier (2012). "Swine as models in biomedical research and toxicology testing." Vet Pathol **49**(2): 344-356.

Taneva, E., K. Crooker, S. H. Park, J. T. Su, A. Ott, N. Cheshenko, I. Szleifer, P. F. Kiser, B. Frank, P. M. Mesquita and B. C. Herold (2015). "Differential Mechanisms of Tenofovir and Tenofovir Disoproxil Fumarate Cellular Transport and Implications for Topical Preexposure Prophylaxis." Antimicrob Agents Chemother **60**(3): 1667-1675.

Thomson, B. R., S. Heinen, M. Jeansson, A. K. Ghosh, A. Fatima, H. K. Sung, T. Onay, H. Chen, S. Yamaguchi, A. N. Economides, A. Flenniken, N. W. Gale, Y. K. Hong, A. Fawzi, X. Liu, T. Kume and S. E. Quaggin (2014). "A lymphatic defect causes ocular hypertension and glaucoma in mice." J Clin Invest **124**(10): 4320-4324.

Tian, W., S. G. Rockson, X. Jiang, J. Kim, A. Begaye, E. M. Shuffle, A. B. Tu, M. Cribb, Z. Nepiyushchikh, A. H. Feroze, R. T. Zamanian, G. S. Dhillon, N. F. Voelkel, M. Peters-Golden, J. Kitajewski, J. B. Dixon and M. R. Nicolls (2017). "Leukotriene B4 antagonism ameliorates experimental lymphedema." Sci Transl Med **9**(389).

Tilney, N. L. (1971). "Patterns of lymphatic drainage in the adult laboratory rat." J Anat **109**(Pt 3): 369-383.

Toland, H. M., K. D. McCloskey, K. D. Thornbury, N. G. McHale and M. A. Hollywood (2000). "Ca(2+)-activated Cl(-) current in sheep lymphatic smooth muscle." Am J Physiol Cell Physiol **279**(5): C1327-1335.

Treuting, P. M., S. M. Dintzis, C. W. Frevert, H. D. Liggitt and K. S. Montine (2012). Comparative anatomy and histology : a mouse and human atlas. Amsterdam ; Boston, Elsevier/Academic Press.

Trevaskis, N. L., L. M. Kaminskas and C. J. Porter (2015). "From sewer to saviour - targeting the lymphatic system to promote drug exposure and activity." Nat Rev Drug Discov **14**(11): 781-803.

Trezza, C., S. L. Ford, W. Spreen, R. Pan and S. Piscitelli (2015). "Formulation and pharmacology of long-acting cabotegravir." Curr Opin HIV AIDS **10**(4): 239-245.

Triacca, V., E. Guc, W. W. Kilarski, M. Pisano and M. A. Swartz (2017). "Transcellular Pathways in Lymphatic Endothelial Cells Regulate Changes in Solute Transport by Fluid Stress." Circ Res **120**(9): 1440-1452.

Turner, D. C., D. Moshkelani, C. S. Shemesh, D. Luc and H. Zhang (2012). "Near-infrared image-guided delivery and controlled release using optimized thermosensitive liposomes." Pharm Res **29**(8): 2092-2103.

Vago, L., M. C. Antonacci, S. Cristina, C. Parravicini, A. Lazzarin, M. Moroni, C. Negri, C. Uberti-Foppa, M. Musicco and G. Costanzi (1989). "Morphogenesis, evolution and prognostic significance of lymphatic tissue lesions in HIV infection." Appl Pathol **7**(5): 298-309.

Vainionpaa, N., R. Butzow, M. Hukkanen, D. G. Jackson, T. Pihlajaniemi, L. Y. Sakai and I. Virtanen (2007). "Basement membrane protein distribution in LYVE-1-immunoreactive lymphatic vessels of normal tissues and ovarian carcinomas." Cell Tissue Res **328**(2): 317-328.

Van den Broeck, W., A. Derore and P. Simoens (2006). "Anatomy and nomenclature of murine lymph nodes: Descriptive study and nomenclatory standardization in BALB/cAnNCrl mice." J Immunol Methods **312**(1-2): 12-19.

van Kampen, J. J., M. L. Reedijk, P. C. Burgers, L. J. Dekker, N. G. Hartwig, I. E. van der Ende, R. de Groot, A. D. Osterhaus, D. M. Burger, T. M. Luider and R. A. Gruters (2010). "Ultra-fast analysis of plasma and intracellular levels of HIV protease inhibitors in children: a clinical application of MALDI mass spectrometry." PLoS One **5**(7): e11409.

Van Rompay, K. K., D. Babusis, Z. Abbott, Y. Geng, K. Jayashankar, J. A. Johnson, J. Lipscomb, W. Heneine, K. Abel and A. S. Ray (2012). "Compared to subcutaneous tenofovir, oral tenofovir disoproxyl fumarate administration preferentially concentrates the drug into gut-associated lymphoid cells in simian immunodeficiency virus-infected macaques." Antimicrob Agents Chemother **56**(9): 4980-4984.

Verbeek, F. P., S. L. Troyan, J. S. Mieog, G. J. Liefers, L. A. Moffitt, M. Rosenberg, J. Hirshfield-Bartek, S. Gioux, C. J. van de Velde, A. L. Vahrmeijer and J. V. Frangioni (2014).

"Near-infrared fluorescence sentinel lymph node mapping in breast cancer: a multicenter experience." Breast Cancer Res Treat **143**(2): 333-342.

Verkade, H. J., M. A. de Bruijn, M. A. Brink, H. Talsma, R. J. Vonk, F. Kuipers and A. K. Groen (1996). "Interactions between organic anions, micelles and vesicles in model bile systems." Biochem J **320 (Pt 3)**: 917-923.

Wagner, J. G. and E. Nelson (1964). "Kinetic Analysis of Blood Levels and Urinary Excretion in the Absorptive Phase after Single Doses of Drug." J Pharm Sci **53**: 1392-1403.

Wallace, A. M., L. K. Han, S. P. Povoski, K. Deck, S. Schneebaum, N. C. Hall, C. K. Hoh, K. K. Limmer, H. Krontiras, T. G. Frazier, C. Cox, E. Avisar, M. Faries, D. W. King, L. Christman and D. R. Vera (2013). "Comparative evaluation of [(99m)tc]tilmanocept for sentinel lymph node mapping in breast cancer patients: results of two phase 3 trials." Ann Surg Oncol **20**(8): 2590-2599.

Ward, J. M., T. J. O'Leary, G. B. Baskin, R. Benveniste, C. A. Harris, P. L. Nara and R. H. Rhodes (1987). "Immunohistochemical localization of human and simian immunodeficiency viral antigens in fixed tissue sections." Am J Pathol **127**(2): 199-205.

Weinberg, R. A. (2014). The biology of cancer. New York, NY, US, Garland Science.

Weinstein, D. B., T. E. Carew and D. Steinberg (1976). "Uptake and degradation of low density lipoprotein by swine arterial smoot muscle cells with inhibition of cholesterol biosynthesis." Biochim Biophys Acta **424**(3): 404-421.

Westhoff, C. (2003). "Depot-medroxyprogesterone acetate injection (Depo-Provera): a highly effective contraceptive option with proven long-term safety." Contraception **68**(2): 75-87.

Wight, T. N. and S. Potter-Perigo (2011). "The extracellular matrix: an active or passive player in fibrosis?" Am J Physiol Gastrointest Liver Physiol **301**(6): G950-955.

Wiig, H. and M. A. Swartz (2012). "Interstitial fluid and lymph formation and transport: physiological regulation and roles in inflammation and cancer." Physiol Rev **92**(3): 1005-1060.

Willard-Mack, C. L. (2006). "Normal structure, function, and histology of lymph nodes." Toxicol Pathol **34**(5): 409-424.

Williams, P. E., H. M. Crauwels and E. D. Basstanie (2015). "Formulation and pharmacology of long-acting rilpivirine." Curr Opin HIV AIDS **10**(4): 233-238.

Xie, P., Q. Xin, S. T. Yang, T. He, Y. Huang, G. Zeng, M. Ran and X. Tang (2017). "Skeleton labeled 13C-carbon nanoparticles for the imaging and quantification in tumor drainage lymph nodes." Int J Nanomedicine **12**: 4891-4899.

Xiong, L., A. J. Shuhendler and J. Rao (2012). "Self-luminescing BRET-FRET near-infrared dots for in vivo lymph-node mapping and tumour imaging." Nat Commun **3**: 1193.

Xu, Z., Q. Wang, Y. Zhuang, B. Frederick, H. Yan, E. Bouman-Thio, J. C. Marini, M. Keen, D. Snead, H. M. Davis and H. Zhou (2010). "Subcutaneous bioavailability of golimumab at 3 different injection sites in healthy subjects." J Clin Pharmacol **50**(3): 276-284.

Yoneya, S., T. Saito, Y. Komatsu, I. Koyama, K. Takahashi and J. Duvoll-Young (1998). "Binding properties of indocyanine green in human blood." Invest Ophthalmol Vis Sci **39**(7): 1286-1290.

Yukl, S. A., S. Gianella, E. Sinclair, L. Epling, Q. Li, L. Duan, A. L. Choi, V. Girling, T. Ho, P. Li, K. Fujimoto, H. Lampiris, C. B. Hare, M. Pandori, A. T. Haase, H. F. Gunthard, M. Fischer, A. K. Shergill, K. McQuaid, D. V. Havlir and J. K. Wong (2010). "Differences in HIV burden and immune activation within the gut of HIV-positive patients receiving suppressive antiretroviral therapy." J Infect Dis **202**(10): 1553-1561.

Zanganeh, S., Y. Xu, C. V. Hamby, M. V. Backer, J. M. Backer and Q. Zhu (2013). "Enhanced fluorescence diffuse optical tomography with indocyanine green-encapsulating liposomes targeted to receptors for vascular endothelial growth factor in tumor vasculature." J Biomed Opt **18**(12): 126014.

Zeng, M., A. T. Haase and T. W. Schacker (2012). "Lymphoid tissue structure and HIV-1 infection: life or death for T cells." Trends Immunol **33**(6): 306-314.

Zhang, F., G. Niu, G. Lu and X. Chen (2011). "Preclinical lymphatic imaging." Mol Imaging Biol **13**(4): 599-612.

Zhao, L., P. Ji, Z. Li, P. Roy and C. G. Sahajwalla (2013). "The antibody drug absorption following subcutaneous or intramuscular administration and its mathematical description by coupling physiologically based absorption process with the conventional compartment pharmacokinetic model." J Clin Pharmacol **53**(3): 314-325.

Zheng, X., D. Xing, F. Zhou, B. Wu and W. R. Chen (2011). "Indocyanine green-containing nanostructure as near infrared dual-functional targeting probes for optical imaging and photothermal therapy." Mol Pharm **8**(2): 447-456.

Zhou, J. F., M. P. Chin and S. A. Schafer (1994). "Aggregation and degradation of indocyanine green." SPIE Proc. Laser Surg.: Adv. Charact., Ther., Syst. IV(2128): 495-505.

Zhu, B. and E. M. Sevick-Muraca (2015). "A review of performance of near-infrared fluorescence imaging devices used in clinical studies." Br J Radiol **88**(1045): 20140547.

Zhuang, Y., Y. Ma, C. Wang, L. Hai, C. Yan, Y. Zhang, F. Liu and L. Cai (2012). "PEGylated cationic liposomes robustly augment vaccine-induced immune responses: Role of lymphatic trafficking and biodistribution." J Control Release **159**(1): 135-142.

Zor, M., I. Yildirim, S. Basal, H. Yaman, M. Ozturk, C. H. Irkilata, S. Goktas and M. Dayanc (2012). "Intralymphatic delivery of platinum-based chemotherapeutics is possible: an experimental study." J Cancer Res Clin Oncol **138**(10): 1679-1682.

APPENDIX A

Below is a complete list of published peer-reviewed manuscripts and academic meeting abstracts authored and co-authored by John C. Kraft during his PhD thesis research.

Manuscripts

1. **Kraft JC**, Freeling JP, Wang Z, Ho RJ. Emerging science and clinical development trends of liposomes and lipid-nanoparticle drug delivery systems. J Pharm Sci 2014; 103(1):29-52.
2. **Kraft JC**, Ho RJ. Interactions of indocyanine green and lipid in enhancing near-infrared fluorescence properties: the basis for near-infrared imaging in vivo. Biochemistry 2014; 53(8):1275-83.
3. Ho RJ, Yu J, Li B, **Kraft JC**, Freeling JP, Koehn J, Shao J. Systems Approach to targeted and long-acting HIV/AIDS therapy. Drug Deliv Transl Res 2015; Aug 28.
4. Shao J, **Kraft JC**, Yu J, Li B, Freeling JP, Koehn J, Ho RJ. Nanodrug formulations to enhance HIV drug exposure in lymphoid tissues and cells: clinical significance and potential impact on treatment and eradication of HIV/AIDS. Nanomedicine (Lond) 2016; 11(5):545-64.
5. **Kraft JC**, McConnachie LA, Koehn J, Kinman L, Collins C, Shen DD, Collier AC, Ho RJY. Long- acting combination HIV therapy enhances and sustains drug levels in plasma and cells in blood and lymph nodes. AIDS. 2017 Mar 27;31(6):765-770.
6. Krogstad EA, Ramanathan R, Nhan C, **Kraft JC**, Blakney AK, Cao S, Ho RJY, Woodrow KA. Nanoparticle-releasing nanofiber composites for enhanced in vivo vaginal retention. Biomaterials. 2017 Nov;(144):1-16.
7. Mu Q, Yu J, McConnachie LA, **Kraft JC**, Gao Y, Gulati GK, Ho RJY. Translation of combination nanodrugs into nanomedicines: lessons learned and future outlook. J Drug Target. 2018 Jan;(10):1-13.
8. **Kraft JC**, McConnachie LA, Koehn J, Kinman L, Sun J, Collier AC, Collins C, Shen DD, Ho RJY. Mechanism-based pharmacokinetic (MBPK) models describe the complex plasma kinetics of three antiretrovirals delivered by a long- acting anti-HIV drug combination nanoparticle formulation. Journal of Controlled Release. 2018 Feb 10;275:229-241.
9. **Kraft JC**, Treuting PM, Ho RJ. Indocyanine green nanoparticles undergo selective lymphatic uptake, distribution, and retention and enable detailed mapping of lymph vessels, nodes, and abnormalities. Journal of Drug Targeting. 2018 Feb 12:1-11.
10. McConnachie LA, Kinman LM, Koehn J, **Kraft JC**, Lane S, Lee W, Collier AC, Ho RJ. Long- acting profile of four drugs in one anti-HIV nanosuspension in non-human primates five weeks following a single injection. J Pharmaceutical Sciences. 2018 Mar 13.
11. **Kraft JC**, Gao Y, Yu D, Ho RJ. Recent developments of nanotherapeutics for targeted and long-acting, combination HIV chemotherapy. European Journal of Pharmaceutics and Biopharmaceutics. European Journal of Pharmaceutics and Biopharmaceutics. 2018.

12. Koehn J, Iwamoto JF, **Kraft JC**, McConnachie LA, Collier AC, Ho RJY. Extended cell and plasma drug levels after one dose of a 3-in-1 nanosuspension containing lopinavir, efavirenz, and tenofovir in non-human primates. AIDS. 2018.

Abstracts

1. **Kraft JC**, Ho RJ. Lipid-Bound Indocyanine Green Particles Enable High Resolution Near-Infrared Diagnostic Imaging of the Lymphatic System. Poster presentation at the Globalization of Pharmaceutics Education Network (GPEN) Conference in Helsinki, Finland, August 2014.
2. **Kraft JC**, Ho RJ. Lipid-Associated Indocyanine Green Nanoparticles Allow Mapping of Lymphatics and Pathology with Near- Infrared Fluorescence Bioimaging. Poster presentation (#W5032) at the AAPS Annual Meeting in San Diego, CA, November 2014.
3. **Kraft JC**, Ho RJ. Localization of Novel ICG Nanoparticles Enable Detection of Cancer-Infiltrated Tissues and Lymphatic Vessel Abnormalities Using High-Resolution Infrared Imaging. Poster presentation at the Vancouver Nanomedicine Day, November 2, 2015.
4. **Kraft JC**, Koehn J, Shao J, Ho RJ. Novel Lipid-Nanoparticles for In Vivo Near-Infrared and Magnetic Resonance Imaging Elucidate Nanoparticle-Bound Small Molecule Distribution in Lymph vs Blood. Oral presentation for short-course symposia on lymphatic drug delivery at the GPEN Conference in Lawrence, KS, November 2016.
5. **Kraft JC**, Koehn J, Shao J, Ho RJ. Novel Lipid-Nanoparticles for In Vivo Near-Infrared and Magnetic Resonance Imaging Elucidate Nanoparticle-Bound Small Molecule Distribution in Lymph vs Blood. Oral poster presentation (27R0830) at the AAPS Annual Meeting in Denver, CO, November 2016.
6. Koehn J, **Kraft JC**, McConnachie L, Kinman L, Lane S, Lee W, Collier A, Ho RJ. Long-Acting 3 HIV-Drugs-In-One Nanoparticle Formulation Intended For Adolescents. Poster #487 at the Conference on Retroviruses and Opportunistic Infections (CROI) Annual Meeting in Boston, MA, March 2018.
7. McConnachie L, Kinman L, Koehn J, **Kraft JC**, Lane S, Lee W, Collier A, Ho RJ. Long-Acting Pharmacokinetics Of 4 HIV Drugs Coformulated In One Nano-Formulation. Poster #488 at the Conference on Retroviruses and Opportunistic Infections (CROI) Annual Meeting in Boston, MA, March 2018.

APPENDIX B

Model Descriptions and Differential Equations

Free ARV Compartmental Models

For each ARV in the free ARV combination, drug was administered as a subcutaneous bolus injection of ng ARV (*ex1*) into compartment q1 (Figure 3A, 3B). In general, intercompartmental transfer was described by first-order rate constants. Initial conditions for q1 was the assigned free ARV dose at t = 0 (*ex1(0)*), while those for all other differential equations were zero.

Glossary of Terms

ex1 = exogenous subcutaneous bolus dose of free ARV (in ng) into q1; ***q1*** = ng ARV in the subcutaneous injection site compartment; ***q2*** = ng ARV in the central compartment; ***q3*** = ng ARV in the peripheral compartment; k_{21} = first-order rate constant of drug distribution from q1 to q2; k_{32} = first-order rate constant of drug distribution from q2 to q3; k_{23} = first-order rate constant of drug distribution from q3 to q2; k_{02} = first-order elimination rate constant of drug distribution from q2.

Differential Equations for TLC-ART101 ARV Compartmental Models

For each ARV in TLC-ART101, drug was administered as a subcutaneous bolus injection of ng ARV (ex1 into compartment q1 if DcNP-associated, or ex2 into compartment q6 if free; Figure 3C, 3D).

DcNP-associated ARVs

$$\frac{d(q1)}{dt} = ex1(t) - k_{21} \cdot q1 - k_{31} \cdot q1 - k_{41} \cdot q1 \quad (2)$$

$$\frac{d(d2_1)}{dt} = k_{T2} \cdot (q1 - d2_1) \quad (3)$$

$$\frac{d(d2_i)}{dt} = k_{T2} \cdot (d2_{i-1} - d2_i) \quad i = 2,3 \quad (4)$$

$$\frac{d(d3_1)}{dt} = k_{T3} \cdot (q1 - d3_1) \quad (5)$$

$$\frac{d(d3_i)}{dt} = k_{T3} \cdot (d3_{i-1} - d3_i) \quad i = 2,3 \quad (6)$$

$$\frac{d(d4_1)}{dt} = k_{T4} \cdot (q1 - d4_1) \quad (7)$$

$$\frac{d(d4_i)}{dt} = k_{T4} \cdot (d4_{i-1} - d4_i) \quad i = 2,3 \quad (8)$$

$$\frac{d(q5)}{dt} = k_{T2} \cdot d2_3 + k_{T3} \cdot d3_3 + k_{T4} \cdot d4_3 - k_{75} \cdot q5 \quad (9)$$

Free ARVs

LPV and RTV:

$$\frac{d(q6)}{dt} = ex2(t) - k_{76} \cdot q6 \quad (10)$$

$$\frac{d(q7)}{dt} = k_{75} \cdot q5 + k_{76} \cdot q6 - k_{07} \cdot q7 \quad (11)$$

TFV:

$$\frac{d(q6)}{dt} = ex2(t) - k_{76} \cdot q6 \quad (12)$$

$$\frac{d(q7)}{dt} = k_{75} \cdot q5 + k_{76} \cdot q6 - k_{87} \cdot q7 - k_{78} \cdot q8 - k_{07} \cdot q7 \quad (13)$$

$$\frac{d(q8)}{dt} = k_{87} \cdot q7 - k_{78} \cdot q8 \quad (14)$$

In general, intercompartmental transfer was described by first-order rate constants. Initial conditions for q1 and q6 were the assigned DcNP-associated (*ex1(0)*) and free (*ex2(0)*) portions of the TLC-ART101 dose, while those for all other differential equations were zero.

Glossary of Terms

ex1 = exogenous subcutaneous bolus dose of DcNP-associated ARV (in ng) into q1; ***ex2*** = exogenous subcutaneous bolus dose of free ARV (in ng) into q6; ***q1*** = ng ARV in the subcutaneous injection site compartment for DcNP-associated ARVs; ***q6*** = ng ARV in the subcutaneous injection site compartment for free ARVs; $d2_i$ = ng ARV in the rapid lymphatic delay sub-compartments; $d3_i$ = ng ARV in the intermediate lymphatic delay sub-compartments; $d4_i$ = ng ARV in the slow lymphatic delay sub-compartments; ***q5*** = ng ARV in the central compartment for DcNP-associated ARVs; ***q7*** = ng ARV in the central compartment for free ARVs; ***q8*** = ng ARV in the peripheral compartment for free ARVs; $k_{T2} = k_{21} = k_{52} = d_{52}(3/tlag1)$ = first-order rate constant of drug distribution from q1 to $d2_1$, from $d2_1$ to $d2_2$, from $d2_2$ to $d2_3$, and from $d2_3$ to q5 ($d2_1$, $d2_2$, and $d2_3$ are the three sub-compartments in series within delay compartment ***d2***), where $d_{52} = 1$ and ***tlag1*** = the overall time delay of transit through d2; $k_{T3} = k_{31} = k_{53} = d_{53}(3/tlag2)$ = first-order rate constant of drug distribution from q1 to $d3_1$, from $d3_1$ to $d3_2$, from $d3_2$ to $d3_3$, and from $d3_3$ to q5 ($d3_1$, $d3_2$, and $d3_3$ are the three sub-compartments in series within delay compartment ***d3***), where $d_{53} = 1$ and ***tlag2*** = the overall time delay of transit through d3; $k_{T4} = k_{41} = k_{54} = d_{54}(3/tlag3)$ = first-order rate constant of drug distribution from q1 to $d4_1$, from $d4_1$ to $d4_2$, from $d4_2$ to $d4_3$, and from $d4_3$ to q5 ($d4_1$, $d4_2$, and $d4_3$ are the three sub-compartments in series within delay compartment ***d4***), where $d_{54} = 1$ and ***tlag3*** = the overall time delay of transit through d4; k_{75} = first-order rate constant of drug distribution from q5 to q7; k_{76} = first-order rate constant of drug distribution from q6 to q7; k_{87} = first-order rate constant of drug distribution from q7 to q8; k_{78} = first-order rate constant of drug distribution from q8 to q7; k_{07} = first-order elimination rate constant of drug distribution from q7.

VITA

John Cavin Kraft II was born in Wichita, Kansas.

In 2007, he earned a Bachelor of Science in Chemistry from The University of Kansas.